Modelling the mechanisms of microsilica particle formation and growth

Raquel González Fariña

Wolfson College

University of Oxford

A thesis submitted for the degree of

Doctor of Philosophy

Michaelmas 2020

Acknowledgements

First of all, I would like to thank my academic supervisors, Robert Van Gorder, James Oliver, and Andreas Münch for their constant support, guidance, and patience for the past three years. To Robert, for always being available to discuss both Mathematics and PhD life, and for his commitment to the supervision through space and time. To Jim, for his valuable ideas and for encouraging me to teach at Jesus College, which made me discover my enthusiasm for teaching. To Andreas, for his continuous engagement with the supervision, helpful advice, and for always reminding me of the big picture.

I would also like to thank my industrial supervisors, Aasgeir Valderhaug, for his drive to keep the research in line with the industrial application, and Ben Sloman, who has been a fantastic link between the mathematical and practical aspects of the project. I am grateful to Elkem ASA for their financial support and opportunity to work on-site during parts of the project, and to my collaborators at Elkem Fiskaa, for the useful discussions about my research. In particular, to Andrea Freitag, Rolf Birkeland, Anne Gry Messenlien, and Egil Vålandsmyr Herland, for their scientific insights, and to Solveig Steinsland for being an incredible host and friend. I would also like to thank Nils Kamfjord, Halvard Tveit, and Merete Tangstad.

I am thankful to all the exceptional people I have shared these past years with in Oxford. First, to the members of InFoMM and especially of Cohort 3, who have been like a family to me. In particular, to Attila for always making time to help, to Clint who made PhD life easier by providing me with wine on a daily basis, and to Fede, whose friendship from the very first day has been invaluable. Many thanks also to Scott, Ana, Matteo, Caoimhe, Nabil, Ferrán, Mary Peyton, and Natalia.

Finally, I'd like to thank my family and friends back in Tenerife who have always been by my side, despite the distance. Most importantly, I'd like to thank my parents and brother, for their unconditional love and support, and without whom none of this would have been possible. ¡Gracias!

Abstract

Microsilica particles arise as a byproduct of silicon furnace operation, created inside high temperature flames due to the combustion reaction of silicon monoxide with oxygen. These nanoparticles, which grow as silicon dioxide vapour condenses on the surface of existing particles, are used in a variety of composite materials. The size and quality of the particles affect the performance of the material used for such applications, and hence control of these quantities is of importance to manufacturers.

Motivated by this, we derive a mathematical model that connects local fluid flow, thermal and chemical conditions of the furnace to the formation and growth of microsilica particles. Since the regions where microsilica particles form are local to a very thin reaction zone, we focus on the dynamics within the flame front. We first study two distinct reductions of the model: the case of initially well-mixed or spatially homogeneous chemical species, and the case of initially separated chemical species. In the latter case, the one-dimensional domain is given by a cross section of the reaction zone and diffusion plays a dominant role in providing material to a combustion front. In order to incorporate fluid flow, we extend the previous work to 2-D by considering a mixing layer approach, that is, by assuming two parallel flows entering the domain with distinct velocities, temperatures, and concentrations. We study how the mixing layer evolves as both streams interact, and how mixing affects the formation and growth of particles. In all cases, we provide asymptotic approximations under various limits and neglecting the effect of the particles on the chemicals and temperature, and numerical solutions of the full model. Our results suggest that oxygen availability and a sufficiently high temperature are essential for the combustion reactions to occur, strongly influencing the width of the reaction zone and the particle size distribution. Furthermore, when the flow is almost uniform, fewer particles form and more of the total mass corresponds to large particles, in contrast with the non-uniform case.

Contents

List of Figures

List of Tables

Chapter 1

Introduction

1.1 Background

Fugitive emissions in the ferroalloy industry represent a threat to both the environment and health. Microsilica or silica fume is a by-product of the manufacture of silicon, ferro-silicon and other silicon alloys, and in the past it was a major source of air pollution until it was captured in filters [69]. In Figure 1.1 we show a picture of one of Elkem ASA's old silicon plants releasing large amounts of silica fume (white smoke) and other harmful products [22]. Elkem ASA is one of the world's leading suppliers of silicon and Elkem Microsilica®, amongst other products. In 1950, it became one of the first companies worldwide to start research into applications of microsilica. However, it was not until the late 1970s when plants started becoming fully smoke-free, as a consequence of air pollution enforcement placed on the silicon production industry in Norway. The collection of the material created a huge disposal problem and research on the uses of microsilica became more intense, with commercial sales to the concrete industry beginning in 1980 [23]. Nowadays, microsilica is utilised in numerous applications but its primary use is still as an additive in high performance concrete, enhancing its properties. The Petronas Towers (Kuala Lumpur), Burj Khalifa (Dubai), and The Great Belt Bridge (Denmark) are examples of infrastructures that were built with a concrete blend containing some percentage of microsilica.

In recent years, new regulatory requirements on lowering NO_x emissions have led to new operating strategies and modifications to the furnace off-gas system design. Silicon furnaces have become more efficient and environmentally friendly with lower emissions of CO_2 per unit silicon produced. However, these changes have also severely affected the microsilica quality, to the point of making it unusable in the customer's process. In addition, most silicon furnaces have doors that are continuously opened by

Figure 1.1: Elkem ASA's silicon plant in Kristiansand (Norway, ca. 1970) releasing silica fume and other harmful gases into the atmosphere. Image provided by Elkem ASA [22].

the operators, exposing them to silica fume and other harmful gases which represents a potential health hazard [57]. Motivated by this, multiple studies aiming to understand the mechanisms of formation and growth of these particles have been carried out, with the objective of controlling the quality and properties of microsilica. In order to properly do so, a full understanding of how the local conditions of the silicon furnace affect the final microsilica output is needed.

1.1.1 The silicon production process

The core of a silicon production plant is the submerged arc furnace, as shown on the left-hand side of Figure 1.2, where we can see a schematic of the whole silicon production process. A typical medium-size furnace has a diameter of around 10 metres and a height of approximately 3 metres, and consists of steel casing walls covered by a refractory material with a carbon lining on the inside capable of withstanding high temperatures of around 3000°C [39, 69]. Raw materials, also called charge materials, such as quartz, carbon, and woodchips are fed directly into the furnace, either manually by an operator through the furnace doors, or through charging tubes. Three electrodes are submerged into the charge supplying the energy required for the production of silicon. The silicon process is highly energy consuming since it requires temperatures

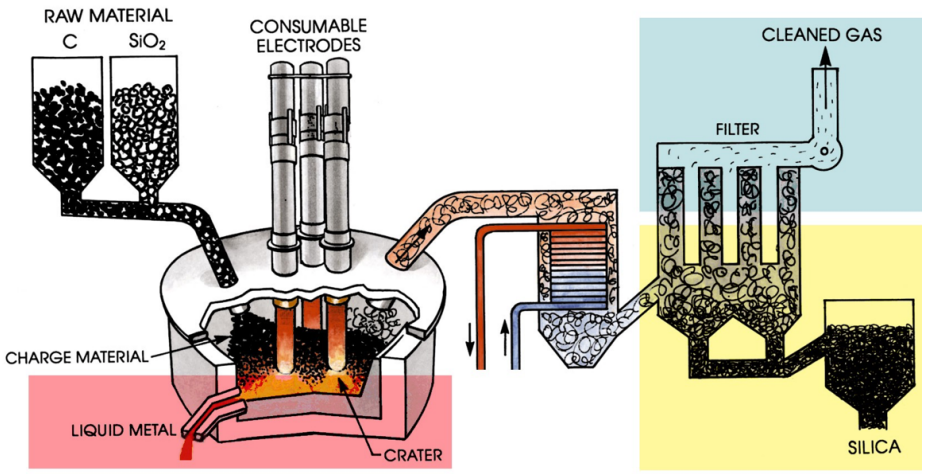

Figure 1.2: Schematic of an arc furnace showing the different processes: see text for details. Reproduced from [69].

around 1800°C in order for the process to run properly. This is obtained from the current supplied by the electrodes which heats the charge through electric arcs. At this high temperature the silicon dioxide present in quartz is reduced to liquid silicon, which is tapped from the bottom of the furnace through a taphole.

The process is cyclical: the raw materials are consumed on the way down to the crater, producing voids on the furnace top which have to be refilled. The crater refers to the open spacing underneath the electrode where the electric arc burns. Sometimes the operator is required to 'stoke' the surface (manually break up the crust region that may form) in order to maintain the raw material flow down into the furnace or to stop gas escaping from the reaction zone of the furnace. The gas from the furnace burns above the charge surface due to the presence of excess air which comes mainly from the opening of the furnace doors and from a small separation gap between the main furnace and the hood above it. The furnace hood collects all the off gases from the process, and the large amount of energy present in this gas can be recovered in heat exchangers and used again to produce electrical energy in a power plant. The smoke collected in the off gas system is cooled down and is made to pass through cyclones where coarse particles are removed to protect the subsequent filtering. Finally, the dust collected through bag house filters consists mainly of amorphous SiO_2, named 'condensed silica fume' or 'microsilica'. The remaining gas, mainly composed of N_2, O_2, CO_2, as well as small amounts of SO_2, and different nitrogen oxides (NO_x), is released to the atmosphere [69].

1.1.2 Chemical species and reactions in a silicon furnace

In order to identify the key physics of the silicon furnace that are involved in the formation of microsilica particles, we first need to understand the basic chemistry underlying the silicon process. A great number of reactions take place in order for Si to be formed. However, the production of the SiO (silicon monoxide) gas is the engine of the furnace reaction chemistry [48]. This gas is mainly formed in the crater area by the reaction between silicon and molten SiO_2,

$$\mathrm{Si(l)} + \mathrm{SiO_2(l)} \rightleftarrows 2\mathrm{SiO(g)}. \tag{1.1.1}$$

Here, (l) denotes a liquid, (g) denotes a gas, and below (s) will denote a solid. Some of this SiO gas is used around the crater area to form liquid silicon by the reaction

$$\mathrm{SiC(s)} + \mathrm{SiO(g)} \rightarrow 2\mathrm{Si(l)} + \mathrm{CO(g)}. \tag{1.1.2}$$

The two gases produced in the furnace craters, SiO and CO, flow upwards. Most of the SiO will react with carbon in an upper region forming SiC by the reaction

$$\mathrm{SiO(g)} + 2\mathrm{C(s)} \rightarrow \mathrm{SiC(s)} + \mathrm{CO(g)}. \tag{1.1.3}$$

If too much carbon is fed to the furnace, too much SiC will be produced and will accumulate. However, if too little carbon is supplied and is not enough to bind all the SiO, some of this gas will condense to form Si and SiO_2.

Some of the silicon monoxide will also reach the furnace top, reacting with O_2 present in the furnace hood to form SiO_2 vapours or microsilica. The CO gas also flows to the furnace hood, reacting with O_2 to form CO_2. These are the two main off-gases of the silicon production process and are directly involved in the formation of microsilica. Thus, throughout this thesis we will focus our attention on the two combustion reactions:

$$2\mathrm{SiO(g)} + \mathrm{O_2(g)} \overset{R_1}{\rightarrow} 2\mathrm{SiO_2(g)}, \tag{1.1.4}$$

$$2\mathrm{CO(g)} + \mathrm{O_2(g)} \overset{R_2}{\rightarrow} 2\mathrm{CO_2(g)}, \tag{1.1.5}$$

which take place above the charge surface, inside the furnace hood. Both of these reactions are exothermic in that they release a large amount of energy, producing really bright flames. However, when the combustion is dominated by the SiO oxidation forming microsilica, the flames colour turns white and the temperature is much higher, reaching around 3000°C. Before the particles form, SiO_2 is in a vapour phase, which

can be treated as an ideal gas. When this vapour reaches saturation, it undergoes a change of state from gas into solid, resulting in the formation of microsilica particles. During this process, a large amount of energy is also released. We remark, however, that there is still a lack of knowledge about the real physical state of SiO_2 prior to nucleation into particles. We will describe the particle formation and growth mechanisms further in the next section. More details on the chemistry of the silicon furnace can be found in [69].

1.1.3 Microsilica

With increased environmental awareness, the use of industrial byproducts, such as microsilica, is an attractive alternative to disposal [75]. The silicon yield through the silicon production process is about 80%, meaning that this percentage of the raw material quartz is reduced to silicon, while approximately some $10 - 25\%$ ends up as microsilica, also called silica fume [23]. Depending on the type of furnace and on demand, different operating strategies can be followed in order to maximise microsilica production and quality over silicon yield.

Silica fume consists mainly of very fine spherical particles of amorphous SiO_2 that form as SiO_2 vapours condense. It is amorphous since the speed at which condensation occurs prevents the particles from forming a crystalline structure. More than 95% of the particles are finer than 1μm (see Figure 1.3), and the material has a specific surface area, or total surface area per unit of mass, of around 20m^2 per gram [69]. Silica particles usually contain some impurities, such as small amounts of iron, magnesium and other alkali oxides. These come from the raw materials, which contain elements with low boiling points that bond with the silica.

The exact mechanisms of formation and growth of microsilica particles are not yet fully understood. In Figure 1.4, we show a schematic summarising the main physical processes involved in the generation of these particles and which are common in the formation of many other aerosols (see [26] for a reference book on fundamentals of aerosol dynamics). Firstly, we have SiO_2 molecules that nucleate into the smallest possible particles once saturation conditions are reached. The surface of these nuclei then grows by condensation, that is, by molecular addition of mass to the surface of the particles. At this stage, particles show a perfectly spherical shape which may be due to surface tension. Some small percentage of the primary particles created show aggregation, like the one attached to the top of the largest particle in Figure 1.3 with an irregular shape. This is believed to happen due to long retention times

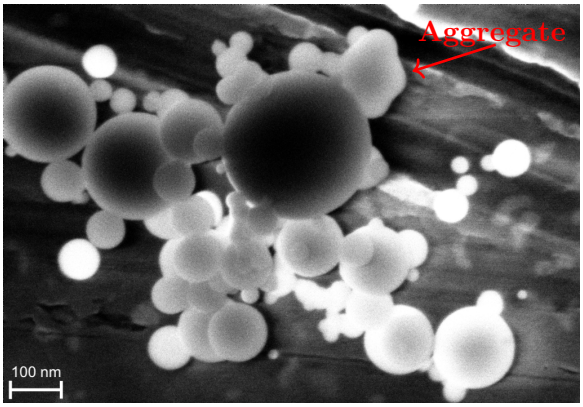

Figure 1.3: Image of microsilica particles taken with a scanning electron microscope. The majority of the particles are perfectly spherical and form agglomerates (weak bonds), while a small percentage form aggregates (some with irregular shape as in the top right corner). Image provided by Elkem ASA [22].

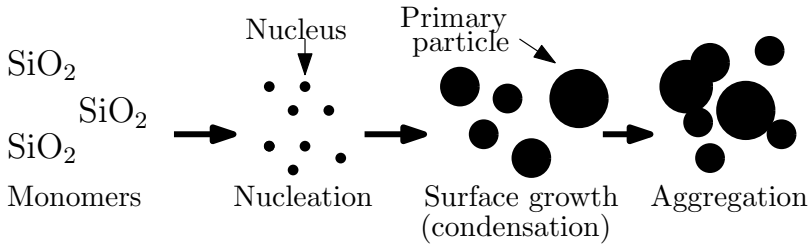

Figure 1.4: Formation and growth mechanisms of microsilica particles.

in high temperature areas, and it is the main cause of a bad quality microsilica. In later stages of the silicon process, when microsilica is collected, cooled, and bagged, a high percentage of particles agglomerate via weak interparticle forces, such as Van-der-Waals forces, as can be seen from Figure 1.3, where most particles are attached to each other [20]. The main difference between aggregation and agglomeration is that in the first case the particles are irreversibly attached to each other, for example by sinter bridges, and the total aggregate surface area is minimized by partial or full coalescence, whereas for the latter process the agglomerate surface area is equal to the sum of the primary particles surface areas, and the weak bonds can be broken easily with a dispersing machine [4, 26].

Good quality silica fume is such that particles do not contain impurities and do not aggregate. Also, depending on the area of application of the material, certain particle sizes or surface areas are preferred for an optimal performance. The main use of the silica fume is as an additive in high performance concrete, since it increases toughness giving a higher bond strength, enhances its durability, lowers the permeability to

chloride and water intrusion significantly, and causes high electrical resistivity. As a result of these enhanced properties, we find it in many highway bridges and marine structures. It is also utilised in the manufacturing of refractories and polymers, and in the oil industry primarily for oil well cementing [55].

It has been shown that modifications in the silicon production process affect not only the microsilica yield, but also the quality of the particle, size, and surface area. These modifications involve changes in operating strategies such as the control of the silicon yield, raw material composition, opening and closing of the doors, and the temperatures of the off gases under the hood. These changes in silica quality have a great impact on the performance of the material in several applications, thus there is a need to study which conditions affect the microsilica properties and, in particular, which conditions are favourable for microsilica formation and growth.

1.2 Literature review

There are three main fields where literature needs to be reviewed before developing a realistic mathematical model of the formation and growth of microsilica particles in silicon furnaces. These are: flows of reactive gas mixtures, formation and growth of aerosols, and previous works on modelling within a silicon furnace. In this section, we give a concise high level review of the most relevant publications on these topics and the interface between them.

1.2.1 Reactive gas mixtures

The first theoretical models for chemically reactive flows were in the field of combustion. Combustion can be divided into premixed and non-premixed. Premixed combustion corresponds to the case where the chemical reactants, fuel and oxidizer, are initially premixed at a molecular scale. Whereas when the reactants are initially separated (non-premixed), a diffusion flame develops at the contact surface between the fuel and oxidizer [63]. In the latter case, mixing of the reactants is a necessary part of the flow behaviour that needs to be studied. Interestingly, simplified models that have been derived for non-premixed combustion are usually less complicated than those for premixed combustion. This is the case when the limit of large chemical reaction rate is taken, allowing the rate term to be eliminated from the flow equations for non-premixed systems only [92]. In this thesis we will study both scenarios without any assumptions on the reaction rate: in Chapter 4 we will focus on the well-mixed case,

whereas in Chapters 5 and 6 we will consider the chemicals to be initially spatially separated.

In the theory of diffusion flames, a non-dimensional parameter of interest is the Damköhler number which is given as the ratio of the characteristic diffusion and the chemical reaction timescales [9, 63]. When the ratio is much larger than unity, the reaction accelerates and the equilibrium composition is quickly approached, and if the ratio is much smaller than unity, the composition is said to be frozen. When the ratio is of order unity, the chemical reaction and the mechanical processes are coupled and we have a relaxing flow, where the details of all the reaction pathways and associated reaction rates must be known, making this case more challenging. Therefore, another distinction can be made based on the rapidity of the chemical kinetics, with infinitely-fast or finite-rate chemistry. In our work, we will look at the more complex case of having finite-rate chemistry, since this limit is needed in order to investigate how particles form while the combustion reaction is happening. This is in contrast to many studies that focus only on one or both of the limiting cases, frozen or equilibrium, due to their simplicity and the availability of analytical solutions. For instance, in [43], a theoretical study of turbulent mixing of reactive gases under both limits is presented, remarking that for low speed flames when fuel is injected into an oxidizer, diffusion is the rate controlling process, and therefore equilibrium chemistry prevails. However, for high-speed flows, such as those occurring in supersonic combustion, the flow timescales are relatively small and frozen chemistry is more realistic. One of the simplest and most famous examples of a diffusion flame is the Burke-Schumann problem [11], which models a flame-surface between two coaxial flows with equal velocities. Some of the assumptions are the Shvab–Zel'dovich approximation [63] which simplifies the equations for the flow, assuming infinitely fast reactions, negligible diffusion in the axial direction compared to the radial direction, and zero radial velocity component.

Most analytical studies of combustion focus on one-dimensional flame fronts, mainly due to the laminar combustion zone being very thin. However, in multiple real situations, like free jets or combustion under conditions of mixing between two gases, we need to consider a second spatial dimension. In this thesis, we will explore the formation of particles assuming both one-dimensional and two-dimensional reaction zones. In many cases, transverse velocities are small compared to that in the main flow direction, and the problem can be simplified by making use of the boundary-layer approximation. For further details on the boundary-layer theory we refer the reader to the textbook by Schlichting et al. [70].

An assumption that some studies related to mixing of reactive chemicals take is that of isothermal conditions in the flow [72, 86]. In the case of combustion this assumption needs to be removed in order to properly describe the fluid flow, and an energy conservation equation must be introduced to describe the temperature variations. The problem of combustion in a laminar mixing zone may be formulated as two semi-infinite streams of gas (combustible and combustion products) flowing parallel with different initial velocities and temperatures. The three main physical processes involved in this problem as described by Marble and Adamson [51] are: (a) the development of the laminar mixing layer between the two streams due to viscous stresses, (b) the development of the temperature field via conduction and convection through the streams, and chemical reaction which eventually distorts the temperature profile making the local temperature exceed that of the hot gas stream, (c) molecular diffusion of the gases into each other together with consumption of the combustible and generation of products. In their analysis, Marble and Adamson [51] first study the initial portion of the mixing zone, where the heat from chemical reaction is small enough that the problem can be solved by perturbing the solution for the mixing without combustion, and assuming that the initial velocity ratio between the streams is unity. Secondly, [51] study the development of the combustion reaction from ignition to the formation of the plane laminar flame front by using a similar approximation to the integral technique developed by von Kárman for boundary layer theory [40]. In Chapters 5 and 6, we will also find both limits: initial development of a mixing layer where the reactions are not relevant and the problem is mainly diffusive, and later development where reactions dominate. In both cases, we will obtain analytical approximations under more relaxed assumptions and use different mathematical techniques to those in [51]. In addition, we will also analyse the coupled particle formation and growth processes within the mixing layer.

Casaccio [13] analyses the mixing of two parallel reactive streams under the influence of an externally induced streamwise pressure gradient, whereas in some other works [44, 51] the pressure is assumed to be constant due to simplicity and since the pressure in flames is nearly uniform [63]. The usual way of approaching the boundary-layer equations is to transform them into ordinary differential equations, called similarity equations, by introducing a change of coordinates involving a stream function [70]. In the case of having a compressible flow, the problem is usually first transformed into a corresponding incompressible flow by making use of the Dorodnitzin-Howarth transformation [35], as in [44, 51].

So far, we have only focused on works concerning laminar flows, however, in

practice, reactive gas flows are often turbulent. The inclusion of turbulence effects in the mixing of reactive gases is of importance since turbulence increases the contact surface between the fuel and oxidizer, and between the unburned and burned gases by stretching and crumpling, which is favourable in combustion. It also supports diffusive phenomena since turbulence transfer is more effective than molecular transfer [63]. In [43], Libby presents a theoretical analysis of combustion in a high speed, turbulent mixing region corresponding to an axisymmetric fuel jet. The equations describing the flow are taken to be the same as for laminar flow but with the variables representing mean turbulent quantities, and a convenient model is introduced for the eddy viscosity which allows the momentum equation to be transformed into an incompressible form. They conclude that small values of the inlet velocity are desirable to guarantee combustion and to reduce the length of the reaction region, in contradiction with their later work on laminar flow [44]. As with the laminar case, we can have turbulent mixing layers. In [85], the equations for the turbulent mixing of a two-dimensional supersonic jet on an ambient supersonic stream are presented. Both streams are composed of a mixture of chemically reactive gases, and so the equation of continuity must be satisfied for each chemical species and for the mixture. During the first steps of the development of the mixing layer, the flow is laminar and molecular action is predominant, while in the later stages it becomes turbulent and turbulent motion is primarily responsible for the transfer phenomena. Since including turbulence effects would make it more challenging to obtain analytical approximations, in most of this thesis we will only be concerned with laminar flow, and we will look at slightly different limits to the ones considered in the majority of the previously mentioned works regarding turbulence.

1.2.2 Aerosol modelling

In many applications reactive flows are responsible for the production of aerosols, meaning a suspension of fine particles in gases or air. That is the case, for instance, in the production of nanoparticles via gas-phase synthesis, soot formation in car engines, and crystals precipitation in liquid-phase reactors. Aerosol science plays a key role in many different fields including atmospheric science and air pollution, and it has been widely studied for many years (for reference books see, *e.g.*, [24, 26]). Since the mechanisms of formation of microsilica particles are not well understood, in order to make some progress we ought to look at the general literature on the formation and growth of aerosol particles.

Particles are usually polydispersed, meaning that one or more properties may differ, such as the diameter, and therefore present a particle size distribution. In the case of nanoparticle synthesis, where the product needs to be manufactured with desired properties since this determines its suitability in the different applications, an accurate prediction of the particle size distribution is required. The theory of polydispersed particle dynamics originated in the work of Smoluchowski [79], and it was initially applied by the atmospheric science community [26], followed by the mechanical and chemical engineering community due to its relevance in engineering problems such as soot formation.

Mathematical modelling of the particle size distribution is carried out via the population balance equation (PBE) or general dynamic equation (GDE). This is a conservation equation for the number density function of particles that accounts for spatial transport, nucleation, growth, coagulation, and breakage of particles [65] (this modelling framework will be used in this thesis to gain a more quantitative understanding of the physical processes that particles undertake). For instance, Pratsinis [62] presented a model on simultaneous nucleation, condensation, and coagulation in aerosol reactors. He assumes the classical Becker-Döring nucleation theory [5], and studies aerosol dynamics in both the free molecule size and continuum regimes. Similarly, Flagan and Lunden [25] emphasise growth by coagulation and coalescence from the vapour phase, and give expressions for the Brownian collision rates for both spherical particles and complex agglomerate structures.

Surface reaction is another common growth mechanism. Artelt *et al.* [3] studied the formation and growth mechanisms during titania formation from the vapour phase. The main particle formation mechanisms described are chemical reactions in the gas phase and nucleation. With respect to primary particle growth, [3] conclude that the reaction on the surface of existing TiO_2 is dominant. Similar studies on nucleation and growth of fine particles have been undertaken for the case of MgO smoke [81] and microalumina particles [6]. The latter explores how the condensation reaction depends on thermal effects. In our work, we will adopt this approach, and will only focus on the continuous growth of the particles by condensation as the main growth mechanism. However, we will consider mass diffusion-driven growth, rather than heat diffusion-driven growth. That is, the rate of change of a particle's size will be determined by the diffusion mass flux between the particle and its surrounding fluid. This approach has been used before for the case of microsilica, *e.g.*, in [42], where the SiO_2 particles are created within clouds in exoplanet atmospheres.

Another example that we find in nature is the growth of crystals. A time-dependent

model of nucleation and growth of spherical crystals in binary melts is studied in [1]. The growth rate is obtained by solving the conservation equations governing heat and mass transfer around the spherical crystal particle. Analytical solutions to the model are obtained with and without fluctuating rates in the particle growth. A similar model is used in [50], but for the cases where the growth of crystals occurs in a supercooled liquid or supersaturated solution. Both of these papers include the effects of particle formation in the conservation equations for the temperature and concentration of the condensed material, and similar source and sink terms will be used in our work.

1.2.3 Fine-particle formation coupled to fluid flow

A large number of studies, such as the ones mentioned in the previous section, solve the PBE without considering the effect of the fluid flow or assuming very simplified flows (*e.g.*, fully mixed systems). Another example is [84], where Ulrich studies the formation of pyrogenic silicas in a furnace and argues that the microscopic zones where individual particles grow are several orders of magnitude smaller than macroscopic turbulent eddies, and therefore ignores any fluid interaction. However, in reality the fluid flow determines the mixing of the chemicals that react or condense resulting in the formation and growth of particles, producing changes of concentration and temperature in the particle environment. Therefore, the flow field has a major effect on particulate systems and moreover the presence of particles may also have a feedback effect on the flow field due to chemical species being consumed.

In [66], Rigopoulos presents a review on the potential and limits of solving the PBE coupled to a variety of different reactive flows. A distinction is made between inertial and non-inertial particles by looking at the Stokes number, defined as the ratio of the particle's momentum response time to a characteristic time of the flow field. If this number is very small, particles will follow the streamlines of the flow, which is a reasonable assumption for small particles as in soot formation or nanoparticle production (*e.g.*, microsilica). Methods of solution for the PBE include: analytical and perturbation methods, moment and approximate moment-based methods, discretisation methods, and Monte-Carlo methods. Their different uses depend on the complexity of the PBE and the fluid flow considered. For instance, if we only considered particle growth, the PBE is a one-dimensional wave equation that can be easily solved with the method of characteristics. As we include more transport and source terms in the equation, analytical techniques are not suitable anymore. The

most widely used method is the method of moments since it transforms the PBE, which is usually an integro-partial differential equation with higher dimensionality, into an equivalent PDE system depending only on space and time, making easier the coupling with fluid dynamics. A full description of this method can be found in [64, 65, 66]. More recent and improved versions are the Quadrature Method of Moments (QMOM) [54] and the Direct Quadrature Method of Moments (DQMOM) [52]. The main limitation of these methods is that the full distribution is not retrieved but only its moments. For instance, in [72], nanoparticle coagulation in a temporal mixing layer is studied, and the evolution of the particle field is obtained by the moment method and by assuming a lognormal distribution for the particle size distribution. The mixing layer in this case is formed when two co-flowing streams of different velocities meet at the trailing edge of a splitter plate. Under the same flow configuration, a different solution method for the PBE is used in [86] to model the formation and growth of titania particles. The nodal/sectional method is used here to approximate the general dynamic equation by dividing the aerosol population into different classes and solving a set of transport equations for each bin. In this thesis, we will consider a very simple PBE to model the particle size distribution, and therefore we are able to use both analytical and moment methods to find a solution to our problem.

Many other studies exist that analyse the effects of laminar flow on the formation and growth of aerosols, and stagnation point flows are a common choice due to their simplicity. Kennedy [41] studies the effects on chemical nucleation of an isothermal stagnation-point laminar mixing layer that forms a condensable monomer. It is concluded that if the Damköhler number for monomer production is small, meaning that the rate of monomer formation is slow, then nucleation of particles is strongly affected by the flow. Alshaarawi and Bisetti [2] use a steady laminar stagnation flow configuration to investigate the interaction between condensing aerosol particles and gas-phase transport across a mixing layer. They conclude that for fast mixing rates, the number density and volume fraction of particles increases with residence time, corresponding to the nucleation regime, whereas for low mixing rates, the number density decreases with residence time and the volume fraction reaches a plateau, corresponding to the condensation regime.

It is important to notice that most aerosols formed by mixing occur in a turbulent flow regime, and it is well known that turbulence alters the product aerosol compared to laminar mixing. The coupling of the population balance equation with turbulent flow is challenging due to the appearance of further closure problems arising from the non-linear particle formation terms. Moreover, processes such as nucleation, growth,

and coagulation depend on local concentrations of the reactive scalars, which are random in a turbulent flow, inducing further randomness to the particle formation process [67]. Raman and Fox [64] do an extensive review describing the complex multiscale interactions between turbulent fluid flow, gas-phase reactions and particle evolution by focusing on the formation of soot and metal-oxide particles in turbulent flames.

An example of some early work in this area is that of Xiong and Pratsinis [93] who studied the gas-phase production of particles in a one-dimensional turbulent plug flow. They use both the sectional and moment methods to solve the population balance equation, with the latter producing better results and being less computationally expensive. For the latter reason and since it is the most straightforward approach for coupling particle formation with CFD, moment or approximate moment-based methods are still the preferred option when solving the PBE under turbulence conditions. Zucca *et al.* [95] implement the PBE in CFD codes for modelling soot formation by approximating it with the DQMOM method. Whereas Zhou *et al.* [94] simulate aerosol formation and growth in a turbulent mixing layer and use the QMOM to describe the dynamics of the condensing droplets. One of their results suggests a high volume fraction of particles on the hot side of the mixing layer, which is related to turbulent mixing that moves particles from the nucleation region (cold side) into the growth region (hot side).

As we mentioned earlier, moment methods do not predict the entire particle size distribution which is not desirable in certain applications. Rigopoulos [67], and more recently Sewerin and Rigopoulos [73], propose a probability density function approach that overcomes the closure problem that arises from Reynolds averaging of the PBE when turbulence is included, and predicts the entire particle size distribution. The method can be used with any growth or coagulation kernels regardless of their dependency with the environment and with the particle size, and can be applied to any flow configuration.

1.2.4 Silicon furnace modelling

With increasing demand of microsilica for different applications, research on how to operate the silicon furnace to produce good quality silica fume is needed. Currently, there are no mathematical models that can predict this, since capturing all the physics associated with the silicon furnace is a complex task. Furthermore, the physical processes involved are hard to quantify due to the difficulties in taking measurements and

carrying out experiments under such vile, high-temperature environments. However, there are simplified models available in the literature that focus on specific processes or parts of the furnace, that are helpful in order to understand our problem.

Several mathematical models [31, 49, 76] have been developed for the heat and mass balances, chemical reactions, and thermodynamics of the furnace. These dynamical models predict the behaviour of the furnace below the charge surface under different operating strategies. However, not many studies have focused on the region above this surface, that is, on the combustion chamber where the silica fume is generated. Regulatory requirements on lowering NOx emissions in the internal and external environment have led to further studies in this area. The PhD work by Kamfjord [39] focuses on the study of NO emissions at different parts of the silicon process. He states that there is a strong correlation between silica fume and NO formation, and that this happens because the SiO combustion that produces silica fume releases a great amount of energy, driving the creation of NO by the reaction between nitrogen and oxygen in air at high temperatures. Kamfjord develops a model of the upper area (or furnace hood) of a pilot furnace to investigate flow fields and the temperature of the various gases. Some simulations were undertaken using COMSOL by considering the Reynolds-averaged Navier-Stokes equations, with the $k - \epsilon$ turbulence model, and heat transfer in the fluids. The NO generation was found to be dependent on where the combusting furnace gases meet the cold air and on the amount of air introduced. Motivated by these findings we carry out similar simulations in Chapter 3, where we also couple the SiO and CO combustion reactions, and solve for all the chemical species concentrations, as well as for the moments of the particle size distribution.

Some silica fume is also produced during refining and casting of the silicon in the taphole area. While the majority of these fumes are captured by a fume hood over the ladle where the liquid silicon is tapped, some can also escape into the indoor environment. Increasing governmental constraints on the working environment have led to a need to quantify and characterize the fumes to which workers are exposed. However, the amount of fume on an industrial scale and the characteristics of the fume, such as particle size and shape, have not been adequately studied. The PhD work by Næss [57] provides a qualitative and quantitative study on the kinetic and mechanistic nature of liquid silicon oxidation during refining. Some experiments showed that the dominant mechanism for the fume production is the surface oxidation of the molten silicon [58]. Kadkhodabeigi [37, 38] introduced a CFD model for a new hood design to capture the taphole gases created during the tapping of the silicon. The three-dimensional model captures air flow around the taphole, heat transfer

mechanisms including radiation, and chemical reactions due to combustion of the off-gases. The differential equations used here include continuity, momentum, and energy conservation. In addition, species transport equations for each of the gases is used, and the $k - \varepsilon$ turbulent model is added to account for the turbulent nature of the process. This type of first principles model could be extended to the full furnace hood geometry.

1.3 Thesis outline

Since the majority of the previous works on silicon furnaces are experimental, and not that many studies have focused on the dynamics within a silicon furnace hood, the exact mechanisms that control the formation and growth of microsilica particles from the combustion of silicon monoxide are not fully understood. The hot temperatures and presence of harmful gases inside a furnace hood make experiments hazardous, costly, and sometimes impossible to perform, and this is where mathematical modelling can help to understand the underlying physics behind the process. The main goal of this thesis is to develop a detailed physics-based model that relates the local fluid flow, thermal and chemical conditions of the furnace hood to the formation and growth of microsilica particles. We will then look at different case scenarios or reductions of this model and provide asymptotic approximations of the solution that we will compare with numerical simulations.

In Chapter 2, we will formulate the full model for a general furnace hood geometry that will serve as a basis for the rest of the chapters. First, we derive a model for the reactive flow mixture that includes equations for the conservation of each chemical species, momentum, and energy, and an equation of state. We consider each chemical to move with the same speed, that is, the barycentric or mixture velocity, and assume that only chemical reactions modify their mass balance. Expressions for the reaction rates are given and are highly dependent on the temperature. Secondly, we will couple this system to a population balance equation for the particle size distribution that accounts for nucleation and growth by condensation on particles. The latter two mechanisms are affected by silicon dioxide concentration and temperature variations, which at the same time are also affected by the formation of particles. Additionally, closed equations for the first three moments of the particle size distribution are derived.

In Chapter 3, we will non-dimensionalise the previous fully-coupled model and will perform steady-state COMSOL simulations for a two-dimensional furnace hood geometry. We will compare the results obtained when looking at different furnace and

flow configurations. First, we will vary the size of the fuel (SiO and CO) inlet which determines how far the chemical species need to travel before reacting. Then we will explore the effect of varying the ratio between the inlet velocity of the fuel and of the air. Whereas the first case will not produce significant differences in our results, the latter case will have a strong effect on the reactions and thus on the particles formation. These simulations will motivate many of the modelling approaches taken in the chapters thereafter.

In Chapter 4, we will look at a reduction of the general model by focusing on the dynamics within a flame or reaction zone, and therefore we will take the velocity of the fluid to be zero. Moreover, in this chapter we will consider the case in which the chemical species are initially well-mixed or spatially homogeneous, hence spatial diffusion is instantaneous. We will non-dimensionalise the resulting simplified ODEs system and will study the decoupled limit as well as the fully coupled limit. The difference is that in the decoupled case, the mass and energy equations influence the particle growth equation but not the other way around (one-way coupling). We will find asymptotic solutions of the chemical-temperature subsystem for an oxygen rich environment in the decoupled case, which are mostly valid for understanding early time dynamics, and numerical solutions for the fully coupled case. An implicit solution will be obtained for the particle size distribution by the method of characteristics, which uses the results obtained for the chemicals and temperature. We observe that in the decoupled case particles will grow indefinitely, whereas in the coupled case the inclusion of a sink term in the silicon dioxide equation means that particle growth stops at a finite time. The influence of changing key model parameters on the particle size distribution is also discussed.

Another reduction of the general model is considered in Chapter 5, where we study the case in which the chemical species are initially spatially separated. This time, diffusion will play a dominant role in providing material to a combustion front that separates the fuel from the oxidizer. We will take the velocity of the fluid to be zero and we will follow a similar analysis to Chapter 4, while including one-dimensional spatial effects along a cross section of the reaction zone. As before, we will obtain an implicit solution for the particle density function and we will study both the decoupled and fully-coupled problems. In the decoupled case we will give asymptotic solutions for the small time and large time limits by performing a regular perturbation and using the WKB method, respectively, whereas only numerical simulations are available for the fully-coupled problem. The dynamics within the core of the reaction zone are found to be similar to those of the well-mixed case, and the current model is

most useful for understanding the distribution of particles over space and time, with larger particles arising in the middle of the reaction zone and smaller ones around the boundaries. Finally, the effect of increasing the initial separation distance between the fuel and oxidizer is also explored.

We will extend the work from Chapter 5 to two dimensions in Chapter 6, where we will also study variations in the variables along the reaction zone, and not only for a cross-section. We will also incorporate fluid flow by considering a mixing layer forming between two parallel flows with different velocities, one composed of oxygen and the other one of fuel. The boundary layer equations for all variables will be derived and we will use the von Mises transformation to obtain similar equations to those that we solved for in Chapter 5. We will start by obtaining asymptotic and numerical solutions for the velocity profile, which will then be used in the solution for the chemicals, temperature and particle size distribution. We will solve for the latter variables following a similar approach to Chapter 5 and will analyse how they are affected by changes to the ratio between the inlet velocity of the fuel and of the air.

We will finish the thesis with a discussion in Chapter 7, followed by some recommendations for the industrial partner, and some aspects of the problem to consider for future work.

1.4 Statement of originality

At the time of submission, one paper, [29], has been published from this thesis, containing part of the work from Chapters 2, 4, and 5. The paper was co-authored by R. González Fariña, A. Münch, J. M. Oliver, and R. A. Van Gorder. The scanning electron microscope images of microsilica particles in Chapter 1 and the experimental data in Chapter 6 were provided by Elkem ASA; this is acknowledged in the corresponding figure caption. The analysis and numerical solutions of the models presented in this thesis were carried out by R. González Fariña under the supervision of A. Münch, J. M. Oliver, and R. A. Van Gorder.

1.5 Acknowledgment of funding

This thesis is based on work supported by the EPSRC Centre for Doctoral Training in Industrially Focused Mathematical Modelling through grant EP/L015803/1 in collaboration with Elkem ASA. I am thankful to Elkem ASA for their financial support and the opportunity to work on-site during parts of this project.

Chapter 2

Model formulation

2.1 Introduction

We begin the mathematical research in this thesis by formulating a full model that describes all the physics involved in the formation and growth of microsilica particles within a furnace hood. This general model will serve as a basis for the rest of the chapters in this thesis, where we find solutions to reduced systems that focus on different aspects of the process under certain simplifying assumptions.

We will consider a generalized furnace hood geometry based on the schematics provided in Figure 2.1. The spatial domain, Ω_x, will solely consist of the furnace hood, highlighted with a green dashed square in Figure 2.1a and sketched in more detail in Figure 2.1b. Note that for our purposes we neglect the presence of the electrodes. We denote $\partial\Omega_x = \partial\Omega_b \cup \partial\Omega_w \cup \partial\Omega_d \cup \partial\Omega_t$ the boundary of the domain as illustrated in Figure 2.1b, where $\partial\Omega_b$, $\partial\Omega_w$, $\partial\Omega_d$, and $\partial\Omega_t$ are defined as follows:

- $\partial\Omega_b$: Bottom side of the domain, corresponding to the charge surface and through which the gases SiO and CO enter the domain;
- $\partial\Omega_w$: Furnace hood wall;
- $\partial\Omega_d$: Door on the furnace wall, or small separation gap between the furnace and furnace hood, through which the air enters the domain;
- $\partial\Omega_t$: Top side of the domain through which the off-gases and particles leave the furnace hood. This is where the exhaust pipe is located.

The remainder of the chapter is divided into two main sections: in the first section we describe a model for the fluid flow, temperature variations and chemical reactions

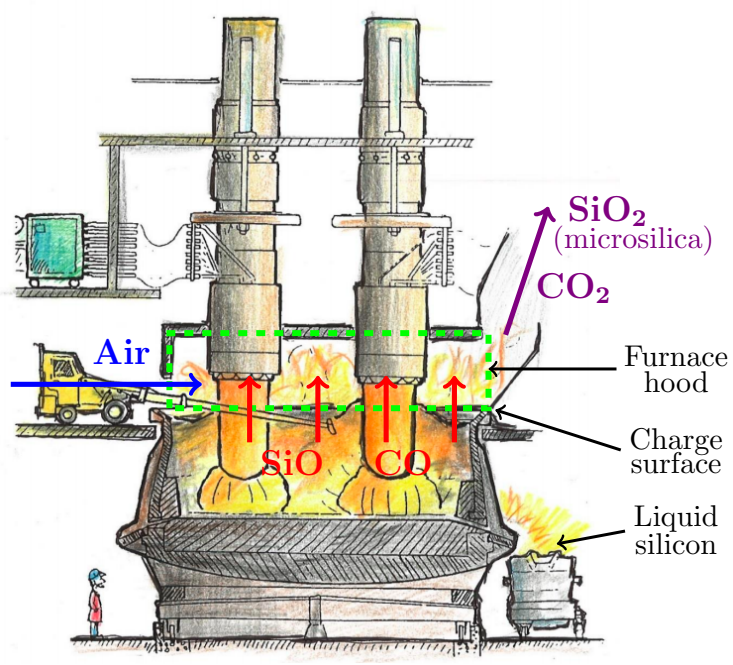

(a) Sketch of a silicon furnace indicating the location of the furnace hood (green dashed square), that is, where the combustion reactions (1.1.4)-(1.1.5) happen. Reproduced from The Si Process Drawings, by Thorsteinn Hannesson [32].

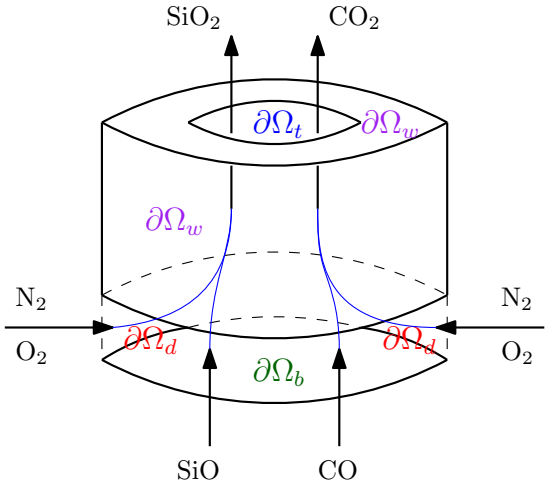

(b) Schematic of the furnace hood domain, Ω_x, and its boundaries, $\partial\Omega_x = \partial\Omega_b \cup \partial\Omega_w \cup \partial\Omega_d \cup \partial\Omega_t$.

Figure 2.1: Generalized furnace hood geometry. The flow comes into the domain from the sides and bottom, both streams react inside the domain forming SiO_2 which condenses to particles, and finally the flow leaves the domain at the top. Since the air comes in through a small gap that separates the furnace hood and the actual furnace below, and since the location of the outlet varies from furnace to furnace, we have taken our domain to be axisymmetric.

inside the furnace hood, while in the second section we focus on the formation and growth of a population of particles. These two models are coupled and are able to predict particle size distributions for different local conditions of the furnace. The key aspects of the work presented here can be found in [29].

2.2 Model of a reactive flow

We are interested in modelling the dynamics of the main chemical species found in the furnace hood above the charge surface: $N_2(g)$, $O_2(g)$, $SiO(g)$, $SiO_2(g)$, $CO(g)$, and $CO_2(g)$. Other compounds such as volatiles are not taken into account. Thus, we model the fluid as a combination of the gaseous species mentioned before, where the only chemical reactions occurring are the combustion reactions

$$2\mathrm{SiO(g)} + \mathrm{O_2(g)} \xrightarrow{R_1} 2\mathrm{SiO_2(g)}, \tag{2.2.1a}$$

$$2\mathrm{CO(g)} + \mathrm{O_2(g)} \xrightarrow{R_2} 2\mathrm{CO_2(g)}. \tag{2.2.1b}$$

Studying the motion of complex fluids requires the analysis of how local quantities that characterise the behaviour of single or multicomponent media evolve over space and time. For this, conservation equations for the mass, momentum and energy are used. Whereas the derivation of these balance equations for one-component media is well known, the derivation for multicomponent gas mixtures, such as the one under study in this work, is not straightforward. Nachbar *et al.* [56] derived conservation equations for multicomponent reacting gas mixtures based on the idea of a multicomponent continuum composed of coexistent continua, each obeying the laws of dynamics and thermodynamics. In the next sections, we will introduce these conservation equations in a similar manner to [63, 90].

2.2.1 Conservation of chemical species

Assuming that the flow is composed of a mixture of the six chemical species mentioned above and consists only of one phase, the first step in the derivation is to obtain continuity equations for the mass of each single species. Let $\rho_j(\mathbf{x}, t)$ be the partial density of species j (*i.e.*, the mass per unit volume of the mixture), where $\mathbf{x}$ denotes position in cartesian coordinates and t time. Assuming that only chemical reactions

modify the mass balance, we have that

$$\frac{\partial \rho_j}{\partial t} + \boldsymbol{\nabla} \cdot (\rho_j \mathbf{v}_j) = \dot{W}_j, \tag{2.2.2}$$

where $\dot{W}_j$ represents the reaction rate of species j and the total mass produced is equal to zero, so that $\sum_{j=1}^{6} \dot{W}_j = 0$. As in [56, 63, 85], the velocity of species $j, \mathbf{v}_j$, is taken as the sum of the mass average velocity of the mixture or barycentric velocity, $\mathbf{v}$, and the diffusion velocity of species j, $\mathbf{V}_j$, that is

$$\mathbf{v}_j = \mathbf{v} + \mathbf{V}_j, \quad \mathbf{v} = \frac{1}{\rho} \sum_{j=1}^{6} \rho_j \mathbf{v}_j, \quad \rho = \sum_{j=1}^{6} \rho_j, \tag{2.2.3}$$

where ρ is the mean density of the mixture. Hence, if we sum the terms in the local balance (2.2.2) over the index $j = 1, \ldots, 6$, we get the mixture mass balance equation or continuity equation, namely

$$\frac{\partial \rho}{\partial t} + \boldsymbol{\nabla} \cdot (\rho \mathbf{v}) = 0. \tag{2.2.4}$$

The diffusive flux for species j is defined by $\mathcal{J}_j = \rho_j \mathbf{V}_j = \rho_j(\mathbf{v}_j - \mathbf{v})$ [63] so the local balance equation for species j becomes

$$\frac{\partial \rho_j}{\partial t} + \boldsymbol{\nabla} \cdot (\rho_j \mathbf{v}) + \boldsymbol{\nabla} \cdot \mathcal{J}_j = \dot{W}_j, \tag{2.2.5}$$

It is common to express the mass balance equation for species j in terms of the mass fraction $Y_j(\mathbf{x}, t)$ by setting $\rho_j = Y_j \rho$ in the previous equation, that is,

$$\rho \frac{\partial Y_j}{\partial t} + \rho \mathbf{v} \cdot \boldsymbol{\nabla} Y_j + \boldsymbol{\nabla} \cdot \mathcal{J}_j = \dot{W}_j, \tag{2.2.6}$$

where we have used equation (2.2.4). Finally, we approximate $\mathcal{J}_j$ with the multicomponent Fick's law of diffusion $\mathcal{J}_j = -\rho D_j \boldsymbol{\nabla} Y_j$, where D_j corresponds to the diffusion rate of species j in the mixture [90]. Hence, (2.2.6) becomes

$$\rho \frac{\partial Y_j}{\partial t} + \rho \mathbf{v} \cdot \boldsymbol{\nabla} Y_j - \boldsymbol{\nabla} \cdot (\rho D_j \boldsymbol{\nabla} Y_j) = \dot{W}_j. \tag{2.2.7}$$

In this thesis, we choose to write the mass conservation equations for each of the chemical species in terms of molar concentrations, $C_j(\mathbf{x}, t)$, in units mol/m^3, by letting

$\rho_j = M_j C_j$ in equation (2.2.5), with M_j being the molar mass of species j. We obtain

$$\frac{\partial C_j}{\partial t} + \boldsymbol{\nabla} \cdot (C_j \mathbf{v}) - \boldsymbol{\nabla} \cdot \left(\rho D_j \boldsymbol{\nabla} \left(\frac{C_j}{\rho} \right) \right) = \dot{Q}_j, \tag{2.2.8}$$

where we have applied Fick's Law of diffusion and where $\dot{Q}_j = \dot{W}_j / M_j$. Note that in this case we did not need to use equation (2.2.4) to derive (2.2.8), however mass is still conserved since $\sum_{j=1}^{6} M_j \dot{Q}_j = 0$. Moreover, we do not need to solve for (2.2.4) since the fluid density, ρ, can be written in terms of the species concentrations [8, 63] as

$$\rho = \sum_{j=1}^{6} M_j C_j. \tag{2.2.9}$$

In summary, the governing equations for all the chemical species involved are the following

$$\frac{\partial C_{\mathrm{N_2}}}{\partial t} + \boldsymbol{\nabla} \cdot \left(C_{\mathrm{N_2}} \mathbf{v} - \rho D_{\mathrm{N_2}} \boldsymbol{\nabla} \left(\frac{C_{\mathrm{N_2}}}{\rho} \right) \right) = 0, \tag{2.2.10a}$$

$$\frac{\partial C_{\mathrm{O_2}}}{\partial t} + \boldsymbol{\nabla} \cdot \left(C_{\mathrm{O_2}} \mathbf{v} - \rho D_{\mathrm{O_2}} \boldsymbol{\nabla} \left(\frac{C_{\mathrm{O_2}}}{\rho} \right) \right) = -R_1 - R_2, \tag{2.2.10b}$$

$$\frac{\partial C_{\mathrm{SiO}}}{\partial t} + \boldsymbol{\nabla} \cdot \left(C_{\mathrm{SiO}} \mathbf{v} - \rho D_{\mathrm{SiO}} \boldsymbol{\nabla} \left(\frac{C_{\mathrm{SiO}}}{\rho} \right) \right) = -2R_1, \tag{2.2.10c}$$

$$\frac{\partial C_{\mathrm{SiO_2}}}{\partial t} + \boldsymbol{\nabla} \cdot \left(C_{\mathrm{SiO_2}} \mathbf{v} - \rho D_{\mathrm{SiO_2}} \boldsymbol{\nabla} \left(\frac{C_{\mathrm{SiO_2}}}{\rho} \right) \right) = 2R_1 - S_C, \tag{2.2.10d}$$

$$\frac{\partial C_{\mathrm{CO}}}{\partial t} + \boldsymbol{\nabla} \cdot \left(C_{\mathrm{CO}} \mathbf{v} - \rho D_{\mathrm{CO}} \boldsymbol{\nabla} \left(\frac{C_{\mathrm{CO}}}{\rho} \right) \right) = -2R_2, \tag{2.2.10e}$$

$$\frac{\partial C_{\mathrm{CO_2}}}{\partial t} + \boldsymbol{\nabla} \cdot \left(C_{\mathrm{CO_2}} \mathbf{v} - \rho D_{\mathrm{CO_2}} \boldsymbol{\nabla} \left(\frac{C_{\mathrm{CO_2}}}{\rho} \right) \right) = 2R_2, \tag{2.2.10f}$$

where R_1 and R_2 are the source terms due to the combustion reactions (2.2.1), and S_C represents a sink term due to the formation of the particles which will be defined in Section 2.3.

Notice that we have included conservation of the two main components in air, N_2 and O_2, which appear to be in much higher concentrations than the rest of the species. The reason to include them is that their concentrations vary along the furnace hood and they contribute towards the total mass, momentum and energy balance in the system. Whereas SiO and CO are competing for the oxygen, we assume the nitrogen to be non-reacting even though in some cases it could react with oxygen to

form NOx compounds. Other reactions may also occur in the furnace hood, such as the Boudouard reaction or the condensation of SiO into SiO_2 and Si, believed to be responsible for the small percentages of silicon found in microsilica particles. Here, we only consider the dominant reactions but note that others could in principle be introduced into the model.

2.2.1.1 Reaction rates

For elementary chemical reactions, the rate of reaction is proportional to some power of the concentrations of the reactants according to the law of mass action. However, for more complex reactions, simplified kinetic models are often adopted, where the powers may not be equal to the stoichiometric coefficients of the reacting species and are usually instead determined experimentally [10, 83, 91]. In our case, the combustion of SiO and CO with oxygen involves some intermediate chemical reactions that are not fully understood. Nonetheless, since the essential nature of the process is that SiO, CO, and oxygen are consumed while products and heat are generated, both combustion reactions are well approximated by one-step irreversible processes represented by (2.2.1). Here we take each reaction to be first order in both reactants [22]. Thus, we adopt the reaction rates given by

$$R_1 = \tilde{K}_1(T) C_{\mathrm{SiO}} C_{\mathrm{O_2}}, \tag{2.2.11a}$$

$$R_2 = \tilde{K}_2(T) C_{\mathrm{CO}} C_{\mathrm{O_2}}. \tag{2.2.11b}$$

The coefficients $\tilde{K}_i(T)$ are typically highly dependent on the temperature and this is included by incorporating an Arrhenius term of the form

$$\tilde{K}_i(T) = A_i \exp\left(-E_i/RT\right), \tag{2.2.12}$$

where E_i is the activation energy of the reaction, A_i is a pre-exponential coefficient, T is the temperature of the system, and $R = 8.314$ J·mol^{-1}K^{-1} is the universal gas constant. Notice that we can easily express the concentrations used in (2.2.11) in terms of partial pressures, p_j, by using Dalton's law of partial pressures [28], namely

$$C_j = \frac{p_j C_T}{p}, \tag{2.2.13}$$

for every chemical species j, where p is the total pressure and C_T is the sum of the concentrations of the species in the gas, that is, the total number of moles per unit

volume, namely

$$p = \sum_{\text{species } j} p_j, \qquad C_T = \sum_{\text{species } j} C_j. \tag{2.2.14}$$

2.2.2 Conservation of momentum

We use the compressible Navier-Stokes equation in order to model the velocity of the fluid, $\mathbf{v}(\mathbf{x}, t)$, taking into account forces due to pressure and viscous stresses. The equation has the following form

$$\frac{\partial}{\partial t}(\rho \mathbf{v}) + \boldsymbol{\nabla} \cdot (\rho \mathbf{v} \otimes \mathbf{v}) = -\boldsymbol{\nabla} p + \boldsymbol{\nabla} \cdot \boldsymbol{\tau}, \tag{2.2.15}$$

where $\otimes$ is the outer product, and where p and ρ represent the total pressure and density of the gas mixture, respectively. The viscous stress tensor is given by

$$\boldsymbol{\tau} = \mu \left(\boldsymbol{\nabla} \mathbf{v} + (\boldsymbol{\nabla} \mathbf{v})^T - \frac{2}{3} \mathbf{I} (\boldsymbol{\nabla} \cdot \mathbf{v}) \right), \tag{2.2.16}$$

with $\mathbf{I}$ denoting the identity tensor, and where μ is the fluid viscosity. Equation (2.2.15) can be derived in a similar manner to the total mass balance equation in the previous section, by summing up the momentum balance equations for each single species with the associated velocity $\mathbf{v}_j$ and stress tensor $\boldsymbol{\sigma}_j$ [63, 70].

In reality, the flow in the furnace hood is turbulent, thus turbulence models based on the Navier-Stokes equations may be used. The common approach is transforming all the equations presented in this chapter by using Favre-averaging, instead of Reynolds averaging (RANS) due to the variability of the gas density, and introducing the so-called $k - \varepsilon$ turbulence model, see, *e.g.*, [61, 95].

2.2.3 Conservation of energy

We now consider how the temperature of the gas mixture, $T(\mathbf{x}, t)$, varies in space and time. In our model, we assume instantaneous heat transfer between gases and particles and, therefore, we only need one temperature. This approximation is valid since microsilica particles are very small ($< 1\mu$m), resulting in heat transfer between gas and condensed phases occurring in a very fast timescale. We remark that considering a different temperature for each phase would make the model more realistic but also the analysis more complicated, and is therefore left as future work.

The temperature is affected by convection, thermal conductivity of the fluid, the

pressure working to compress the fluid, viscous dissipation, and by heat released by the chemical reactions and by the change of state due to the formation of the particles. Thus, we have the conservation of energy equation [70],

$$\frac{\partial}{\partial t}\left(\rho c_p T\right) + \boldsymbol{\nabla}\cdot\left(\rho c_p T\mathbf{v}\right) - \boldsymbol{\nabla}\cdot\left(k\boldsymbol{\nabla}T\right) = \tilde{\beta}T\left(\frac{\partial p}{\partial t} + \mathbf{v}\cdot\boldsymbol{\nabla}p\right) + \Phi + S_R + S_T, \quad (2.2.17)$$

where c_p and k denote the effective heat capacity and thermal conductivity of the fluid, both assumed to be constant. Since the volume fraction of the particles is very small compared to the gas mixture, we have neglected the heat capacity of the particles from the definition. Furthermore, since air is the dominant component in the gas mixture, both c_p and k can be approximated by the corresponding values for air.

The parameter $\tilde{\beta}$ represents the coefficient of thermal expansion, with units K^{-1}, and the dissipation function is defined as

$$\Phi = \boldsymbol{\nabla}\cdot\left(\boldsymbol{\tau}\mathbf{v}\right) - \mathbf{v}\boldsymbol{\nabla}\cdot\boldsymbol{\tau}. \quad (2.2.18)$$

The source term due to the chemical reactions is given by

$$S_R = \Delta H_1 R_1 + \Delta H_2 R_2, \quad (2.2.19)$$

where ΔH_i is the heat release of reaction i, and the heat source due to particle condensation, S_T, will be given in Section 2.3.

It is possible to incorporate radiation effects into equation (2.2.17), as in, *e.g*, [76]. However, radiation is usually small compared to other terms in the system and has therefore been neglected. This assumption has been taken before in similar models for silicon furnaces [77].

In order to close the system of equations, we need an equation of state that relates the state variables: concentration of species, pressure, and temperature. We first assume each species of the mixture to behave according to the ideal gas equation [63], namely

$$p_j = \rho_j \frac{R}{M_j} T. \quad (2.2.20)$$

Adding up equations (2.2.20) over the index j we end up with the general ideal gas law,

$$p = \frac{\rho R T}{\mathcal{M}} \quad \text{with} \quad \frac{1}{\mathcal{M}} = \sum_{j=1}^{6} \frac{Y_j}{M_j}, \quad (2.2.21)$$

that in terms of molar concentrations is given by

$$p = C_T RT, \tag{2.2.22}$$

as in [76], where C_T is given by (2.2.14).

We can now take the coefficient of thermal expansion in (2.2.17), $\tilde{\beta}$, to be given in terms of a partial differentiation of the equation of state [70], namely

$$\tilde{\beta} = -\frac{1}{\rho}\left(\frac{\partial \rho}{\partial T}\right)_p = \frac{1}{T}, \tag{2.2.23}$$

where in the last equality of (2.2.23) we have used the form of the ideal gas law given in (2.2.21).

2.3 Particle formation and growth

In the previous section, we stated a model for the chemical reactions, temperature and fluid flow. Now, we look into the modelling of the particle formation and growth mechanisms via a population balance equation or general dynamic equation.

We are concerned with a population of particles with different sizes that are dispersed in a continuous phase they interact with. We assume that particles form under certain conditions that depend on the local chemical species concentrations and temperature. As soon as particles form, they start growing at rates that also depend on the local variables in the system.

The usual way of modelling these types of systems is through a population balance equation, that we will describe first in this section, coupled to the transport equations derived for the reactive fluid flow in the previous sections. We will then derive the form of the nucleation and growth rates which depend on intrinsic properties of the particle and condensing material. We will finish by introducing equations for the moments of the particle size distribution which will prove useful in order to obtain solutions of the system.

2.3.1 Population balance equation (PBE)

Following, for example, [26], we let $\mathrm{d}N_0$ be the number density or number concentration of particles, that is, the number of particles per unit volume of gas, at a given spatial location $\mathbf{x}$, at a given time t and with internal coordinate in the range $[s, s + \mathrm{d}s]$. The

internal coordinate is what characterises the particle type. In this work, s will represent particle diameter, and other typical internal coordinates are volume, surface area and surface chemical composition. We remark that microsilica particles are spherical, hence considering the diameter to determine their size is a sensible choice. In summary, the particle phase space comprises the external coordinates, or spatial distribution of particles, and internal coordinates, or properties intrinsic to each individual particle.

The particle size distribution function or number density function $n(s, \mathbf{x}, t)$ is defined by

$$\mathrm{d}N_0 = n(s, \mathbf{x}, t)\mathrm{d}s, \tag{2.3.1}$$

and its dimensions, when the internal coordinate is particle diameter, are m^{-4}. A population balance equation for the number density function is a conservation equation that accounts for convection and diffusion terms for each dimension of the phase space, and source terms due to birth and death processes related to aggregation and breakage of particles. In particular, the rate of change of the internal coordinate, particle size, is called growth velocity and represents phenomena such as expansion, evaporation, or as in our case, condensation.

In order to derive the PBE, we start with the number balance of entities, which is given in the Lagrangian or material coordinate system as

$$\frac{\mathrm{d}}{\mathrm{d}t}\int_{\Omega(t)} n(s, \mathbf{x}, t)\mathrm{d}V = \int_{\Omega(t)} h(s, \mathbf{x}, t)\mathrm{d}V, \tag{2.3.2}$$

for a time dependent control region, Ω, of the particle state space, $\Omega_s \times \Omega_x$, that is convected with the fluid so that it always consists of the same fluid particles, and where $\mathrm{d}V$ is an infinitesimal volume in the particle state space [80]. The left-hand side of (2.3.2) represents the rate of change of the total number of particles in the control region. Since the total number only changes due to death and birth of particles, the function $h(s, \mathbf{x}, t)$, on the right-hand side, is a generalized source term considering these phenomena. In the Eularian frame, (2.3.2) can be rewritten as

$$\int_{\Omega(t)} \left[\frac{\partial n(s, \mathbf{x}, t)}{\partial t} + \boldsymbol{\nabla}_n \cdot (n(s, \mathbf{x}, t)\mathbf{v}_n(s, \mathbf{x}, t)) - h(s, \mathbf{x}, t)\right] \mathrm{d}V = 0, \tag{2.3.3}$$

where $\mathbf{v}_n = \{\mathbf{v}_\mathbf{x}, \hat{G}\}$ includes the spatial velocity and growth rate of particles, respectively, and $\boldsymbol{\nabla}_n = \{\boldsymbol{\nabla}, \boldsymbol{\nabla}_s\}$. Since the latter expression must be satisfied for any region Ω, the integrand must be equal to zero. We therefore deduce the population balance

equation

$$\frac{\partial n}{\partial t} + \boldsymbol{\nabla} \cdot (n\mathbf{v_x}) + \frac{\partial}{\partial s}\left(n\hat{G}\right) = h. \tag{2.3.4}$$

In order to account for random fluctuations in the flow and growth velocities, we can include diffusion coefficients as in [26, 64], and the PBE (2.3.4) becomes

$$\frac{\partial n}{\partial t} + \boldsymbol{\nabla} \cdot (n\mathbf{v_x} - D_p \boldsymbol{\nabla} n) + \frac{\partial}{\partial s}\left(n\hat{G} - D_s \frac{\partial n}{\partial s}\right) = h, \tag{2.3.5}$$

where D_p represents the particle-phase diffusivity, and D_s may in general depend on the growth rate and as an approximation it can be taken to be proportional to $\hat{G}$ [50].

We remark that even though the behaviour of any single entity in a population may be regarded as random, when the number of entities is large, the behaviour of the population is considered deterministic. In this sense, the PBE should not be viewed as a stochastic equation, but as an equation that predicts average information, since the number density function n is the average of the actual number density [65].

2.3.1.1 Assumptions

Microsilica particles are categorised as small particles, with an average diameter of 100nm [20]. Therefore, we assume that they are non-inertial particles and follow the streamlines of the flow. In terms of the PBE, this implies that $\mathbf{v_x}$ in (2.3.5) is equal to the velocity of the gas mixture, $\mathbf{v}$, as in Section 2.2.

As we mentioned in Chapter 1, after nucleation, the growth of the primary particles is purely by condensation, that is, by molecular addition of mass to the surface of existing particles, which is the main focus of this thesis. Additionally, a high percentage of the primary particles agglomerate via weak interparticle forces and a very small percentage shows aggregation as defined in Section 1.1.3. Since agglomeration at late stages of the process is not very relevant to industrial scale production (since the weak bonds can be broken easily with a dispersing machine [10]), and aggregation does not occur frequently, we will not study these mechanisms in this work and will only focus on the formation and growth of the primary particles through condensation. Moreover, since during the formation and growth of silica fume there is no breakage of the particles, we set $h = 0$ in (2.3.5). Please refer to [65] for more details on how to model aggregation and breakage of particles using a population balance equation.

Let $s_{\min}$ be the minimum particle size required for nucleation to occur, under the

previous assumptions the PBE (2.3.5) becomes

$$\frac{\partial n}{\partial t} + \boldsymbol{\nabla} \cdot (n\mathbf{v} - D_p \boldsymbol{\nabla} n) + \frac{\partial}{\partial s}\left(n\hat{G} - D_s \frac{\partial n}{\partial s}\right) = 0, \tag{2.3.6}$$

for $t > 0$, $\mathbf{x} \in \Omega_x$, and $s \geq s_{\min}$. The diffusion terms are often neglected or omitted, sometimes due to the lack of knowledge of the physical mechanisms involved [64, 94]. However, the particle-phase or molecular diffusivity, D_p may be retained in order to account for turbulent diffusivity which may play an important role in particle growth [95]. In addition, the D_s term is often added into (2.3.6) when needed for stability of numerical solutions, though we set $D_s = 0$ throughout most of this thesis. We will discuss these assumptions further in the next chapters.

Equation (2.3.6) must be supplemented with initial and boundary conditions which will be discussed in detail in Section 2.4.2. Now, if we let the nucleation rate, *i.e.* the rate at which new particles form, be $\hat{J}$ particles per unit volume per unit time, and if we further assume that new particles form at the smallest possible size $s_{\min}$, this rate should be equal to the particle flux in at $s = s_{\min}$, giving the boundary condition

$$n\hat{G} - D_s \frac{\partial n}{\partial s} = \hat{J} \quad \text{at} \quad s = s_{\min}, \tag{2.3.7}$$

for $t > 0$ and $x \in \Omega_x$, as in [65]. Since the total number of particles can only increase by nucleation, we impose the far-field condition

$$n \to 0 \quad \text{as} \quad s \to \infty \qquad \Rightarrow \qquad \hat{G}n - D_s \frac{\partial n}{\partial s} \to 0 \quad \text{as} \quad s \to \infty, \tag{2.3.8}$$

for $D_s > 0$, which is sometimes referred to as a regularity condition [65]. The spatial boundary conditions for n, as well as for the variables introduced in Section 2.2, will be discussed in Section 2.4.2 where we will study the geometry of the domain in more detail.

In order to close the model, we need to determine the form of the rate expressions for nucleation, $\hat{J}$, and surface growth, $\hat{G}$, of particles.

2.3.2 Nucleation rate

In this section, we give a short derivation of the nucleation rate, $\hat{J}$, taken from classical nucleation theory: further details can be found in, *e.g.*, [24, 87]. We consider homogeneous nucleation as opposed to heterogeneous meaning that the new thermodynamic phase forms spontaneously and randomly rather than at nucleation sites on surfaces.

The rate at which nucleation of particles occurs is determined by the probability of forming the critical nucleus diameter, s_c. This is the diameter that maximises the change in Gibbs free energy, as we shall now describe.

Thus, consider the change in Gibbs free energy, $\Delta\mathcal{G}$, accompanying the formation of a single embryo of pure material SiO_2 of diameter s containing g molecules of SiO_2. Let n_T be the number of molecules initially in the pure vapour. After the embryo forms, the number of vapour molecules remaining is $n = n_T - g$. Thus,

$$\begin{aligned}\Delta\mathcal{G} &= n\mathcal{G}_V + g\mathcal{G}_C + \pi s^2\gamma - n_T\mathcal{G}_V \\ &= g(\mathcal{G}_C - \mathcal{G}_V) + \pi s^2\gamma \\ &= \frac{\pi s^3}{6v_C}(\mathcal{G}_C - \mathcal{G}_V) + \pi s^2\gamma, \end{aligned} \tag{2.3.9}$$

where $\mathcal{G}_V$ and $\mathcal{G}_C$ are the free energy of a molecule in a vapour and condensed phase, respectively, γ is the surface energy, and we have used $gv_C = (\pi s^3)/6$ for v_C, the volume occupied by a molecule in the condensed phase. Thus, the free energy can be divided into two terms: one for the increase in volume of the embryo and another one for the creation of surface.

The specific Gibbs energy change can be related to the volume and pressure by $d\mathcal{G} = V\,dp$ for isothermal conditions. Therefore, if v_V is the volume of a molecule in the vapour phase, $d\mathcal{G} = (v_V - v_C)dp$, and since $v_C \ll v_V$, $d\mathcal{G} = v_V dp$. According to the ideal gas law $v_V = k_B T/p$, where k_B is the Boltzmann constant, and integrating the difference in Gibbs free energy we obtain the following:

$$\mathcal{G}_V - \mathcal{G}_C = k_B T \int_{p_0}^{p_{SiO_2}} \frac{dp}{p} = k_B T \ln S_e, \tag{2.3.10}$$

where $S_e = p_{SiO_2}/p_0 > 1$ is the saturation ratio which depends on the vapour partial pressure, p_{SiO_2}, and saturated vapour pressure, p_0. From Dalton's law of partial pressures (2.2.13), this is equivalent to $S_e = C_{SiO_2}/C_e$ where C_e is the saturation or equilibrium concentration of SiO_2—we will use this form of S_e throughout this work. Note that this ratio is always greater than one since nucleation only occurs when the vapour is supersaturated.

Hence, equation (2.3.9) becomes

$$\Delta\mathcal{G} = -\frac{\pi s^3}{6v_C} k_B T \ln S_e + \pi s^2\gamma, \tag{2.3.11}$$

where the first term in the sum represents the volume free energy of an embryo, and

the second term is the surface free energy. We need to find the maximum of this expression with respect to s, since it corresponds to where the particle is at equilibrium with the surrounding vapour. Elementary calculus reveals that the maximum value, $\Delta\mathcal{G}^*$, is obtained for the critical diameter

$$s_c = \frac{4\gamma v_C}{k_B T \ln S_e}. \tag{2.3.12}$$

For this critical size, the nucleation rate is usually given according to the classical nucleation theory by using the Boltzmann's distribution for the maximal Gibbs free energy as in [24, 94]:

$$\hat{J} = J_0 \exp\left(-\frac{\Delta\mathcal{G}^*}{k_B T}\right) = J_0 \exp\left(-\frac{16\pi\gamma^3 v_C^2}{3(k_B T)^3 (\ln S_e)^2}\right). \tag{2.3.13}$$

We take the form of the nucleation rate coefficient J_0 from [94] as

$$J_0 = \frac{p_{\mathrm{SiO_2}} \chi_{\mathrm{SiO_2}}}{k_B T}\sqrt{\frac{2\gamma}{\pi m}}, \tag{2.3.14}$$

with m and $\chi_{\mathrm{SiO_2}}$ the molecular mass and mole fraction of SiO_2 respectively, although throughout this thesis it will be considered to be a constant.

2.3.3 Surface growth rate

Consider a particle of pure species SiO_2 in air that also contains vapour molecules of SiO_2. Following, for example, [26], we can find mathematical expressions for the growth rate, $\hat{G}$, describing mass transfer rates between gas and condensed phases for the different flow regimes of the gas around the particle. These regimes are determined by studying the Knudsen number, defined as the ratio of the mean free path of the gas molecules, λ, to the particle radius, $s/2$, namely

$$\mathrm{Kn} = \frac{2\lambda}{s}. \tag{2.3.15}$$

The limit $\mathrm{Kn} \ll 1$ corresponds to the continuum regime where the gas can be thought of as a continuous fluid around the particle, while the limit $\mathrm{Kn} \gg 1$ is called the kinetic or free-molecular regime and the flow consists of a series of discrete collisions of the gas molecules with the particle. There is a transition regime for $0.1 < \mathrm{Kn} < 10$ [19, 94]. In this section, we review a microscale model for a single stationary particle, which is also affected by far-field conditions to the particle obtained from the macroscale

model derived in Section 2.2.

2.3.3.1 Continuum regime (Kn $\ll 1$)

We consider a relatively large particle of diameter s growing by condensation, that is, diffusion of mass to its surface. In order to determine the mass flux, we assume that the vapour concentration profile around the spherical particle is quasi-steady. This approximation is valid since the time of significant changes in vapour concentration within the furnace hood is much longer than the characteristic time for relaxation of the vapour concentration profile around the particle to its steady-state value $\tau_c = (s/2)^2/D_{\mathrm{SiO_2}}$ [24, 87]. Furthermore, as we mentioned earlier in this section, microsilica particles adopt the main fluid velocity, and therefore we can assume the growing particle to be stationary with respect to the surrounding vapour and we neglect the advective transport of the vapour. Due to the symmetry of the problem we use spherical coordinates, and with r being distance from the centre of the particle, the molar concentration $C(r,t)$ satisfies

$$\frac{D_{\mathrm{SiO_2}}}{r^2}\frac{\partial}{\partial r}\left(r^2\frac{\partial C}{\partial r}\right) = 0 \quad \text{for} \quad r > \frac{s}{2}, \tag{2.3.16}$$

where $D_{\mathrm{SiO_2}}$ is the diffusivity of the condensing species. The boundary conditions are $C = C_e$ at $r = s/2$, that is, the concentration is at equilibrium at the particle surface, and $C = C_{\mathrm{SiO_2}}$ at $r = \infty$, where $C_{\mathrm{SiO_2}}$ is the bulk vapour concentration. Solving (2.3.16) subject to these boundary conditions gives

$$\frac{C - C_e}{C_{\mathrm{SiO_2}} - C_e} = 1 - \frac{s}{2r}. \tag{2.3.17}$$

The rate of condensation (units $[\mathrm{mol}\cdot\mathrm{s}^{-1}]$), F, is given as the product of the particle surface area and the mass flux at the particle's surface, that is,

$$F = \pi s^2 D_{\mathrm{SiO_2}}\left(\frac{\partial C}{\partial r}\right)\Bigg|_{r=s/2} = 2\pi D_{\mathrm{SiO_2}}(C_{\mathrm{SiO_2}} - C_e)s. \tag{2.3.18}$$

Thus, if $v_p = (4/3)\pi(s/2)^3$ denotes the volume of the particle, the rate of particle volume growth is

$$\frac{\mathrm{d}v_p}{\mathrm{d}t} = \frac{\mathrm{d}}{\mathrm{d}t}\left(\frac{\pi}{6}s^3\right) = F\frac{M_{\mathrm{SiO_2}}}{\rho_p} = \frac{2\pi M_{\mathrm{SiO_2}} D_{\mathrm{SiO_2}}(C_{\mathrm{SiO_2}} - C_e)s}{\rho_p}, \tag{2.3.19}$$

where M_{SiO_2} and ρ_p are the molecular weight and density of the condensed material SiO_2. The diameter growth rate (units $m \cdot s^{-1}$) is therefore given by

$$\frac{ds}{dt} = \frac{4M_{SiO_2} D_{SiO_2} (C_{SiO_2} - C_e)}{\rho_p s}. \tag{2.3.20}$$

The vapour concentration at the particle surface, C_e, is usually expressed as the product of the vapour concentration of SiO_2 over a flat surface, C_0, and a factor greater than one that expresses the increase in vapour concentration when the surface is curved, the so-called Kelvin factor [24, 26], namely

$$C_e = C_0 \exp\left(\frac{4\gamma v_C}{s k_B T}\right). \tag{2.3.21}$$

As described in [94], in some cases (2.3.20) is written in terms of partial pressures instead of molar concentrations. Recall that we can go from one to the other by using Dalton's law.

2.3.3.2 Free-molecular regime (Kn $\gg$ 1)

In the case in which the mean free path of the gas surrounding the microsilica particle is large compared to the size of the growing particle itself (free-molecule regime) [78], classical kinetic theory is applied in order to determine the growth rate. We assume the particle to be spherical, and do not take into account any interaction forces between the particle and vapour. In this case, we need to determine the form for the effusion flux or molecular flux, $\mathcal{F}$, that is, the collision rate of gas molecules hitting a unit surface in one direction in unit time. The expression for the flux reads

$$\mathcal{F} = \frac{dN}{dS dt}, \tag{2.3.22}$$

where dN represents number of molecules and dS is the elementary surface. Since molecules approach the surface from all directions and at different velocities, we will first consider the number of molecules coming from a specific direction (θ, φ) within the body angle $d\Psi$ around it, and with a speed in the interval dv around v, $dN_{v,\theta,\varphi}$. This can be interpreted as the number of molecules within a slant cylinder with base dS and height $v \cos\theta dt$. The volume of this cylinder is $dV = dS v \cos\theta dt$ and hence the number of molecules in it can be given as $dN_V = \mathcal{N} dV$, where $\mathcal{N}$ represents concentration of molecules in the volume. From this total number of molecules we

need to pick the ones with the given velocity interval specified by v, θ, φ, namely

$$\mathrm{d}N_{v,\theta,\varphi} = \mathrm{d}N_V D(v) v^2 \mathrm{d}v \mathrm{d}\Psi. \tag{2.3.23}$$

The latter comes from the general definition of the distribution function of molecules in the space of velocities (v_x, v_y, v_z), $D(v_x, v_y, v_z)$, via

$$\mathrm{d}N = N D(v_x, v_y, v_z) \mathrm{d}v_x \mathrm{d}v_y \mathrm{d}v_z, \tag{2.3.24}$$

where N $(= \mathrm{d}N_V)$ represents the total number of molecules, and after expressing the elementary volume in the spherical coordinates

$$\mathrm{d}v_x \mathrm{d}v_y \mathrm{d}v_z \equiv \mathrm{d}^3 v = v^2 \mathrm{d}v \sin\theta \mathrm{d}\theta \mathrm{d}\varphi. \tag{2.3.25}$$

Note that the elementary body angle found in (2.3.23) is defined as

$$\mathrm{d}\Psi = \sin\theta \mathrm{d}\theta \mathrm{d}\varphi. \tag{2.3.26}$$

Now, since the area of a sphere of unit radius is 4π, the number of molecules within the spherical shell of width $\mathrm{d}v$ becomes

$$\mathrm{d}N_{\mathrm{shell}} = \mathrm{d}N_V D(v) 4\pi v^2 \mathrm{d}v = \mathrm{d}N_V g(v) \mathrm{d}v, \tag{2.3.27}$$

where we have introduced the distribution function over molecular speeds

$$g(v) = 4\pi v^2 D(v) \tag{2.3.28}$$

in the last equality in (2.3.27).

We can now use (2.3.28) to write (2.3.23) in terms of $g(v)$, namely

$$\mathrm{d}N_{v,\theta,\varphi} = \mathrm{d}N_V g(v) \mathrm{d}v \frac{\mathrm{d}\Psi}{4\pi} = \mathcal{N} \mathrm{d}S v \cos\theta \mathrm{d}t g(v) \mathrm{d}v \frac{\sin\theta \mathrm{d}\theta \mathrm{d}\varphi}{4\pi}, \tag{2.3.29}$$

where the last equality comes from the definitions of $\mathrm{d}N_V$ and of $\mathrm{d}\Psi$. Integrating (2.3.29) over v, θ, φ and using (2.3.22), we finally obtain the effusion flux in the form

$$\mathcal{F} = \int \frac{\mathrm{d}N_{v,\theta,\varphi}}{\mathrm{d}S \mathrm{d}t} = \mathcal{N} \int_0^\infty v g(v) \mathrm{d}v \frac{1}{4\pi} \int_0^{\frac{\pi}{2}} \sin\theta \cos\theta \mathrm{d}\theta \int_0^{2\pi} \mathrm{d}\varphi = \frac{1}{4} \mathcal{N} \bar{c}, \tag{2.3.30}$$

where $\bar{c} = \int_0^\infty v g(v) \mathrm{d}v$ is the mean molecular velocity. It can be proven that the

functional form of $g(v)$ corresponds to the Maxwell-Boltzman distribution, however this derivation is out of the scope of this thesis and we refer the reader to [12] for further details. Taking this into consideration, the mean velocity, which corresponds to the mean of the Maxwell-Boltzman distribution, becomes

$$\bar{c} = \sqrt{\frac{8k_BT}{\pi m}}, \tag{2.3.31}$$

where m is the atomic mass of SiO_2. Therefore, (2.3.30) reads

$$\mathcal{F} = \frac{1}{4}(C_{SiO_2} - C_e)\sqrt{\frac{8k_BT}{\pi m}}, \tag{2.3.32}$$

where we have used $(C_{SiO_2} - C_e)$ instead of $\mathcal{N}$ to be consistent with the notation in (2.3.20). The rate of condensation, F, to the particle surface is obtained by multiplying the effusion flux by the surface area of the particle [24], giving

$$F = (C_{SiO_2} - C_e)\sqrt{\frac{k_BT}{2\pi m}}\pi s^2. \tag{2.3.33}$$

As in (2.3.19), the rate of particle volume growth is

$$\frac{\mathrm{d}v}{\mathrm{d}t} = F\frac{M_{SiO_2}}{\rho_p} = \sqrt{\frac{k_BT}{2\pi m}}(C_{SiO_2} - C_e)\pi s^2\frac{M_{SiO_2}}{\rho_p}, \tag{2.3.34}$$

thus the diameter growth rate is

$$\frac{\mathrm{d}s}{\mathrm{d}t} = \frac{2M_{SiO_2}}{\rho_p}\sqrt{\frac{k_BT}{2\pi m}}(C_{SiO_2} - C_e). \tag{2.3.35}$$

Note that unlike with the previous regime, this formula does not depend on the size of the particle itself.

2.3.3.3 Transition regime ($0.1 < \mathrm{Kn} < 10$)

For particle growth between the free-molecule and continuum regimes, the expression for the condensation rate in the continuum regime is usually extended by adding an interpolation factor, $f(\mathrm{Kn})$,

$$\frac{\mathrm{d}s}{\mathrm{d}t} = \frac{4M_{SiO_2}D_{SiO_2}(C_{SiO_2} - C_e)}{\rho_p s}f(\mathrm{Kn}). \tag{2.3.36}$$

The interpolation factor is such that for small Knudsen numbers, the growth rate tends to (2.3.20), and for very large Knudsen numbers, it tends to (2.3.35). Several approaches for the form of $f(\mathrm{Kn})$ are available in the literature [71]. For instance, Dahneke's approach [71] states that

$$f(\mathrm{Kn}) = \frac{1 + \mathrm{Kn}}{1 + 2\mathrm{Kn} + 2\mathrm{Kn}^2}, \tag{2.3.37}$$

with the mean free path included in the definition of the Knudsen number approximated by

$$\lambda = \frac{2D_{\mathrm{SiO_2}}}{\bar{c}}. \tag{2.3.38}$$

In addition, since it is well known that microsilica particles do not shrink (or evaporate), $\mathrm{d}s/\mathrm{d}t \geq 0$, so in our model we will take

$$\hat{G} = \frac{\mathrm{d}s}{\mathrm{d}t}\mathcal{H}\left(C_{\mathrm{SiO_2}} - C_e\right) \tag{2.3.39}$$

as the particle growth rate, with $\mathrm{d}s/\mathrm{d}t$ as in (2.3.36) and where $\mathcal{H}$ represents the Heaviside function. This guarantees that the flux of material is onto the particle and means that particle growth 'turns on' for levels of SiO_2 concentration above saturation and 'switches off' for concentrations below saturation. The assumption that evaporation plays a negligible role is also made in [94], where the growth rate is set to zero for values of the partial pressure of the condensing material below equilibrium.

In Figure 2.2, we show the particle growth rate with respect to the particle diameter for the three regimes just mentioned, using Dahneke's interpolation formula for the transition regime. We notice that the growth rate remains constant with respect to s in the free molecular regime (black dashed line), while it decreases as $1/s$ for the continuum regime (red dashed line). The blue dots indicate the minimum and maximum values of s such that $0.1 < \mathrm{Kn} < 10$. The interpolation formula (blue) approximates well both regimes for small and large particle sizes and gives a smooth transition between them.

Experiments [22] show that the majority of microsilica primary particles are smaller than 1μm, with a mean particle size of 100nm. Therefore, since $2\lambda \approx 2 - 4.31 \times 10^{-6}$m over the temperature range $T = 370\mathrm{K} - 1713\mathrm{K}$, the majority of the particles that we are interested in are within the kinetic regime and we will simply use (2.3.35) as $\mathrm{d}s/\mathrm{d}t$ in (2.3.39) throughout the rest of this thesis.

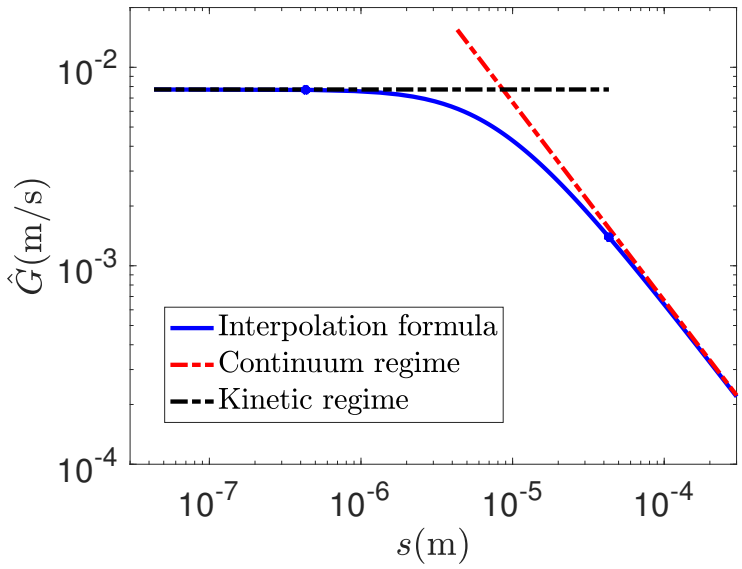

Figure 2.2: Growth rate for the kinetic, transition, and continuum regimes as given in (2.3.36)-(2.3.38).

2.3.4 Coupling the particle growth and chemical reactions

The particle formation and growth model is coupled to the chemical species concentrations and temperature directly via the growth rate for condensation, $\hat{G}$ and the nucleation rate, $\hat{J}$. These rates depend on the concentration of vapour silicon dioxide, C_{SiO_2}, predicted by (2.2.10d) and on the temperature of the system given by (2.2.17).

Moreover, in order to account for the material consumed and heat produced due to the formation of the particles, we add a sink term S_C (units $[\mathrm{mol}\cdot\mathrm{m}^{-3}\cdot\mathrm{s}^{-1}]$) in (2.2.10d) and a source term S_T (units $[\mathrm{J}\cdot\mathrm{m}^{-3}\cdot\mathrm{s}^{-1}]$) in (2.2.17). The form of these terms comes from integrating the particle density, n, times the mass flux through the surface of a spherical particle, F (as defined in (2.3.18) for the continuum regime and in (2.3.33) for the kinetic regime), over all particle diameters. That is,

$$S_C = \int_{s_{\min}}^{\infty} Fn\mathrm{d}s = \frac{\pi}{2}\frac{\rho_p}{M_{\mathrm{SiO}_2}}\int_{s_{\min}}^{\infty} s^2\hat{G}n\mathrm{d}s, \tag{2.3.40}$$

where we have written it in terms of the growth rate, $\hat{G}$, as given in (2.3.39) with $\mathrm{d}s/\mathrm{d}t$ taken from either (2.3.20) or (2.3.35) depending on the regime under study. If we also consider the size change due to particle fluctuations as in (2.3.6), the sink

term transforms to

$$S_C = \frac{\pi}{2}\frac{\rho_p}{M_{\mathrm{SiO_2}}}\int_{s_{\min}}^{\infty} s^2\left(\hat{G}n - D_s\frac{\partial n}{\partial s}\right)\mathrm{d}s, \tag{2.3.41}$$

see, *e.g.*, [50]. Since mass transfer is the driving mechanism for particle growth, the source term for the energy released due to the formation of the particles is proportional to (2.3.40). We simply multiply it by the enthalpy of formation of the particle, ΔH_p, which has physical units $\left[\mathrm{J}\cdot\mathrm{mol}^{-1}\right]$ or equivalently by $L_V\frac{M_{\mathrm{SiO_2}}}{\rho_p}$, where L_V is the specific latent heat for condensation with units $[\mathrm{J}\cdot\mathrm{m}^{-3}]$. This is,

$$S_T = L_V\frac{M_{\mathrm{SiO_2}}}{\rho_p}S_C. \tag{2.3.42}$$

Since the form of the sink (S_C) and source (S_T) terms in the SiO_2 concentration and temperature equations respectively is written in terms of an integral, our system is extremely hard to solve in its current form. In the next section we will see how, for the free-molecular regime, which is the one we are interested in, we can transform the system, without making any further assumptions, so that there are no integro-differential equations.

2.3.5 Moments of the distribution

Let M_k be the kth raw moment of the n distribution, namely

$$M_k = \int_{s_{\min}}^{\infty} s^k n\mathrm{d}s. \tag{2.3.43}$$

For the free-molecular case, where the growth rate of microsilica particles is given by (2.3.39) and (2.3.35), we can write the integrals in the expressions derived for S_C and S_T in the previous section in terms of moments of the distribution. Note that this holds for any growth rate that does not depend implicitly on the particle size so that we can take $\hat{G}$ in (2.3.40)-(2.3.41) outside of the integral. At the same time, D_s needs to be independent of s.

We begin by integrating (2.3.41) by parts and using the far-field condition (2.3.8) to deduce that

$$S_C = \frac{\rho_p}{L_V M_{\mathrm{SiO_2}}}S_T = \frac{\pi\rho_p}{2M_{\mathrm{SiO_2}}}\left(\hat{G}M_2 + D_s\left((s_{\min})^2 n(s_{\min},\boldsymbol{x},t) + 2M_1\right)\right). \tag{2.3.44}$$

Now, we add three extra PDEs to the system for the zeroth, first, and second moments

of the particle size distribution n, in the following way. We multiply the PDE (2.3.6) by s^k, for $k = 0, 1, 2$, and integrate in each case with respect to s between $s_{\min}$ and ∞, making use of conditions (2.3.7)-(2.3.8). For instance, for $k = 0$, we integrate (2.3.6) in s to give

$$\frac{\partial}{\partial t}\left(\int_{s_{\min}}^{\infty} n\mathrm{d}s\right) + \boldsymbol{\nabla}\cdot\left(\left(\int_{s_{\min}}^{\infty} n\mathrm{d}s\right)\mathbf{v} - D_p\boldsymbol{\nabla}\left(\int_{s_{\min}}^{\infty} n\mathrm{d}s\right)\right) = -\left[n\hat{G} - D_s\frac{\partial n}{\partial s}\right]_{s_{\min}}^{\infty}. \tag{2.3.45}$$

Using the definition of M_0 as in (2.3.43) with $k = 0$ and applying conditions (2.3.7) and (2.3.8) on the right hand side of (2.3.45), we obtain the following PDE for the zeroth moment of the particle size distribution,

$$\frac{\partial M_0}{\partial t} + \boldsymbol{\nabla}\cdot(M_0\mathbf{v} - D_p\boldsymbol{\nabla}M_0) = \hat{J}. \tag{2.3.46a}$$

In a similar way, we obtain the following equations for M_1 and M_2,

$$\frac{\partial M_1}{\partial t} + \boldsymbol{\nabla}\cdot(M_1\mathbf{v} - D_p\boldsymbol{\nabla}M_1) = s_{\min}\hat{J} + \hat{G}M_0 + D_s n(s_{\min}, \boldsymbol{x}, t), \tag{2.3.46b}$$

$$\frac{\partial M_2}{\partial t} + \boldsymbol{\nabla}\cdot(M_2\mathbf{v} - D_p\boldsymbol{\nabla}M_2) = (s_{\min})^2\hat{J} + 2\hat{G}M_1 + 2D_s\left(s_{\min}n(s_{\min}, \boldsymbol{x}, t) + M_0\right). \tag{2.3.46c}$$

The moment equations (2.3.46) are coupled to the concentrations and temperature through $\hat{J}$ and $\hat{G}$ and to the particle distribution equation through the value of n at the minimum particle size $s_{\min}$. In addition, the SiO_2 concentration and temperature equations are coupled to M_1, M_2 and $n(s_{\min})$ through (2.3.44). However, note that if we take $D_s = 0$, the concentrations, temperature, momentum and moments equations decouple completely from n and we can solve (2.2.10), (2.2.15), (2.2.17), (2.2.22) and (2.3.46) separately from equation (2.3.6), which as mentioned before is significantly more challenging to solve due to the extra dimension, s.

A similar approach has been considered elsewhere [59, 66, 88] for solving related population balance models in terms of moments.

2.4 Full model

In this section we summarise the full model derived in the previous sections and prescribe initial and boundary conditions for the furnace hood geometry described in Figure 2.1 in Section 2.1.

2.4.1 Governing equations

For $(\mathbf{x}, t) \in \Omega_x \times (0, \infty)$, the governing equations are given by

$$\frac{\partial C_{\mathrm{N_2}}}{\partial t} + \boldsymbol{\nabla} \cdot \left(C_{\mathrm{N_2}} \mathbf{v} - \rho D_{\mathrm{N_2}} \boldsymbol{\nabla} \left(\frac{C_{\mathrm{N_2}}}{\rho} \right) \right) = 0, \tag{2.4.1a}$$

$$\frac{\partial C_{\mathrm{O_2}}}{\partial t} + \boldsymbol{\nabla} \cdot \left(C_{\mathrm{O_2}} \mathbf{v} - \rho D_{\mathrm{O_2}} \boldsymbol{\nabla} \left(\frac{C_{\mathrm{O_2}}}{\rho} \right) \right) = -R_1 - R_2, \tag{2.4.1b}$$

$$\frac{\partial C_{\mathrm{SiO}}}{\partial t} + \boldsymbol{\nabla} \cdot \left(C_{\mathrm{SiO}} \mathbf{v} - \rho D_{\mathrm{SiO}} \boldsymbol{\nabla} \left(\frac{C_{\mathrm{SiO}}}{\rho} \right) \right) = -2R_1, \tag{2.4.1c}$$

$$\frac{\partial C_{\mathrm{SiO_2}}}{\partial t} + \boldsymbol{\nabla} \cdot \left(C_{\mathrm{SiO_2}} \mathbf{v} - \rho D_{\mathrm{SiO_2}} \boldsymbol{\nabla} \left(\frac{C_{\mathrm{SiO_2}}}{\rho} \right) \right) = 2R_1 - S_C, \tag{2.4.1d}$$

$$\frac{\partial C_{\mathrm{CO}}}{\partial t} + \boldsymbol{\nabla} \cdot \left(C_{\mathrm{CO}} \mathbf{v} - \rho D_{\mathrm{CO}} \boldsymbol{\nabla} \left(\frac{C_{\mathrm{CO}}}{\rho} \right) \right) = -2R_2, \tag{2.4.1e}$$

$$\frac{\partial C_{\mathrm{CO_2}}}{\partial t} + \boldsymbol{\nabla} \cdot \left(C_{\mathrm{CO_2}} \mathbf{v} - \rho D_{\mathrm{CO_2}} \boldsymbol{\nabla} \left(\frac{C_{\mathrm{CO_2}}}{\rho} \right) \right) = 2R_2, \tag{2.4.1f}$$

with

$$\frac{\partial \rho}{\partial t} + \boldsymbol{\nabla} \cdot (\rho \mathbf{v}) = 0, \tag{2.4.1g}$$

$$\frac{\partial}{\partial t} (\rho \mathbf{v}) + \boldsymbol{\nabla} \cdot (\rho \mathbf{v} \otimes \mathbf{v}) = -\boldsymbol{\nabla} p + \boldsymbol{\nabla} \cdot \boldsymbol{\tau}, \tag{2.4.1h}$$

and

$$\frac{\partial}{\partial t} (\rho c_p T) + \boldsymbol{\nabla} \cdot (\rho c_p T \mathbf{v} - k \boldsymbol{\nabla} T) = \frac{\partial p}{\partial t} + \mathbf{v} \cdot \boldsymbol{\nabla} p + \Phi + S_R + S_T, \tag{2.4.1i}$$

as well as

$$\frac{\partial M_0}{\partial t} + \boldsymbol{\nabla} \cdot (M_0 \mathbf{v} - D_p \boldsymbol{\nabla} M_0) = \hat{J}, \tag{2.4.1j}$$

$$\frac{\partial M_1}{\partial t} + \boldsymbol{\nabla} \cdot (M_1 \mathbf{v} - D_p \boldsymbol{\nabla} M_1) = s_{\min} \hat{J} + \hat{G} M_0 + D_s n(s_{\min}, \boldsymbol{x}, t), \tag{2.4.1k}$$

$$\frac{\partial M_2}{\partial t} + \boldsymbol{\nabla} \cdot (M_2 \mathbf{v} - D_p \boldsymbol{\nabla} M_2) = (s_{\min})^2 \hat{J} + 2\hat{G} M_1 + 2D_s \left(s_{\min} n(s_{\min}, \boldsymbol{x}, t) + M_0 \right), \tag{2.4.1l}$$

together with the equation of state

$$p = \sum_{\text{species j}} C_j RT. \tag{2.4.2}$$

We model the number density function of particles with the following population balance equation

$$\frac{\partial n}{\partial t} + \boldsymbol{\nabla} \cdot (n\mathbf{v} - D_p \boldsymbol{\nabla} n) + \frac{\partial}{\partial s}\left(n\hat{G} - D_s \frac{\partial n}{\partial s}\right) = 0, \tag{2.4.3}$$

for $(s, \mathbf{x}, t) \in (s_{\min}, \infty) \times \Omega_x \times (0, \infty)$. The definitions of the constitutive laws found in equations (2.4.1)-(2.4.3) are given in Table 2.1.

Constitutive law	Definition
R_1	$A_1 \exp\left(-E_1/RT\right) C_{\text{SiO}} C_{\text{O}_2}$
R_2	$A_2 \exp\left(-E_2/RT\right) C_{\text{CO}} C_{\text{O}_2}$
S_R	$\Delta H_1 R_1 + \Delta H_2 R_2$
S_C	$\frac{\pi \rho_p}{2M_{\text{SiO}_2}} \left(\hat{G} M_2 + D_s \left((s_{\min})^2 n(s_{\min}, \boldsymbol{x}, t) + 2M_1\right)\right)$
S_T	$\frac{\pi L_V}{2} \left(\hat{G} M_2 + D_s \left((s_{\min})^2 n(s_{\min}, \boldsymbol{x}, t) + 2M_1\right)\right)$
$\hat{G}$	$\frac{2M_{\text{SiO}_2}}{\rho_p} \sqrt{\frac{k_B T}{2\pi m}} (C_{\text{SiO}_2} - C_e) \mathcal{H}\left(C_{\text{SiO}_2} - C_e\right)$
$\hat{J}$	$J_0 \exp\left(-\frac{16\pi\gamma^3 v_C^2}{3(k_B T)^3 (\ln\left(C_{\text{SiO}_2}/C_e\right))^2}\right)$
C_e	$C_0 \exp\left(\frac{4\gamma v_C}{s k_B T}\right)$
ρ	$\sum_{\text{species j}} M_j C_j$
$\boldsymbol{\tau}$	$\mu\left(\boldsymbol{\nabla}\mathbf{v} + (\boldsymbol{\nabla}\mathbf{v})^T - \frac{2}{3}\mathbf{I}(\boldsymbol{\nabla} \cdot \mathbf{v})\right)$
Φ	$\boldsymbol{\nabla} \cdot (\boldsymbol{\tau}\mathbf{v}) - \mathbf{v}\boldsymbol{\nabla} \cdot \boldsymbol{\tau}$

Table 2.1: Definitions of the constitutive laws found in the model (2.4.1)-(2.4.3).

2.4.2 Boundary and initial conditions

We propose the following boundary conditions. At the bottom of the domain, we prescribe unidirectional flow, Dirichlet boundary conditions for the temperature and concentrations of SiO and CO, zero concentration for the reaction products and species

in air, and we assume that there are no particles. Thus, for $\mathbf{x} \in \partial\Omega_b$, $t > 0$, $s > s_{\min}$,

$$\mathbf{v} = -v_1\boldsymbol{\nu}, \quad T = T_1, \quad C_{\mathrm{SiO}} = C_{\mathrm{SiO},0}, \quad C_{\mathrm{CO}} = C_{\mathrm{CO},0}, \tag{2.4.4a}$$

$$C_j = 0, \text{ for } j \notin \{\mathrm{SiO}, \mathrm{CO}\}, \quad n = M_i = 0, \text{ for } i = 0, 1, 2, \tag{2.4.4b}$$

where v_1, T_1, $C_{\mathrm{SiO},0}$, and $C_{\mathrm{CO},0}$, are prescribed values, and $\boldsymbol{\nu}$ is the outward normal to the corresponding surface. On the walls of the furnace hood, we apply a no-slip condition, thermal insulation, and no flux of species and particles. Thus, for $\boldsymbol{x} \in \partial\Omega_w$, $t > 0$, $s > s_{\min}$,

$$\mathbf{v} = \mathbf{0}, \quad \frac{\partial T}{\partial \nu} = \frac{\partial C_j}{\partial \nu} = \frac{\partial n}{\partial \nu} = \frac{\partial M_i}{\partial \nu} = 0, \text{ for all species } j, \text{ and } i = 0, 1, 2. \tag{2.4.5}$$

At the door, we assume unidirectional flow of air entering the furnace. We prescribe values for the temperature and species N_2 and O_2 concentrations, while we consider zero concentration of the remaining species and no particles through the door. Thus, for $\mathbf{x} \in \partial\Omega_d$, $t > 0$, $s > s_{\min}$,

$$\mathbf{v} = -v_2\boldsymbol{\nu}, \quad T = T_2, \quad C_{\mathrm{N}_2} = C_{\mathrm{N}_2,0}, \quad C_{\mathrm{O}_2} = C_{\mathrm{O}_2,0}, \tag{2.4.6a}$$

$$C_j = n = M_i = 0, \text{ for the rest of species } j, \text{ and } i = 0, 1, 2. \tag{2.4.6b}$$

At the top of the domain we have the outlet, where we consider atmospheric pressure and assume the outflow to be perpendicular to the boundary. The heat, species concentration, and particles fluxes are purely advective. Thus, at $\mathbf{x} \in \partial\Omega_t$, $t > 0$, $s > s_{\min}$,

$$(\boldsymbol{I} - \boldsymbol{\nu}\boldsymbol{\nu}^T)\mathbf{v} = \mathbf{0}, \quad \boldsymbol{\nu}^T(-p\boldsymbol{I} + \boldsymbol{\tau})\boldsymbol{\nu} = -p_{\mathrm{atm}}, \tag{2.4.7a}$$

$$\frac{\partial T}{\partial \nu} = \frac{\partial C_j}{\partial \nu} = \frac{\partial n}{\partial \nu} = \frac{\partial M_i}{\partial \nu} = 0, \text{ for all species } j, \text{ and for } i = 0, 1, 2. \tag{2.4.7b}$$

With respect to the size variable s, we assume that all newly formed particles have size $s_{\min}$ and are created with a non-constant nucleation rate given by (2.3.13) that depends on the temperature and SiO_2 concentration, namely

$$\hat{G}n - D_s\frac{\partial n}{\partial s} = \hat{J} \quad \text{at} \quad s = s_{\min.} \tag{2.4.8}$$

In addition, if $D_s > 0$, we impose the far-field condition given by

$$n \to 0 \quad \text{as} \quad s \to \infty. \tag{2.4.9}$$

The initial conditions can be written as

$$C_j = C_{j,\mathrm{i}}(\mathbf{x}), \quad T = T_{\mathrm{i}}(\mathbf{x}), \quad \mathbf{v} = \mathbf{v}_{\mathrm{i}}(\mathbf{x}), \quad n = M_0 = M_1 = M_2 = 0 \quad \text{at} \quad t = 0, \tag{2.4.10}$$

for all species j, and where the form of the functions $C_{j,\mathrm{i}}(\mathbf{x})$, $T_{\mathrm{i}}(\mathbf{x})$ and $\mathbf{v}_{\mathrm{i}}(\mathbf{x})$ will be discussed in further chapters depending on the limit under study.

A full list of the dimensional parameters used in the reactive flow model is given in Table 2.2, whereas the dimensional parameters appearing in the model for the formation and growth of the particles are given in Table 2.3.

The values for the input chemical concentrations, temperatures and velocities in Table 2.2 are taken from real data and their ranges are due to their variability depending on furnace operation. The diffusion coefficients for all the chemicals are taken from both [53] and [57] and are in the range 10^{-5} – 10^{-3} m^2/s. The enthalpies of combustion are very large, approximately 10^5 J/mol, since the reactions are highly exothermic and were calculated with the software HSC Chemistry [68]. With respect to the reaction rates, the CO reaction is much more well-known than the SiO, thus more references are found in the literature for its activation energy and reaction rate constant, see for instance [82]. For the SiO reaction rate, we use the data found in [39] for an equivalent reaction that gives reasonable results. Properties such as the density and thermal conductivity of the gas are taken as the corresponding ones for air since it is the dominant component in the mixture. Note that the concentration of air that enters the furnace, $C_{\mathrm{N_2},0}$ and $C_{\mathrm{O_2},0}$, as well as, the velocities of the fuel and air streams, vary depending on the furnace type and operating strategies. Thus, these parameters can be controlled by operators. In later chapters, we will study the effects of modifying the ratio of fuel to oxygen concentrations, and the ratio of both streams velocities, on the final microsilica output.

There are some parameter values in Table 2.3 that have been estimated, such as, D_s and the saturation concentration coefficient, C_0, with a minimum of 0 for the instantaneous formation of particles and a maximum of 1 taken from the SiO input. The latter two will be left as control parameters and we will determine the sensitivity of solutions on both. The value of $s_{\min}$ is taken as the smallest microsilica particle size seen in experiments [22].

Parameter	Typical value	Units	Reference
$C_{N_2,0}$	$20 - 1200$	mol/m^3	Input concentration of N_2[1]
$C_{O_2,0}$	$5 - 300$	mol/m^3	Input concentration of O_2[1]
$C_{SiO,0}$	1	mol/m^3	Input concentration of SiO[1]
$C_{CO,0}$	1	mol/m^3	Input concentration of CO[1]
T_1	1713	K	Temperature of the fuel entering[1]
T_2	1073	K	Temperature of the air entering[1]
v_1	$0.5 - 5$	m/s	Velocity of the fuel entering[1]
v_2	$5 - 10$	m/s	Velocity of the air entering[1]
D_{N_2}	1.783×10^{-5}	m^2/s	[53]
D_{O_2}	4.700×10^{-4}	m^2/s	[57]
D_{SiO}	3.900×10^{-4}	m^2/s	[57]
D_{SiO_2}	3.900×10^{-4}	m^2/s	Taken to be the same as D_{SiO}
D_{CO}	1.804×10^{-5}	m^2/s	[53]
D_{CO_2}	1.429×10^{-5}	m^2/s	[53]
c_p	1005	J/(kg·K)	[39]
ΔH_1	3.930×10^5	J/mol	Enthalphy of SiO combustion[2]
ΔH_2	1.395×10^5	J/mol	Enthalphy of CO combustion[2]
A_1	1.000×10^7	$m^3/(mol \cdot s)$	[39]
A_2	1.800×10^4	$m^3/(mol \cdot s)$	[82]
E_1	27196	J/mol	[39]
E_2	9974.65	J/mol	[82]
R	8.314	J/(mol·K)	Universal gas constant
ρ_0	0.3529	kg/m^3	Density of air[3]
k	5.784×10^{-2}	W/(m·K)	Thermal conductivity of air[3]
μ	4.826×10^{-5}	kg/(m· s)	Viscosity of air[3]
M_{N_2}	2.801×10^{-2}	kg/mol	Molar mass of N_2
M_{O_2}	3.200×10^{-2}	kg/mol	Molar mass of O_2
M_{SiO}	4.408×10^{-2}	kg/mol	Molar mass of SiO
M_{SiO_2}	6.008×10^{-2}	kg/mol	Molar mass of SiO_2
M_{CO}	2.801×10^{-2}	kg/mol	Molar mass of CO
M_{CO_2}	4.401×10^{-2}	kg/mol	Molar mass of CO_2

Table 2.2: Typical values of dimensional parameters in the reactive flow model. [1]Estimated value from [22]. [2]Obtained from the software HSC Chemistry. [3]Since air is the dominant component in the fluid. At $T = 1000$ K and $P = 1$ atm.

Parameter	Typical value	Units	Reference
C_0	$0-1$	$\mathrm{mol/m^3}$	Estimated
m	9.960×10^{-26}	kg	Atomic mass of SiO_2
ρ_p	2196	$\mathrm{kg/m^3}$	Density of SiO_2
$s_{\min}$	10^{-8}	m	Smallest particle seen in experiments[1]
D_p	$< 5.2 \times 10^{-9}$	$\mathrm{m^2/s}$	Determined from Stokes-Einstein theory[2]
D_s	$0-10^{-8}$	$\mathrm{m^2/s}$	Estimated
J_0	10^{25}	$1/(\mathrm{m^3 \cdot\ s})$	[47]
v_C	4.536×10^{-29}	$\mathrm{m^3}$	Volume of a molecule of SiO_2
γ	3.200×10^{-2}	$\mathrm{J/m^2}$	[22]
k_B	1.3806×10^{-23}	J/K	Boltzman's constant
L_V	2.193×10^{10}	$\mathrm{J/m^3}$	[46]

Table 2.3: Typical values of dimensional parameters in the particle formation model. [1]Estimated value from [22]. [2]Stokes-Einstein theory approximates the diffusion coefficient of a particle of radius r as $D_p = \frac{k_B T_1}{6\pi\mu r}$.

2.5 Summary

In conclusion, motivated by the two combustion reactions happening within a furnace hood (2.2.1), one of them responsible for the formation of microsilica particles, we have derived a mathematical model for a reactive flow by introducing conservation equations for the momentum, temperature, chemical concentrations and an equation of state. The fluid considered is a combination of all the chemicals involved in the reactions, which are all gases, thus compressibility effects were included.

In the second part of the chapter, we introduced the notion of a population balance equation which is generally used to model the formation and growth of particles. This equation usually accounts for different particle physics such as nucleation, continuous growth, breakage and aggregation, though the key physics involved in microsilica particle formation were highlighted and a simplified equation was presented. In order to close the system, we derived expressions for the particles' growth rate for both regimes, continuum and kinetic, and for the nucleation rate by maximizing the Gibbs free energy. Both expressions depend on the SiO_2 concentration and temperature variations taken from the reactive flow model. Finally, we added the effects of particle growth on the SiO_2 concentration and temperature by including a sink and a source term on the respective equations. We concluded that, when $D_s = 0$, the amount of SiO_2 consumed and heat generated from particle growth only depends on the second moment of the particle size distribution, n, and not on the whole distribution. Equations for the first three raw moments of the distribution were derived from the

simplified population balance equation. We finished by introducing the boundary and initial conditions for the full model for a generalised furnace hood geometry.

As mentioned earlier, the full model derived in this chapter will serve as a basis for the rest of the chapters, in which we will find solutions to simplified subproblems having non-dimensionalised in each case in the most appropriate manner. Full numerical simulations of the model presented here will be given in Chapter 3 for the corresponding two-dimensional domain connected to the axis of symmetry of Ω_x.

Chapter 3

COMSOL simulations of the full furnace hood model

We start the analysis of our problem by using the software COMSOL [14] to carry out steady-state simulations of the full system of equations, (2.4.1)-(2.4.2), for a representative two-dimensional geometry of the furnace hood. These simulations will give us some preliminary insights into the dynamics of our system before we focus our attention on the dominant mechanisms and perform asymptotic analyses in the chapters that follow. Therefore, this chapter is a separate case and will mainly be used to motivate and justify our modelling approach in the remainder of the thesis.

3.1 Definition of the two-dimensional domain

A schematic of the domain that we will use in the COMSOL simulations is shown in Figure 3.1, which is a 2D version of the 3D axisymmetric domain introduced in Figure 2.1b in Chapter 2. Therefore, the same boundary conditions as in Section 2.4.2 apply here. On the walls, which correspond to $\delta\Omega_w$ in Figure 2.1b, we apply a no-slip condition, thermal insulation, and no flux of chemical species and particles. At the air inlet, which corresponds to the furnace door, that is, $\delta\Omega_d$, we have unidirectional flow of magnitude v_2, a fixed temperature T_2, prescribed molar concentrations for the oxygen and nitrogen, $C_{\mathrm{O}_2,0}$ and $C_{\mathrm{N}_2,0}$, zero concentration of the remaining species and no particles. At the outlet, that is, $\delta\Omega_t$, we have similar outflow conditions as in (2.4.7) so we assume atmospheric pressure, the flow to be perpendicular to the boundary, and the heat, species, and particles fluxes to be purely advective. The only boundary that is slightly different to what was presented in Chapter 2 is the bottom boundary of the domain, which has been divided into an active and an inactive charge

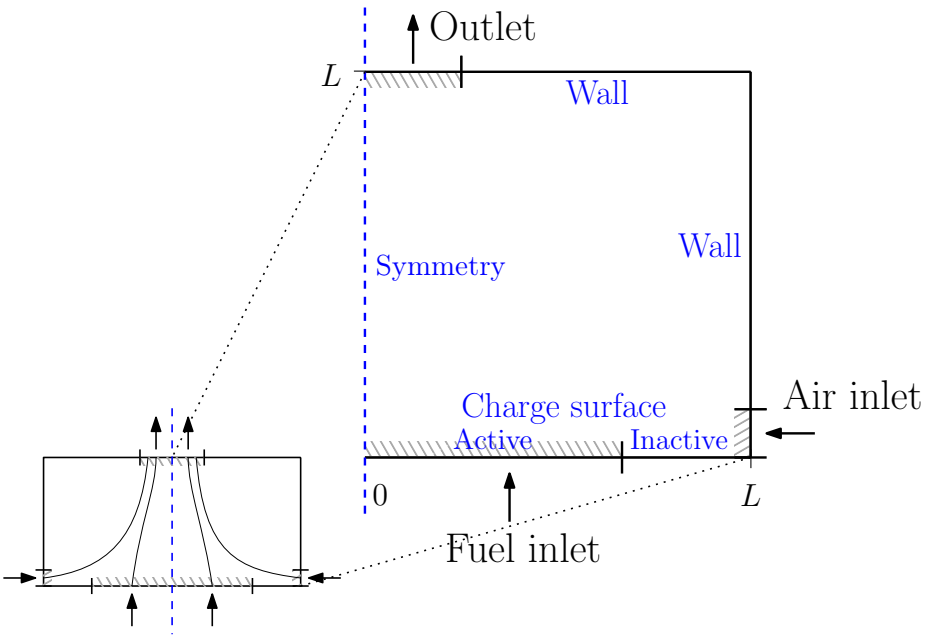

Figure 3.1: Schematic of the two-dimensional domain considered in the COMSOL simulations of the full model. The inlets and outlet are represented with grey dashed rectangles and with an arrow indicating the direction of the flow. Other boundaries of the domain are specified in blue fonts. On the bottom left side, there is a small diagram of the full 2D furnace hood to place into context the current domain that we are considering.

regions. The active zone corresponds to the place through which the fuel comes into the furnace hood and therefore conditions (2.4.4) for $\partial\Omega_b$ apply here. Thus, at this boundary the flow is unidirectional and with a magnitude equal to v_1, the temperature is given by T_1, the SiO and CO concentrations are prescribed and equal to $C_{\mathrm{SiO},0}$ and $C_{\mathrm{CO},0}$ respectively, and we have zero concentration of the remaining species and no particles through the inlet. On the other hand, the inactive part of the charge surface acts as a wall and therefore its boundary conditions are the same as for $\partial\Omega_w$, (2.4.5), but instead of thermal insulation we fix the temperature value and make it equal to T_2. Additionally, we apply symmetry conditions (no flux) of all variables on the left boundary of the domain, depicted in Figure 3.1 with a dashed blue line. The value of all parameters just mentioned can be found in Table 2.2.

3.2 Non-dimensionalisation

Before attempting a solution to the two-dimensional version of the system (2.4.1)-(2.4.2), we non-dimensionalise the equations by scaling the variables in the following

way:

$$T = (T_1 - T_2)\tilde{T} + T_2, \tag{3.2.1}$$

where T_1 is the temperature of the fuel as it enters the furnace hood and T_2 is the temperature of the air coming from outside the furnace (in practice $T_2 < T_1$),

$$C_j = C_{j,0}\tilde{C}_j, \tag{3.2.2}$$

where $C_{j,0}$ represents the typical input concentration of the reactant j, and while for the products we take $C_{\mathrm{SiO_2},0} = C_{\mathrm{SiO},0}$ and $C_{\mathrm{CO_2},0} = C_{\mathrm{CO},0}$ since we expect their maximum amount to be equal to the initial amount of the respective reactant as given by (2.2.1). We choose a typical furnace lengthscale to scale our space variables, that is,

$$x = L\tilde{x}, \tag{3.2.3}$$

$$y = L\tilde{y}, \tag{3.2.4}$$

with $L = 4$m being the height and the radius of the furnace hood as shown in Figure 3.1. The air inlet velocity, v_2, as in Table 2.2 is used to scale the velocity field, namely

$$u = v_2\tilde{u}, \tag{3.2.5}$$

$$v = v_2\tilde{v}, \tag{3.2.6}$$

and the density of air, ρ_0, to scale the total density of the mixture, that is,

$$\rho = \rho_0\tilde{\rho}. \tag{3.2.7}$$

Since inertial forces are dominant over viscous forces within the fluid, we select an inertial pressure scaling by using the latter two scalings for the velocity and the density in the following way,

$$p = \rho_0 v_2^2 \tilde{p}. \tag{3.2.8}$$

Finally, we scale the moments of the particle size distribution with the ratio between the nucleation and growth rate coefficients, times the critical diameter for nucleation

raised to the relevant power. Thus, we have that for $i = 0, 1, 2$,

$$M_i = \frac{J_0}{G_0} s_{\min}^{i+1} \tilde{M}_i, \tag{3.2.9}$$

where J_0 is given in Table 2.3, and

$$G_0 = \frac{2MC_{\mathrm{SiO}_2,0}}{\rho_p} \sqrt{\frac{k_B(T_1 - T_2)}{2\pi m}} \approx 6.502 \times 10^{-3}, \tag{3.2.10}$$

with units m/s, comes from the definition of the particle growth rate, $\hat{G}$, as given in Table 2.1.

With these scalings and neglecting the over tilde notation, our governing equations become the following. For every chemical species j in the mixture, we have that

$$u\frac{\partial C_j}{\partial x} + v\frac{\partial C_j}{\partial y} - \frac{1}{\mathrm{Pe}_j}\left[\frac{\partial}{\partial x}\left(\rho\frac{\partial}{\partial x}\left(\frac{C_j}{\rho}\right)\right) + \frac{\partial}{\partial y}\left(\rho\frac{\partial}{\partial y}\left(\frac{C_j}{\rho}\right)\right)\right] = \gamma_j, \tag{3.2.11a}$$

where the reaction terms are given by

$$\gamma_{\mathrm{N}_2} = 0, \tag{3.2.11b}$$

$$\gamma_{\mathrm{O}_2} = -\frac{a}{2}\left(\mathrm{Da}_1 K_1(T) C_{\mathrm{O}_2} C_{\mathrm{SiO}} + \mathrm{Da}_2 K_2(T) C_{\mathrm{O}_2} C_{\mathrm{CO}}\right), \tag{3.2.11c}$$

$$\gamma_{\mathrm{SiO}} = -\mathrm{Da}_1 K_1(T) C_{\mathrm{O}_2} C_{\mathrm{SiO}}, \tag{3.2.11d}$$

$$\gamma_{\mathrm{SiO}_2} = \mathrm{Da}_1 K_1(T) C_{\mathrm{O}_2} C_{\mathrm{SiO}} - \xi_1 G M_2, \tag{3.2.11e}$$

$$\gamma_{\mathrm{CO}} = -\mathrm{Da}_2 K_2(T) C_{\mathrm{O}_2} C_{\mathrm{CO}}, \tag{3.2.11f}$$

$$\gamma_{\mathrm{CO}_2} = \mathrm{Da}_2 K_2(T) C_{\mathrm{O}_2} C_{\mathrm{CO}}, \tag{3.2.11g}$$

with the dimensionless Arrhenius terms being

$$K_i(T) = \exp\left(-\frac{E_i}{R\left((T_1 - T_2)T + T_2\right)}\right), \quad i = 1, 2. \tag{3.2.11h}$$

All dimensionless parameters that appear in the non-dimensionalisation can be found in Table 3.1 and will be described at the end of this section.

The two-dimensional momentum equations become

$$\frac{\partial}{\partial x}(\rho u) + \frac{\partial}{\partial y}(\rho v) = 0, \tag{3.2.12a}$$

$$\rho\left(u\frac{\partial u}{\partial x}+v\frac{\partial u}{\partial y}\right)=-\frac{\partial p}{\partial x}+\frac{1}{\mathrm{Re}}\left(\frac{\partial^2 u}{\partial x^2}+\frac{\partial^2 u}{\partial y^2}+\frac{1}{3}\frac{\partial}{\partial x}\left(\frac{\partial u}{\partial x}+\frac{\partial v}{\partial y}\right)\right), \tag{3.2.12b}$$

$$\rho\left(u\frac{\partial v}{\partial x}+v\frac{\partial v}{\partial y}\right)=-\frac{\partial p}{\partial y}+\frac{1}{\mathrm{Re}}\left(\frac{\partial^2 v}{\partial x^2}+\frac{\partial^2 v}{\partial y^2}+\frac{1}{3}\frac{\partial}{\partial y}\left(\frac{\partial u}{\partial x}+\frac{\partial v}{\partial y}\right)\right), \tag{3.2.12c}$$

and the dimensionless temperature equation is

$$\rho\left(u\frac{\partial T}{\partial x}+v\frac{\partial T}{\partial y}\right)-\frac{1}{\mathrm{Pe}}\left(\frac{\partial^2 T}{\partial x^2}+\frac{\partial^2 T}{\partial y^2}\right)=\mathrm{Ec}\left(u\frac{\partial p}{\partial x}+v\frac{\partial p}{\partial y}\right)+\phi_1 K_1(T)C_{\mathrm{O}_2}C_{\mathrm{SiO}}$$
$$+\phi_2 K_2(T)C_{\mathrm{O}_2}C_{\mathrm{CO}}+\xi_2 G M_2, \tag{3.2.13}$$

where in (3.2.13) we have neglected viscous dissipation effects.

After scaling the variables, the equations for the moments of the particle size distribution become the following

$$u\frac{\partial M_0}{\partial x}+v\frac{\partial M_0}{\partial y}-\frac{1}{\mathrm{Pe}^*}\left(\frac{\partial^2 M_0}{\partial x^2}+\frac{\partial^2 M_0}{\partial y^2}\right)=\omega J, \tag{3.2.14a}$$

$$u\frac{\partial M_1}{\partial x}+v\frac{\partial M_1}{\partial y}-\frac{1}{\mathrm{Pe}^*}\left(\frac{\partial^2 M_1}{\partial x^2}+\frac{\partial^2 M_1}{\partial y^2}\right)=\omega\left(J+GM_0\right), \tag{3.2.14b}$$

$$u\frac{\partial M_2}{\partial x}+v\frac{\partial M_2}{\partial y}-\frac{1}{\mathrm{Pe}^*}\left(\frac{\partial^2 M_2}{\partial x^2}+\frac{\partial^2 M_2}{\partial y^2}\right)=\omega\left(J+2GM_1\right), \tag{3.2.14c}$$

where we have neglected fluctuations in the growth rate of the particles and have set $D_s=0$ in (2.4.1k)-(2.4.1l). The non-dimensional particle growth and nucleation rates found in the equations above are the following

$$G=\sqrt{T+T^*}\left(C_{\mathrm{SiO}_2}-C_{\mathrm{sat}}\right)\mathcal{H}\left(C_{\mathrm{SiO}_2}-C_{\mathrm{sat}}\right) \tag{3.2.15}$$

and

$$J=\exp\left(-\frac{\lambda_0}{\left(\frac{T}{T^*}+1\right)^3\ln^2\left(\frac{C_{\mathrm{SiO}_2}}{C_{\mathrm{sat}}}\right)}\right), \tag{3.2.16}$$

respectively. Finally, the dimensionless equation of state that relates the state variables is given by

$$p=\theta(T+T^*)\left(C_{\mathrm{N}_2}+C_{\mathrm{O}_2}+a\left(C_{\mathrm{SiO}}+C_{\mathrm{SiO}_2}+C_{\mathrm{CO}}+C_{\mathrm{CO}_2}\right)\right). \tag{3.2.17}$$

We have not included the population balance equation (2.4.3) into the simulations in this chapter and only solve for the moments of the distribution, however analytical and numerical solutions to this equation will be provided in the following chapters.

The non-dimensionalisation has introduced 22 dimensionless parameters that can be found in Table 3.1, along with their definition in terms of dimensional parameters and estimated value. In the dimensionless model, we have a total of 8 Péclet numbers, which are defined as the ratio between the advective and diffusive transport rates. For mass transfer, the Péclet numbers (Pe_j, for the chemical species j) are defined in terms of the chemical species diffusivities and are of order $10^4 - 10^6$, indicating that the dominating transport mechanism is convection. Similarly, for heat transfer, Pe is given in terms of the thermal diffusivity and is approximately 10^5, while the Péclet number for the particle distribution, Pe^*, is given in terms of the particle phase diffusivity and is estimated to be around 10^9. In both cases, advection dominates over diffusion, especially for the case of small particles suspended in the gas mixture.

In the non-dimensionalisation we have assumed that the initial value of all the chemical species not present in air, is exactly the same, that is $C_{\mathrm{SiO},0} = C_{\mathrm{SiO_2},0} = C_{\mathrm{CO},0} = C_{\mathrm{CO_2},0}$, and we also have that $C_{\mathrm{N_2},0} = C_{\mathrm{O_2},0}$. Thus, a represents the ratio of the maximum concentration of these species to the maximum concentration of oxygen (or nitrogen), and is usually a small parameter. Since in the simulations we have taken, $C_{\mathrm{O_2},0} = 50$ and $C_{\mathrm{SiO},0} = 1$, we have that $a = 0.02$, whereas in further chapters it will be taken as a control parameter.

With respect to the chemical reactions, we have two Damköhler numbers, $\mathrm{Da}_1 \approx 10^8$ and $\mathrm{Da}_2 \approx 10^5$, which are defined as the ratio between the respective reaction rate and the convective mass transport rate. These parameters measure the strength of the SiO and CO combustion reactions, respectively, and as it happens in reality, the SiO reaction is several orders of magnitude faster than the CO reaction. In general, both parameters are very large compared to the other terms that appear in (3.2.11), which indicates that the reactions dominate the system. This is expected when studying combustion reactions and is why the limit of infinitely fast chemistry, also called Burke-Schumann limit, is usually adopted in combustion theory [11]. Furthermore, the condensation reaction of SiO_2 into particles is as relevant as the combustion reactions, and we have that $\xi_1 \approx 10^5$ which determines the material used in the formation and growth of particles. Similarly, the parameters $\phi_1 \approx 10^8$, $\phi_2 \approx 10^5$, and $\xi_2 \approx 10^5$ determine the energy released due to the SiO and CO combustion reactions and due to the formation and growth of the particles, respectively. On the other hand, the Eckert number, Ec, is approximately 10^{-4} which suggests that the effects of pressure changes on the energy balance can be neglected.

Dimensionless parameter	Relation with dimensional parameters	Typical value
$\mathrm{Pe}_{\mathrm{N_2}}$	$\frac{v_2 L}{D_{\mathrm{N_2}}}$	2.247×10^6
$\mathrm{Pe}_{\mathrm{O_2}}$	$\frac{v_2 L}{D_{\mathrm{O_2}}}$	8.511×10^4
$\mathrm{Pe}_{\mathrm{SiO}}$	$\frac{v_2 L}{D_{\mathrm{SiO}}}$	1.026×10^5
$\mathrm{Pe}_{\mathrm{SiO_2}}$	$\frac{v_2 L}{D_{\mathrm{SiO_2}}}$	1.026×10^5
$\mathrm{Pe}_{\mathrm{CO}}$	$\frac{v_2 L}{D_{\mathrm{CO}}}$	2.222×10^6
$\mathrm{Pe}_{\mathrm{CO_2}}$	$\frac{v_2 L}{D_{\mathrm{CO_2}}}$	2.799×10^6
a	$\frac{C_{\mathrm{SiO},0}}{C_{\mathrm{O_2},0}}$	0.02
Da_1	$\frac{2LC_{\mathrm{O_2},0}A_1}{v_2}$	4×10^8
Da_2	$\frac{2LC_{\mathrm{O_2},0}A_2}{v_2}$	7.2×10^5
ξ_1	$\frac{\pi \rho_p J_0 (s_{\min})^3 L}{2 v_2 C_{\mathrm{SiO_2},0} M_{\mathrm{SiO_2}}}$	2.297×10^5
Re	$\frac{v_2 L \rho_0}{\mu}$	2.925×10^5
Pe	$\frac{v_2 L \rho_0 c_p}{k}$	2.4527×10^5
Ec	$\frac{v_2^2}{c_p (T_1 - T_2)}$	1.555×10^{-4}
ϕ_1	$\frac{L \Delta H_1 A_1 C_{\mathrm{SiO},0} C_{\mathrm{O_2},0}}{\rho_0 c_p v_2 (T_1 - T_2)}$	3.436×10^8
ϕ_2	$\frac{L \Delta H_2 A_2 C_{\mathrm{CO},0} C_{\mathrm{O_2},0}}{\rho_0 c_p v_2 (T_1 - T_2)}$	2.213×10^5
ξ_2	$\frac{\pi L_V J_0 (s_{\min})^3 L}{2 \rho_0 c_p v_2 (T_1 - T_2)}$	6.070×10^5
Pe^*	$\frac{v_2 L}{D_p}$	2.853×10^9
ω	$\frac{2LM_{\mathrm{SiO_2}} C_{\mathrm{SiO_2},0}}{\rho_p v_2 s_{\min}} \sqrt{\frac{k_B (T_1 - T_2)}{2\pi m}}$	2.601×10^5
T^*	$\frac{T_2}{T_1 - T_2}$	1.677
C_{sat}	$\frac{C_0}{C_{\mathrm{SiO_2},0}}$	0.1
λ_0	$\frac{16\pi\gamma^3 v_C^2}{3 k_B^3 T_2^3}$	0.3474
θ	$\frac{R(T_1 - T_2) C_{\mathrm{O_2},0}}{\rho_0 v_2^2}$	7.539×10^2

Table 3.1: Definitions and typical values for non-dimensional parameters used in the system of equations (3.2.11)-(3.2.17). The parameters are determined from values in Table 2.2 and Table 2.3, with $C_{\mathrm{O_2},0} = 50$, $v_2 = 10$, $C_0 = 0.1$, and $D_p = 1.402 \times 10^{-8}$.

The parameter $\omega \approx 10^5$ found in (3.2.14) is defined as the growth rate coefficient, G_0, times the timescale for our problem, L/v_2, divided by $s_{\min}$, and so it determines the speed of particle growth. With respect to the dimensionless parameters found in the dimensionless growth and nucleation rates, (3.2.15) and (3.2.16), we have that T^* is the ratio between the air temperature and the difference between the fuel and air temperatures, while λ_0 depends on intrinsic properties of microsilica particles such as the surface energy and molecular volume of SiO_2. Furthermore, the dimensionless saturation concentration is given by

$$C_{\text{sat}} = \frac{\tilde{C}_e}{C_{\text{SiO}_2,0}} = \frac{C_0}{C_{\text{SiO}_2,0}} \exp\left(\frac{\delta}{s(T+T^*)}\right) \approx \frac{C_0}{C_{\text{SiO}_2,0}}, \tag{3.2.18}$$

where $\delta = 4\gamma v_C/(s_{\min} k_B(T_1 - T_2)) \approx 10^{-2}$ depends on material properties of the particle. We take the saturation concentration to be constant since the Kelvin factor (*i.e.*, the exponential part of (3.2.18)) is approximately one for all values of s since $\delta \ll 1$, whereas s, T and T^* are approximately of order one. Moreover, as s or T increase, the exponential will become even closer to one. The smallest the particle and the temperature can be is $s = 1$ and $T = 1$ (dimensionless), and for these values we have that $C_{\text{sat}} C_{\text{SiO}_2,0}/C_0 \approx 1.0248$. After approximating the exponential in (3.2.18) as one, we are left with a constant estimated value for C_{sat} between 0 and 1. In this chapter, we have taken $C_{\text{sat}} = 0.1$, and in further chapters we will explore how the solution changes as we vary the value of this parameter. The dimensionless equation of state also contains the parameter $\theta = 7.539 \times 10^2$, which depends on the universal gas constant and on typical values of the state variables.

The final dimensionless parameter that we need to mention is the Reynolds number, which represents the ratio of inertial forces to viscous forces. Since the gas mixture considered in our model has a very low viscosity, it makes the Reynolds number great enough ($\text{Re} = L v_2 \rho_0/\mu \approx 10^5$) to consider the pattern of the flow to be turbulent. In this case, inertial forces dominate which tend to produce eddies and related localised structures that may trap particles, allowing them to recirculate through reaction zones multiple times before they are ejected from the furnace through the hood. Therefore, the COMSOL simulations of the system (3.2.11)-(3.2.17) that we will carry out in this chapter will also include turbulence effects.

A turbulent flow field is characterised by velocity fluctuations in all directions. Turbulence models use mathematical derivations based on the Navier-Stokes equations and introduce closure hypothesis requiring empirical input, see *e.g.* [60]. The common approach is to assume that the motion is random and adopt a statistical treatment.

Reynolds-Averaged Navier-Stokes (RANS) equation is based on representing the velocity vector as a fluctuation about a mean component [60]. However, for compressible flows, the density fluctuations give rise to additional terms and Favre-averaging is used instead. When averaging the equations, a new unknown appears, the Reynolds stresses. This is the first closure problem for turbulence modelling and is overcome by assuming that the turbulence is of a purely diffusive nature and introducing the eddy viscosity, also called turbulent viscosity. This parameter depends on the kinetic energy, k, and on the dissipation rate of turbulent kinetic energy, ε, which are also solved for as part of the model [14]. The latter is what is called the $k-\varepsilon$ turbulence model. Since only this chapter in the thesis is concerned with turbulence, we do not show the exact form of the equations here, however, we refer the reader to [61] for more details on turbulence modelling.

3.3 Numerical simulations

We now present the results from the COMSOL simulations of the system (3.2.11)-(3.2.17) including turbulence, for different furnace and flow configurations. We will first compare the solutions obtained when we vary the size of the fuel inlet, or active charge surface. This will determine how far the chemical species need to travel before encountering and interacting with each other, and a similar scenario will be explored further in Chapter 5 by varying the initial separation distance between the reactants. Secondly, we will vary the fuel to air ratio of inlet velocities, and explore how different input velocities affect the formation of particles. This case will also be studied in more depth in Chapter 6.

We remark that having such large parameter values in our model, as shown in Table 3.1, makes the simulations more difficult to perform and hence the order of magnitude of certain parameters has been reduced accordingly in order for the simulations to converge. These are the parameters involved in the mass and heat production due to the combustion reactions and due to the formation of particles. The actual values used in the simulations are

$$\begin{aligned} \mathrm{Da}_1 &= 4\times 10^3, & \mathrm{Da}_2 &= 7.2\times 10^2, & \xi_1 &= 2.297\times 10^2,\\ \phi_1 &= 3.436\times 10^3, & \phi_2 &= 2.213\times 10^2, & \xi_2 &= 6.070\times 10^2, \end{aligned} \tag{3.3.1}$$

with the rest of dimensionless parameters taking values from Table 3.1. Note that the

values in (3.3.1) are quite far off the original values presented in Table 3.1, however the simulations will still allow us to gain useful insight into the key physical effects of the process.

3.3.1 Varying the size of the fuel inlet

Depending on the type of furnace and on the operational strategies, the active part of the charge surface can have different sizes. This means that the off-gases, SiO and CO, that enter the furnace hood through the charge surface may do so through a radius that can extend up to the air inlet. The inactive part of the charge does not play any role. As a consequence, when the fuel inlet is small, the oxygen will have to travel a longer distance to encounter the CO and SiO and react.

In Figure 3.2 we show (a)-(b) velocity and (c)-(d) temperature variations in the domain for both cases, (left) large and (right) small fuel inlet. We have selected the inlet velocity ratio between the fuel and oxidizer to be $\lambda = v_1/v_2 = 0.3$ so that there is more mixing between the two streams. We observe that since the oxygen stream is faster it will make its way into the region mostly occupied by the fuel. With respect to the temperature, we find a much colder area on the top where most of the oxygen is located, and a hotter area at the bottom where the hot gases coming from the interior of the furnace are located. Moreover, the region in between is the hottest, corresponding to the heat released by the chemical reactions, and will therefore be a good indication of where the reaction zone is located. There are not that many differences between a small and a large inlet, with slightly larger temperatures for a small fuel inlet, and slightly larger velocities around the outlet for a large inlet. The general behaviour seems to remain the same in both cases, but with the reactions occurring closer to the middle of the furnace hood when the fuel inlet is small.

We show the chemical concentrations corresponding to the SiO reaction in Figure 3.3. These are the oxygen (a)-(b), silicon monoxide (c)-(d), and silicon dioxide (e)-(f) molar concentrations. As expected, we find that the majority of the oxygen is located at the top right of the domain, while most of the SiO is on the bottom left, with the middle layer corresponding to the reaction zone where the SiO_2 is produced. At the origin of the mixing layer in panels (e)-(f), where the O_2 and SiO meet for the first time, there is a large production of SiO_2. This is followed by the consumption of silicon dioxide due to the formation and growth of the particles, and therefore its concentration is lower as we move along the reaction layer and towards the outlet. Note also that if we looked at a cross section of the reaction zone in (e) or (f), the

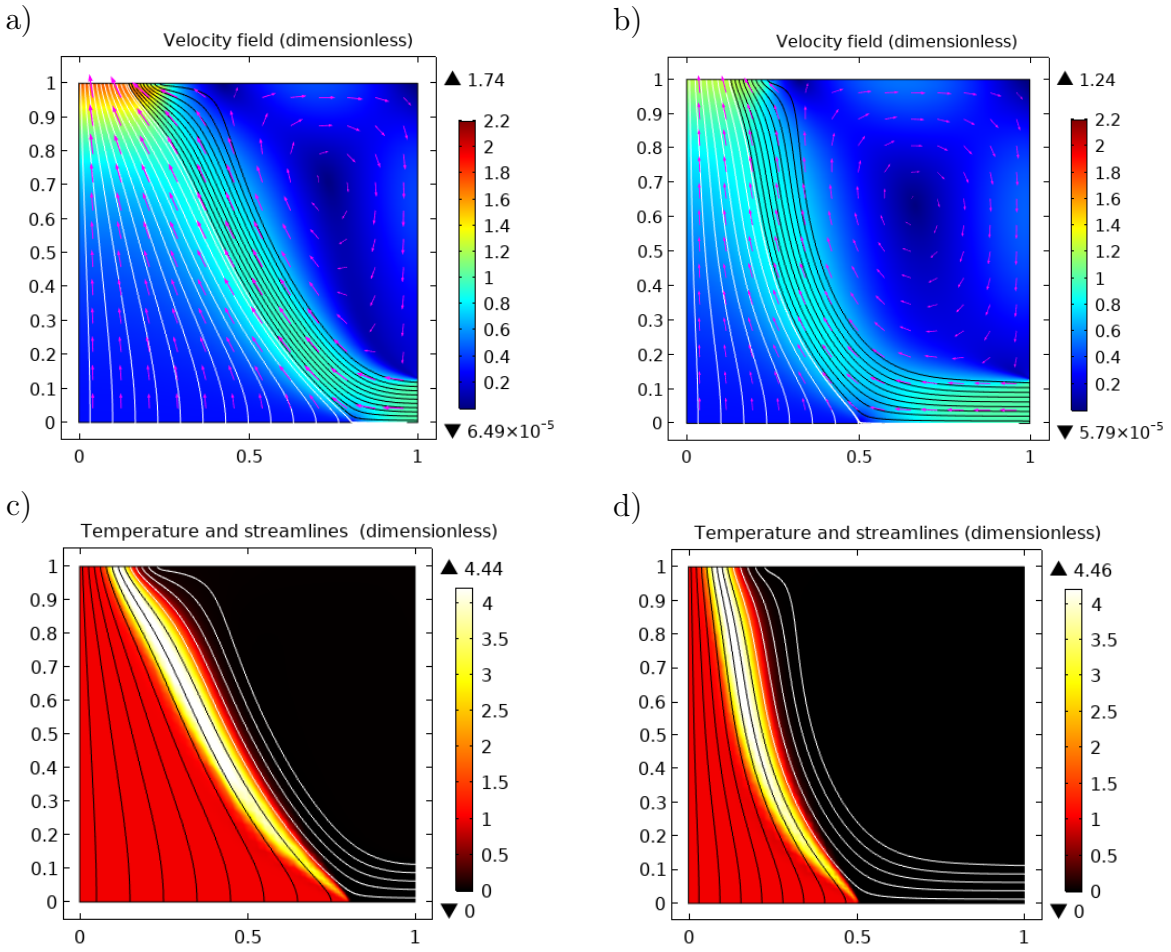

Figure 3.2: Velocity field (a)-(b) and temperature (c)-(d) heatmaps obtained from solving problem (3.2.11)-(3.2.17) including turbulence effects, using the software COMSOL. The pictures on the left, (a) and (c), correspond to a larger fuel inlet, and the ones on the right, (b) and (d), to a smaller fuel inlet. We have taken the ratio of inlet velocities between the fuel and oxidizer to be $v_1/v_2 = 0.3$.

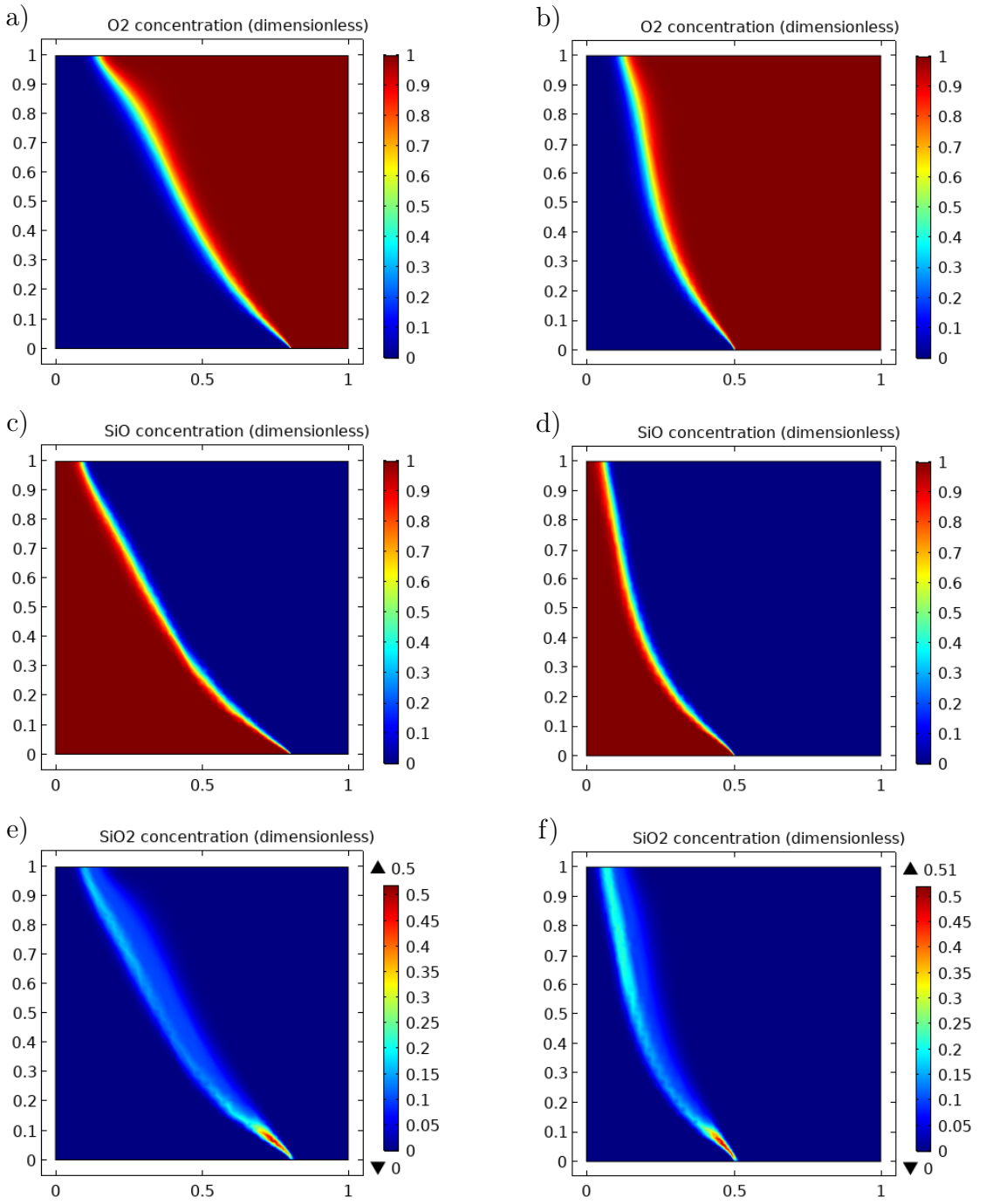

Figure 3.3: (a)-(b) Oxygen (O_2), (c)-(d) silicon monoxide (SiO), and (e)-(f) silicon dioxide (SiO_2) concentrations from solving problem (3.2.11)-(3.2.17) including turbulence effects, using the software COMSOL. The pictures on the left correspond to a larger fuel inlet and the ones on the right to a smaller fuel inlet. We have taken the ratio of inlet velocities between the fuel and oxidizer to be $v_1/v_2 = 0.3$.

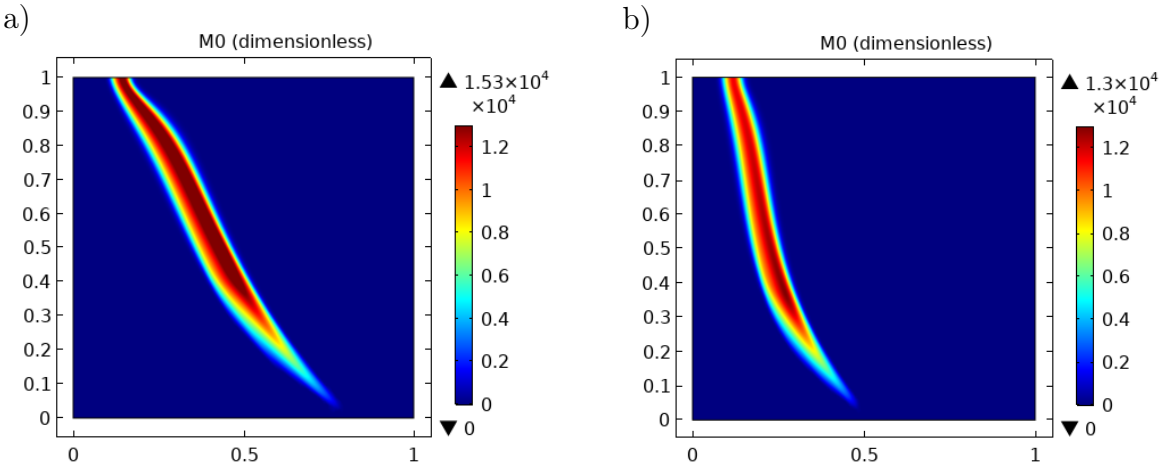

Figure 3.4: Number density of microsilica particles (M_0) from solving problem (3.2.11)-(3.2.17) including turbulence effects, using the software COMSOL. This is for a larger fuel inlet in (a), and for a smaller fuel inlet in (b). We have taken the ratio of inlet velocities between the fuel and oxidizer to be $v_1/v_2 = 0.3$.

SiO_2 concentration is the highest towards the middle.

Finally, the total number of particles density, M_0, is shown in Figure 3.4 and is the largest towards the middle of the reaction zone, with very few particles forming at the origin where the chemicals first meet. When the fuel inlet is smaller and the chemicals need to travel a longer distance, fewer particles form.

Note that we have not included the results for the nitrogen, which has a similar behaviour to the oxygen, and for the chemical species corresponding to the CO reaction, which mimic those in the SiO reaction. The main difference is that, due to the CO reaction being slower than the SiO, less CO_2 will be produced and the reaction zone is wider. Moreover, there is no sink of CO_2 so the concentration remains almost constant along the reaction layer.

3.3.2 Varying the fuel and oxygen inlet velocities

The air and fuel inlet velocities may depend on many factors related to the operation and type of furnace. For instance, the input air velocity is slower when the air enters through the small separation gap between the furnace hood and the charge surface, compared to when it does so through the furnace doors when they open. In addition, even though the SiO and CO velocities do not change significantly under normal furnace conditions, these gases can sometimes escape at slightly larger velocities due to, for instance, stoking of the charge surface. However, in all cases the inlet velocity

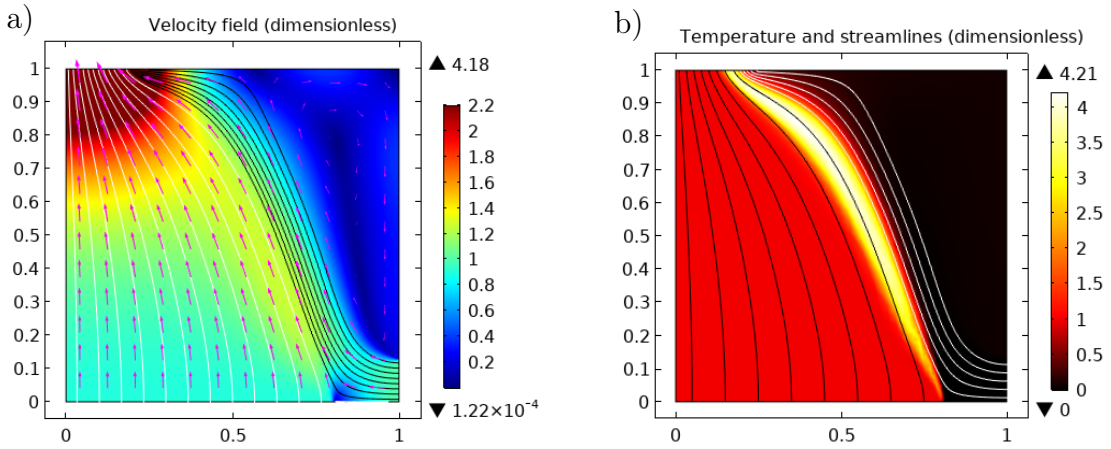

Figure 3.5: Velocity field (a), and temperature (b) from solving problem (3.2.11)-(3.2.17) including turbulence effects, using the software COMSOL. We have taken the ratio of inlet velocities between the fuel and oxidizer to be very close to 1 so that there is less mixing between the chemicals, and in particular $v_1/v_2 = 0.9$.

of the air, v_2, is considered to be larger to that of the fuel, v_1, and thus, the ratio of velocities $\lambda = v_1/v_2$ is always less than 1. In the previous section, we took $\lambda = 0.3$ so that there was more mixing between the two streams. Now, we will explore the effect of taking very similar velocities for both streams, and let $\lambda = 0.9$. Only the large size fuel inlet will be shown in this case, and therefore we will compare the results to the left-side panels in Figures 3.2-3.4.

We present in Figure 3.5 the results for the (a) velocity field, and (b) temperature, and in Figure 3.6 we show the (a) oxygen, (b) silicon monoxide and (c) silicon dioxide concentrations, and (d) total number of microsilica particles. We observe that in this case the reaction zone is located a bit further from the axis of symmetry since the oxygen cannot travel as far into the domain when both stream velocities are similar. There is a significant increase in the magnitude of the velocity in Figure 3.5 (a), especially towards the outlet of the domain. However, the temperature in (b) within the reaction zone is slightly lower compared to the previous section, due to the reaction zone being wider.

With respect to the chemicals in Figure 3.6, we observe that when both streams have similar velocities, the SiO_2 as in (c) starts being consumed due to particle formation and growth at a later location along the mixing layer, and that far fewer particles form as in (d). We also see this effect in reality, with almost uniform flows implying larger residence time of particles within the reaction zone, and therefore larger and fewer particles forming [22].

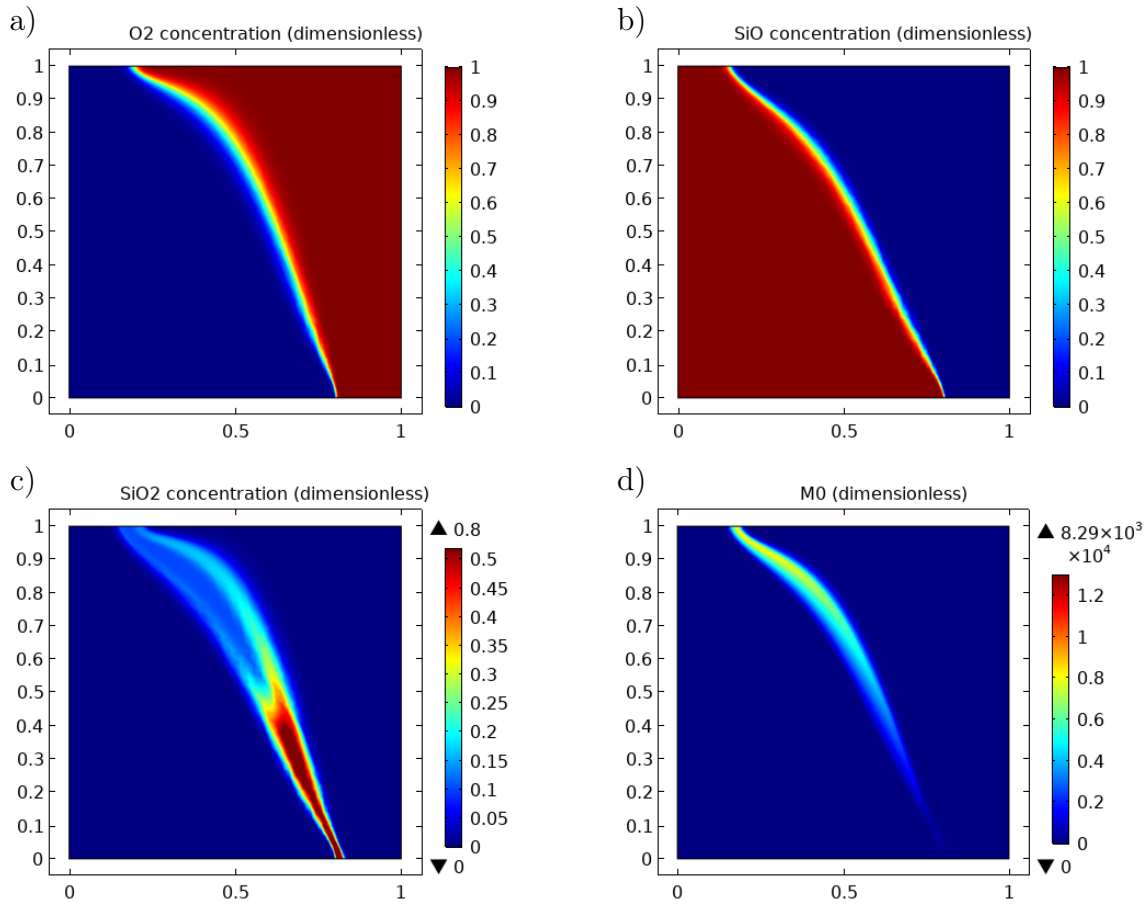

Figure 3.6: Oxygen (a), silicon monoxide (b), and silicon dioxide (c) concentrations, and number density of microsilica particles (d) from solving problem (3.2.11)-(3.2.17) including turbulence effects, using the software COMSOL. We have taken the ratio of inlet velocities between the fuel and oxidizer to be very close to 1 so that there is less mixing between the chemicals, and in particular $v_1/v_2 = 0.9$.

3.4 Discussion

In this chapter we have carried out steady-state COMSOL simulations of the model derived in Chapter 2 for a two-dimensional geometry representative of the furnace hood. After defining the two-dimensional domain and its boundaries, we proceeded to non-dimensionalise the governing equations. We did so by scaling all variables with characteristic scales for the regime under study in this chapter. However, we remark that this non-dimensionalisation is unique to this chapter, and since in the rest of the thesis we will look at a different regime, only a few of the dimensionless parameters presented here will also appear in our later analysis of the problem.

After identifying the dimensionless groups and estimated values, we performed the COMSOL simulations, for which it was necessary to reduce the order of magnitude of certain parameters as given in (3.3.1). First, we compared the results for a small and a large fuel inlet and concluded that the dynamics of the variables are very similar regardless of the inlet size. We then kept the large fuel inlet and explored the effects of varying the ratio of velocities between the fuel and air streams. Our numerical simulations suggest that when the velocity ratio is close to one, the reaction zone is wider and the temperature increase due to the reactions is smaller. This results in fewer particles forming, with the opposite effect happening when the difference between the velocities is larger and more mixing is involved.

An interesting feature that we observe from the previous simulations, is that most of the action happens within a reaction layer, whereas there is no SiO_2 or particles trapped within the stable vortex located at the top right corner of the domain. Motivated by this finding and in order to obtain a more quantitative understanding of the process, in the remainder of this thesis we will focus on the dynamics within a reaction zone forming between a stream of O_2 and a stream of fuel, rather than in the whole furnace geometry. We will do so by selecting a smaller lengthscale and timescale characteristic of the combustion reactions and such that they capture the dynamics of the different variables within the reaction zone. The new non-dimensionalisation of the model will overcome the appearance of the very large dimensionless parameters seen in this chapter and will allow us to perform an asymptotic analysis of the problem.

Furthermore, microscopic zones where individual particles grow may be several orders of magnitude smaller than macroscopic turbulent eddies [84], with the reaction zones highly localized within the turbulent flow. This suggests that the narrow reaction zones that we will study in the next chapters will likely still exist within the larger flow, embedded within boundary layers formed near the interface of O_2 and SiO.

Chapter 4

The well-mixed chemical species limit

In this chapter, a much simpler version of the model derived in Chapter 2 is presented. Motivated by the COMSOL simulations from Chapter 3, we focus on the dynamics of the chemicals, temperature, and particles within a narrow reaction zone rather than in the whole furnace geometry. Thus for this small scale, we greatly simplify the model by considering the case where the chemical species are initially well-mixed, with uniform initial concentrations and temperature. For this limit, where spatial diffusion is instantaneous, the concentrations and temperature are independent of space for all $t \geq 0$. This assumption is best viewed as a simplification of the spatial structure taken in order to better qualitatively understand the dynamics taking place within the interior of the reaction zone, whereas in the next chapter we will more accurately depict the macroscopic scale structure of the reaction zone between two larger non-reacting regions.

The well-mixed assumption requires neglecting the fluid flow and density variations in the fluid. Hence, $\rho = \rho_0$, so we do not consider the effects of compressibility. As a consequence, the conservation equation for N_2 (2.4.1a) decouples from the others as it does not contribute to the density, and since it is not of particular interest we do not include it in this model. Subsequent work will consider more realistic flow regimes, but for now, this assumption is sufficient to study the regions local to a reaction zone where the microsilica is produced. Moreover, for most of this chapter we will neglect random fluctuations in the growth rate of particles, as in, *e.g.*, [94], and hence we will set $D_s = 0$ from the outset.

With the latter assumptions we are left with a system of time-dependent ODEs, in addition to the PDE for the number density function which is time and particle size dependent, and we can obtain some analytical and numerical results while looking at different parameter regimes. This simple model gives further insight into particle

formation and growth within a reaction zone by focusing on the evolution of the reactions and the particle size distribution over time and ignoring spatial effects, such as, how the chemicals mix together. This will prove useful in later chapters where we extend the model so that we have a moving flame front or when we consider a more realistic fluid flow. Part of the work developed in this chapter can be found in [29].

4.1 Non-dimensionalisation

Referring back to the model derived in Section 2.4.1 of Chapter 2 and under the previous assumptions, we do not need to solve for (2.4.1g), and all spatial convection and diffusion terms in the rest of the equations are neglected. We non-dimensionalise the resulting equations (2.4.1b)-(2.4.1f), (2.4.1i)-(2.4.1l) and (2.4.3) by scaling the variables in a similar way to Chapter 3. We use the same scalings for the temperature and the concentrations, namely

$$T = (T_1 - T_2)\tilde{T} + T_2, \tag{4.1.1}$$

and

$$C_j = C_{j,0}\tilde{C}_j, \tag{4.1.2}$$

where $C_{j,0}$ represents the input concentration of the reactant j, and again for the products we have taken $C_{\mathrm{SiO_2},0} = C_{\mathrm{SiO},0}$ and $C_{\mathrm{CO_2},0} = C_{\mathrm{CO},0}$.

We choose the timescale of the problem with the dominant reaction kinetics, that is, from R_1 which is the fastest of the reactions. We select it this way since we want to focus on the reaction zone where particles form and not on the whole furnace hood, and R_1 is precisely the reaction that produces SiO_2 that then condenses into microsilica particles. Therefore, we scale time as it follows

$$t = t_0\tilde{t} = \frac{1}{2A_1 C_{\mathrm{O_2},0}} \exp\left(\frac{E_1}{RT_1}\right)\tilde{t}, \tag{4.1.3}$$

where $t_0 = 10^{-9} - 10^{-8}$ seconds, for parameter values taken from Table 2.2. This is consistent with characteristic timescales found for combustion reactions, see *e.g.* [89]. Note that the timescale (4.1.3) is very sensitive to the value selected for the temperature of the fuel as it enters the furnace hood, and for a lower temperature, say $T_1 = 400$ K, we have that $t_0 \approx 10^{-4}$.

We scale the particle diameter, s, with the critical diameter for nucleation, $s_{\min}$,

which is assumed to be a constant throughout this thesis as given in Table 2.3. The number density function is scaled with the ratio between nucleation and growth rate coefficients, J_0 as given in Table 2.3 and G_0 as defined in (3.2.10), respectively. Finally, the moments of the distribution are scaled as in Chapter 3 with a combination of the latter two scalings for the particle diameter and number density. Therefore, we have the following

$$s = s_{\min}\tilde{s}, \quad n = \frac{J_0}{G_0}\tilde{n}, \quad M_i = \frac{J_0}{G_0}s_{\min}^{i+1}\tilde{M}_i, \quad \text{for} \quad i = 0, 1, 2. \tag{4.1.4}$$

With these scalings and dropping the over tilde notation, the dimensionless reduced system reads

$$\begin{aligned}
\frac{\mathrm{d}C_{\mathrm{O}_2}}{\mathrm{d}t} &= -\frac{a}{2}\left(f_1(T)C_{\mathrm{O}_2}C_{\mathrm{SiO}} + \varepsilon f_2(T)C_{\mathrm{O}_2}C_{\mathrm{CO}}\right), && \text{(4.1.5a)}\\
\frac{\mathrm{d}C_{\mathrm{SiO}}}{\mathrm{d}t} &= -f_1(T)C_{\mathrm{O}_2}C_{\mathrm{SiO}}, && \text{(4.1.5b)}\\
\frac{\mathrm{d}C_{\mathrm{SiO}_2}}{\mathrm{d}t} &= f_1(T)C_{\mathrm{O}_2}C_{\mathrm{SiO}} - \zeta_1 G M_2, && \text{(4.1.5c)}\\
\frac{\mathrm{d}C_{\mathrm{CO}}}{\mathrm{d}t} &= -\varepsilon f_2(T)C_{\mathrm{O}_2}C_{\mathrm{CO}}, && \text{(4.1.5d)}\\
\frac{\mathrm{d}C_{\mathrm{CO}_2}}{\mathrm{d}t} &= \varepsilon f_2(T)C_{\mathrm{O}_2}C_{\mathrm{CO}}, && \text{(4.1.5e)}\\
\frac{\mathrm{d}T}{\mathrm{d}t} &= h_1 f_1(T)C_{\mathrm{O}_2}C_{\mathrm{SiO}} + \varepsilon h_2 f_2(T)C_{\mathrm{O}_2}C_{\mathrm{CO}} + \zeta_2 G M_2, && \text{(4.1.5f)}\\
\frac{\mathrm{d}M_0}{\mathrm{d}t} &= G^* J, && \text{(4.1.5g)}\\
\frac{\mathrm{d}M_1}{\mathrm{d}t} &= G^* J + G^* G M_0, && \text{(4.1.5h)}\\
\frac{\mathrm{d}M_2}{\mathrm{d}t} &= G^* J + 2G^* G M_1, && \text{(4.1.5i)}
\end{aligned}$$

for $t > 0$. The dimensionless initial conditions at $t = 0$ are given by

$$C_{\mathrm{O}_2} = C_{\mathrm{SiO}} = C_{\mathrm{CO}} = T = 1, \quad C_{\mathrm{SiO}_2} = C_{\mathrm{CO}_2} = M_0 = M_1 = M_2 = 0, \tag{4.1.6}$$

where we have taken the initial concentration of the reactants, O_2, CO, and SiO, to be constant and equal to the corresponding input concentration, $C_{j,0}$, and where we have assumed that initially there is no SiO_2, CO_2 or particles produced. We have chosen the initial temperature to be the same as the temperature of the fuel entering the furnace hood, T_1, so $T = 1$ in the dimensionless temperature scale.

The non-dimensionalisation has introduced a number of dimensionless parameters

$(a, \varepsilon, \zeta_1, \zeta_2, h_1, h_2, G^*)$ and constitutive laws (f_1, f_2, J, G) that we shall now describe. A full list of the dimensionless parameters found in this model, their relation with dimensional parameters, and estimated values is found in Table 4.1. Note that a, J and G are exactly as described in Chapter 3, however we have also included their definitions here for consistency.

Firstly, as in the previous chapter we have assumed that the initial value of all the chemical species, $C_{j,0}$, is exactly the same (except for the oxygen), that is $C_{\mathrm{SiO},0} = C_{\mathrm{SiO_2},0} = C_{\mathrm{CO},0} = C_{\mathrm{CO_2},0}$. Thus, a represents again the ratio of the maximum concentration of these species to the maximum concentration of oxygen. In some cases, we may have an oxygen-rich environment such that the amount of any chemical with respect to oxygen is very small, and in general, $a = 10^{-3} - 0.2$. Another small parameter that will prove useful is the ratio between the CO and SiO reaction rates, $\varepsilon \approx 10^{-3}$, which shows that the SiO reaction is the fastest. The coefficients, $\zeta_1 \approx 10^{-2}$ and $\zeta_2 \approx 10^{-1}$, determine the mass consumed and energy released due to the formation and growth of particles, and in further sections we will study how these affect the chemicals and temperature profiles, as well as the particle size distribution. The parameters $h_1 = 0.85$ and $h_2 = 0.3$ in the energy equation measure the balance between the reactant concentration needed to give off heat and the role of the respective reaction on generating heat. Finally, $G^* \approx 10^{-2}$ is defined as the growth rate coefficient G_0 times the timescale for our problem, t_0, divided by $s_{\min}$, and so it determines the speed of particle growth.

The dimensionless Arrhenius terms in the reaction rates are slightly different to the previous chapter and have now the form

$$f_j(T) = \exp\left(-\frac{E_j}{R}\left(\frac{1}{(T_1 - T_2)T + T_2} - \frac{1}{T_1}\right)\right), \quad j = 1, 2, \tag{4.1.7}$$

where E_j, R, T_1, and T_2 are dimensional parameters as described in Table 2.2. The non-dimensional particle growth and nucleation rates are given exactly as in (3.2.15)-(3.2.16), namely

$$G = \sqrt{T + T^*}\,(C_{\mathrm{SiO_2}} - C_{\mathrm{sat}})\,\mathcal{H}\,(C_{\mathrm{SiO_2}} - C_{\mathrm{sat}}) \tag{4.1.8}$$

and

$$J = \exp\left(-\frac{\lambda_0}{\left(\frac{T}{T^*} + 1\right)^3 \ln^2\left(\frac{C_{\mathrm{SiO_2}}}{C_{\mathrm{sat}}}\right)}\right), \tag{4.1.9}$$

respectively. The dimensionless parameters found in (4.1.8)-(4.1.9), that is, T^*, C_{sat},

Dimensionless parameter	Relation with dimensional parameters	Typical value
a	$\frac{C_{\mathrm{SiO},0}}{C_{\mathrm{O}_2,0}}$	$10^{-3} - 0.2$
ε	$\frac{A_2}{A_1}\exp\left(\frac{E_1-E_2}{RT_1}\right)$	6.031×10^{-3}
h_1	$\frac{C_{\mathrm{SiO},0}\Delta H_1}{2(T_1-T_2)\rho_0 c_p}$	0.8591
h_2	$\frac{C_{\mathrm{CO},0}\Delta H_2}{2(T_1-T_2)\rho_0 c_p}$	0.3073
α_1	$\exp\left(-\frac{E_1}{R}\left(\frac{1}{T_2}-\frac{1}{T_1}\right)\right)$	0.3200
α_2	$\exp\left(-\frac{E_2}{R}\left(\frac{1}{T_2}-\frac{1}{T_1}\right)\right)$	0.6585
ζ_1	$\frac{\pi\rho_p J_0(s_{\min})^3}{4M_{\mathrm{SiO}_2}A_1 C_{\mathrm{O}_2,0}C_{\mathrm{SiO}_2,0}}\exp\left(\frac{E_1}{RT_1}\right)$	3.875×10^{-2}
ζ_2	$\frac{\pi L_V J_0(s_{\min})^3}{4\rho_0 c_p A_1 C_{\mathrm{O}_2,0}(T_1-T_2)}\exp\left(\frac{E_1}{RT_1}\right)$	0.1024
T^*	$\frac{T_2}{T_1-T_2}$	1.677
G^*	$\frac{M_{\mathrm{SiO}_2}C_{\mathrm{SiO}_2,0}\sqrt{T_1-T_2}}{\rho_p A_1 C_{\mathrm{O}_2,0}s_{\min}}\sqrt{\frac{k_B}{2\pi m}}\exp\left(\frac{E_1}{RT_1}\right)$	4.389×10^{-2}
C_{sat}	$\frac{C_0}{C_{\mathrm{SiO}_2,0}}$	$0 - 1$
λ_0	$\frac{16\pi\gamma^3 v_C^2}{3k_B^3 T_2^3}$	0.3474

Table 4.1: Definitions and typical values for non-dimensional parameters used in the model. We treat a and C_{sat} as control parameters, whereas the other parameters are determined from values in Table 2.2 and Table 2.3 with $C_{\mathrm{O}_2,0} = 5$.

and λ_0, were already described in Section 3.2 and have also been added into Table 4.1.

Note that both, a and C_{sat} will be used as control parameters in the model, and in further sections we will study the sensitivity of solutions to them. There are two remaining dimensionless parameters in Table 4.1 that we have not mentioned since they will come into play later on in the chapter. These are α_1 and α_2 which will arise from linearising the Arrhenius terms in Section 4.3.2.

With respect to the particle formation and growth problem, the dimensionless population balance equation reads

$$\frac{\partial n}{\partial t} + G^* G(t)\frac{\partial n}{\partial s} = 0 \tag{4.1.10a}$$

for $s > 1$ and $t > 0$, and the dimensionless boundary and initial conditions are

$$G(t)n = J(t) \qquad \text{at} \qquad s = 1, \quad t > 0, \tag{4.1.10b}$$

$$n = 0 \qquad \text{at} \qquad t = 0, \quad s > 1. \tag{4.1.10c}$$

To sum up, in this section we have stated a time-dependent dimensionless model for the temperature, chemicals and moments of the particle size distribution, which includes material consumption and heat release due to particle formation, both proportional to the growth rate times the second moment of the distribution. Additionally, we have given a time-dependent dimensionless problem for the number density function of particles, that includes nucleation and growth of particles of all sizes, with both processes depending on the temperature and on the SiO_2 concentration profiles. These models present a total of 12 dimensionless parameters as described above and as given in Table 4.1. In the next sections, we will show approximate and numerical solutions for all variables in the system.

4.2 Analytical solution of the particle density equation

We notice that after neglecting fluctuations in the growth rate of the particles ($D_s = 0$), the population balance equation for n becomes a one-dimensional wave equation as given in (4.1.10a). For this simple case, we can use the method of characteristics to find an analytical solution for the particle density function, n, by solving the problem (4.1.10) in terms of the growth rate G and nucleation rate J functions defined in (4.1.8)-(4.1.9).

From looking at equation (4.1.5c) and its corresponding initial condition we can predict that initially, the SiO_2 concentration is monotonically increasing from zero as reaction (2.2.1a) takes place. Then, once the concentration reaches the saturation value, C_{sat}, particles will start forming, and after some time the SiO_2 will decrease due to mass consumption from particle growth. Therefore, we define $t_{\min}$ to be the minimal value of t such that $C_{SiO_2}(t_{\min}) = C_{\text{sat}}$. Note that if such value $t_{\min}$ does not exist and the SiO_2 never reaches saturation, particles will never form.

In the case where $t \leq t_{\min}$, problem (4.1.10) reduces to

$$\frac{\partial n}{\partial t} = 0 \quad \text{for} \quad s > 1, \tag{4.2.1}$$

$$n = 0 \quad \text{at} \quad t = 0, \tag{4.2.2}$$

since the growth rate (4.1.8) becomes zero due to the presence of the Heaviside function. Hence the solution is $n = 0$ for all particle sizes. This makes sense since no particles are formed before the concentration reaches saturation.

For the second case where $t > t_{\min}$, we use the method of characteristics to obtain a parametric solution for n. For characteristics emanating from $t = t_{\min}$, we need to solve the following system of ODEs:

$$n_\tau = 0, \tag{4.2.3a}$$
$$s_\tau = G^* G(\tau), \tag{4.2.3b}$$
$$t_\tau = 1, \tag{4.2.3c}$$

where τ parametrizes time along a characteristic. The initial data is given by $n = 0$, $s = s_1$ and $t = t_{\min}$ for $\tau = 0$, and where $s_1 > 1$. The characteristic curves in this case are given by

$$s(t, s_1) = s_1 + G^* \int_{t_{\min}}^{t} G(\tau) \mathrm{d}\tau, \tag{4.2.4}$$

with $s_1 > 1$, and the solution is always $n = 0$. These correspond to the curves above the red characteristic in Figure 4.1. For characteristic curves emerging from $s = 1$, we need to solve the same system (4.2.3) but with initial data given by $n = J(t_1)/G(t_1)$, $s = 1$ and $t = t_1$ for $\tau = 0$, and where $t_1 > t_{\min}$. Now the characteristic curves are given implicitly by

$$s(t, t_1) = 1 + G^* \int_{t_1}^{t} G(\tau) \mathrm{d}\tau, \tag{4.2.5}$$

with $t_1 > t_{\min}$, and the solution is the following

$$n = \frac{J(t_1)}{G(t_1)}. \tag{4.2.6}$$

These correspond to the curves below the red characteristic in Figure 4.1. Note that the dividing characteristic that bounds both regions is given implicitly by

$$s^*(t) = 1 + G^* \int_{t_{\min}}^{t} G(\tau) \mathrm{d}\tau, \tag{4.2.7}$$

and represents how the diameter of a particle originated at $t = t_{\min}$ with size $s = 1$ (the critical diameter for nucleation) varies with time t. See Figure 4.1 for a plot of all the characteristic curves. These curves transport information from each of the boundaries to the rest of the domain, and n is constant along them by definition. The dividing characteristic (red curve) separates the domain in two regions: the region above it, where the solution is $n = 0$, and the region below it, where n is given by (4.2.5)-(4.2.6). Moreover, we can express the characteristic curves derived in (4.2.4)

and (4.2.5) in terms of $s^*(t)$ in the following way

$$s(t, s_1) = s^*(t) + s_1 - 1, \quad s_1 > 1, \tag{4.2.8}$$

$$s(t, t_1) = s^*(t) - s^*(t_1) + 1, \quad t_1 > t_{\min}, \tag{4.2.9}$$

respectively. Therefore, we have proved that all characteristic curves are simply translations in s of $s^*(t)$.

We can determine the validity of the solution for n by computing the Jacobian for both subproblems (above and below $s^*(t)$), and checking when it becomes zero meaning that the solution breaks down. For characteristics emanating from $t = t_{\min}$ we find

$$\mathcal{J} = \frac{\partial(s,t)}{\partial(s_1,\tau)} = \frac{\partial s}{\partial s_1}\frac{\partial t}{\partial \tau} - \frac{\partial s}{\partial \tau}\frac{\partial t}{\partial s_1} = 1, \tag{4.2.10}$$

and for characteristics emerging from $s = 1$ we have the following

$$\mathcal{J} = \frac{\partial(s,t)}{\partial(\tau,t_1)} = \frac{\partial s}{\partial \tau}\frac{\partial t}{\partial t_1} - \frac{\partial s}{\partial t_1}\frac{\partial t}{\partial \tau} = G^* G(t_1). \tag{4.2.11}$$

For the first case, the Jacobian is never zero, whereas for the second one it would depend on the form of the growth rate, G. However, in our case, we have that $G(t) > 0$ for all $t > t_{\min}$ from the definition of the growth rate given in (4.1.8).

Notice that an explicit solution for n cannot always be found for all approximations of G due to the difficulty of obtaining t_1 from (4.2.5). In Section 4.3.4.2, we will consider an asymptotic analysis near the red characteristic curve in Figure 4.1 and will derive explicit approximations of the characteristic curves and solution.

Motivated by the solution above, we now study how the diameter of a single particle, s_0, grows with time, and how this relates to the previous model (4.1.10) for the growth of a collection of particles with different sizes. The dimensionless single particle growth model is the following:

$$\frac{\mathrm{d}s_0}{\mathrm{d}t} = G^* G(t), \quad t > t_{\min}, \tag{4.2.12a}$$

$$s_0 = 1 \quad \text{at} \quad t = t_{\min}, \tag{4.2.12b}$$

where $G(t)$ is the dimensionless growth rate as in (4.1.8). Notice that in this case there is no nucleation rate; instead, the single particle forms at the critical time where the SiO_2 concentration is above saturation, $t = t_{\min}$, and with critical size $s_0 = 1$. The

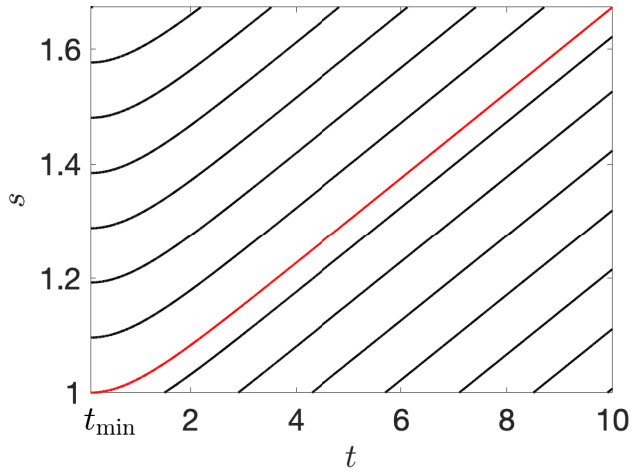

Figure 4.1: Characteristic curves corresponding to the population balance equation (4.1.10a). The red curve (4.2.7) passes through the origin $(t_{\min}, 1)$ and divides the domain in two regions with different solutions for n. Above this curve, $n = 0$, while below this curve, n is given by (4.2.5)-(4.2.6). The different characteristic curves shown are for values of s_1 and t_1 equally spaced. Note that these curves are defined in terms of the growth rate G as given in (4.1.8) which depends on C_{SiO_2} and T. Here we have taken the SiO_2 concentration and temperature from the solution to the decoupled problem which will be presented in Section 4.3.

solution to problem (4.2.12) is straightforward, namely

$$s_0(t) = 1 + G^* \int_{t_{\min}}^{t} G(\tau)\mathrm{d}\tau = s^*(t). \tag{4.2.13}$$

This result coincides with the dividing characteristic found before (equation (4.2.7)), that is, the red curve in Figure 4.1. This curve corresponds to the maximum possible particle size found for each t (recall that above the curve, $n = 0$). Thus, the single particle model predicts that the particles with the largest size are the ones that were created at the critical time, $t = t_{\min}$, which is reasonable since they have had the most time to grow.

4.3 Zero coupling regime: $\zeta_1 = \zeta_2 = 0$

In this section, we study the system of equations (4.1.5) for the case in which the parameters ζ_1 and ζ_2 are zero or negligibly small, so we do not include the sink and source terms in (4.1.5c) and (4.1.5f), respectively. This case corresponds to the

decoupled problem. Thus, we first obtain approximate solutions for the temperature and species concentrations, and then in Section 4.3.4 we use these results in (4.2.6) to find the number density function, n. In reality, the decoupled problem is valid when the formation of the particles does not affect the species concentrations and the temperature, which happens for initial times in the process or in the case where there is plenty SiO_2 available and its rate of depletion is small.

Thus, we shall set $\zeta_1 = \zeta_2 = 0$. Several conservation laws for the concentrations and temperature will shortly become apparent and we no longer need to solve for the moments of the distribution since they decouple from the system. Combining (4.1.5d) and (4.1.5e), we obtain

$$C_{\mathrm{CO_2}}(t) = 1 - C_{\mathrm{CO}}(t), \tag{4.3.1}$$

and combining (4.1.5b) and (4.1.5c), we find

$$C_{\mathrm{SiO_2}}(t) = 1 - C_{\mathrm{SiO}}(t). \tag{4.3.2}$$

Now, using (4.1.5a), (4.1.5b), and (4.1.5d), we have

$$C_{\mathrm{O_2}}(t) = 1 - \frac{a}{2}[(1 - C_{\mathrm{SiO}}(t)) + (1 - C_{\mathrm{CO}}(t))], \tag{4.3.3}$$

and finally combining (4.1.5b), (4.1.5d), and (4.1.5f), we obtain

$$T(t) = 1 + h_1(1 - C_{\mathrm{SiO}}(t)) + h_2(1 - C_{\mathrm{CO}}(t)). \tag{4.3.4}$$

Making use of these conservation laws, we eliminate $C_{\mathrm{O_2}}$, $C_{\mathrm{SiO_2}}$, $C_{\mathrm{CO_2}}$, and T, obtaining the coupled system

$$\begin{aligned}
\frac{\mathrm{d}C_{\mathrm{SiO}}}{\mathrm{d}t} =& - f_1\big(1 + h_1(1 - C_{\mathrm{SiO}}) + h_2(1 - C_{\mathrm{CO}})\big) \\
&\times \left(1 - \frac{a}{2}[(1 - C_{\mathrm{SiO}}) + (1 - C_{\mathrm{CO}})]\right) C_{\mathrm{SiO}}, \qquad (4.3.5a) \\
\frac{\mathrm{d}C_{\mathrm{CO}}}{\mathrm{d}t} =& - \varepsilon f_2\big(1 + h_1(1 - C_{\mathrm{SiO}}) + h_2(1 - C_{\mathrm{CO}})\big) \\
&\times \left(1 - \frac{a}{2}[(1 - C_{\mathrm{SiO}}) + (1 - C_{\mathrm{CO}})]\right) C_{\mathrm{CO}}, \qquad (4.3.5b)
\end{aligned}$$

subject to $C_{\mathrm{SiO}}(0) = C_{\mathrm{CO}}(0) = 1$. By looking at the equilibrium solutions of the system (4.3.5), that is, by setting the right hand-sides of both equations to zero, and using (4.3.3), we notice that oxygen depletion is a possible solution. However, this only occurs for $a \geq 1$, and since in our problem, we have assumed that the initial

concentration of oxygen is much larger than that of the fuel ($a < 0.2$), we will not consider this case in our analysis.

4.3.1 Disparate reaction rates: $\varepsilon \ll 1$

In order to understand the dynamics of (4.3.5), we first make several observations. First, for any $C_{\mathrm{SiO}}(t), C_{\mathrm{CO}}(t) \in (0, 1]$, we have that

$$\begin{aligned} 0 <& f_1 \left(1 + h_1(1 - C_{\mathrm{SiO}}) + h_2(1 - C_{\mathrm{CO}})\right) \\ &\times \left(1 - \frac{a}{2}[(1 - C_{\mathrm{SiO}}) + (1 - C_{\mathrm{CO}})]\right) C_{\mathrm{SiO}} \leq f_1 \left(1 + h_1 + h_2\right), \end{aligned} \tag{4.3.6a}$$

$$\begin{aligned} 0 <& f_2 \left(1 + h_1(1 - C_{\mathrm{SiO}}) + h_2(1 - C_{\mathrm{CO}})\right) \\ &\times \left(1 - \frac{a}{2}[(1 - C_{\mathrm{SiO}}) + (1 - C_{\mathrm{CO}})]\right) C_{\mathrm{CO}} \leq f_2 \left(1 + h_1 + h_2\right), \end{aligned} \tag{4.3.6b}$$

thus $C_{\mathrm{SiO}}(t)$ and $C_{\mathrm{CO}}(t)$ are monotone decreasing from 1 to 0. Additionally, since $0 < \varepsilon \ll 1$, where ε is the ratio between the two reaction rates, the dynamics of (4.3.5b) are on a slower timescale than those of (4.3.5a).

First, we will look at the fast timescale problem as defined in (4.3.5). Expanding $C_{\mathrm{SiO}}(t)$ and $C_{\mathrm{CO}}(t)$ in powers of ε in the following way

$$C_{\mathrm{SiO}}(t) = C^{(0)}_{\mathrm{SiO}}(t) + \varepsilon C^{(1)}_{\mathrm{SiO}}(t) + \cdots, \tag{4.3.7a}$$

$$C_{\mathrm{CO}}(t) = C^{(0)}_{\mathrm{CO}}(t) + \varepsilon C^{(1)}_{\mathrm{CO}}(t) + \cdots, \tag{4.3.7b}$$

the leading order problem reads

$$\begin{aligned} \frac{\mathrm{d}C^{(0)}_{\mathrm{SiO}}}{\mathrm{d}t} =& - f_1\big(1 + h_1(1 - C^{(0)}_{\mathrm{SiO}}) + h_2(1 - C^{(0)}_{\mathrm{CO}})\big) \\ &\times \left(1 - \frac{a}{2}[(1 - C^{(0)}_{\mathrm{SiO}}) + (1 - C^{(0)}_{\mathrm{CO}})]\right) C^{(0)}_{\mathrm{SiO}}, \end{aligned} \tag{4.3.8a}$$

$$\frac{\mathrm{d}C^{(0)}_{\mathrm{CO}}}{\mathrm{d}t} = 0, \tag{4.3.8b}$$

with initial conditions $C^{(0)}_{\mathrm{SiO}}(0) = C^{(0)}_{\mathrm{CO}}(0) = 1$. Solving for (4.3.8b) first, subject to the corresponding initial condition, we have that

$$C^{(0)}_{\mathrm{CO}}(t) = 1. \tag{4.3.9}$$

Therefore, C_{CO} is slowly varying and at lowest order it is constant, relative to the

timescale on which C_{SiO} varies. Placing (4.3.9) into (4.3.8a), we are left with

$$\frac{\mathrm{d}C^{(0)}_{\mathrm{SiO}}}{\mathrm{d}t} = -f_1\left(1+h_1(1-C^{(0)}_{\mathrm{SiO}}(t))\right)\left(1-\frac{a}{2}(1-C^{(0)}_{\mathrm{SiO}}(t))\right)C^{(0)}_{\mathrm{SiO}}(t), \tag{4.3.10}$$

that we will solve later on.

Now, introducing the slow timescale $\tau = \varepsilon t$, the system (4.3.5) becomes

$$\begin{aligned}\varepsilon\frac{\mathrm{d}C_{\mathrm{SiO}}}{\mathrm{d}\tau} =& -f_1\big(1+h_1(1-C_{\mathrm{SiO}})+h_2(1-C_{\mathrm{CO}})\big)\\ &\times\left(1-\frac{a}{2}[(1-C_{\mathrm{SiO}})+(1-C_{\mathrm{CO}})]\right)C_{\mathrm{SiO}}, \qquad (4.3.11a)\\ \frac{\mathrm{d}C_{\mathrm{CO}}}{\mathrm{d}\tau} =& -f_2\big(1+h_1(1-C_{\mathrm{SiO}})+h_2(1-C_{\mathrm{CO}})\big)\\ &\times\left(1-\frac{a}{2}[(1-C_{\mathrm{SiO}})+(1-C_{\mathrm{CO}})]\right)C_{\mathrm{CO}}. \qquad (4.3.11b)\end{aligned}$$

Expanding the variables $C_{\mathrm{SiO}}(\tau)$ and $C_{\mathrm{CO}}(\tau)$ again in powers of ε such that

$$\begin{aligned}C_{\mathrm{SiO}}(\tau) &= C^{(0)}_{\mathrm{SiO}}(\tau)+\varepsilon C^{(1)}_{\mathrm{SiO}}(\tau)+\cdots, \qquad (4.3.12a)\\ C_{\mathrm{CO}}(\tau) &= C^{(0)}_{\mathrm{CO}}(\tau)+\varepsilon C^{(1)}_{\mathrm{CO}}(\tau)+\cdots, \qquad (4.3.12b)\end{aligned}$$

the leading order problem in the slow timescale reads

$$\begin{aligned}0 =& -f_1\big(1+h_1(1-C^{(0)}_{\mathrm{SiO}})+h_2(1-C^{(0)}_{\mathrm{CO}})\big)\\ &\times\left(1-\frac{a}{2}[(1-C^{(0)}_{\mathrm{SiO}})+(1-C^{(0)}_{\mathrm{CO}})]\right)C^{(0)}_{\mathrm{SiO}}, \qquad (4.3.13a)\\ \frac{\mathrm{d}C^{(0)}_{\mathrm{CO}}}{\mathrm{d}\tau} =& -f_2\left(1+h_1(1-C^{(0)}_{\mathrm{SiO}}))+h_2(1-C^{(0)}_{\mathrm{CO}}))\right)\\ &\times\left(1-\frac{a}{2}[(1-C^{(0)}_{\mathrm{SiO}}))+(1-C^{(0)}_{\mathrm{CO}}))]\right)C^{(0)}_{\mathrm{CO}}), \qquad (4.3.13b)\end{aligned}$$

subject to $C^{(0)}_{\mathrm{CO}}(0) = 1$ so that it matches the solution of the fast timescale. Moreover, we have that $C_{\mathrm{SiO}}(t)$ is rapidly varying and nears its equilibrium value before $C_{\mathrm{CO}}(\tau)$ responds. We can compute this equilibrium value by setting (4.3.5a) to zero, and this is only true when $C_{\mathrm{SiO}} = 0$, where we have taken into account (4.1.7) and (4.3.6a). Therefore, we approximate $C_{\mathrm{SiO}}(\tau)$ as zero, and set

$$C^{(0)}_{\mathrm{SiO}}(\tau) = 0, \tag{4.3.14}$$

in (4.3.13b) to obtain

$$\frac{\mathrm{d}C_{\mathrm{CO}}^{(0)}}{\mathrm{d}\tau} = -f_2\left(1 + h_1 + h_2(1 - C_{\mathrm{CO}}^{(0)}(\tau))\right)\left(1 - \frac{a}{2}[2 - C_{\mathrm{CO}}^{(0)}(\tau)]\right)C_{\mathrm{CO}}^{(0)}(\tau). \tag{4.3.15}$$

Solving (4.3.10) and (4.3.15) in their respective timescales by quadrature, we obtain the implicit relations

$$\int_{C_{\mathrm{SiO}}^{(0)}}^{1} \frac{\mathrm{d}\xi}{f_1\left(1 + h_1(1-\xi)\right)\left(1 - \frac{a}{2}(1-\xi)\right)\xi} = t, \tag{4.3.16a}$$

$$\int_{C_{\mathrm{CO}}^{(0)}}^{1} \frac{\mathrm{d}\xi}{f_2\left(1 + h_1 + h_2(1-\xi)\right)\left(1 - \frac{a}{2}(2-\xi)\right)\xi} = \tau, \tag{4.3.16b}$$

where it is clear that $C_{\mathrm{SiO}}^{(0)}, C_{\mathrm{CO}}^{(0)} \to 0$ as $t \to \infty$, as expected. In order to obtain more explicit representations of the solutions, we must make further assumptions.

4.3.2 Approximating the Arrhenius terms

We shall at times find it convenient to approximate the Arrhenius terms in the reaction kinetics (4.1.7) with linear approximations, $f_j(T) \approx F_j(T)$, where

$$F_j(T) = \alpha_j + (1 - \alpha_j)T \quad \text{with} \quad \alpha_j = \exp\left(-\frac{E_j}{R}\left(\frac{1}{T_2} - \frac{1}{T_1}\right)\right). \tag{4.3.17}$$

To obtain (4.3.17), we have computed the linear interpolation polynomial passing through the points $T = 0$ and $T = 1$, corresponding to the dimensionless air and fuel inlet temperatures, respectively. The error estimate for this approximation based on the initial data for T is

$$\max_{T\in[0,1]} \frac{|f_1(T) - F_1(T)|}{|f_1(T)|} = 0.031 \quad \text{and} \quad \max_{T\in[0,1]} \frac{|f_2(T) - F_2(T)|}{|f_2(T)|} = 0.027, \tag{4.3.18}$$

for parameter values in Table 4.1. Hence, the maximal relative error for $0 \leq T \leq 1$ is around 3% (see Figure 4.2).

In the next sections we will see that at certain spatial locations and times the temperature can go up to 2 approximately. For this case, the curves in Figure 4.2 would go up again in the interval $1 \leq T \leq 2$, and the maximal relative error for the whole interval, $0 \leq T \leq 2$, is around 3% for F_1 and 8% for F_2. We conclude that the error of this approximation is low enough over the range of temperatures considered so that the qualitative behaviour of the solutions is unaltered.

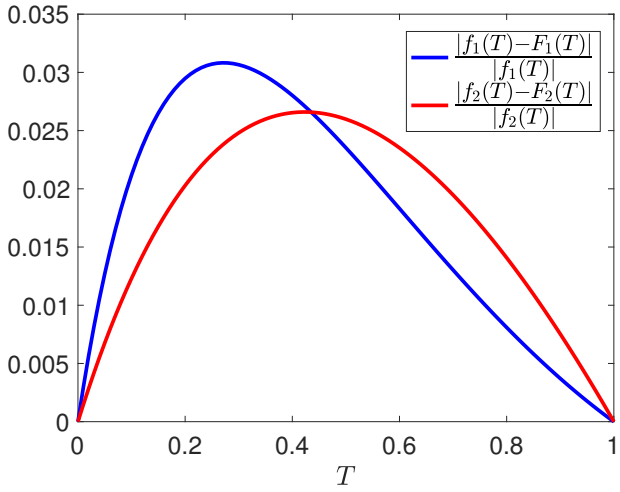

Figure 4.2: Relative error of approximations (4.3.17) to the Arrhenius terms.

Notice that the temperature will only go above 2 when we solve the fully coupled problem numerically, however there is no need for an approximation of the Arrhenius terms in this case.

4.3.3 Oxygen-rich environment limit: $a \ll 1$

Making use of the approximation (4.3.17), equations (4.3.10) and (4.3.15) become,

$$\frac{\mathrm{d}C_{\mathrm{SiO}}}{\mathrm{d}t} = -\left(\alpha_1 + (1-\alpha_1)[1 + h_1(1-C_{\mathrm{SiO}})]\right)\left(1 - \frac{a}{2}(1-C_{\mathrm{SiO}})\right)C_{\mathrm{SiO}}, \tag{4.3.19a}$$

$$\frac{\mathrm{d}C_{\mathrm{CO}}}{\mathrm{d}\tau} = -\left(\alpha_2 + (1-\alpha_2)[1 + h_1 + h_2(1-C_{\mathrm{CO}})]\right)\left(1 - \frac{a}{2}[2-C_{\mathrm{CO}}]\right)C_{\mathrm{CO}}, \tag{4.3.19b}$$

where we have neglected the superscript notation. Recall that the ratio between the initial concentration of any of the fuel components and oxygen, a, is such that $0 < a \leq 0.2$. This is due to the large amount of oxygen that enters the furnace hood from the outside, compared to the amount of the other chemicals coming from the interior of the furnace. We therefore treat a as a small parameter, $a \ll 1$, and at lowest order in a, the ODEs (4.3.19) become quadratic rather than cubic. Solving these lowest order equations subject to $C_{\mathrm{SiO}}(0) = 1$ and $C_{\mathrm{CO}}(0) = 1$, respectively, we

find that the asymptotic solutions in the small a limit are

$$C_{\mathrm{SiO}}(t) = \frac{1 + h_1\,(1-\alpha_1)}{\exp\left(\left[1 + h_1\,(1-\alpha_1)\right] t\right) + h_1\,(1-\alpha_1)} + \mathcal{O}(a), \tag{4.3.20a}$$

$$C_{\mathrm{CO}}(t) = \frac{1 + (h_1+h_2)\,(1-\alpha_2)}{(1 + h_1\,(1-\alpha_2))\exp\left(\left[1 + (h_1+h_2)\,(1-\alpha_2)\right]\varepsilon t\right) + h_2\,(1-\alpha_2)} + \mathcal{O}(a). \tag{4.3.20b}$$

Asymptotic solutions for all remaining quantities can be obtained from (4.3.20) and the earlier mentioned conservation laws (4.3.1)-(4.3.4). We plot the approximate solutions in Figure 4.3 for one small value of a (top) and the upper bound $a = 0.2$ (bottom). In both cases, since there is plenty of oxygen available for combustion, SiO_2 and CO_2 are produced as the reactants (SiO and CO) are being consumed. We see that since C_{CO} and $C_{\mathrm{CO_2}}$ evolve on a slower timescale than the rest of the chemical concentrations, the second combustion reaction (1.1.5) has barely started while the first one (1.1.4) is finished, within the chosen timescale t. Also, since the reactions are highly exothermic, the temperature of the system increases. When comparing the analytical approximations (solid line) to the numerical simulations (dashed line) we find good agreement, even for relatively large values of a, so the approximate solution retains validity in the physically relevant parameter regime.

Now, if we look at the long time behaviour of C_{CO} and $C_{\mathrm{CO_2}}$ as they both equilibrate, the asymptotic solution is still a good approximation when compared to the numerical solution as shown in Figure 4.4, with the accuracy of the approximation improving as a becomes small. To improve the approximation for the maximal range of a (say, near $a = 0.2$), one may find the $\mathcal{O}(a)$ terms in (4.3.20). However, the level of accuracy in the leading order expansions is sufficient for us to draw qualitative conclusions on the dynamics of C_{CO} and $C_{\mathrm{CO_2}}$ in the oxygen-rich environment.

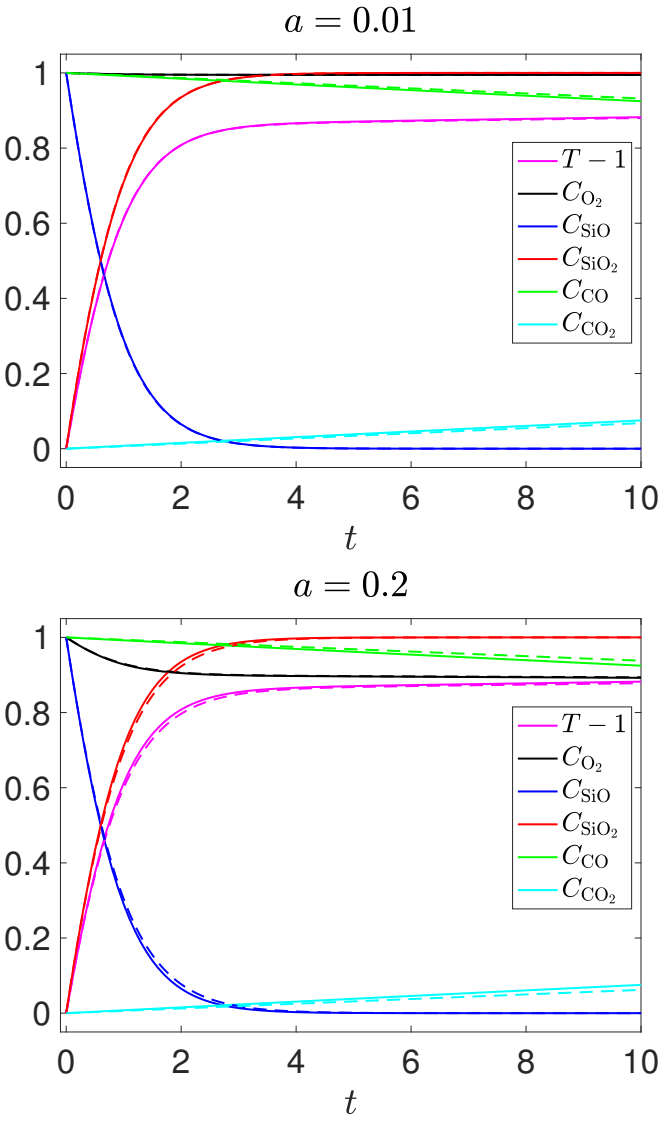

Figure 4.3: Dimensionless chemical concentrations and temperature from solving the problem (4.1.5) numerically (dashed line) and analytically (solid line) assuming $\zeta_1 = \zeta_2 = 0$. We compare the solutions for $a = 0.01$ (top) and $a = 0.2$ (bottom). We fix $C_{\text{sat}} = 0.1$, with other parameters taking values listed in Table 4.1.

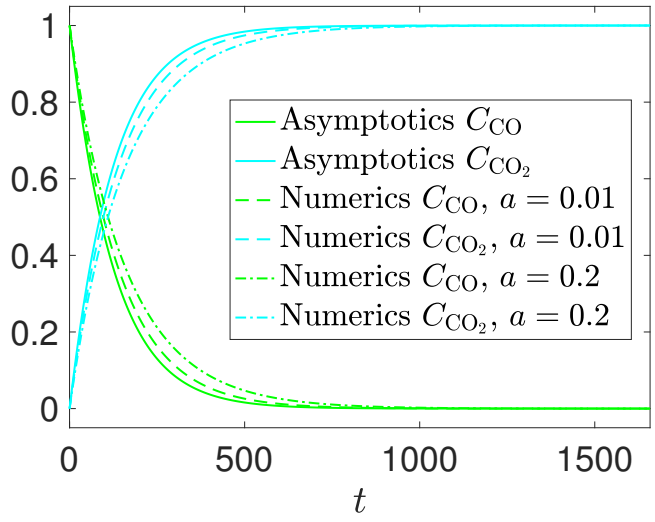

Figure 4.4: Long time behaviour of the asymptotic (solid line) and numerical (dashed and dash-dotted) solutions for CO and CO_2 concentrations. Dash lines correspond to $a = 0.01$ in the numerics and dash-dotted lines to $a = 0.2$.

4.3.4 Particle size distribution

4.3.4.1 Comparison of numerical and approximate solutions

The analytical solution obtained for the population balance equation (4.1.10a) in Section 4.2 is written in terms of the growth rate (G) and nucleation rate (J) functions as in (4.1.8) and (4.1.9), which depend on the SiO_2 concentration and temperature. Using the numerical solutions obtained for SiO_2 and T in the previous section, we plot the nucleation and growth rates in Figure 4.5. Both functions experience a fast increase initially while the SiO reaction is happening and then they keep increasing at a much slower rate until the CO reaction finishes completely. Note that the behaviour of G is very similar to that of the concentration of SiO_2.

Now, in Figure 4.6 we show the solution for the number density function of particles, n, with respect to s given by (4.2.5) and (4.2.6), where we take C_{SiO_2} and T from both the analytical approximations (solid line) and numerical simulations (dashed line) in the previous section with $a = 0.2$ and $\zeta_1 = \zeta_2 = 0$. The direction of the black arrow indicates increasing time from $t = 1$ to $t = 10$. The main difference we see between the particle density functions obtained using the approximation is the position of the peaks. This is due to the small shift in the C_{SiO_2} curves in Figure 4.3, which results in the concentration reaching the saturation point at a slightly different time t_{min} in each case. Here, we have chosen $C_{sat} = 0.1$, thus $t_{min} = 0.106$ in the numerics (dashed

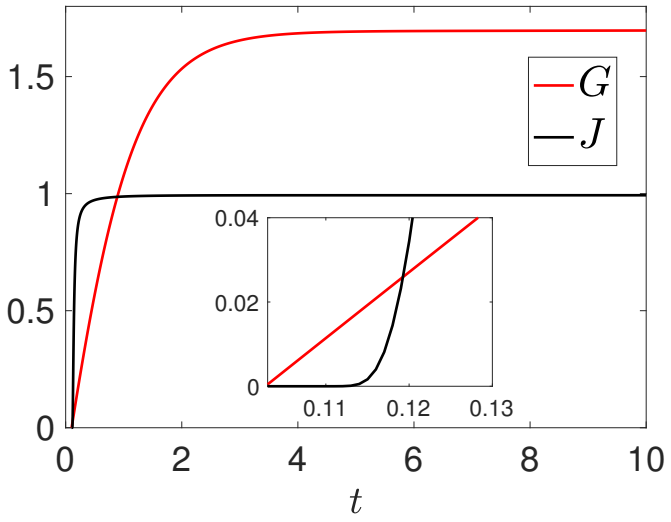

Figure 4.5: Dimensionless growth (G) and nucleation (J) rates as defined in (4.1.8) and (4.1.9), respectively, and where we have taken C_{SiO_2} and T from the numerical results for the decoupled problem obtained in Section 4.3.3.

line) and $t_{\min} = 0.102$ in the approximate solution (solid line). Since in the latter case the particles start growing at an earlier time, they grow to be slightly larger.

Note that we can approximate the value of $t_{\min}$ from its definition and by making use of the approximations obtained in Section 4.3. We have that $1 - C_{\mathrm{SiO}}(t_{\min}) = C_{\mathrm{SiO}_2}(t_{\min}) = C_{\mathrm{sat}}$, and employing the solution (4.3.20a), we find

$$t_{\min} = \frac{1}{1 + h_1\,(1 - \alpha_1)} \log\left(\frac{1 + h_1\,(1 - \alpha_1)\,C_{\mathrm{sat}}}{1 - C_{\mathrm{sat}}}\right) + \mathcal{O}(a) \tag{4.3.21}$$

as $a \to 0$. We conclude from this formula that as the saturation concentration increases, the critical time for nucleation is larger, up to the value $C_{\mathrm{sat}} = 1$ where nucleation never happens (see Figure 4.7).

Referring back to Figure 4.6, we see that as time evolves the peaks move to the right, meaning that the particles grow with no bound. In Section 4.4, where we reincorporate the sink term due to particle formation into the SiO_2 conservation equation, particle growth will stop at a finite time. In fact, all curves in Figure 4.6 are translations of each other and they move with a non-constant speed given by the slope of the red characteristic in Figure 4.1 as defined in (4.2.7), that is, $\mathrm{d}s^*/\mathrm{d}t = G^*G(t)$. The latter statement is true since we showed in (4.2.8) that all characteristic curves are translations of $s^*(t)$, and therefore all particles have the same growth rate profile

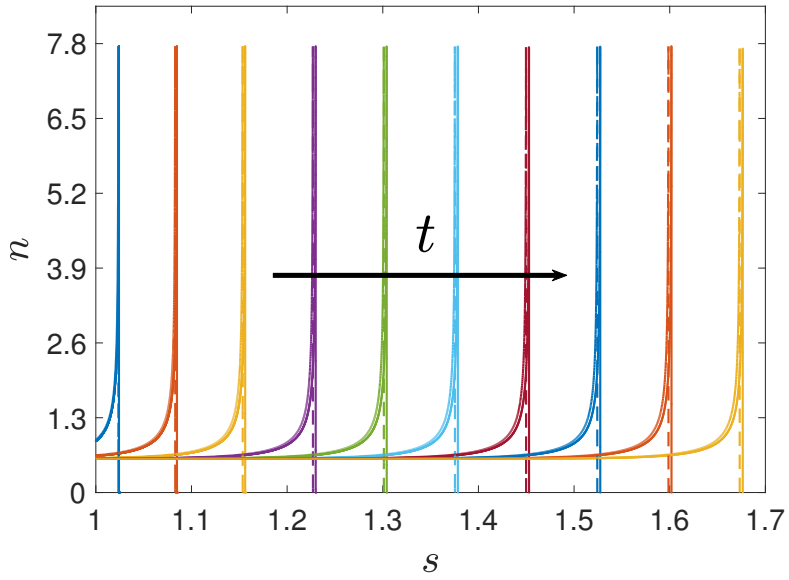

Figure 4.6: Dimensionless number density function of particles for different values of t from 1 to 10 with an increment of 1. The curves are obtained from solving the problem (4.1.5f)-(4.1.5e), with $\zeta_1 = \zeta_2 = 0$, numerically (dashed line) and approximately (solid line) for $a = 0.2$ and using the formulae (4.2.5) and (4.2.6) for n. The distribution shifts to the right as t increases. We have chosen the saturation concentration as $C_{\text{sat}} = 0.1$. See Figure 4.8 (black solid line) for the same plot in a log-scale.

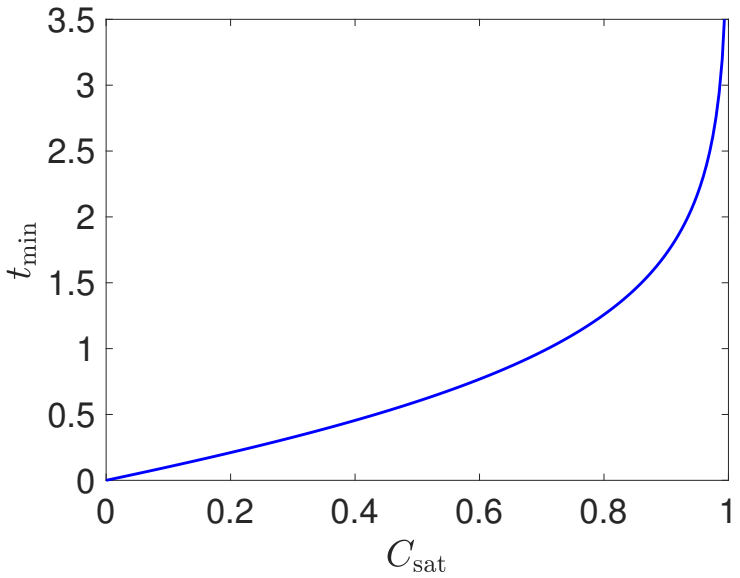

Figure 4.7: Approximated values of t_{min} with respect to C_{sat} from (4.3.21). The rest of dimensionless parameters appearing in (4.3.21) are taken from Table 4.1.

regardless of when they were created or how big they are. This would not be true if, for instance, we were considering particles in the continuum regime, where the growth rate (2.3.20) depends on s. Therefore, by looking at Figure 4.1 we conclude that particle growth is almost linear for all times, except for initial times when it is slightly slower. Moreover, the position of the peaks in Figure 4.6 is determined approximately by the dividing characteristic $s^*(t)$, which is equivalent to the solution of the single particle growth model (4.2.12).

With respect to the shape of n for a fixed time, we find a uniform distribution at smaller sizes and a peak around the largest sizes. The largest number of particles are of the largest sizes and these are the particles that originated very close to $t = t_{\min}$ and so they have had a longer time to grow. This high density of particles is due to the many particles that formed in a very short time interval right after $t = t_{\min}$. We can see this from studying the nucleation boundary condition (4.1.10b) and by looking at Figure 4.5. Initially, the nucleation rate, J, is much larger than G which is almost zero, resulting in a peak. After some time, they both reach almost constant values, and the ratio J/G is much lower than before, with particle growth dominating over nucleation. The latter corresponds to the uniform part of the distribution.

The height of the peak comes from maximising $J(t)/G(t)$ which is the form of the solution for n when $t > t_{\min}$. This value is finite since by definition G is never zero for values of t above the critical time for nucleation, $t_{\min}$. Moreover, as t approaches $t_{\min}$, J will go to zero before G does, as it can be seen from the form of the expressions for nucleation and growth rates (4.1.8)-(4.1.9) and from the zoomed in box inside Figure 4.5. Therefore, as $t \to t_{\min}$, we have that $n \to 0$, which corresponds to the right side of the peak which shows a sudden drop to zero. We will study the shape of the peak in more detail in the next section.

4.3.4.2 Asymptotics near the peak of the distribution

In order to better understand the shape of the peak in Figure 4.6, we consider an asymptotic analysis near the red characteristic. We use the approximated solutions for C_{SiO_2} and T from Section 4.3, neglecting terms which evolve on the slow timescale $\tau = \varepsilon t$, thus setting $C_{CO}(t) \approx 1$ for $t \ll \varepsilon^{-1}$. We also neglect $\mathcal{O}(a)$ terms as before.

There are two regions to consider, a peak and a uniform distribution, as we can see from Figure 4.8, where we show the solution corresponding to the last peak in Figure 4.6 ($t = 10$) in a semi-log plot with a black solid curve. Note that in this plot we have flipped the horizontal axis and have translated the curve by $s^*(t = 10)$. Moreover, if we were to plot the rest of the peaks in Figure 4.8, they would lay exactly on top of

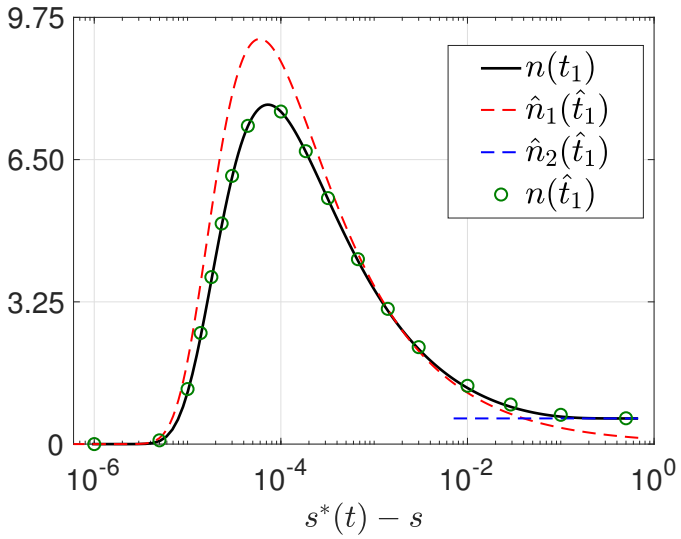

Figure 4.8: Semi-log plot for the number density function (black) and asymptotic approximations (dashed lines and circles).

the current peak since they correspond to a translation of s by $s^*(t)$, and the only difference is that the right side (or uniform part) of the peak would be shorter.

Each region, peak and uniform part, has a timescale associated. The first timescale corresponds to $0 < t - t_{\min} \ll 1$, for which $0 < s^*(t) - s \ll 1$, and we have the observed peak in Figures 4.6 and 4.8. For $t - t_{\min} \gg 1$, we have the flat region of uniform distribution away from the peak, which corresponds to $C_{SiO_2} \sim 1$ and $T(t) \sim 1 + h_1$, as seen in Figure 4.3. The reaction leading to particle growth happens before the very large timescales on which C_{CO} will play a role, so we consider $1 \ll t - t_{\min} \ll \varepsilon^{-1}$ for our second timescale.

On the small timescale, $0 < t - t_{\min} \ll 1$, we start by expanding the approximate solutions for C_{SiO_2} and T found in Section 4.3 in powers of $t - t_{\min}$, namely

$$C_{SiO_2}(t) = C_{sat} + (1 - C_{sat})\,(1 + h_1(1 - \alpha_1)C_{sat})\,(t - t_{\min}) + \mathcal{O}\left((t - t_{\min})^2\right), \tag{4.3.22a}$$

$$T(t) = 1 + h_1 C_{sat} + h_1(1 - C_{sat})\,(1 + h_1(1 - \alpha_1)C_{sat})\,(t - t_{\min}) + \mathcal{O}\left((t - t_{\min})^2\right). \tag{4.3.22b}$$

The latter expressions allow us to approximate the characteristic curves (4.2.5) by the

formula

$$s-1=\frac{G^*}{2}\sqrt{T^*+1+h_1C_{\rm sat}}(1-C_{\rm sat})\left(1+h_1(1-\alpha_1)C_{\rm sat}\right)\\ \times\left\{(t-t_{\rm min})^2-(t_1-t_{\rm min})^2\right\}, \tag{4.3.23}$$

where we have used

$$\sqrt{T^*+1+h_1C_{\rm sat}+h_1(1-C_{\rm sat})\left(1+h_1(1-\alpha_1)C_{\rm sat}\right)(t-t_{\rm min})}\\ \approx\sqrt{T^*+1+h_1C_{\rm sat}}. \tag{4.3.24}$$

We find

$$t_1=t_{\rm min}+\sqrt{(t-t_{\rm min})^2-\frac{s-1}{\frac{G^*}{2}\sqrt{T^*+1+h_1C_{\rm sat}}(1-C_{\rm sat})\left(1+h_1(1-\alpha_1)C_{\rm sat}\right)}}, \tag{4.3.25}$$

and similarly for (4.2.7), we obtain

$$s^*(t)=1+\frac{G^*}{2}\sqrt{T^*+1+h_1C_{\rm sat}}(1-C_{\rm sat})\left(1+h_1(1-\alpha_1)C_{\rm sat}\right)(t-t_{\rm min})^2. \tag{4.3.26}$$

Therefore, we may write

$$t_1\approx\hat{t}_1=t_{\rm min}+\sqrt{\frac{s^*(t)-s}{\frac{G^*}{2}\sqrt{T^*+1+h_1C_{\rm sat}}(1-C_{\rm sat})\left(1+h_1(1-\alpha_1)C_{\rm sat}\right)}}, \tag{4.3.27}$$

where it will be convenient to define the moving coordinate $S=s^*(t)-s$. We remark that the small $t-t_{\rm min}$ regime corresponds to the small S regime. We evaluate the exact solution $n(t_1)$ at the explicit approximation of t_1 as given by (4.3.27) and plot it in Figure 4.8 (with green circles) to find that it matches the real solution (black solid line) everywhere. As such, the approximate characteristic curves result in nearly the same ones as for the exact solution (plotted numerically), and do not introduce significant error.

From the implicit form of the exact solution, $n(s,t)=J(t_1)/G(t_1)$, we now use the approximation of t_1 to construct an approximation $\hat{n}_1$ to n which is explicit in the variables. We find

$$n=\frac{\exp\left\{-\lambda_0\left(\frac{T(t_1)}{T^*}+1\right)^{-3}\left[\ln\left(\frac{C_{{\rm SiO}_2}(t_1)}{C_{\rm sat}}\right)\right]^{-2}\right\}}{\sqrt{T^*+T(t_1)}\left(C_{{\rm SiO}_2}(t_1)-C_{\rm sat}\right)}\approx\hat{n}_1(S)=\frac{\Gamma}{\sqrt{S}}\exp\left(-\frac{\Lambda}{S}\right), \tag{4.3.28}$$

where Γ and Λ are constants which depend on model parameters:

$$\Gamma = \sqrt{\frac{G^*}{2\sqrt{T^* + 1 + h_1 C_{\text{sat}}}(1 - C_{\text{sat}})\left(1 + h_1(1 - \alpha_1)C_{\text{sat}}\right)}}, \tag{4.3.29a}$$

$$\Lambda = \frac{\lambda_0 G^* T^{*3} C_{\text{sat}}^2}{2\left(T^* + 1 + h_1 C_{\text{sat}}\right)^{5/2}(1 - C_{\text{sat}})\left(1 + h_1(1 - \alpha_1)C_{\text{sat}}\right)}. \tag{4.3.29b}$$

From (4.3.28), the position and height of the peak are given by

$$s_{\text{p}} = s^*(t) - 2\Lambda \quad \text{and} \quad \hat{n}_1(s_{\text{p}}) = \exp(-1/2)\frac{\Gamma}{\sqrt{2\Lambda}}, \tag{4.3.30}$$

respectively. Note that the position is time-dependent but the amplitude is not. Using the values for the dimensionless parameters from Table 4.1 with $C_{\text{sat}} = 0.1$, we find $\Gamma = 0.117$ and $\Lambda = 3.268 \times 10^{-5}$. We plot the approximation (4.3.28) with a red dashed curve in Figure 4.8 and find that the width of the peak is well represented, as is the rate of change on each side of the peak, while the height of the peak is slightly overestimated (and would, in principle, be improved by the inclusion of higher order terms).

On the larger timescale, $1 \ll t - t_{\min} \ll \varepsilon^{-1}$, we have

$$C_{\text{SiO}_2}(t) = 1 - \mathcal{O}(\exp\{-(1 + h_1(1 - \alpha_1))t\}), \tag{4.3.31a}$$

$$T(t) = 1 + h_1 - \mathcal{O}(\exp\{-(1 + h_1(1 - \alpha_1))t\}), \tag{4.3.31b}$$

thus we approximate $C_{\text{SiO}_2}(t) \approx 1$ and $T(t) \approx 1 + h_1$. Similar to the above, we approximate the characteristic curves by

$$\begin{aligned} s &= 1 + G^* \int_{t_1}^{t} \sqrt{T^* + T(\tau)}\left(C_{\text{SiO}_2}(t) - C_{\text{sat}}\right) d\tau \\ &\approx 1 + G^* \sqrt{T^* + 1 + h_1}(1 - C_{\text{sat}})\left(t - t_1\right), \end{aligned} \tag{4.3.32}$$

and the dividing characteristic by

$$s^*(t) \approx 1 + G^* \sqrt{T^* + 1 + h_1}(1 - C_{\text{sat}})\left(t - t_{\min}\right). \tag{4.3.33}$$

From this we note that the characteristic curves become lines once $S = \mathcal{O}(1)$, consistent with what is observed in Figure 4.1 once s is an $\mathcal{O}(1)$ distance away from the curve

$s^*(t)$ (shown in red). Manipulating these equations, we obtain

$$t_1 = t_{\min} + \frac{S}{G^*\sqrt{T^* + 1 + h_1}(1 - C_{\text{sat}})}, \tag{4.3.34}$$

where again $S = s^*(t) - s$ is the moving coordinate. We then have

$$n \approx \hat{n}_2 = \frac{\exp\left\{-\lambda_0 \left(\frac{1+h_1}{T^*} + 1\right)^{-3} \left[\ln\left(\frac{1}{C_{\text{sat}}}\right)\right]^{-2}\right\}}{\sqrt{T^* + 1 + h_1}\,(1 - C_{\text{sat}})}, \tag{4.3.35}$$

where $\hat{n}_2$ is a constant. Using parameter values from Table 4.1 as well as $C_{\text{sat}} = 0.1$, we find $\hat{n}_2 \approx 5.773 \times 10^{-1}$, which is consistent with the value n levels off to in Figure 4.8 as S becomes $\mathcal{O}(1)$ ($n \approx \hat{n}_2$ corresponds to the blue dashed line).

To summarise, the previous results provide an explicit formula for n in terms of well-known parameters, capturing the qualitative behaviour of the particle size distribution, with the small time ($0 < t - t_{\min} \ll 1$) approximation $\hat{n}_1(\hat{t}_1)$ capturing the peak, and the intermediate time ($1 \ll t - t_{\min} \ll \varepsilon^{-1}$) approximation $\hat{n}_2(\hat{t}_1)$ providing the uniform distribution away from the peak. The largest timescale, $t - t_{\min} \gg \varepsilon^{-1}$, will not play a strong role in modifying the distribution n (which is on the two timescales felt by C_{SiO_2}), and hence we do not consider it.

4.3.5 Sensitivity analysis

We will now explore how the particle size distribution is affected by changes to two physically relevant parameters. The first parameter that we will vary is the saturation concentration, C_{sat}, which determines the critical time for particle nucleation. Secondly, we will solve the dimensionless version of the population balance equation (2.4.3) numerically under the assumptions stated at the beginning of this chapter but with $D_s > 0$. And thus, we will study how the final size distribution of particles is affected when we account for fluctuations in the particle growth velocity.

4.3.5.1 Varying the saturation concentration

The value of the saturation concentration, C_0, as in Table 2.3 is not well-defined in the literature and in this work we treat it as a parameter that can be varied from zero to one. In this section, we will explore how a different choice for the value of its dimensionless version $C_{\text{sat}} = C_0/C_{\text{SiO}_2,0}$ changes the final distribution of particles. In Figure 4.9 we show the number density function of particles at the final time, taken

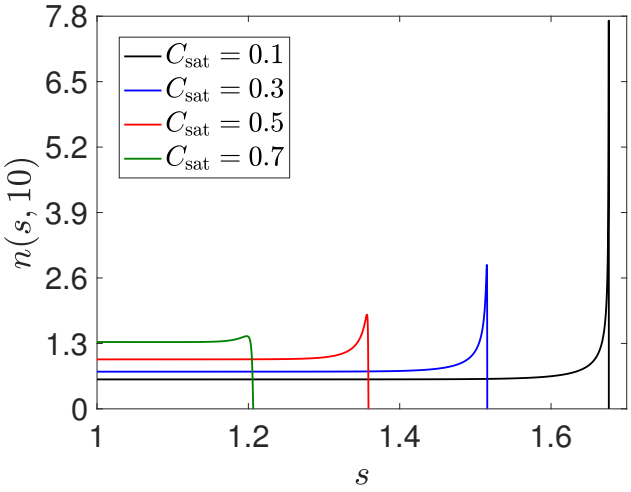

Figure 4.9: Dimensionless number density function of particles at time $t = 10$ for different values of the saturation concentration C_{sat} and for $\zeta_1 = \zeta_2 = 0$. Here, we have used the analytical solution for n given by (4.2.5)-(4.2.6).

to be $t = 10$, for increasing values of the saturation concentration from 0.1 to 0.7. As we can see from Figure 4.7, the larger C_{sat}, the larger the critical time t_{min} at which particles start forming, and so particles will not grow as much during the selected time; the position of the peak will be closer to $s = 1$. The height of the peak decreases for larger C_{sat}, whereas the value that n levels off to at $s = 1$ increases.

We can quantify the above conclusions by looking at the formulae derived in the previous section. First, with respect to the position of the peak, s_p in (4.3.30), we notice that Λ as in (4.3.29b) decreases as C_{sat} increases, meaning that the position is closer to the value of $s^*(t)$ which also becomes smaller (see (4.3.26)). Now, if we study the formula for the height of the peak, $\hat{n}_1(s_p)$ as in (4.3.30), we can see that the term $\Gamma/\sqrt{2\Lambda}$ behaves as $1/C_{\text{sat}}^{7/4}$, thus the height of the peak decreases as C_{sat} becomes larger. On the other hand, the value of $\hat{n}_2$ from (4.3.35), which determines the level of the distribution at $s = 1$, will increase since it is dominated by the exponential which becomes very large as C_{sat} increases due to the term $1/\left(\ln(1/C_{\text{sat}})\right)^2$.

In terms of the particle physics, we conclude that the smaller the saturation concentration of SiO_2, the more particles are produced and the larger they are. Moreover, as the saturation concentration increases, the particle size distribution becomes almost uniform.

4.3.5.2 Varying the particle size coordinate diffusivity

The dimensionless version of the population balance equation (2.4.3) under the assumptions taken at the beginning of the chapter and with $D_s > 0$ is given by

$$\frac{\partial n}{\partial t} + G^* \frac{\partial}{\partial s}\left(Gn - d_s \frac{\partial n}{\partial s}\right) = 0 \tag{4.3.36a}$$

for $s > 1$ and $t > t_{\min}$ such that $C_{SiO_2}(t_{\min}) = C_{\text{sat}}$, and with dimensionless boundary and initial conditions

$$Gn - d_s \frac{\partial n}{\partial s} = J \qquad \text{at} \qquad s = 1, \quad t > t_{\min}, \tag{4.3.36b}$$

$$n = 0 \qquad \text{at} \qquad t = t_{\min}, \quad s > 1, \tag{4.3.36c}$$

with $d_s = D_s/(G_0 s_{\min})$. Now, if we choose the diffusion coefficient in the particle size coordinate, D_s, to be proportional to the dimensional particle growth rate, $\hat{G}$, as in, for example, [50], the respective dimensionless diffusivity reads

$$d_s(t) = \frac{\beta}{s_{\min}} G(t), \tag{4.3.37}$$

where β is the coefficient of proportionality and G is given as in (4.1.8). Since an analytical solution of problem (4.3.36)-(4.3.37) is not possible, we solve it numerically by using a finite differences scheme. We show the numerical solution in Figure 4.10 at two time steps, $t = 5$ and $t = 10$, and for different values of the coefficient β. We observe that for a fix time t, as d_s becomes larger the peak height decreases and the distribution becomes almost uniform and less localised around specific particle sizes. Therefore, it is clear from Figure 4.10 that diffusion in the paticle size space smoothes the particle size distribution, and as a consequence larger particles are produced for larger values of d_s. For comparison purposes, we have also included the analytical solution for n obtained in Section 4.2 when $D_s = 0$ with a black line, and we expect that as $d_s \to 0$, both the numerical and analytical solutions will become identical. A similar behaviour in the shape of the distributions when varying d_s is also found in [1], where a stepwise behaviour is obtained in the diffusionless regime, and fluctuations lead to smooth bell-shaped distributions. Moreover, by comparing the two different times selected in Figure 4.10, this effect becomes more apparent as time moves forward, whereas initially, the growth rate (and therefore $d_s(t)$) is small, or almost zero, and the particle size distribution resembles more the one obtained analytically in the diffusionless regime.

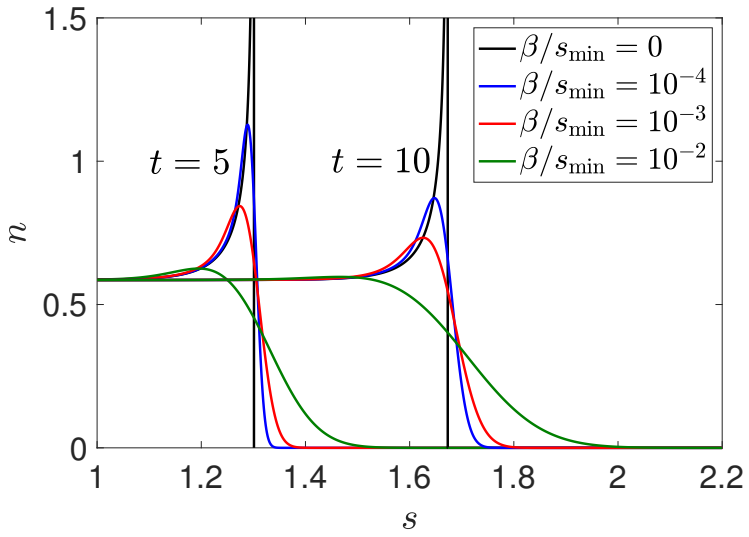

Figure 4.10: Dimensionless number density function of particles at times $t = 5$ and $t = 10$ for different values of the particle size diffusivity defined in (4.3.37) and for $\zeta_1 = \zeta_2 = 0$. These results are obtained from solving the particle formation and growth problem (4.3.36) numerically, where we have chosen $C_{\text{sat}} = 0.1$.

4.4 Numerical solution of the fully-coupled system

In this section, we include the effects of particle formation and growth on the chemical concentrations and temperature, *i.e.* we take $\zeta_1, \zeta_2 > 0$. We solve the coupled system of ODEs (4.1.5) numerically subject to initial conditions (4.1.6), and plot some typical results in Figures 4.11 and 4.12 in which we use the parameters in Table 4.1 with $a = 0.2$ and $C_{\text{sat}} = 0.1$.

The main differences in Figure 4.11 compared to the decoupled case in Section 4.3 (Figure 4.3) are on the SiO_2 concentration and temperature profiles due to the inclusion of the sink and source terms respectively. The SiO_2 concentration (red solid curve in Figure 4.11a) reaches a maximum while the SiO combustion reaction occurs, and later decreases as SiO_2 is consumed due to particle growth, finally converging to the equilibrium value $C_{SiO_2} = C_{\text{sat}}$ for large time. The latter can be seen from setting the right hand sides of (4.1.5) to zero, which gives $G = 0$ assuming $M_2, C_{O_2} \neq 0$ as $t \to \infty$. The temperature, shown in Figure 4.11b, also increases initially due to the combustion reaction, yet further increases due to energy given off during particle formation. As a reference, we have added the numerical solutions for SiO_2 and T for the decoupled case with dashed lines.

In Figure 4.12 we plot the first few moments of the distribution n: the number of particles, M_0, the mean, $\mu = M_1/M_0$, and the variance, $\sigma^2 = M_2/M_0 - \mu^2$. All moments

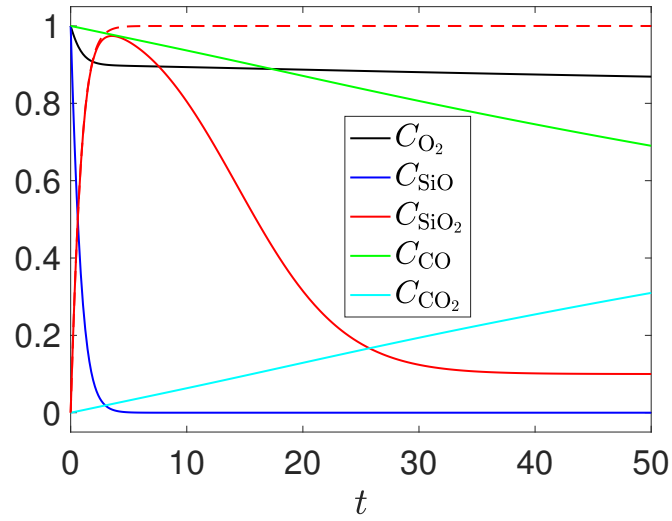

(a)

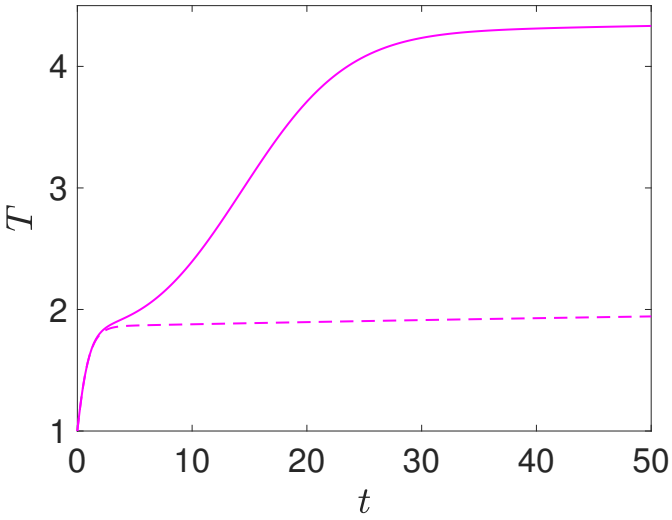

(b)

Figure 4.11: (a) Chemical concentrations and (b) temperature from solving the fully coupled system (4.1.5)-(4.1.6) numerically with $a = 0.2$ and $C_{\text{sat}} = 0.1$, and other parameters taking values from Table 4.1. The dashed lines correspond to the numerical solutions for the SiO_2 concentration (red) and temperature (pink) for the decoupled case.

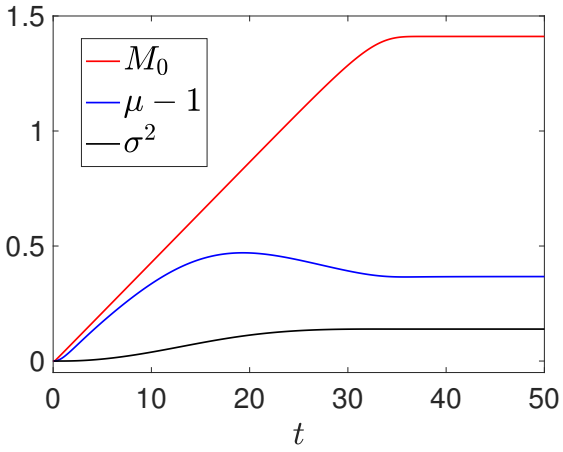

Figure 4.12: Number of particles (red), mean (blue) and variance (black) of the particle size distribution from solving the fully coupled problem (4.1.5)-(4.1.6) numerically with $a = 0.2$ and $C_{\text{sat}} = 0.1$, and other parameters from Table 4.1.

approach a constant value for large time, meaning that particles will eventually stop forming and growing, and therefore the particle density function will not change anymore. Whereas M_0 and σ^2 are monotonically increasing, the mean increases up to a maximum value and then it will decrease before reaching the equilibrium value. This is due to a large amount of very small particles forming at later times which will be clearer from plotting the particle size distribution.

Now, we use the above numerical results for the concentration of SiO_2 and temperature in the analytical solution obtained for n in Section 4.2, as we did with the decoupled case. The peak in the particle density function, n, plotted in Figure 4.13a, moves to the right with time as particles grow as in Figure 4.6, for initial times. However, as the available C_{SiO_2} decreases toward the saturation concentration (around $t = 25$), the value of $n = J/G$ at $s = 1$ gets very large forming a second peak around the smallest particle size. Many particles are created (due to the increasing temperature), but they cannot grow large (due to the limited availability of SiO_2). We can also study the formation of this second peak by looking at the form of the nucleation and growth rates for the fully-coupled case as shown in Figure 4.14. We observe a similar behaviour to the decoupled case in that the growth rate starts decreasing before the nucleation rate does, and hence J/G becomes large resulting in a peak. Once more, J vanishes before G does (see zoomed in box) so that the peak height is finite and $n \to 0$ as $t \to \infty$.

The critical time at which the small particle size peak appears can be determined,

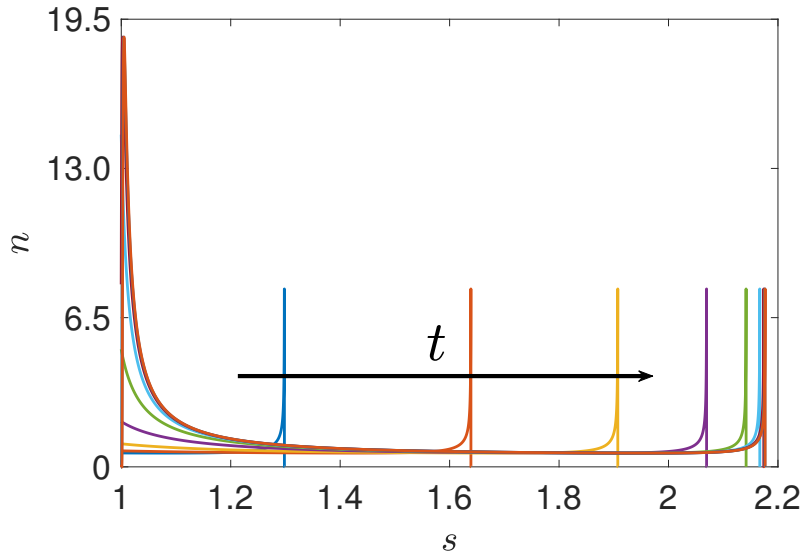

(a)

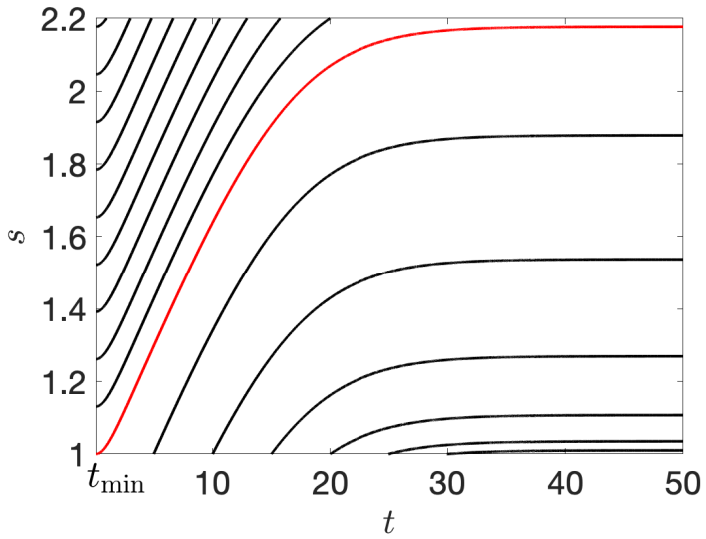

(b)

Figure 4.13: (a) Dimensionless number density function and (b) characteristic curves from solving numerically the fully coupled system (4.1.5)-(4.1.6) and using these reults in (4.2.5)-(4.2.6). We take $C_{\text{sat}} = 0.1$ and $a = 0.2$, with other parameters chosen from Table 4.1. The direction of the arrow in (a) indicates increasing time from $t = 5$ to $t = 45$, with an increment of 5 at every iteration.

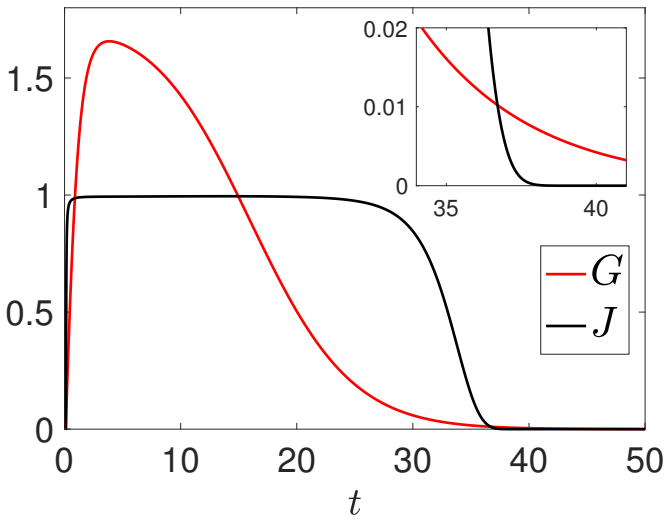

Figure 4.14: Dimensionless growth (G) and nucleation (J) rates as defined in (4.1.8) and (4.1.9), respectively, and where we have taken C_{SiO_2} and T from the numerical results for the fully-coupled problem obtained in Section 4.4.

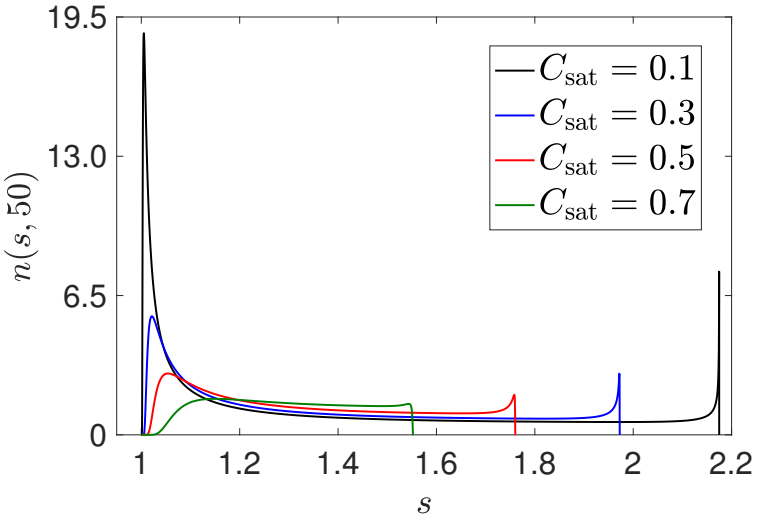

Figure 4.15: Dimensionless number density function of particles at time $t = 50$ for different values of the saturation concentration C_{sat} between 0.1 and 0.7, $a = 0.2$ and other parameters taking values from Table 4.1.

for instance, by looking at the value where the mean of the distribution in Figure 4.12 starts decreasing, that is, approximately $t = 20$. We can also determine this by looking at the characteristic curves for the fully-coupled problem as given in Figure 4.13b. This time, particle growth stops after some critical time and the slope of the characteristic curves, given by $G^*G(t)$, becomes zero. Thus, the maximum particle size is given by the value that the red characteristic approaches, approximately 2.2 for the case plotted.

The final number density function ($t = 50$), which can be seen in black in Figure 4.15, corresponds to a bimodal distribution around the minimum and maximum particle size. The existence of such a bimodal distribution for particle size is in agreement with previous experimental studies [20] where the particle size distribution of well-dispersed microsilica from localised areas was found to be bimodal, with a submicron range of particle sizes containing most of the particle mass, and a micron range with fewer but much larger particles. As in the previous section, in Figure 4.15 we explore how the number density function changes when we vary the value of the parameter C_{sat}. As before, we will have fewer and smaller particles for larger values of C_{sat} since they have less time to grow before the SiO_2 is consumed.

Now we do a similar analysis of the shape of the peaks to the one in Section 4.3.4.2, and we plot both peaks (for the smallest and largest particle size) on a semi-log plot in Figure 4.16. Notice that the order of the peaks in Figure 4.16 is the opposite to the one found in Figure 4.13a, and that the values on the horizontal axis of Figure 4.16b are inverted. We use the same formulae as in Section 4.3.4.2 to obtain an approximation for the large particle-size peak (red dashed line) and uniform distribution between peaks (blue dashed line). However, in the coupled case these approximations are only valid for early times, and the late time peak shown in Figure 4.16b (around $s = 1$) is only found numerically.

Finally, we remark that in the majority of this chapter and in the rest of this thesis we have chosen $D_s = 0$ since the exact form of this term is not fully understood and since it is generally introduced for stability of numerical solutions of the PBE (4.1.10a). Even though in this work this term is not really needed since we can solve the PDE for n analytically, it may be useful when adding extra physical effects into the particle formation and growth problem. However, solving the fully-coupled system numerically when $D_s > 0$ is computationally expensive since we would need to simultaneously solve 9 ODEs coupled with a PDE (notice the dependence of (2.4.1d), (2.4.1i), and (2.4.1j)-(2.4.1l) on n). Moreover, when D_s is large enough, fluctuations lead to smooth bell-shaped particle size distributions, on the other hand, for small values of D_s the

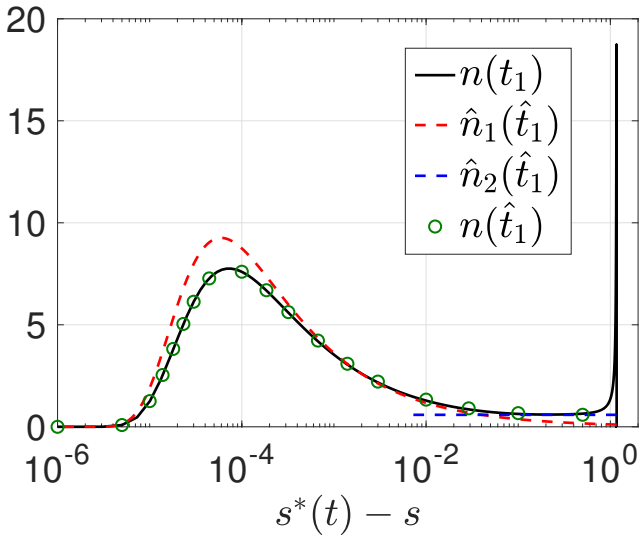

(a) Semi-log plot for n around s^*

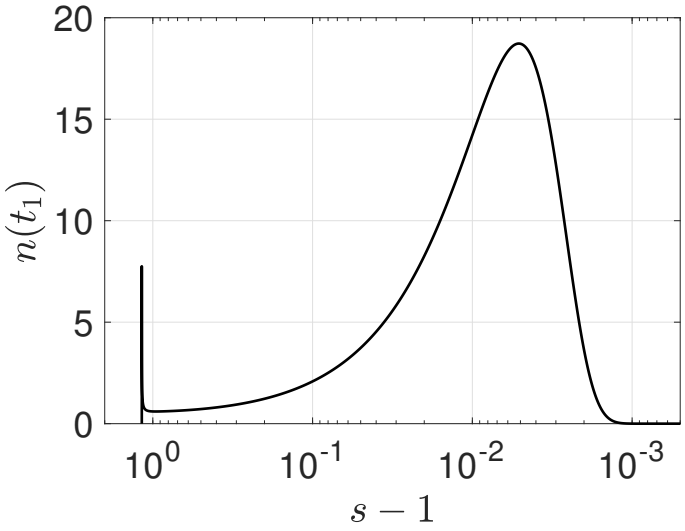

(b) Semi-log plot for n around 1

Figure 4.16: Semi-log plots for the number density function around (a) $s = s^*$ zooming in the large particle-size peak, and around (b) $s = 1$ zooming in the small particle-size peak. In (a) we show, as in the decoupled case, the numerical results for n (black solid line), the solution for n near the peak with approximated characteristics (4.3.23) (green circles), and the approximations for the peak (red dashed line) and uniform part (blue dashed line) taken from (4.3.28) and (4.3.35) respectively, whereas in (b) we only show the numerical result for n. Here, we take $a = 0.2$ and $C_{\text{sat}} = 0.1$, and other parameters as in Table 4.1.

peaks in the distributions remain high and narrow, similar to when $D_s = 0$, and they become difficult to resolve numerically. For the latter, a moving mesh with higher refinement around the position of the peak may be considered.

4.5 Discussion

Motivated by the dynamics of the chemicals and temperature within the reaction zone, which is the region where particles form, we reduced the model in Chapter 2 by making several simplifying assumptions. The main one was to consider all of the chemicals to be well-mixed initially with uniform initial concentrations and temperature. With this, there is no spatial dependence in the system and only time dependence. Diffusion plays no role, and the dynamics modelled are most valid on a small lengthscale within the reaction zone. Other assumptions considered in this chapter include taking the velocity of the fluid to be zero everywhere and neglecting the effects of compressibility.

In the case where the mass and energy equations inform the particle growth equation, but not the other way around ($\zeta_1 = \zeta_2 = 0$), we obtained approximate solutions for small a, that is for an oxygen-rich environment (which is the physically relevant limit), and these compared favourably with numerical simulations. The SiO reaction occurs much faster than the CO reaction, and if enough oxygen is available, all of the initial SiO will be consumed; hence, the same number of moles of SiO_2 will be produced. As the sink term in the mass conservation was neglected, particles continued to grow, since the particle mass was negligible compared to the total mass of SiO_2 remaining. However, when the particle growth process was coupled back to the mass and energy conservation ($\zeta_1, \zeta_2 > 0$ in which case only numerical simulations were possible), we observed that the number and size of particles formed was limited, with particle growth ending once the mass of SiO_2 was depleted. Therefore, the approximations obtained for $\zeta_1 = \zeta_2 = 0$ and $a \ll 1$ are most useful either for understanding early-time dynamics (before SiO_2 is depleted due to particle formation and growth), or for certain furnace operation strategies where O_2 is plentiful, and the rate of depletion of SiO_2 is small (*i.e.*, when the reaction R_1 in (1.1.4) produces a sufficiently large quantity of SiO_2 so that it is not depleted rapidly by the sink term (2.3.40)). The sink term (2.3.40) therefore sets the timescale for the fully coupled system.

In addition, we find that increasing the saturation or equilibrium concentration of SiO_2 (for instance, by decreasing the temperature of the system) will result in a decrease in mean particle size, although this parameter depends on other environmental

factors, and may be more challenging to control in practical applications. We also conclude that the inclusion of fluctuations on the velocity of particle growth smoothes the peaks in the particle size distribution and results in larger particles being produced, but this case was only explored for the decoupled problem.

Our results suggest that certain model parameters such as the concentration of other chemicals with respect to oxygen, a, or the saturation concentration, C_{sat}, can be used to control microsilica production. For instance, the larger a is, the slower the reactions are, and if a is sufficiently large, not all of the SiO will be consumed by the reaction, thus less SiO_2 will be produced. This will affect the number and size of the particles since there is less SiO_2 available.

Chapter 5

Initially spatially separated chemical species

In this chapter, we extend the work done in Chapter 4 by considering a similar model but with a different initial configuration for the chemicals and temperature. Initially, instead of uniform distributions, we have two non-reacting zones separated by a flame front or reaction zone which evolves spatially over time. The flame front is the region that separates the fuel (SiO and CO) from the oxidizer (O_2). More precisely, it is the area where they both mix and the combustion reaction takes place, thus releasing chemical energy in the form of heat, provided the temperatures are large enough to permit reactions. In this region, SiO_2 is created and thus particles form. We consider a simplified, one-dimensional geometry for our model given by a cross section of the reaction zone or flame front, that is $z \in (-\infty, \infty)$. Here, C_{O_2} is initially at maximal concentration as $z \to \infty$, whereas C_{SiO} and C_{CO} are initially at maximal concentration as $z \to -\infty$ (see Figure 5.1 for a schematic diagram).

We greatly simplify the flow problem by taking the velocity of the fluid to be zero everywhere without loss of generality as in Chapter 4. This assumption is valid to study regions local to a reaction zone where microsilica particles are produced, whereas in the following chapter we will consider more realistic fluid mechanics and configurations within the furnace hood. Once again, we assume no density variations in the fluid and set $D_s = 0$ so that there are no fluctuations in the growth rate of particles. Part of the work developed in this chapter, as well as in Chapters 2 and 4, can be found in [29].

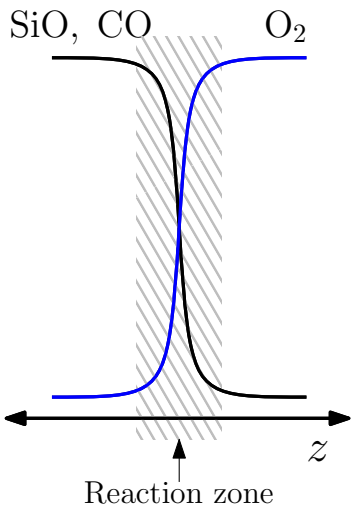

Figure 5.1: Initially separated chemical species. The reaction zone is the region where both the fuel (SiO, CO) and oxidizer (O_2) are present and the conditions are favourable for the reactions 2.2.1 to take place.

5.1 Non-dimensional model

We non-dimensionalise the equations (2.4.1i), (2.4.1b)-(2.4.1l), and (2.4.3) under the previous assumptions by using the same dimensionless scalings as in Section 4.1. Additionally, the spatial scale is taken with the dominant diffusion D_{O_2}, namely

$$z = \sqrt{D_{O_2} t_0}\tilde{z} = \sqrt{\frac{D_{O_2}}{2A_1 C_{O_2,0}}} \exp\left(\frac{E_1}{2RT_1}\right)\tilde{z}. \tag{5.1.1}$$

With these scalings and dropping the over tilde notation, the dimensionless equations read

$$\frac{\partial C_{O_2}}{\partial t} - \frac{\partial^2 C_{O_2}}{\partial z^2} = -\frac{a}{2}\left(f_1(T) C_{O_2} C_{SiO} + \varepsilon f_2(T) C_{O_2} C_{CO}\right), \tag{5.1.2a}$$

$$\frac{\partial C_{SiO}}{\partial t} - d_{SiO}\frac{\partial^2 C_{SiO}}{\partial z^2} = -f_1(T) C_{O_2} C_{SiO}, \tag{5.1.2b}$$

$$\frac{\partial C_{SiO_2}}{\partial t} - d_{SiO_2}\frac{\partial^2 C_{SiO_2}}{\partial z^2} = f_1(T) C_{O_2} C_{SiO} - \zeta_1 G M_2, \tag{5.1.2c}$$

$$\frac{\partial C_{CO}}{\partial t} - d_{CO}\frac{\partial^2 C_{CO}}{\partial z^2} = -\varepsilon f_2(T) C_{O_2} C_{CO}, \tag{5.1.2d}$$

$$\frac{\partial C_{CO_2}}{\partial t} - d_{CO_2}\frac{\partial^2 C_{CO_2}}{\partial z^2} = \varepsilon f_2(T) C_{O_2} C_{CO}, \tag{5.1.2e}$$

$$\frac{\partial T}{\partial t} - \mathrm{Le}\frac{\partial^2 T}{\partial z^2} = h_1 f_1(T) C_{\mathrm{O}_2} C_{\mathrm{SiO}} + \varepsilon h_2 f_2(T) C_{\mathrm{O}_2} C_{\mathrm{CO}} + \zeta_2 G M_2, \quad (5.1.2\mathrm{f})$$

$$\frac{\partial M_0}{\partial t} - d_p \frac{\partial^2 M_0}{\partial z^2} = G^* J, \quad (5.1.2\mathrm{g})$$

$$\frac{\partial M_1}{\partial t} - d_p \frac{\partial^2 M_1}{\partial z^2} = G^* J + G^* G M_0, \quad (5.1.2\mathrm{h})$$

$$\frac{\partial M_2}{\partial t} - d_p \frac{\partial^2 M_2}{\partial z^2} = G^* J + 2 G^* G M_1, \quad (5.1.2\mathrm{i})$$

for $-\infty < z < \infty$, $t > 0$. The coefficients in front of the second order derivatives above represent the ratio between the diffusion coefficient of the variable and the oxygen diffusivity, as given in Table 5.1. The rest of the dimensionless parameters are the same as in the well-mixed limit studied in Chapter 4. The Arrhenius terms (f_1 and f_2), and the growth (G) and nucleation (J) rates are given by (4.1.7), (4.1.8) and (4.1.9), respectively, and note that they all now depend on space as well as time.

In the configuration studied in this chapter, C_{O_2} is present primarily in the region $z > 0$, C_{SiO} and C_{CO} in the region $z < 0$, with a small overlap. This is analogous to adding large quantities of oxygen into the top or side of a furnace in more complicated geometries. Hence, the dimensionless far-field conditions are the following:

$$C_{\mathrm{O}_2} = C_{\mathrm{SiO}_2} = C_{\mathrm{CO}_2} = 0, \quad C_{\mathrm{SiO}} = C_{\mathrm{CO}} = T = 1 \qquad \text{as} \quad z \to -\infty, \quad (5.1.3\mathrm{a})$$

$$C_{\mathrm{O}_2} = 1, \quad C_{\mathrm{SiO}} = C_{\mathrm{CO}} = T = 0, \quad \frac{\partial C_{\mathrm{SiO}_2}}{\partial z} = \frac{\partial C_{\mathrm{CO}_2}}{\partial z} = 0 \qquad \text{as} \quad z \to \infty. \quad (5.1.3\mathrm{b})$$

Since SiO_2 and CO_2 are produced within the reaction zone in the middle of the domain, we do not know the exact value that their concentrations will take as $z \to \infty$. Therefore, we have considered the diffusive fluxes of both species to tend to zero. Later in the chapter, we will see that the concentrations of the reaction products end up being zero as $z \to \pm\infty$, so the prescribed conditions are satisfied.

The dimensionless initial conditions are given by

$$C_X = \frac{C_{X,i}(z)}{C_{X,0}}, \quad T = \frac{T_i(z) - T_2}{T_1 - T_2}, \quad M_0 = M_1 = M_2 = 0 \quad \text{at} \quad t = 0, \quad (5.1.4)$$

and they are compatible with the boundary conditions (5.1.3). That is, we have that the behaviour of all variables as $z \to \pm\infty$ also holds at $t = 0$.

Finally, the particle formation and growth problem in non-dimensional form reads

$$\frac{\partial n}{\partial t} - d_p \frac{\partial^2 n}{\partial z^2} + G^* G(z,t) \frac{\partial n}{\partial s} = 0 \quad (5.1.5\mathrm{a})$$

for $-\infty < z < \infty$, $s > 1$, $t > 0$, with dimensionless initial and boundary conditions

$$n = 0 \qquad \text{at} \quad t = 0, \tag{5.1.5b}$$

$$G(z,t)n = J(z,t) \qquad \text{at} \quad s = 1. \tag{5.1.5c}$$

Estimated values of the newly introduced dimensionless parameters can be found in Table 5.1, while the rest were defined in the preceding chapter and can be found in Table 4.1. The smallest of the parameters is the ratio between the particle-phase diffusivity and the oxygen diffusivity, $d_p \approx 10^{-5}$, which will be therefore neglected in further sections. With respect to the chemicals diffusivity coefficients, d_X, we find order one coefficients for SiO and SiO_2 meaning that they diffuse at a similar speed to the oxygen, whereas CO and CO_2 diffuse slower compared to oxygen and their coefficients are of order 10^{-2}. Additionally, the Lewis number, $\mathrm{Le} \approx 10^{-1}$, compares the thermal diffusivity to the oxygen diffusivity. In summary, in the model presented in this section we have a total of 18 dimensionless groups, taken from both Tables 4.1 and 5.1.

5.2 Analytical solution of the particle density equation

Since the parameter $d_p \approx 10^{-5}$ found in equation (5.1.5a), which represents molecular diffusion, is negligible relative to the chemical and thermal diffusivities, the resulting PDE is equivalent to (4.1.10a). Therefore, the analytical solution is similar to the one found for the case of initially well-mixed chemical species, but with an additional z dependence arising from the spatial variations in C_{SiO_2} and T. Taking $C_{SiO_2}(z, t_{\min}(z)) = C_{\mathrm{sat}}$, we find that the solution for the particle density is given implicitly by

$$n = \frac{J(z,t_1)}{G(z,t_1)} \quad \text{with} \quad s = 1 + G^* \int_{t_1}^{t} G(z,\tau)\mathrm{d}\tau, \quad t_1 > t_{\min}(z), \tag{5.2.1}$$

for $t > t_{\min}(z)$. The solution is $n = 0$ for $t \leq t_{\min}(z)$. Notice that in this case we need to be careful with the domain of definition of the solution since the value of $t_{\min}$ varies with z. The dependence of J and G on C_{SiO_2} and T is given in (4.1.9) and (4.1.8) respectively.

Dimensionless parameter	Relation with dimensional parameters	Typical value
d_{SiO}	$\frac{D_{\mathrm{SiO}}}{D_{\mathrm{O_2}}}$	0.8298
$d_{\mathrm{SiO_2}}$	$\frac{D_{\mathrm{SiO_2}}}{D_{\mathrm{O_2}}}$	0.8298
d_{CO}	$\frac{D_{\mathrm{CO}}}{D_{\mathrm{O_2}}}$	3.829×10^{-2}
$d_{\mathrm{CO_2}}$	$\frac{D_{\mathrm{CO_2}}}{D_{\mathrm{O_2}}}$	3.040×10^{-2}
Le	$\frac{k}{\rho_0 c_p D_{\mathrm{O_2}}}$	0.3470
d_p	$\frac{D_p}{D_{\mathrm{O_2}}}$	$< 1.106 \times 10^{-5}$

Table 5.1: Definitions and typical values for non-dimensional parameters used in the model derived for the initially spatially separated chemicals configuration. The parameters are determined from values in Tables 2.2 and 2.3.

5.3 Analytical solution for a coupled chemical - temperature subsystem

The set of equations (5.1.2) constitute a nonlinear, nonlocal reaction-diffusion system. To make any progress outside of numerical simulations, we shall need to make further simplifying assumptions. Firstly, we neglect the coupling to the moments, and set ζ_1 and ζ_2 to be equal to zero as in Section 4.3. We will include these coupling parameters later when obtaining numerical simulations and compare them to the asymptotic solutions. Further, since $\varepsilon < \zeta_1$ by an order of magnitude, we set $\varepsilon = 0$ and neglect the slower reaction. Finally, observing that d_{SiO} and Le are of order one, we set $d_{\mathrm{SiO}} = \mathrm{Le} = 1$ to have equal diffusion rates, which greatly simplifies the solution. Under these assumptions, the equations governing the dominant reaction are

$$\frac{\partial C_{\mathrm{O_2}}}{\partial t} - \frac{\partial^2 C_{\mathrm{O_2}}}{\partial z^2} = -\frac{a}{2} f_1(T) C_{\mathrm{O_2}} C_{\mathrm{SiO}}, \tag{5.3.1a}$$

$$\frac{\partial C_{\mathrm{SiO}}}{\partial t} - \frac{\partial^2 C_{\mathrm{SiO}}}{\partial z^2} = -f_1(T) C_{\mathrm{O_2}} C_{\mathrm{SiO}}, \tag{5.3.1b}$$

$$\frac{\partial T}{\partial t} - \frac{\partial^2 T}{\partial z^2} = h_1 f_1(T) C_{\mathrm{O_2}} C_{\mathrm{SiO}}, \tag{5.3.1c}$$

subject to the initial conditions

$$C_{\mathrm{O}_2}(0,z) = \mathcal{H}(z), \tag{5.3.1d}$$
$$C_{\mathrm{SiO}}(0,z) = \mathcal{H}(-z), \tag{5.3.1e}$$
$$T(0,z) = \mathcal{H}(-z), \tag{5.3.1f}$$

which are consistent with the far-field conditions (5.1.3).

Defining the quantities

$$w_1(z,t) = C_{\mathrm{O}_2} - \frac{a}{2}C_{\mathrm{SiO}}, \tag{5.3.2a}$$
$$w_2(z,t) = T + h_1 C_{\mathrm{SiO}}, \tag{5.3.2b}$$

we find from equations (5.3.1) that our problem becomes the following decoupled system,

$$\frac{\partial w_1}{\partial t} - \frac{\partial^2 w_1}{\partial z^2} = 0, \tag{5.3.3a}$$
$$\frac{\partial w_2}{\partial t} - \frac{\partial^2 w_2}{\partial z^2} = 0, \tag{5.3.3b}$$

with conditions

$$w_1 \to -\frac{a}{2}, \quad w_2 \to 1 + h_1 \quad \text{as} \quad z \to -\infty, \tag{5.3.3c}$$
$$w_1 \to 1, \quad w_2 \to 0 \quad \text{as} \quad z \to \infty. \tag{5.3.3d}$$

Solving (5.3.3) with appropriate Heaviside functions centred at $z = 0$ as initial data, we find the solutions

$$w_1(z,t) = \frac{1+\mathrm{erf}(\eta)}{2} - \frac{a(1-\mathrm{erf}(\eta))}{4} = \phi(\eta) - \frac{a}{2}\phi(-\eta), \tag{5.3.4a}$$
$$w_2(z,t) = (1+h_1)\frac{1-\mathrm{erf}(\eta)}{2} = (1+h_1)\phi(-\eta), \tag{5.3.4b}$$

where

$$\phi(\eta) = \frac{1}{2}\big(1+\mathrm{erf}(\eta)\big), \tag{5.3.5}$$

and

$$\eta(z,t) = \frac{z}{2\sqrt{t}} \tag{5.3.6}$$

is the similarity variable.

From the definitions of w_1 and w_2 (5.3.2), we determine that

$$C_{O_2} = \phi(\eta) - \frac{a}{2}\left(\phi(-\eta) - C_{SiO}\right), \tag{5.3.7a}$$

$$T = \phi(-\eta) + h_1\left(\phi(-\eta) - C_{SiO}\right). \tag{5.3.7b}$$

We now search for a solution for the SiO concentration. Using (5.3.7) into (5.3.1b), the equation for C_{SiO} decouples from the rest and reads

$$\begin{aligned}\frac{\partial C_{SiO}}{\partial t} - \frac{\partial^2 C_{SiO}}{\partial z^2} = &-f_1\big(\phi(-\eta) + h_1\left(\phi(-\eta) - C_{SiO}\right)\big) \\ &\times \left(\phi(\eta) - \frac{a}{2}\left(\phi(-\eta) - C_{SiO}\right)\right) C_{SiO},\end{aligned} \tag{5.3.8}$$

where η is given as in (5.3.6).

5.3.1 The small t limit

To look for a solution of (5.3.8) in the small-time limit $t \to 0^+$, we first introduce the rescaling of variables

$$t = \epsilon^2 \tilde{t}, \qquad z = \epsilon \tilde{z}, \tag{5.3.9}$$

with $\epsilon \ll 1$. This rescaling puts (5.3.8) into the form

$$\begin{aligned}\frac{\partial C_{SiO}}{\partial \tilde{t}} - \frac{\partial^2 C_{SiO}}{\partial \tilde{z}^2} = &-\epsilon^2 f_1\big(\phi(-\eta) + h_1\left(\phi(-\eta) - C_{SiO}\right)\big) \\ &\times \left(\phi(\eta) - \frac{a}{2}\left(\phi(-\eta) - C_{SiO}\right)\right) C_{SiO}.\end{aligned} \tag{5.3.10}$$

Expanding C_{SiO} in powers of ϵ^2 as

$$C_{SiO} = C_{SiO}^{(0)} + \epsilon^2 C_{SiO}^{(2)} + \mathcal{O}(\epsilon^4), \tag{5.3.11}$$

the leading order problem is diffusion dominated and is given by

$$\frac{\partial C_{SiO}^{(0)}}{\partial \tilde{t}} - \frac{\partial^2 C_{SiO}^{(0)}}{\partial \tilde{z}^2} = 0, \qquad C_{SiO}^{(0)}(0,\tilde{z}) = \mathcal{H}(-\tilde{z}). \tag{5.3.12}$$

To solve problem (5.3.12) we look for a similarity solution of the form $C_{\mathrm{SiO}}^{(0)} = u(\eta)$, where η is given as in (5.3.6). Hence, (5.3.12) becomes the following ODE and far-field conditions

$$\frac{\mathrm{d}^2u}{\mathrm{d}\eta^2}+2\eta\frac{\mathrm{d}u}{\mathrm{d}\eta} = 0, \tag{5.3.13a}$$

$$u \to 0 \quad \text{as} \quad \eta \to \infty, \tag{5.3.13b}$$

$$u \to 1 \quad \text{as} \quad \eta \to -\infty, \tag{5.3.13c}$$

with solution

$$u = \phi(-\eta). \tag{5.3.14}$$

Using the solution obtained for the leading order problem, the second order problem can be written as

$$\frac{\partial C_{\mathrm{SiO}}^{(2)}}{\partial \tilde{t}} - \frac{\partial^2 C_{\mathrm{SiO}}^{(2)}}{\partial \tilde{z}^2} = -f_1\big(\phi(-\eta)\big)\phi(\eta)\phi(-\eta), \quad C_{\mathrm{SiO}}^{(2)}(0,\tilde{z}) = 0, \tag{5.3.15}$$

with general solution

$$C_{\mathrm{SiO}}^{(2)}(\tilde{z},\tilde{t}) = \int_0^{\tilde{t}}\int_{-\infty}^{\infty} \frac{-f_1\big(\phi(-\eta(r,s))\big)\phi(\eta(r,s))\phi(-\eta(r,s))}{2\sqrt{\pi(\tilde{t}-s)}} \exp\left(\frac{-(\tilde{z}-r)^2}{4(\tilde{t}-s)}\right) \mathrm{d}r\mathrm{d}s. \tag{5.3.16}$$

However, we find that the leading order approximation for the small t limit is good enough, and hence using (5.3.7) we find the following approximate solutions of the system in terms of the original variables,

$$C_{\mathrm{SiO}}(z,t) = \phi\left(-\frac{z}{2\sqrt{t}}\right) + \mathcal{O}(\epsilon^2), \tag{5.3.17a}$$

$$C_{\mathrm{O}_2}(z,t) = \phi\left(\frac{z}{2\sqrt{t}}\right) + \mathcal{O}(\epsilon^2), \tag{5.3.17b}$$

$$T(z,t) = \phi\left(-\frac{z}{2\sqrt{t}}\right) + \mathcal{O}(\epsilon^2), \tag{5.3.17c}$$

as $t \to 0^+$. Thus the heat and mass transfer mechanism in the small time limit is diffusion away from the initial conditions.

We solve the initial-boundary value problem (5.3.1) numerically by the method of lines, discretising the PDEs in space and integrating the resulting ODEs in time. We use appropriate Heaviside functions centred at the origin, as given in (5.3.1d)-(5.3.1f), as initial data when numerically solving the discretised system. In Figure 5.2, we show

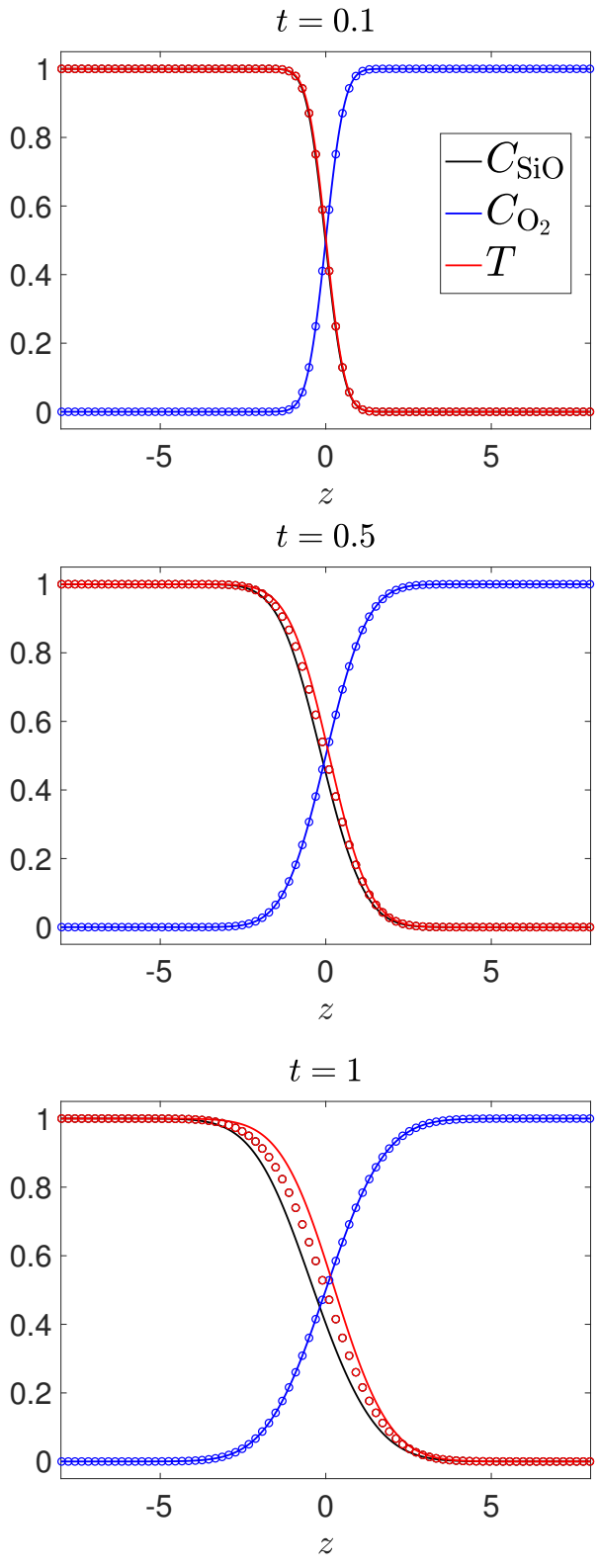

Figure 5.2: Plot of the approximate asymptotic solution for small t (5.3.17) (circles) and numerical solution (solid lines) for SiO (black) and O_2 (blue) concentrations, and temperature (red) from solving problem (5.3.1). We have taken $a = 0$ for consistency with Section 5.3.2 and the rest of parameter values are taken from Table 4.1.

the numerical results (solid lines) and compare them to the small-time asymptotic approximation (circles) given in (5.3.17) for three different times: $t = 0.1, 0.5, 1$. The approximation becomes worse as time increases and the solution stops being purely diffusive.

5.3.2 The large t limit

To study the behaviour of the system in the long time limit $t \to \infty$ we take a different scaling of variables to the previous section, namely

$$t = \frac{1}{\epsilon^2}\tilde{t}, \qquad z = \frac{1}{\epsilon}\tilde{z}, \tag{5.3.18}$$

for $\epsilon \ll 1$, which puts (5.3.8) into the form

$$\begin{aligned}\epsilon^2\left(\frac{\partial C_{\mathrm{SiO}}}{\partial \tilde{t}} - \frac{\partial^2 C_{\mathrm{SiO}}}{\partial \tilde{z}^2}\right) = -f_1\big(\phi(-\eta) + h_1\left(\phi(-\eta) - C_{\mathrm{SiO}}\right)\big) \\ \times\left(\phi(\eta) - \frac{a}{2}\left(\phi(-\eta) - C_{\mathrm{SiO}}\right)\right) C_{\mathrm{SiO}}.\end{aligned} \tag{5.3.19}$$

Therefore, in the long time limit, we must resolve a moving front which corresponds to the reaction zone. Motivated in part by the application of similar approaches to other reaction-diffusion systems in the literature [7, 17, 18, 34], we consider a WKB approximation in order to resolve the sharp front. We take the ansatz

$$C_{\mathrm{SiO}}(\tilde{z}, \tilde{t}) = \exp\left(-v(\tilde{z}, \tilde{t})\right), \tag{5.3.20}$$

with $v(\tilde{z}, \tilde{t}) = \mathcal{O}(\epsilon^{-\beta})$ for some $\beta > 0$ to be determined. As the phase term v grows, localized rapid decay of the exponential results in a moving front. Using the WKB ansatz in equation (5.3.19), and neglecting the small parameter a in the reaction term (as we did in Section 4.3.3), equation (5.3.19) becomes

$$\epsilon^2\left(\frac{\partial v}{\partial \tilde{t}} - \frac{\partial^2 v}{\partial \tilde{z}^2} + \left(\frac{\partial v}{\partial \tilde{z}}\right)^2\right) = f_1\big((1 + h_1)\phi(-\eta)\big)\phi(\eta) + \mathcal{R}, \tag{5.3.21}$$

where the error term,

$$\mathcal{R} = \left[f_1\left((1 + h_1)\phi(-\eta) - h_1 C_{\mathrm{SiO}}\right) - f_1\left((1 + h_1)\phi(-\eta)\right)\right]\phi(\eta), \tag{5.3.22}$$

results from omitting the explicit dependence of C_{SiO} in the argument of the f_1 term given in (5.3.8). We expand v as

$$v(\tilde{z},\tilde{t}) = \epsilon^{-\beta}\sum_{\ell=0}^{\infty}\epsilon^{\beta\ell}V_\ell(\tilde{z},\tilde{t}) \quad \text{as} \quad \epsilon \to 0, \tag{5.3.23}$$

and placing this into (5.3.21), we obtain the dominant balances which determine β: the time derivative term is $\mathcal{O}(\epsilon^{2-\beta})$, the dominant diffusion term is $\mathcal{O}(\epsilon^{2-2\beta})$, and the reaction term is $\mathcal{O}(\epsilon^0)$. Of the three possibilities, only the balance between the dominant diffusion term and the reaction kinetics is consistent with our assumptions and gives a value of $\beta > 0$. Taking the resulting $\beta = 1$ and placing (5.3.23) into (5.3.21), we find

$$\left(\frac{\partial V_0}{\partial \tilde{z}}\right)^2 + \epsilon\left(\frac{\partial V_0}{\partial \tilde{t}} - \frac{\partial^2 V_0}{\partial \tilde{z}^2} + 2\frac{\partial V_0}{\partial \tilde{z}}\frac{\partial V_1}{\partial \tilde{z}}\right) + \mathcal{O}(\epsilon^2) = f_1\left((1+h_1)\phi(-\eta)\right)\phi(\eta) + \mathcal{R}. \tag{5.3.24}$$

Within the reaction zone, that is, the region where $C_{\mathrm{SiO}}, C_{\mathrm{O}_2}, T > 0$ so that $R_1 > 0$, we have that $C_{\mathrm{SiO}} = \mathcal{O}(e^{-1/\epsilon})$ and $\eta = \mathcal{O}(1)$. Since f_1 in (4.1.7) is positive and bounded with bounded derivative, there exists an $\mathcal{O}(1)$ constant $R_0 > 0$ such that

$$|\mathcal{R}| = |h_1 f_1' C_{\mathrm{SiO}}\phi(\eta)| < R_0\phi(\eta)C_{\mathrm{SiO}} = \mathcal{O}(e^{-1/\epsilon}), \tag{5.3.25}$$

and hence $\mathcal{R}$ is exponentially small within the reaction zone.

To the left of the reaction zone, $C_{\mathrm{SiO}} = \mathcal{O}(1)$ by looking at the far-field condition, and $\eta \gg 1$. In this region, we find the upper bound $\phi(\eta) < e^{-\eta^2}$, while $0 \le C_{\mathrm{SiO}} \le \phi(-\eta) \le 1$. Hence,

$$|\mathcal{R}| < [f_1(1+h_1) - f_1(0)]e^{-\eta^2} = \mathcal{O}(e^{-\eta^2}), \tag{5.3.26}$$

and $\mathcal{R}$ is exponentially small in this region as well. Finally, to the right of the reaction zone, $C_{\mathrm{SiO}} = 0$ and so $\mathcal{R}$ is identically zero. As the expansion (5.3.23) is algebraic, the exponentially small term $\mathcal{R}$ is subdominant at each order in the expansion (5.3.23), and can be ignored when solving (5.3.24).

At leading order, $\mathcal{O}(1)$, we see that (5.3.24) gives

$$\left(\frac{\partial V_0}{\partial \tilde{z}}\right)^2 = f_1\left((1+h_1)\phi(-\eta)\right)\phi(\eta). \tag{5.3.27}$$

Solving for V_0 and taking the positive root so that the expansion in the WKB ansatz gives decay rather than blow-up for large time, we find

$$V_0(\tilde{z},\tilde{t}) = 2\tilde{t}^{1/2}\int_{-\infty}^{\eta(\tilde{z},\tilde{t})-\eta_0}\sqrt{f_1\left((1+h_1)\phi(-\sigma)\right)\phi(\sigma)}d\sigma. \tag{5.3.28}$$

Since information about the initial configuration is lost in this long time limit, we have taken $\eta-\eta_0$ as the upper limit of the integral (5.3.28). Exploiting such a shift in the similarity variable can prove useful, and for our purposes, we will use it to calibrate the large-time asymptotics to numerical simulations of the exact solution.

We then have

$$C_{\mathrm{SiO}}(\tilde{z},\tilde{t}) = \exp\left(-\epsilon^{-1}V_0(\tilde{z},\tilde{t})+\mathcal{O}(1)\right) \quad \text{as} \quad t\to\infty. \tag{5.3.29}$$

For large yet finite t, $\lim_{\tilde{z}\to-\infty} C_{\mathrm{SiO}} = 1$ while $\lim_{\tilde{z}\to\infty} C_{\mathrm{SiO}} = 0$, in agreement with the far-field conditions on C_{SiO}, so no additional scaling of C_{SiO} is required at leading order.

Taking the $\mathcal{O}(\epsilon)$ terms from (5.3.24), we find

$$\frac{\partial V_0}{\partial\tilde{t}} - \frac{\partial^2 V_0}{\partial\tilde{z}^2} + 2\frac{\partial V_0}{\partial\tilde{z}}\frac{\partial V_1}{\partial\tilde{z}} = 0. \tag{5.3.30}$$

We require $V_1\to 0$ as $\tilde{z}\to-\infty$ to obey the far-field condition $C_{\mathrm{SiO}}\to 1$ as $\tilde{z}\to-\infty$, and solving (5.3.30) subject to this condition, we have

$$V_1(\tilde{z},\tilde{t}) = \frac{1}{2}\int_{-\infty}^{\tilde{z}}\frac{V_{0,\tilde{z}\tilde{z}}(\sigma,\tilde{t}) - V_{0,\tilde{t}}(\sigma,\tilde{t})}{V_{0,\tilde{z}}(\sigma,\tilde{t})}\partial\sigma. \tag{5.3.31}$$

The first order correction, $V_1(\tilde{z},\tilde{t})$, will slightly correct the core structure near the moving front, but we find agreement with numerical solutions is already good at leading order, and omit higher order terms for sake of brevity.

Having determined the large-time asymptotics for C_{SiO}, we write the solution in terms of the original variables and construct an approximate solution for (5.3.1) making use of (5.3.7)

$$C_{\mathrm{SiO}}(z,t) \sim \exp\left(-2\sqrt{t}\int_{-\infty}^{\frac{z}{2\sqrt{t}}-\eta_0}\sqrt{f_1\left((1+h_1)\phi(-\sigma)\right)\phi(\sigma)}d\sigma\right), \tag{5.3.32a}$$

$$C_{\mathrm{O}_2}(z,t) \sim \phi\left(\frac{z}{2\sqrt{t}}\right), \tag{5.3.32b}$$

$$\begin{aligned} T(z,t) \sim & \phi\left(-\frac{z}{2\sqrt{t}}\right)(1+h_1) \\ & - h_1\exp\left(-2\sqrt{t}\int_{-\infty}^{\frac{z}{2\sqrt{t}}-\eta_0}\sqrt{f_1\left((1+h_1)\phi(-\sigma)\right)\phi(\sigma)}d\sigma\right), \end{aligned} \tag{5.3.32c}$$

as $t \to \infty$. The latter two quantities follow from (5.3.7), and the fact that the temperature depends on both diffusion and on a source which involves the asymptotic solution for C_{SiO}.

We can use the approximation obtained for C_{SiO}, for both limits small and large t, to find an approximate solution for the SiO_2 concentration. Defining the quantity $w_3 = C_{\mathrm{SiO}} + C_{\mathrm{SiO}_2}$ and assuming $d_{\mathrm{SiO}_2} = 1$, we obtain from equations (5.3.1b) and (5.1.2c) with $\zeta_1 = 0$, the following problem,

$$\frac{\partial w_3}{\partial t} - \frac{\partial^2 w_3}{\partial z^2} = 0, \qquad w_3(0,z) = \mathcal{H}(-z). \tag{5.3.33}$$

which is identical to (5.3.12). Hence, we determine that

$$C_{\mathrm{SiO}_2}(z,t) = \phi(-\eta) - C_{\mathrm{SiO}}(z,t). \tag{5.3.34}$$

As there will in general be an offset in the large-time asymptotics as large time expansions neglect initial data, we calibrate the long time asymptotics to the numerical simulations of problem (5.3.1) by choosing η_0 in (5.3.32) to match both the asymptotic solution and the numerics at the unique value of z where $C_{\mathrm{SiO}} = 0.5$ at $t = 2000$, finding $\eta_0 = 0.258$. In Figure 5.3, we compare both the large-time asymptotic solution (dashed lines) given in (5.3.32) and (5.3.34), and the numerical results (solid lines), showing that the agreement between the two solutions remains good as time decreases up to $t = 100$.

We observe the reaction front moving to the left as SiO is being consumed by the combustion reaction with the much more plentiful ($a \ll 1$) oxygen. Due to its relative abundance, the oxygen slowly spreads due to diffusion, with a relatively small proportion of the oxygen reacting with SiO. The temperature behind the reaction

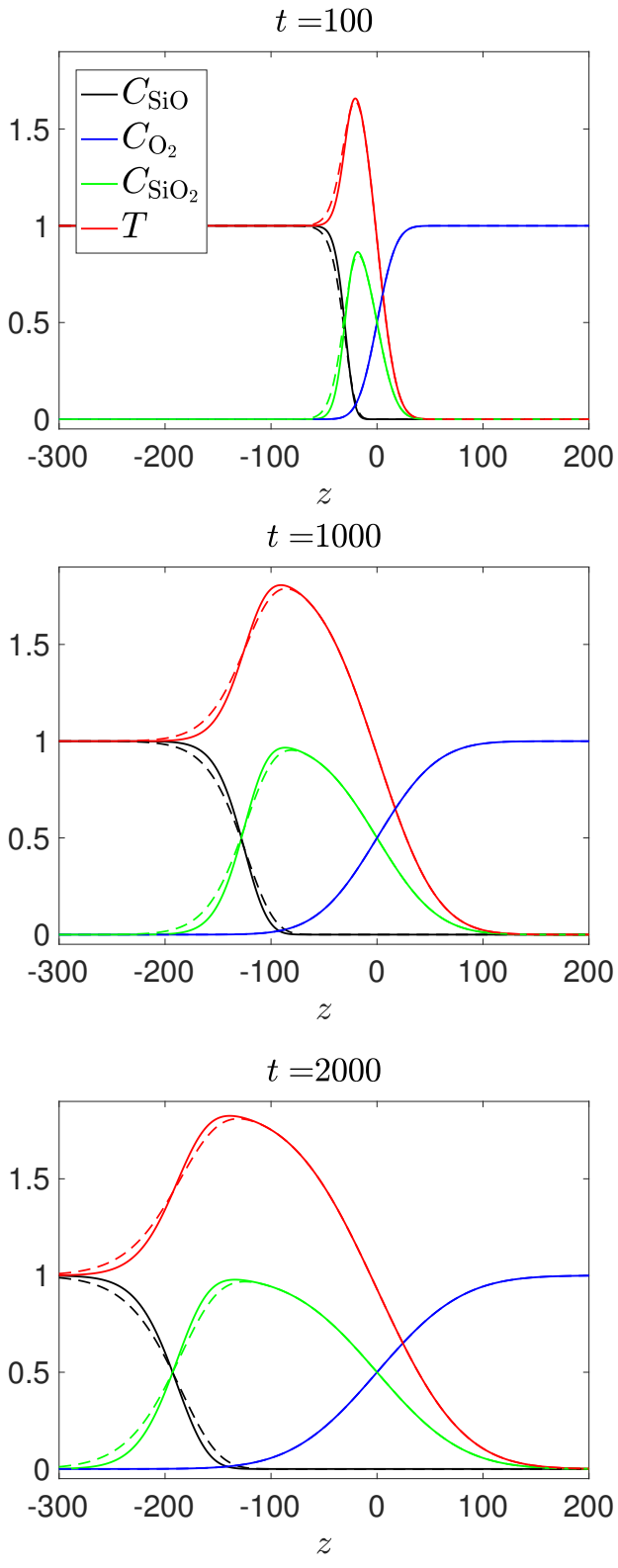

Figure 5.3: Plot of the approximate asymptotic solution (5.3.32) and (5.3.34) (dashed lines) and numerical simulation (solid lines) for SiO (black), O_2 (blue), and SiO_2 (green) concentrations, and temperature (red) from solving problem (5.3.1).

front grows rapidly over time due to the combustion reaction, before levelling off to $T \sim 1 + h_1$ within the core region as the reaction slows. The hot reaction zone broadens as the front moves toward the left, with many of the new reactions between SiO and oxygen occurring near the front. The SiO_2 concentration has a similar profile to the temperature, growing rapidly over time as the SiO is being consumed, and levelling off to $C_{SiO_2} \sim 1$ once the reaction slows down. A similar behaviour for the chemicals and temperature was seen in the COMSOL simulations in Chapter 3 when looking at a cross-section of the reaction layer, with the variables reaching their highest value towards the middle.

The first step in the analysis that we have carried out in Sections 5.3.1 and 5.3.2 was to rescale t and z with some arbitrary small and large parameters, respectively. We remark that to avoid introducing new parameters, we could have written equation (5.3.8) in terms of t and η variables from the outset and then taken the small t and large t limits directly. We have used the latter notation in [29] to perform the same analysis and the solutions obtained are identical.

5.4 Numerical solution of the fully-coupled model

Similarly to Section 4.4 for the well-mixed case, we now solve the full system of equations (5.1.2) numerically for spatially separated initial data given by

$$C_{O_2} = \mathcal{H}(z), \quad C_{SiO} = C_{CO} = T = \mathcal{H}(-z), \quad C_{SiO_2} = C_{CO_2} = M_0 = M_1 = M_2 = 0, \tag{5.4.1}$$

at $t = 0$. We then use these results in the analytical solution for n found in Section 5.2. We follow the same numerical scheme outlined at the end of Section 5.3.2, that is, the method of lines. This method involves discretizing all PDEs in (4.1.5) in space while leaving the time variable continuous, which leads to a large system of ODEs that is then numerically integrated in time.

We plot numerical solutions for C_{SiO_2} and T in Figure 5.4 for both $\zeta_1 = \zeta_2 = 0$ (left) and $\zeta_1, \zeta_2 > 0$ (right), comparing each side-by-side at different values of time. In both cases, there is initially zero concentration of SiO_2, and after a critical time the concentration increases and starts spreading slightly toward the left since it forms from the reaction between O_2 and SiO, moving left with the reaction region as shown in Figure 5.3. In the case of $\zeta_1, \zeta_2 > 0$, where we include a sink of SiO_2 due to the particle formation (Figure 5.4d), the concentration of SiO_2 decreases after time,

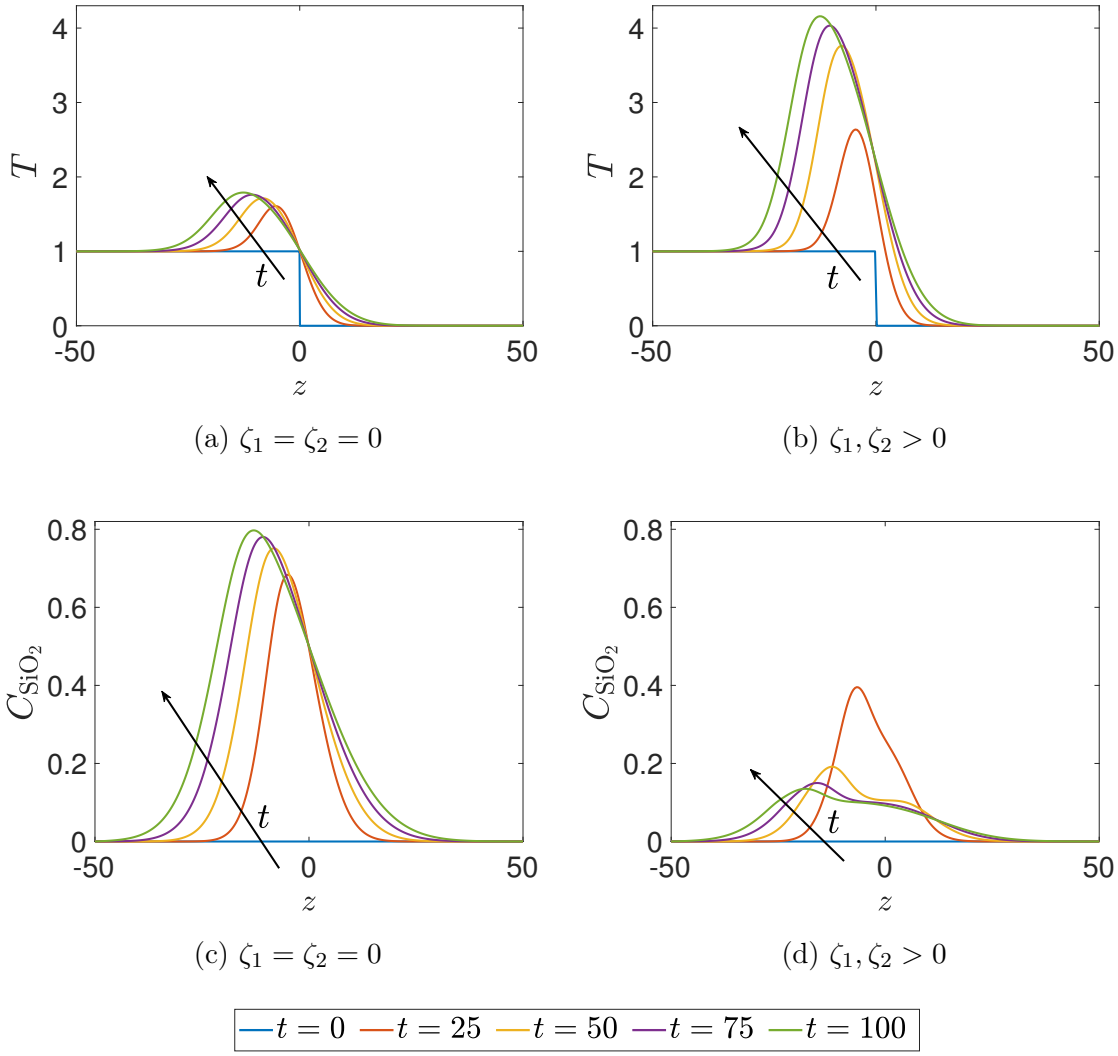

Figure 5.4: (a,b) Temperature and (c,d) concentration of SiO_2 (C_{SiO_2}) variations in z, for different times equally spaced from $t = 0$ to 100 as shown in the legend. This is for the case $\zeta_1 = \zeta_2 = 0$ in (a,c), and $\zeta_1, \zeta_2 > 0$ in (b,d). We choose $a = 0.2$, $C_{sat} = 0.1$, with all other parameters as given in Tables 4.1 and 5.1.

since C_{SiO_2} is used up and rate limiting. In both limits the temperature increases with time, however, when $\zeta_1, \zeta_2 > 0$, heat is released during the particle formation process, and the extent of the temperature increase within the reaction zone is much greater. Therefore, although the asymptotic solutions are reasonable for a qualitative understanding of the dynamics, including the coupling of the particle growth back into the chemical-temperature system ($\zeta_1, \zeta_2 > 0$) is needed for quantitative accuracy, and to determine how fast SiO_2 is used in the formation and growth of particles. One can therefore view the $\zeta_1 = \zeta_2 = 0$ limit as modelling a situation where there is plentiful SiO_2 which is never used up due to a slow rate of particle growth, whereas the case of $\zeta_1, \zeta_2 > 0$ models the situation where SiO_2 is strongly rate limited, and is used up in particle growth more rapidly than it is produced in the reaction zone.

To better understand properties of the particle distribution, n, we use the numerical solution for the chemistry-temperature system in the analytical formula (5.2.1) for n, and plot n over s and z for various time values in Figure 5.5. The largest particles (largest s) are located in the centre of the reaction zone (as they have had more time to grow), whereas smaller, newly formed particles are located near the boundary of the zone. The region with particles ($n > 0$) grows in spatial extent with the reaction zone, and the highest density of particles is at the boundary near the reaction front. In the case where there is coupling of the particle growth back into the chemistry-temperature system, $\zeta_1, \zeta_2 > 0$, we observe a resurgence of small particles being formed over the entire reaction zone, rather than just near the boundary (see lower right panel of Figure 5.5). We hypothesise that this originates from the comparatively high temperatures arising in the fully coupled system, which results in the last of the SiO_2 being used up to rapidly make smaller particles, after which point the process ends as SiO_2 is depleted, with these particles growing no further. Our theoretical results showing a build-up of smaller particles (in addition to the existing larger particles) are in agreement with earlier experimental findings [58].

The mean and variance of the particle distribution are shown in Figure 5.6. The mean size of the particles, as well as their variance, is larger when $\zeta_1, \zeta_2 = 0$, since in this case there is more SiO_2 produced than is used in particle formation. This is also apparent from Figure 5.5. In contrast, when $\zeta_1, \zeta_2 > 0$, the SiO_2 is used in finite time, hence there is less material available for particle growth, and smaller particles result. Panels on the right-hand side of Figure 5.6 are akin to spatial generalizations of the well-mixed case shown in Figure 4.12.

Whereas the heatmaps in Figure 5.5 help to visualise how the different-size particles are distributed across the reaction zone, for practical purposes, we would also like

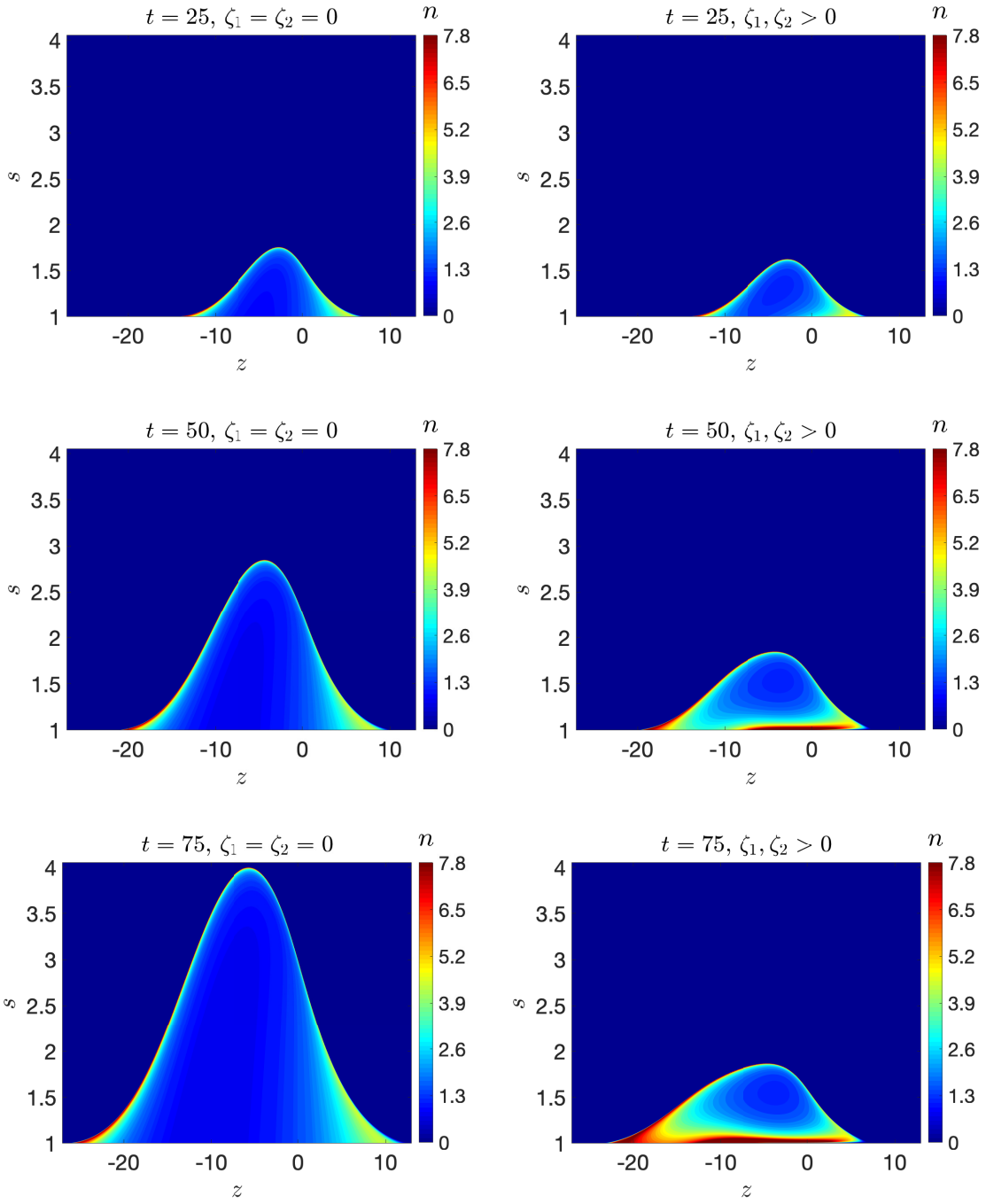

Figure 5.5: Heat maps for n with respect to s and z, for different values of time $t = 25, 50, 75$ from top to bottom. This is for the case $\zeta_1 = \zeta_2 = 0$ (left) and $\zeta_1, \zeta_2 > 0$ (right). We choose $a = 0.2$, $C_{\text{sat}} = 0.1$, with all other parameters as given in Tables 4.1 and 5.1.

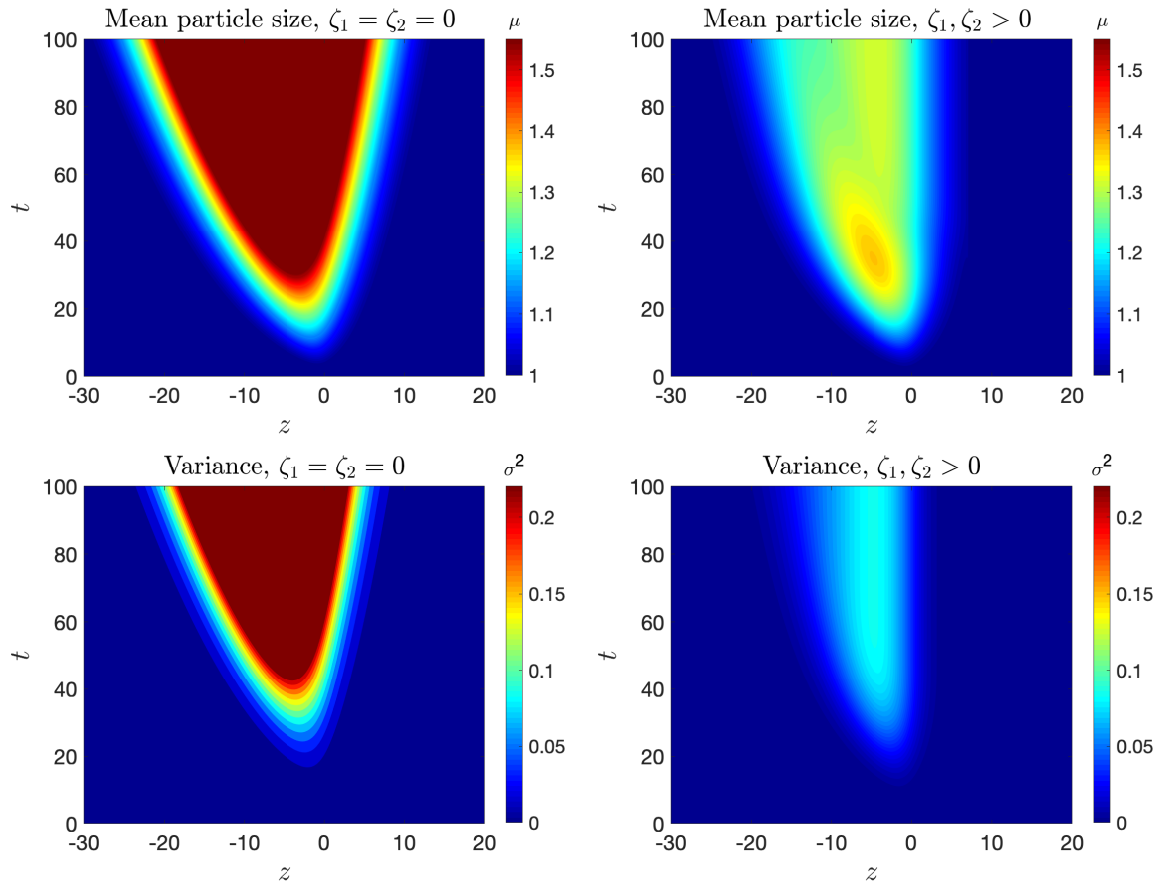

Figure 5.6: Heat maps for μ and σ^2 from top to bottom with respect to t and z. The figures on the left are for the case $\zeta_1 = \zeta_2 = 0$, and the ones on the right for $\zeta_1, \zeta_2 > 0$. We choose $a = 0.2$, $C_{\text{sat}} = 0.1$, with all other parameters as given in Tables 4.1 and 5.1.

to compute the size distribution of the total microsilica output in the entire domain considered. Therefore, we integrate our results for n in z and show the resulting plots versus s in Figure 5.7 for increasing values of time as indicated by the arrow. We observe that for the decoupled case, the particle size increases with no bound as time evolves, whereas in the fully-coupled case particle growth stops at a finite time, similarly to what we obtained in the well-mixed case. In addition, the particle density is the largest for the fully-coupled problem and in both cases reaches its maximum at the smallest particle sizes. This is due to the large number of small particles being formed near the boundaries of the reaction zone (with fewer and larger particles in the middle) but also throughout the entire domain for later times in the fully-coupled case. As a consequence, even though for a fixed z position we can see from Figure 5.5 that we would get a particle size distribution with a peak at the largest particle size in the

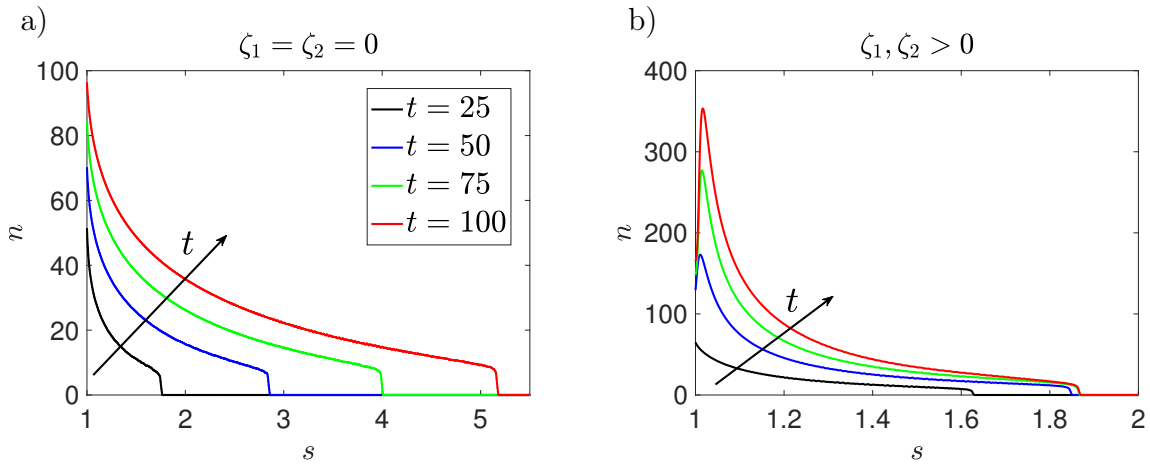

Figure 5.7: Particle size distribution for different times after integrating in space the results for the spatially separated chemicals case. This is for the (a) decoupled ($\zeta_1 = \zeta_2 = 0$) and (b) fully-coupled ($\zeta_1, \zeta_2 > 0$) problems.

decoupled case, and two peaks at the smallest and largest size for the fully-coupled case (as for the well-mixed problem in Chapter 4), this is not the case anymore when we account for particles in the whole reaction zone.

5.5 The effect of the initial separation distance between the fuel and oxidizer

So far we have considered that initially the fuel and oxidizer are next to each other, each occupying a different half of the domain. However, in reality there may be cases where both chemicals need to travel or diffuse first, before entering in contact with each other and reacting. Intuition tells us that the larger the initial separation distance, the slower and less powerful the reactions are, and this will have an effect on the microsilica particle formation and growth. We explore this effect by looking at the same problem as in the previous sections, (5.1.2), but with slightly different initial conditions for the reactants and for the temperature to those defined in (5.4.1).

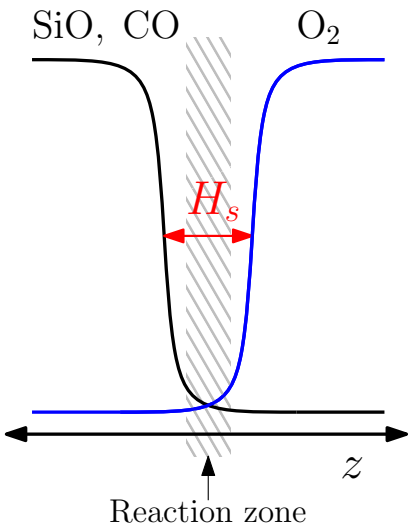

Figure 5.8: Initially separated chemical species by a distance H_s. The reaction zone is smaller when H_s is large since the chemicals need to diffuse first before reacting.

In dimensionless form, these are

$$C_{O_2}(0,z) = \frac{1}{2}\left(1+\operatorname{erf}\left(z-H_s\right)\right), \tag{5.5.1a}$$

$$C_{SiO}(0,z) = C_{CO}(0,z) = \frac{1}{2}\left(1+\operatorname{erf}\left(-z\right)\right), \tag{5.5.1b}$$

$$T(0,z) = \frac{1}{2}\left(1-\operatorname{erf}\left(z-\frac{H_s}{2}\right)\right), \tag{5.5.1c}$$

where H_s represents the initial separation distance between the chemicals as indicated in Figure 5.8. We have taken error functions instead of Heavisides to account for the presence of some material in between the fuel and oxidizer, which is more physically realistic. Moreover, taking an error function for the initial temperature allows for a smooth transition from the hotter region to the colder one. Note that these new initial conditions (5.5.1) are valid since they are consistent with the far-field limits (5.1.3). The initial conditions for the rest of the variables remain the same as in (5.4.1).

5.5.1 Asymptotic solution for a simplified subsystem

Similarly to what was done in Section 5.3, we can obtain analytical approximations of the chemical-temperature subsystem (5.3.1) with initial conditions accounting for the initial separation between the fuel and the oxidizer. We take equivalent conditions to those defined in (5.5.1) but we will write them in terms of Heaviside functions which

makes the analysis easier, namely

$$C_{\mathrm{O}_2}(0,z) = \mathcal{H}\left(z - H_s\right), \tag{5.5.2a}$$

$$C_{\mathrm{SiO}}(0,z) = \mathcal{H}\left(-z\right), \tag{5.5.2b}$$

$$T(0,z) = \mathcal{H}\left(\frac{H_s}{2} - z\right). \tag{5.5.2c}$$

Note that we can always translate time forward in the solution to the current problem formulation with Heaviside functions (5.5.2), to obtain the solution to the problem with error functions as initial conditions (5.5.1) since they are both equivalent. This is what we will do later in this section when comparing the analytics to numerical results.

We proceed as in Section 5.3, and define the quantities

$$w_1(z,t) = C_{\mathrm{O}_2} - \frac{a}{2}C_{\mathrm{SiO}}, \tag{5.5.3a}$$

$$w_2(z,t) = T + h_1 C_{\mathrm{SiO}}. \tag{5.5.3b}$$

This time, from equations (5.3.1) and initial conditions (5.5.2), our problem becomes

$$\frac{\partial w_1}{\partial t} - \frac{\partial^2 w_1}{\partial z^2} = 0, \tag{5.5.4a}$$

$$\frac{\partial w_2}{\partial t} - \frac{\partial^2 w_2}{\partial z^2} = 0, \tag{5.5.4b}$$

with initial conditions

$$w_1(0,z) = \mathcal{H}\left(z - H_s\right) - \frac{a}{2}\mathcal{H}\left(-z\right), \tag{5.5.4c}$$

$$w_2(0,z) = \mathcal{H}\left(\frac{H_s}{2} - z\right) + h_1\mathcal{H}\left(-z\right). \tag{5.5.4d}$$

We can split each of these problems, for w_1 and for w_2, into two easier to solve problems respectively, and find similarity solutions for each of the subproblems. That is, for w_1 we solve

$$\frac{\partial w_{11}}{\partial t} - \frac{\partial^2 w_{11}}{\partial \bar{z}^2} = 0, \tag{5.5.5a}$$

$$\frac{\partial w_{12}}{\partial t} - \frac{\partial^2 w_{12}}{\partial z^2} = 0, \tag{5.5.5b}$$

subject to

$$w_{11}(0,\bar{z}) = \mathcal{H}(\bar{z}), \tag{5.5.5c}$$
$$w_{12}(0,z) = \mathcal{H}(-z), \tag{5.5.5d}$$

where $\bar{z} = z - H_s$. We obtain the similarity solutions

$$w_{11} = \phi(\eta(\bar{z},t)), \quad w_{12} = \phi(-\eta(z,t)), \tag{5.5.6}$$

with the functions η and ϕ defined as in (5.3.5)-(5.3.6). Therefore, since $w_{11} - aw_{12}/2$ satisfies (5.5.4a) and the respective initial condition in (5.5.4c), and the solution to this problem is unique, we have found the general solution

$$w_1(z,t) = \phi\left(\frac{z-H_s}{2\sqrt{t}}\right) - \frac{a}{2}\phi\left(\frac{-z}{2\sqrt{t}}\right). \tag{5.5.7}$$

Similarly, for problem (5.5.4b) and (5.5.4d), we find the general solution

$$\begin{aligned} w_2(z,t) &= \phi(-\eta(\hat{z},t)) + h_1\phi(-\eta(z,t)) \\ &= \phi\left(-\frac{z-H_s/2}{2\sqrt{t}}\right) - \frac{a}{2}\phi\left(\frac{-z}{2\sqrt{t}}\right), \end{aligned} \tag{5.5.8}$$

with $\hat{z} = z - H_s/2$. From the definitions of w_1 and w_2 we obtain the following solutions for C_{O_2} and T,

$$C_{O_2} = \phi\left(\frac{z-H_s}{2\sqrt{t}}\right) - \frac{a}{2}\left(\phi\left(-\frac{z}{2\sqrt{t}}\right) - C_{SiO}\right), \tag{5.5.9a}$$
$$T = \phi\left(-\frac{z-H_s/2}{2\sqrt{t}}\right) + h_1\left(\phi\left(-\frac{z}{2\sqrt{t}}\right) - C_{SiO}\right). \tag{5.5.9b}$$

We now search for a solution for the SiO concentration by using (5.5.9) into (5.3.1b) such that the equation for C_{SiO} decouples from the rest. Moreover, we introduce the change of variables $t = H_s^2\tilde{t}$, $z = H_s\tilde{z}$, which will prove useful in the following analysis. The equation for C_{SiO} becomes

$$\begin{aligned} \frac{\partial C_{SiO}}{\partial \tilde{t}} - \frac{\partial^2 C_{SiO}}{\partial \tilde{z}^2} = -H_s^2 f_1\big(\phi\left(-\eta(\tilde{z}-1/2,\tilde{t})\right) + h_1\left(\phi\left(-\eta(\tilde{z},\tilde{t})\right) - C_{SiO}\right)\big) \\ \times\left(\phi(\eta(\tilde{z}-1,\tilde{t})) - \frac{a}{2}\left(\phi(-\eta(\tilde{z},\tilde{t})) - C_{SiO}\right)\right) C_{SiO}, \end{aligned} \tag{5.5.10}$$

with $\eta(z,t) = z/(2\sqrt{t})$ and $\phi(\eta) = (1+\mathrm{erf}(\eta))/2$.

We now explore both limits, $H_s \ll 1$ (small separation distance), and $H_s \gg 1$ (large separation distance), in a similar manner to the small and large t limits from Section 5.3, respectively.

5.5.1.1 The small H_s limit

Taking $\epsilon = H_s \ll 1$ and expanding C_{SiO} in equation (5.5.10) in powers of ϵ^2, we have that the solution to the leading order problem is purely diffusive, namely

$$C_{\mathrm{SiO}}^{(0)} = \phi\left(-\frac{\tilde{z}}{2\sqrt{\tilde{t}}}\right), \tag{5.5.11}$$

and the solution to the second order problem is given by

$$\begin{aligned} C_{\mathrm{SiO}}^{(2)}(\tilde{z},\tilde{t}) = -\int_0^{\tilde{t}}\int_{-\infty}^{\infty} \frac{f_1\big(\phi(-\eta(r-1/2,s))\big)\phi(\eta(r-1,s))\phi(-\eta(r,s))}{2\sqrt{\pi(\tilde{t}-s)}} \\ \times \exp\left(\frac{-(\tilde{z}-r)^2}{4(\tilde{t}-s)}\right) \mathrm{d}r\mathrm{d}s. \end{aligned} \tag{5.5.12}$$

Threfore, using (5.5.9), we have the following approximate solutions in terms of the original variables

$$C_{\mathrm{SiO}}(z,t) = \phi\left(-\frac{z}{2\sqrt{t}}\right) + \mathcal{O}(H_s^2), \tag{5.5.13a}$$

$$C_{\mathrm{O_2}}(z,t) = \phi\left(\frac{z-H_s}{2\sqrt{t}}\right) + \mathcal{O}(H_s^2), \tag{5.5.13b}$$

$$T(z,t) = \phi\left(-\frac{z-H_s/2}{2\sqrt{t}}\right) + \mathcal{O}(H_s^2), \tag{5.5.13c}$$

where we have only included leading order terms for simplicity and since they are enough to provide a good approximation for the small H_s limit.

5.5.1.2 The large H_s limit

To study the behaviour of the solutions when the initial separation distance between the chemicals is large, we now let $\epsilon = 1/H_s \ll 1$ and use the WKB ansatz

$$C_{\mathrm{SiO}} = \exp\left(-\frac{v(\tilde{z},\tilde{t})}{\epsilon}\right) \tag{5.5.14}$$

in equation (5.5.10), with $v = V_0(\tilde{z},\tilde{t}) + \epsilon V_1(\tilde{z},\tilde{t}) + \mathcal{O}(\epsilon^2)$. Following an equivalent analysis to Section 5.3.2, we have that

$$V_0(\tilde{z},\tilde{t}) = \int_{-\infty}^{\tilde{z}-z_0\epsilon} \sqrt{f_1\left(\phi\left(-\frac{r-1/2}{2\sqrt{\tilde{t}}}\right) + h_1\phi\left(-\frac{r}{2\sqrt{\tilde{t}}}\right)\right)\phi\left(\frac{r-1}{2\sqrt{\tilde{t}}}\right)}\mathrm{d}r, \quad (5.5.15)$$

for some arbitrary parameter z_0 that we will choose such that the analytics match the numerical results. Finally, using (5.5.9), the approximate solutions to leading order for large H_s in terms of the original variables read

$$C_{\mathrm{SiO}}(z,t) \sim \exp\left(-\int_{-\infty}^{z-z_0} \sqrt{f_1\left(\phi\left(-\frac{\sigma-H_s/2}{2\sqrt{t}}\right) + h_1\phi\left(-\frac{\sigma}{2\sqrt{t}}\right)\right)\phi\left(\frac{\sigma-H_s}{2\sqrt{t}}\right)}\mathrm{d}\sigma\right),$$

$$C_{\mathrm{O_2}}(z,t) \sim \phi\left(\frac{z-H_s}{2\sqrt{t}}\right), \quad (5.5.16a)$$

$$T(z,t) \sim \phi\left(-\frac{z-H_s/2}{2\sqrt{t}}\right) + h_1\phi\left(-\frac{z}{2\sqrt{t}}\right) - h_1\exp\left(-\int_{-\infty}^{z-z_0} \sqrt{f_1\left(\phi\left(-\frac{\sigma-H_s/2}{2\sqrt{t}}\right) + h_1\phi\left(-\frac{\sigma}{2\sqrt{t}}\right)\right)\phi\left(\frac{\sigma-H_s}{2\sqrt{t}}\right)}\mathrm{d}\sigma\right), \quad (5.5.16b)$$

as $t \to \infty$. We can check that for $H_s = 0$ we recover the same solutions as in (5.3.32) by taking an appropriate change of variables in the latter integrals.

Finally, since the equation and initial condition for the SiO_2 concentration remain the same as in Section 5.3, we have that it is again given in terms of the SiO concentration in the same way as in (5.3.34), but where we take C_{SiO} from (5.5.13a) for small H_s and from (5.5.16a) for the large H_s limit.

In Figures 5.9 and 5.10 we show the small and large H_s approximations (circles), respectively, compared to numerical results (solid line) for different H_s and time values. The dynamics of the chemicals are the following: first, the SiO and O_2 will diffuse into each other (the point where they both cross is further up in Figures 5.9 (b) and (d) with respect to (a) and (c) respectively), secondly, when they finally meet each other and their concentrations are large enough for a reaction to occur, SiO will start being consumed by the much more abundant oxygen and the reaction dominates the

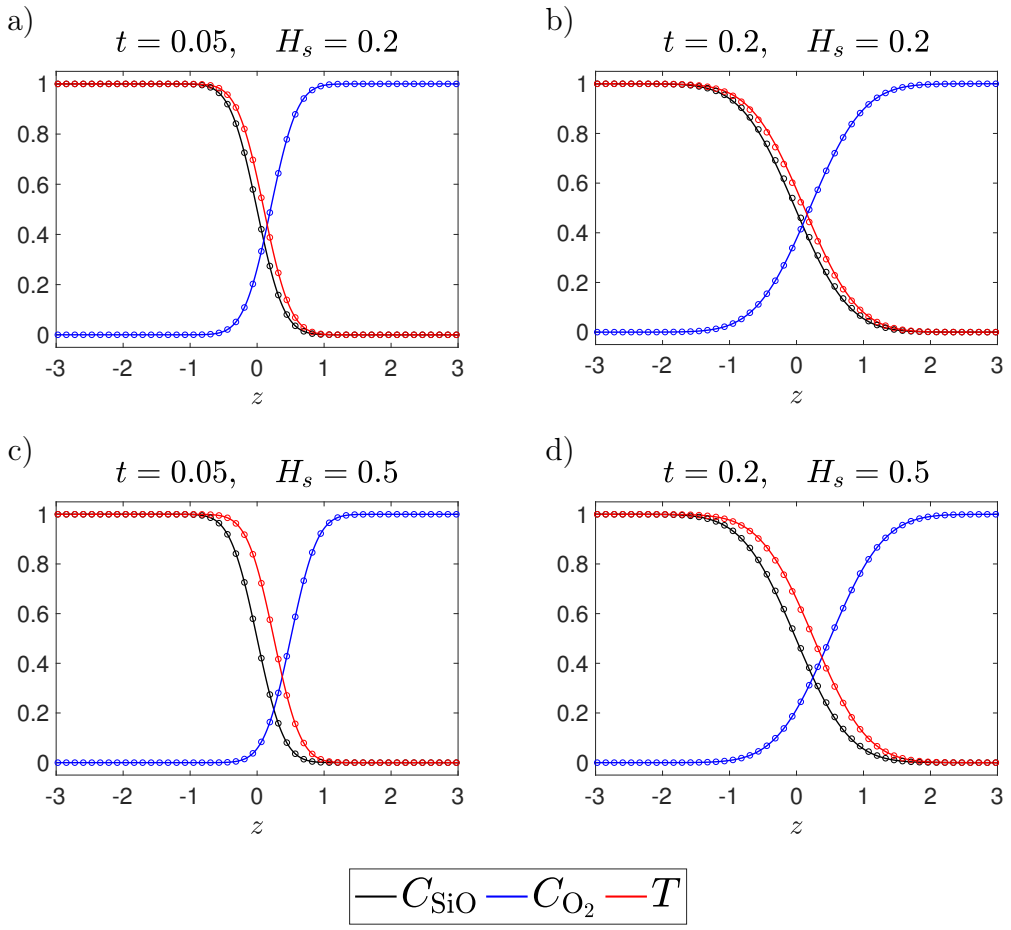

Figure 5.9: Approximate asymptotic solutions (circles) for small H_s as given in (5.5.13), compared to numerical solutions (solid lines) from solving problem (5.3.1) subject to the initial conditions (5.5.1). This is for increasing times from left to right and increasing values of H_s from top to bottom.

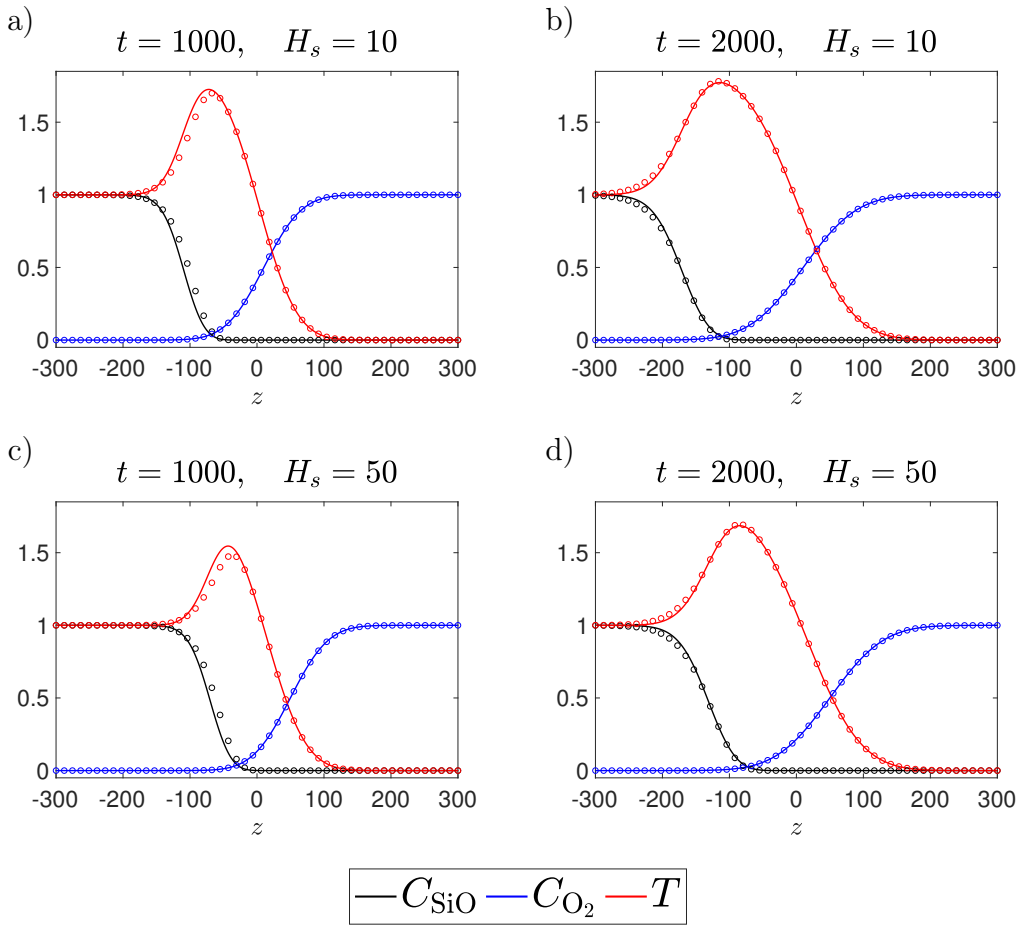

Figure 5.10: Approximate asymptotic solutions (circles) for large H_s as given in (5.5.16), compared to numerical solutions (solid lines) from solving problem (5.3.1) subject to the initial conditions (5.5.1). This is for increasing times from left to right and increasing values of H_s from top to bottom.

process (the SiO front will move away from the oxygen) as in Figure 5.10.

Note that for the small H_s case, since in the previous analysis we scaled time with H_s^2, we need to select small times relative to the value of H_s for the approximations to be valid. This is because as H_s increases, the timescale of the whole process is larger, therefore, the diffusive part of the process lasts longer. Hence, for the small times selected $t = 0.05$ and $t = 0.2$, the lowest error in the approximation will be for the $H_s = 0.5$ case. Similarly, for the large H_s approximations we need to select large time values with respect to H_s. Since the reaction will happen at a later time for a larger H_s, for the two selected times $t = 1000$ and $t = 2000$, the lowest error in the approximation will be achieved for $H_s = 10$. Finally, comparing Figures 5.10 (a) and (d) we observe that in (a) the reaction zone is narrower but there is a larger concentration of the chemicals, and therefore the temperature is larger too. We conclude that even though the temperature and chemicals will eventually reach the same equilibrium regardless of the value of H_s (at slightly different times), the reaction zone will be wider when H_s is large. We remark that the conclusions we have drawn here are for the decoupled case and slightly different dynamics will be obtained when we solve the fully-coupled system numerically in the next section.

5.5.2 Numerical solution of the fully-coupled system for $H_s > 0$

In this section, we solve the fully-coupled system (5.1.2) with initial conditions accounting for the initial separation distance between the chemicals and given by (5.5.1). The results are qualitatively the same as in Section 5.4, with the incorporation of the sink and source terms due to the particles ($\zeta_1, \zeta_2 > 0$) only affecting the temperature and SiO_2 concentration, respectively. Their profiles are similar to those found in Figures 5.4b and 5.4d, regardless of the H_s value, and the only difference is in the magnitudes. In Figure 5.11, we show the maximum value along the reaction zone, for the (a) SiO reaction rate, (b) temperature, and (c) SiO_2 concentration, with respect to time and for different values of H_s. We observe that as H_s increases, the reaction starts at a slightly later time and is less powerful. This is valid for all times (note that the curves in (a) are below each other for all t) and is due to less availability of material to react since it has to diffuse first. As a consequence, the temperature within the reaction zone will be lower and less SiO_2 will be produced.

Less SiO_2 availability and lower temperatures will mean that fewer and smaller particles will be produced. In Figure 5.12 (a)-(d) we show heatmaps for n at times $t = 25$ and $t = 75$, comparing the cases $H_s = 0$ and $H_s = 3$ side by side. From looking

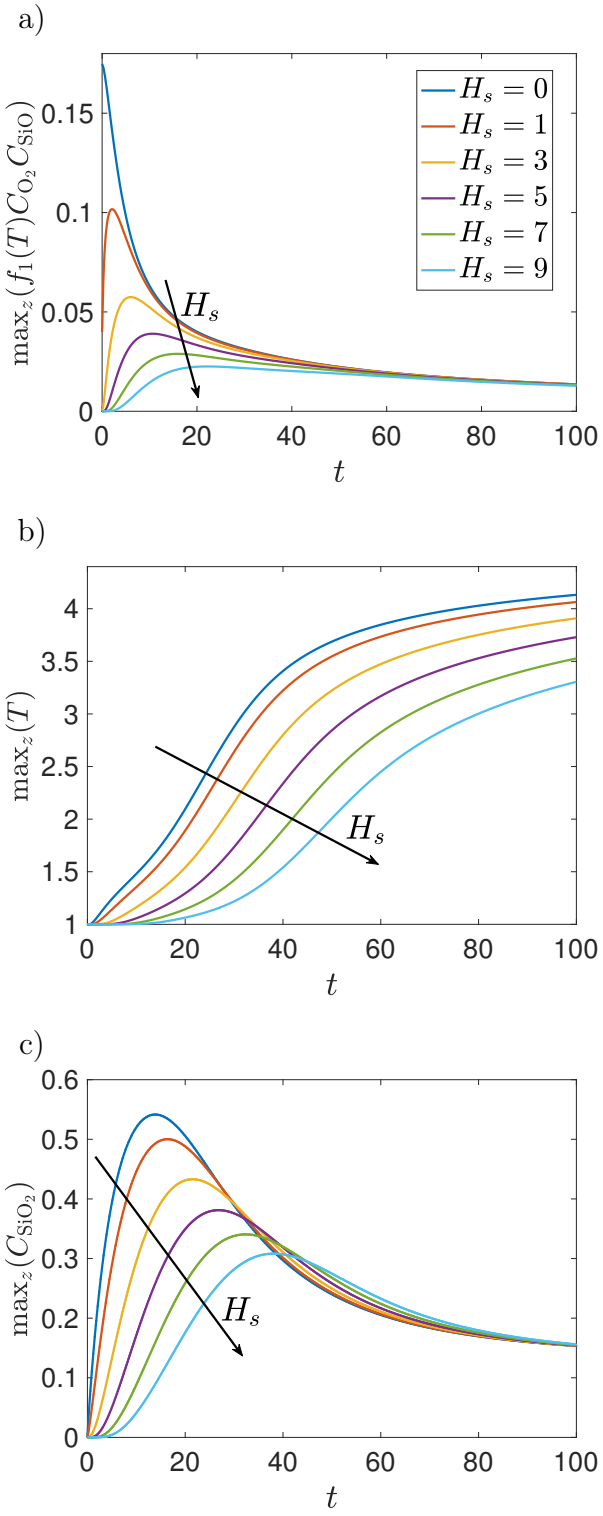

Figure 5.11: Maximum value in z of the (a) reaction rate, (b) temperature, and (c) SiO_2 concentration with respect to time and for increasing values of H_s as indicated by the direction of the arrow.

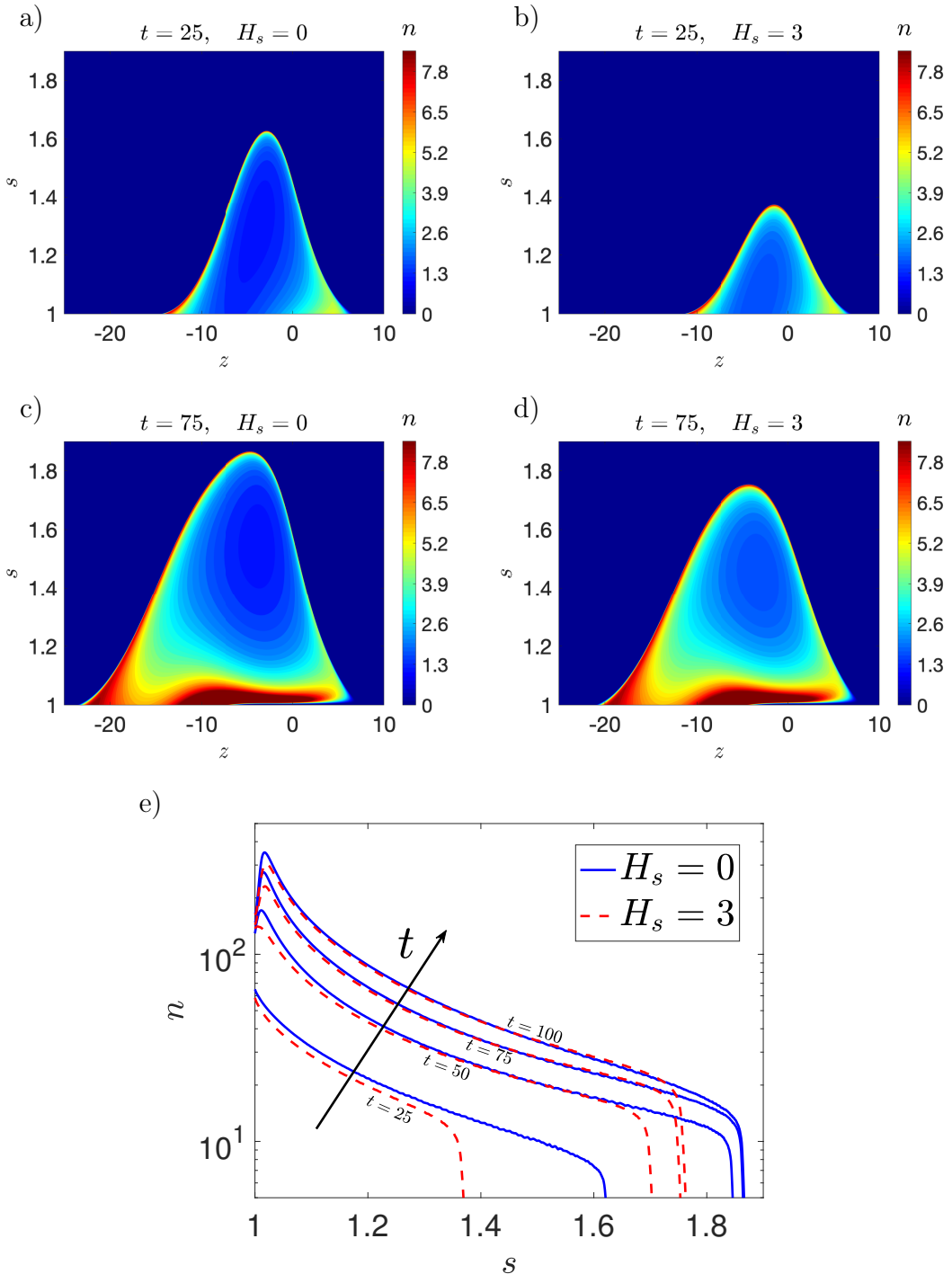

Figure 5.12: (a)-(d) Heat maps for n with respect to s and z for times $t = 25, 75$ from top to bottom and separation distance $H_s = 0, 3$ from left to right. (e) Particle size distribution for different times $t = 25, 50, 75, 100$ after integrating in space the results for n. Blue solid lines are for $H_s = 0$ and dashed red lines for $H_s = 3$. In the latter case fewer particles form and they do not grow as large.

at the spatial distribution of the particles in the heatmaps, we observe that more large particles are located toward the left of the domain compared to the right side for $H_s = 0$, whereas the plots are more symmetric as H_s becomes large. Furthermore, we have integrated the results in z and show the particle size distribution for times $t = 25, 50, 75, 100$ in panel (e) comparing again $H_s = 0$ (solid blue lines) and $H_s = 3$ (dashed red lines). These results suggest that as the initial separation between the chemicals, H_s, increases, the particle size distribution will converge at a later time. In addition, the larger H_s the smaller the particles will be, with a maximum particle size of approximately $s = 1.86$ for $H_s = 0$, and $s = 1.76$ for $H_s = 3$. From looking at the area below the curves in Figure 5.12 (e), we also conclude that when the initial separation distance between the reactants is larger, fewer particles form. This is consistent with the conclusions that we drew from the COMSOL simulations for a small fuel inlet in Section 3.3.1 of Chapter 3, where the chemicals needed to travel a longer distance before reacting.

5.6 Discussion

We have extended the work from Chapter 4 by taking into account spatial variations along a cross section of the reaction zone. In this new configuration, we have assumed that the chemical species are initially spatially separated, with O_2 plentiful on one side of the domain and the other chemical species plentiful on the other side of the domain. We followed a similar structure to the previous chapter and first solved a simplified subsystem for the dominant reaction and temperature, without including the particles effect ($\zeta_1 = \zeta_2 = 0$). We obtained asymptotic solutions for the small time limit by performing a regular perturbation, and for the long time limit by using the WKB method, and both compared well with numerical simulations. We found that initially, the solution is purely diffusive for all chemical species whereas at later times reactions dominate the process. As O_2 is the most plentiful of the reactants, the reaction zone propagates toward the other fuel components through diffusion. Since the material sink and heat source terms due to particle formation were neglected, particles continued growing with no bound since there is plenty SiO_2 for condensation. However, when we solved numerically the fully-coupled system ($\zeta_1, \zeta_1 > 0$), we observed that particle growth stops once the SiO_2 mass is depleted.

We notice that the dynamics within the core of the reaction zone are indeed similar to those of the spatially well-mixed case, verifying our intuition that the well-mixed case is indeed a simple yet effective representation of the dynamics within the flame.

The longest-lived and largest particles arise in the centre of the reaction zone, where SiO_2 is most abundant, and these match best with the predictions from the well-mixed limit. Meanwhile, the full spatial model is useful for better understanding the distribution of particles sizes over space and time, with gradually smaller particles being produced toward the boundary of the reaction zone. However, we found that the particle size distribution arising from considering particles that form in the whole reaction zone, and not just at a specific spatial location, is localised around the smallest particle size and the large particle size peak disappears. This is due to a large amount of very small particles forming at later times as the SiO_2 decays exponentially to its equilibrium.

Finally, we explored the effect of increasing the initial separation distance between the chemicals by changing the initial conditions of the problem. We followed a similar analysis to before and obtained asymptotic solutions that compared favourably with numerical simulations. Our results suggest that if the chemicals are initially far away from each other, they need to diffuse first and the reactions are less powerful since there is less material available to react at all times. As a consequence, fewer and smaller particles form.

The work provided in this chapter gives a qualitative underlying of the physical processes at play when microsilica is produced, yet in order to improve the quantitative agreement with experiments and real-world furnace observations, there are some extensions to consider. The most immediate extension is to consider a more realistic flow configuration within the furnace hood and solve the previous model coupled to a momentum equation, and this is what we will do in the next chapter.

Chapter 6

The effect of fluid flow on particle growth

In the previous two chapters of this thesis, we have neglected the effects of the fluid flow on the particles formation and growth mechanisms by either ignoring spatial variations in the variables (well-mixed) or by considering the velocity of the fluid to be zero everywhere (spatially separated). Moreover, we have only looked at one spatial dimension along the cross-section of a reaction zone. We are now interested in extending the work from Chapters 4-5 by introducing a new spatial dimension and considering more realistic fluid mechanics.

Motivated by the results obtained from the COMSOL simulations in Chapter 3, the flow problem will consist of a mixing layer forming between a stream of O_2 and a stream of SiO. We will focus again on the reaction zone, and we will explore transverse as well as streamwise changes in all variables in the system. Furthermore, in this chapter we will pay attention to how the chemicals, temperature, and particle size distribution are affected by the input velocities of the two different streams that interact leading to the formation of the particles. We focus on varying the value of these velocities since in practice they can be controlled and since we obtained significant differences in the results when we studied this case in the COMSOL simulations in Section 3.3.2 of Chapter 3.

6.1 Derivation of the mixing layer problem

We focus our attention on the mixing layer that forms when the oxygen stream meets and mixes with the fuel (CO and SiO) stream, since it is in this region where the reactions occur and where particles form and grow. Thus, consider a semi-

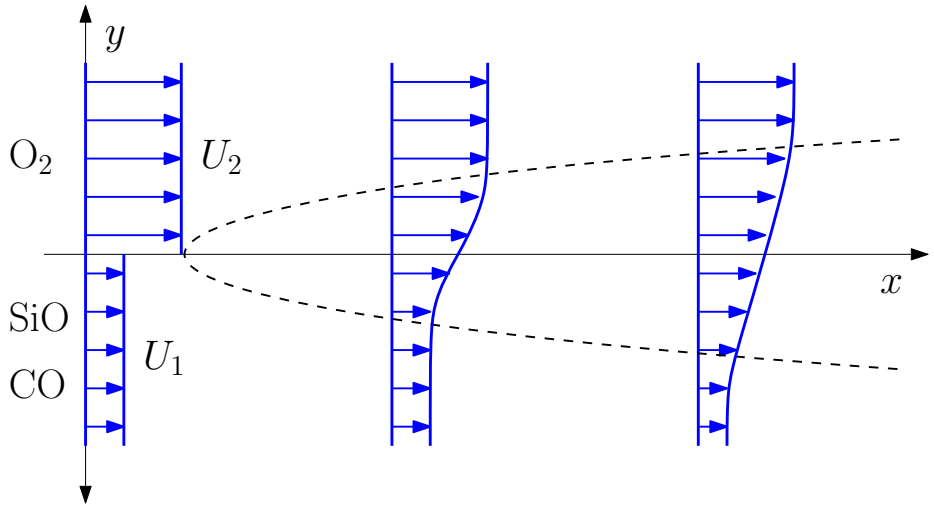

Figure 6.1: Schematic of a mixing layer between a stream of oxygen parallel to a stream composed of SiO and CO.

infinite domain as in the sketch in Figure 6.1, where at the origin, $x = 0$, we have two unperturbed parallel flows entering with different velocities, temperatures and chemical compositions. The top stream will be composed solely of oxygen which enters at a much faster velocity and at a lower temperature than the bottom stream which corresponds to the fuel. Therefore, the top of the domain will mainly consist of oxygen, whereas the bottom corresponds to the area dominated by the fuel. The transition from one velocity, U_1, to the other velocity, $U_2 > U_1$, takes place within a thin mixing zone, whose thickness increases in the x-direction as indicated with dashed lines in the schematic [70].

Whereas in Chapter 5, we only looked at the dynamics in a cross-section of the reaction layer, that is, along the y-direction in Figure 6.1, we are now also interested in studying how the reactive layer evolves in the x-direction, streamwise to the flow. Ultimately, we would like to explore the effect of the mixing between the two streams on the formation and growth of the microsilica particles.

We use the same governing equations that we derived in Chapter 2, that is, (2.4.1), for two spatial dimensions, x and y. Note that the independent variable, z, that appeared in Chapter 5 to indicate distance along a cross-section of the reaction zone, corresponds to y here. In addition, since in the previous two chapters we did not consider compressibility effects, for consistency we assume that the same holds here.

Finally, we remark that even though in both Chapter 3 and this chapter, we are considering a two-dimensional geometry for the problem, the lengthscales considered here are much smaller than those in the COMSOL simulations of the full furnace

hood. Therefore, it is reasonable to take a laminar mixing layer approach, since the reaction zones where particles form are most likely embedded within the macroscopic turbulent flow described in Chapter 3.

6.1.1 Non-dimensionalisation and assumptions

We non-dimensionalise the incompressible form of the system (2.4.1) in two-dimensions using the same scalings for the variables as in Chapters 4 and 5. Hence, in this section we will only define the scalings for those variables that have not appeared in the previous two chapters. First, we scale the spatial variables for the new domain given in Figure 6.1 in the following way,

$$y = y_0\tilde{y}, \quad x = x_0\tilde{x}. \tag{6.1.1}$$

Since y represents the direction along a cross-section of the reaction layer, its scaling is the same as the one taken for z in (5.1.1) in Chapter 5, that is,

$$y_0 = \sqrt{D_{O_2} t_0}, \tag{6.1.2}$$

where the timescale, t_0, was given in (4.1.3). From the COMSOL simulations in Chapter 3 we observe that the reaction zone is thin and long, which is usually the case for the majority of combustion problems [10]. Therefore, we have that the aspect ratio of the reaction layer is

$$\epsilon = \frac{y_0}{x_0} \ll 1. \tag{6.1.3}$$

Now, we pick the x lengthscale in terms of the y lengthscale and the aspect ratio, that is,

$$x_0 = \frac{y_0}{\epsilon} = \frac{1}{\epsilon}\sqrt{D_{O_2} t_0}. \tag{6.1.4}$$

We scale each velocity, streamwise (u) and transverse (v), with the respective lengthscale over the timescale in the following way,

$$u = u_0\tilde{u} = \frac{1}{\epsilon}\sqrt{\frac{D_{O_2}}{t_0}}\tilde{u}, \qquad v = v_0\tilde{v} = \sqrt{\frac{D_{O_2}}{t_0}}\tilde{v}. \tag{6.1.5}$$

Finally, the remaining variable that we need to scale is the pressure, and we have that

$$p = \rho_0 u_0^2 \tilde{p} = \frac{\rho_0 D_{O_2}}{\epsilon^2 t_0} \tilde{p}, \tag{6.1.6}$$

where ρ_0 represents the density of the mixture and is given in Table 2.2. Neglecting the over tilde notation, the non-dimensional flow problem reads

$$\frac{\partial u}{\partial t} + u\frac{\partial u}{\partial x} + v\frac{\partial u}{\partial y} = -\frac{\partial p}{\partial x} + \epsilon^2 \mathrm{Sc}\frac{\partial^2 u}{\partial x^2} + \mathrm{Sc}\frac{\partial^2 u}{\partial y^2}, \tag{6.1.7a}$$

$$\frac{\partial v}{\partial t} + u\frac{\partial v}{\partial x} + v\frac{\partial v}{\partial y} = -\frac{1}{\epsilon^2}\frac{\partial p}{\partial y} + \epsilon^2 \mathrm{Sc}\frac{\partial^2 v}{\partial x^2} + \mathrm{Sc}\frac{\partial^2 v}{\partial y^2}, \tag{6.1.7b}$$

$$\frac{\partial u}{\partial x} + \frac{\partial v}{\partial y} = 0, \tag{6.1.7c}$$

for $x > 0$, $-\infty < y < \infty$, and $t > 0$, and where we have introduced a new dimensionless parameter, the Schmidt number, defined as the ratio between the kinematic viscosity and the chemical diffusivity, namely

$$\mathrm{Sc} = \frac{\nu}{D_{O_2}}, \tag{6.1.8}$$

where $\nu = \mu/\rho_0$. Note that the kinematic viscosity varies depending on the temperature of the system, however for the range of temperatures considered in this problem, the Schmidt number is of order unity.

Similarly, for the chemicals, temperature, moments, and particle size distribution we have the following

$$\frac{\mathrm{D}C_{O_2}}{\mathrm{D}t} - \epsilon^2\frac{\partial^2 C_{O_2}}{\partial x^2} - \frac{\partial^2 C_{O_2}}{\partial y^2} = -\frac{a}{2}\left(f_1(T)C_{O_2}C_{SiO} + \varepsilon f_2(T)C_{O_2}C_{CO}\right), \tag{6.1.9a}$$

$$\frac{\mathrm{D}C_{SiO}}{\mathrm{D}t} - d_{SiO}\left(\epsilon^2\frac{\partial^2 C_{SiO}}{\partial x^2} + \frac{\partial^2 C_{SiO}}{\partial y^2}\right) = -f_1(T)C_{O_2}C_{SiO}, \tag{6.1.9b}$$

$$\frac{\mathrm{D}C_{SiO_2}}{\mathrm{D}t} - d_{SiO_2}\left(\epsilon^2\frac{\partial^2 C_{SiO_2}}{\partial x^2} + \frac{\partial^2 C_{SiO_2}}{\partial y^2}\right) = f_1(T)C_{O_2}C_{SiO} - \zeta_1 G M_2, \tag{6.1.9c}$$

$$\frac{\mathrm{D}C_{CO}}{\mathrm{D}t} - d_{CO}\left(\epsilon^2\frac{\partial^2 C_{CO}}{\partial x^2} + \frac{\partial^2 C_{CO}}{\partial y^2}\right) = -\varepsilon f_2(T)C_{O_2}C_{CO}, \tag{6.1.9d}$$

$$\frac{\mathrm{D}C_{CO_2}}{\mathrm{D}t} - d_{CO_2}\left(\epsilon^2\frac{\partial^2 C_{CO_2}}{\partial x^2} + \frac{\partial^2 C_{CO_2}}{\partial y^2}\right) = \varepsilon f_2(T)C_{O_2}C_{CO}, \tag{6.1.9e}$$

$$\frac{\mathrm{D}T}{\mathrm{D}t} - \mathrm{Le}\left(\epsilon^2\frac{\partial^2 T}{\partial x^2} + \frac{\partial^2 T}{\partial y^2}\right) = h_1 f_1(T) C_{\mathrm{O}_2} C_{\mathrm{SiO}} + \varepsilon h_2 f_2(T) C_{\mathrm{O}_2} C_{\mathrm{CO}} + \zeta_2 G M_2, \tag{6.1.9f}$$

$$\frac{\mathrm{D}M_0}{\mathrm{D}t} - d_p\left(\epsilon^2\frac{\partial^2 M_0}{\partial x^2} + \frac{\partial^2 M_0}{\partial y^2}\right) = G^* J, \tag{6.1.9g}$$

$$\frac{\mathrm{D}M_1}{\mathrm{D}t} - d_p\left(\epsilon^2\frac{\partial^2 M_1}{\partial x^2} + \frac{\partial^2 M_1}{\partial y^2}\right) = G^* J + G^* G M_0, \tag{6.1.9h}$$

$$\frac{\mathrm{D}M_2}{\mathrm{D}t} - d_p\left(\epsilon^2\frac{\partial^2 M_2}{\partial x^2} + \frac{\partial^2 M_2}{\partial y^2}\right) = G^* J + 2G^* G M_1, \tag{6.1.9i}$$

$$\frac{\mathrm{D}n}{\mathrm{D}t} - d_p\left(\epsilon^2\frac{\partial^2 n}{\partial x^2} + \frac{\partial^2 n}{\partial y^2}\right) = -G^* G\frac{\partial n}{\partial s}, \tag{6.1.9j}$$

for $x > 0$, $-\infty < y < \infty$, $t > 0$, and $s > 1$, and where the material derivative is defined as

$$\frac{\mathrm{D}}{\mathrm{D}t} = \frac{\partial}{\partial t} + u\frac{\partial}{\partial x} + v\frac{\partial}{\partial y}. \tag{6.1.10}$$

Note that all variables have the same velocity (u, v) as it was derived in Chapter 2. In the system above we have not introduced any new dimensionless parameters to the ones that we had already defined in the previous chapters in Tables 4.1 and 5.1, apart from ϵ. Moreover, the dimensionless Arrhenius terms, f_1 and f_2, growth and nucleation rates, G and J, are the same as in (4.1.7)-(4.1.9), respectively, but note that now they depend on the independent variables x, y, and t.

Since we have taken ϵ to be small, in the limit $\epsilon \to 0$, the equations governing the flow, (6.1.7), reduce to the Prandtl boundary-layer equations [70], namely

$$\frac{\partial u}{\partial t} + u\frac{\partial u}{\partial x} + v\frac{\partial u}{\partial y} = -\frac{\partial p}{\partial x} + \mathrm{Sc}\frac{\partial^2 u}{\partial y^2}, \tag{6.1.11a}$$

$$0 = -\frac{\partial p}{\partial y}, \tag{6.1.11b}$$

$$\frac{\partial u}{\partial x} + \frac{\partial v}{\partial y} = 0, \tag{6.1.11c}$$

for $x > 0$, $-\infty < y < \infty$, and $t > 0$. The dimensionless inflow condition for the streamwise velocity is equivalent to the configuration shown in Figure 6.1 at $x = 0$,

that is,

$$u(0,y,t) = \frac{U_2}{u_0} = u_2 \qquad \text{for } y > 0, \quad t > 0, \tag{6.1.12a}$$

$$u(0,y,t) = \frac{U_1}{u_0} = \lambda u_2 = u_1 \qquad \text{for } y < 0, \quad t > 0, \tag{6.1.12b}$$

where $\lambda = U_1/U_2$ is the ratio of the two inlet velocities. Away from the mixing layer there is an outer region where the flow is uniform with constant ambient pressure in the $x-$direction, such that the relevant matching conditions are

$$u \to u_2 \quad \text{as} \quad y \to \infty, \tag{6.1.13a}$$

$$u \to u_1 \quad \text{as} \quad y \to -\infty. \tag{6.1.13b}$$

Moreover, matching the pressure we have that $\partial p/\partial x = 0$ [70] and hence the system (6.1.11) becomes

$$\frac{\partial u}{\partial t} + u\frac{\partial u}{\partial x} + v\frac{\partial u}{\partial y} = \mathrm{Sc}\frac{\partial^2 u}{\partial y^2}, \tag{6.1.14a}$$

$$\frac{\partial u}{\partial x} + \frac{\partial v}{\partial y} = 0, \tag{6.1.14b}$$

for $x > 0$, $-\infty < y < \infty$, and $t > 0$. The steady-state version of (6.1.14) corresponds to the flow equations that we will study in the rest of this chapter.

Similarly, in the limit $\epsilon \to 0$, the dimensionless boundary-layer equations for the remaining variables are the following

$$\frac{\mathrm{D}C_{\mathrm{O_2}}}{\mathrm{D}t} - \frac{\partial^2 C_{\mathrm{O_2}}}{\partial y^2} = -\frac{a}{2}\left(f_1(T)C_{\mathrm{O_2}}C_{\mathrm{SiO}} + \varepsilon f_2(T)C_{\mathrm{O_2}}C_{\mathrm{CO}}\right), \tag{6.1.15a}$$

$$\frac{\mathrm{D}C_{\mathrm{SiO}}}{\mathrm{D}t} - d_{\mathrm{SiO}}\frac{\partial^2 C_{\mathrm{SiO}}}{\partial y^2} = -f_1(T)C_{\mathrm{O_2}}C_{\mathrm{SiO}}, \tag{6.1.15b}$$

$$\frac{\mathrm{D}C_{\mathrm{SiO_2}}}{\mathrm{D}t} - d_{\mathrm{SiO_2}}\frac{\partial^2 C_{\mathrm{SiO_2}}}{\partial y^2} = f_1(T)C_{\mathrm{O_2}}C_{\mathrm{SiO}} - \zeta_1 GM_2, \tag{6.1.15c}$$

$$\frac{\mathrm{D}C_{\mathrm{CO}}}{\mathrm{D}t} - d_{\mathrm{CO}}\frac{\partial^2 C_{\mathrm{CO}}}{\partial y^2} = -\varepsilon f_2(T)C_{\mathrm{O_2}}C_{\mathrm{CO}}, \tag{6.1.15d}$$

$$\frac{\mathrm{D}C_{\mathrm{CO_2}}}{\mathrm{D}t} - d_{\mathrm{CO_2}}\frac{\partial^2 C_{\mathrm{CO_2}}}{\partial y^2} = \varepsilon f_2(T)C_{\mathrm{O_2}}C_{\mathrm{CO}}, \tag{6.1.15e}$$

$$\frac{\mathrm{D}T}{\mathrm{D}t} - \mathrm{Le}\frac{\partial^2 T}{\partial y^2} = h_1 f_1(T)C_{\mathrm{O_2}}C_{\mathrm{SiO}} + \varepsilon h_2 f_2(T)C_{\mathrm{O_2}}C_{\mathrm{CO}} + \zeta_2 GM_2, \tag{6.1.15f}$$

$$\frac{\mathrm{D}M_0}{\mathrm{D}t} = G^*J, \tag{6.1.15g}$$
$$\frac{\mathrm{D}M_1}{\mathrm{D}t} = G^*J + G^*GM_0, \tag{6.1.15h}$$
$$\frac{\mathrm{D}M_2}{\mathrm{D}t} = G^*J + 2G^*GM_1, \tag{6.1.15i}$$
$$\frac{\mathrm{D}n}{\mathrm{D}t} = -G^*G\frac{\partial n}{\partial s}, \tag{6.1.15j}$$

for $x > 0$, $-\infty < y < \infty$, $s > 1$, and $t > 0$. Therefore, we have that diffusion in the x-direction is negligible for all variables. Note that we have also neglected diffusion in the y-direction for the moments and particle size distribution, as in the earlier chapters, since the parameter $d_p \sim 10^{-5}$ is very small compared to the rest of dimensionless parameters in our problem.

In the sections to follow, we will study the steady-state problem, and will therefore only need boundary conditions for all variables. The inlet conditions are written in terms of Heaviside functions that reflect the discontinuous jump in the temperature, O_2, SiO and CO concentrations, from one stream to the other occurring at $x = 0$. Since no reaction products have formed at $x = 0$, we have that $C_{SiO_2}(0, y) = C_{CO_2}(0, y) = 0$. Moreover, the far-field conditions as $y \to \pm\infty$ are such that they match the free stream values of the variables, and are equivalent to conditions (5.1.3), that is,

$$C_{O_2} = 1, \quad C_{SiO} = C_{CO} = T = C_{SiO_2} = C_{CO_2} = 0 \quad \text{as} \quad y \to \infty, \tag{6.1.16a}$$
$$C_{O_2} = C_{SiO_2} = C_{CO_2} = 0, \quad C_{SiO} = C_{CO} = T = 1 \quad \text{as} \quad y \to -\infty. \tag{6.1.16b}$$

With respect to the particle formation problem, we have that no particles have formed yet at $x = 0$, since the concentration of SiO_2 is zero, and therefore

$$n = M_0 = M_1 = M_2 = 0 \quad \text{at} \quad x = 0, \tag{6.1.17a}$$

with their far-field values also being zero following the behaviour of C_{SiO_2}. Moreover, the same nucleation boundary condition that we have used in previous chapters holds here, namely

$$G(x, y)n = J(x, y) \quad \text{at} \quad s = 1, \tag{6.1.17b}$$

where the dimensionless growth, G, and nucleation, J, rates were given in (4.1.8) and (4.1.9), respectively. These rates now depend on SiO_2 concentration and temperature profiles defined on the whole spatial domain, that is, for $x > 0$ and $-\infty < y < \infty$.

6.1.2 Von Mises transformation

Consider the steady-state version of the boundary-layer equations (6.1.14)-(6.1.15). The most common approach to solving these equations is to first transform them by introducing a change of coordinates involving a stream function [70]. For the flow problem (6.1.14) this results in the Blasius equation, which is a third order ordinary differential equation that only depends on the similarity variable η. On the other hand, the system (6.1.15) transforms into reaction-advection-diffusion equations with variable coefficients and with (x, η) as independent variables instead of (x, y). Whereas asymptotic solutions are possible for the Blasius equation, the other equations are more challenging and different limits have been taken in the literature when attempting a solution to similar systems. A frequent assumption made is considering all variables to depend only on the similarity variable η and not on x and then assuming either frozen [45] or equilibrium [44] chemistry. Another common approach is Taylor expanding the variables for small x and solving for some small order terms that only depend on the similarity variable η [30, 51].

In our work, we will not change our coordinate system in the same way as mentioned above, but instead we will apply the von Mises transformation [70], namely

$$u = \frac{\partial \psi}{\partial y}, \quad v = -\frac{\partial \psi}{\partial x}, \tag{6.1.18}$$

directly on (6.1.14)-(6.1.15). Under this transformation, we keep the independent variable x and only change the variable y to the stream function ψ, that is, we have (x, ψ) rather than (x, y), which will simplify our equations significantly. An equivalent ODE to the Blasius equation will be obtained for the flow problem, and equations (6.1.15) will reduce to reaction-diffusion equations similar to those that we solved for in Chapter 5. Von Mises transformation has been applied before in many works dealing with reactions in boundary layers. For instance, it is employed in [15] to simplify the boundary-layer equations close to a surface where a reaction occurs; since the reaction term is in the boundary condition in this paper, separable solutions are possible in this case. Moreover, in [43], von Mises transformation is used to reduce the equations for a turbulent mixing layer, which are then solved analytically by either considering a frozen or an equilibrium flow.

Introducing the new coordinates $\xi = x$, $\psi = \psi(x, y)$, we obtain

$$\frac{\partial u}{\partial x} = \frac{\partial u}{\partial \xi} - v\frac{\partial u}{\partial \psi}, \tag{6.1.19}$$

$$\frac{\partial u}{\partial y} = 0 + u\frac{\partial u}{\partial \psi}. \tag{6.1.20}$$

Hence, using x instead of the dummy variable ξ, equation (6.1.14a) becomes

$$\frac{\partial u}{\partial x} = \mathrm{Sc}\frac{\partial}{\partial \psi}\left(u\frac{\partial u}{\partial \psi}\right), \tag{6.1.21}$$

for $x > 0$ and $-\infty < \psi < \infty$. Similarly, the equations for the concentrations, temperature, moments, and number density function, (6.1.15), reduce to

$$\frac{\partial C_{\mathrm{O_2}}}{\partial x} - \frac{\partial}{\partial \psi}\left(u\frac{\partial C_{\mathrm{O_2}}}{\partial \psi}\right) = -\frac{a}{2u}\left(f_1(T)C_{\mathrm{O_2}}C_{\mathrm{SiO}} + \varepsilon f_2(T)C_{\mathrm{O_2}}C_{\mathrm{CO}}\right), \tag{6.1.22a}$$

$$\frac{\partial C_{\mathrm{SiO}}}{\partial x} - d_{\mathrm{SiO}}\frac{\partial}{\partial \psi}\left(u\frac{\partial C_{\mathrm{SiO}}}{\partial \psi}\right) = -\frac{1}{u}f_1(T)C_{\mathrm{O_2}}C_{\mathrm{SiO}}, \tag{6.1.22b}$$

$$\frac{\partial C_{\mathrm{SiO_2}}}{\partial x} - d_{\mathrm{SiO_2}}\frac{\partial}{\partial \psi}\left(u\frac{\partial C_{\mathrm{SiO_2}}}{\partial \psi}\right) = \frac{1}{u}\left(f_1(T)C_{\mathrm{O_2}}C_{\mathrm{SiO}} - \zeta_1 G M_2\right), \tag{6.1.22c}$$

$$\frac{\partial C_{\mathrm{CO}}}{\partial x} - d_{\mathrm{CO}}\frac{\partial}{\partial \psi}\left(u\frac{\partial C_{\mathrm{CO}}}{\partial \psi}\right) = -\frac{\varepsilon}{u}f_2(T)C_{\mathrm{O_2}}C_{\mathrm{CO}}, \tag{6.1.22d}$$

$$\frac{\partial C_{\mathrm{CO_2}}}{\partial x} - d_{\mathrm{CO_2}}\frac{\partial}{\partial \psi}\left(u\frac{\partial C_{\mathrm{CO_2}}}{\partial \psi}\right) = \frac{\varepsilon}{u}f_2(T)C_{\mathrm{O_2}}C_{\mathrm{CO}}, \tag{6.1.22e}$$

with

$$\frac{\partial T}{\partial x} - \mathrm{Le}\frac{\partial}{\partial \psi}\left(u\frac{\partial T}{\partial \psi}\right) = \frac{1}{u}\left(h_1 f_1(T)C_{\mathrm{O_2}}C_{\mathrm{SiO}} + \varepsilon h_2 f_2(T)C_{\mathrm{O_2}}C_{\mathrm{CO}} + \zeta_2 G M_2\right), \tag{6.1.22f}$$

and

$$u\frac{\partial M_0}{\partial x} = G^* J, \tag{6.1.22g}$$

$$u\frac{\partial M_1}{\partial x} = G^* J + G^* G M_0, \tag{6.1.22h}$$

$$u\frac{\partial M_2}{\partial x} = G^* J + 2G^* G M_1, \tag{6.1.22i}$$

for $x > 0$ and $-\infty < \psi < \infty$. Finally, the population balance equation for the particle

size distribution becomes

$$u\frac{\partial n}{\partial x} = -G^* G\frac{\partial n}{\partial s}, \tag{6.1.23}$$

for $x > 0$, $-\infty < \psi < \infty$, and $s > 1$. The latter equations (6.1.22)-(6.1.23) resemble those that we solved for in Chapter 5, (5.1.2), but with a non-constant diffusivity given by the streamwise velocity, u, where a diffusion term is present. Moreover, the reaction terms on the right-hand sides of all the equations are multiplied by $1/u$. Notice that under this transformation we have lost the dependence on the transverse velocity v, and we only need to solve for u.

In order to return to our original coordinates later on, we have to find an inversion formula for the von Mises transformation. Integrating $u(x, \psi)$ as in (6.1.18), we have that ψ is given implicitly in terms of x and y by the following expression

$$y(x, \psi) = \int_0^{\psi} \frac{\mathrm{d}\bar{\psi}}{u(x, \bar{\psi})}. \tag{6.1.24}$$

The latter formula (6.1.24) can also be used to compute the flow streamlines on each of which ψ is constant.

6.2 Asymptotic approximation to the mixing layer problem

In this section we will find asymptotic solutions to the system (6.1.21)-(6.1.22). Firstly, since the momentum equation (6.1.21) decouples from the rest of the equations, we will start by solving for the streamwise velocity, u. We will then use the approximate solution for u in the chemical-temperature subsystem that we will solve by looking at different parameter regimes under certain simplifying assumptions. The asymptotic approximations will be compared to numerical simulations in all cases.

6.2.1 Momentum equation

In order to solve the transformed momentum equation,

$$\frac{\partial u}{\partial x} = \mathrm{Sc}\frac{\partial}{\partial \psi}\left(u\frac{\partial u}{\partial \psi}\right), \tag{6.2.1a}$$

subject to the boundary conditions

$$u \to u_2 \quad \text{as} \quad \psi \to \infty, \tag{6.2.1b}$$

$$u \to u_1 \quad \text{as} \quad \psi \to -\infty, \tag{6.2.1c}$$

we seek a similarity solution of the form

$$u = u_2 g(\eta), \quad \eta(x, \psi) = \frac{\psi}{\sqrt{2\mathrm{Sc} u_2 x}}. \tag{6.2.2}$$

Under the change of variables (6.2.2), equation (6.2.1a) reduces to the following ODE,

$$(gg')' + \eta g' = 0 \tag{6.2.3a}$$

for $-\infty < \eta < \infty$, subject to the boundary conditions

$$g \to 1 \quad \text{as} \quad \eta \to \infty, \tag{6.2.3b}$$

$$g \to \lambda \quad \text{as} \quad \eta \to -\infty, \tag{6.2.3c}$$

where $\lambda = u_1/u_2 < 1$, and where the prime denotes differentiation with respect to the similarity variable η. If the ratio of velocities is close to 1, we can introduce a perturbation in the boundary data in (6.2.3) by setting $\lambda = 1 - \delta$, with $0 < \delta \ll 1$. Considering the two stream velocities to be similar is a reasonable assumption since as both streams enter the furnace, their velocity may change before approaching the mixing layer so that the difference between both velocities in the layer is not that abrupt.

Now, expanding g in powers of δ in the following way

$$g(\eta) = g_0(\eta) + \delta g_1(\eta) + \delta^2 g_2(\eta) + \mathcal{O}(\delta^3), \tag{6.2.4}$$

the $\mathcal{O}(1)$ problem is given by

$$(g_0 g_0')' + \eta g_0' = 0, \tag{6.2.5a}$$

$$g_0 \to 1 \quad \text{as} \quad \eta \to \pm\infty, \tag{6.2.5b}$$

and the solution is found to be $g_0(\eta) = 1$. The $\mathcal{O}(\delta)$ problem reads

$$g_1'' + \eta g_1' = 0, \tag{6.2.6a}$$

$$g_1 \to 0 \quad \text{as} \quad \eta \to \infty, \tag{6.2.6b}$$

$$g_1 \to -1 \quad \text{as} \quad \eta \to -\infty, \tag{6.2.6c}$$

which can be integrated to give

$$g_1(\eta) = \frac{1}{2}\left(\operatorname{erf}\left(\frac{\eta}{\sqrt{2}}\right) - 1\right). \tag{6.2.7}$$

Finally, the $\mathcal{O}(\delta^2)$ problem has the form

$$g_2'' + \eta g_2' = Q(\eta), \tag{6.2.8a}$$

$$g_2 \to 0 \quad \text{as} \quad \eta \to \pm\infty, \tag{6.2.8b}$$

where

$$Q(\eta) = -(g_1 g_1')' = -\frac{\exp(-\eta^2)}{4\pi}\left(2 + \exp\left(\frac{\eta^2}{2}\right)\sqrt{2\pi}\eta \operatorname{erfc}\left(\frac{\eta}{\sqrt{2}}\right)\right), \tag{6.2.8c}$$

which we solve by the method of variations of parameters. The fundamental solutions are

$$g_{2,1}(\eta) = 1, \quad g_{2,2}(\eta) = \operatorname{erf}\left(\frac{\eta}{\sqrt{2}}\right), \tag{6.2.9}$$

and hence the solution is given by

$$g_2(\eta) = (C_1 - q_1(\eta))g_{2,1}(\eta) + (C_2 + q_2(\eta))g_{2,2}(\eta), \tag{6.2.10}$$

where C_1 and C_2 are arbitrary constants and where

$$q_1(\eta) = \int_0^\eta \frac{g_{2,2}(\tilde{\eta})Q(\tilde{\eta})}{W(\tilde{\eta})}\mathrm{d}\tilde{\eta}, \qquad q_2(\eta) = \int_0^\eta \frac{g_{2,1}(\tilde{\eta})Q(\tilde{\eta})}{W(\tilde{\eta})}\mathrm{d}\tilde{\eta}. \tag{6.2.11}$$

The Wronskian in (6.2.11) is given by

$$W(\eta) = g_{2,1}(\eta)g_{2,2}(\eta)' - g_{2,2}(\eta)g_{2,1}(\eta)' = \sqrt{\frac{2}{\pi}}\exp\left(-\frac{\eta^2}{2}\right). \tag{6.2.12}$$

Finally, applying the boundary conditions (6.2.8b) we obtain the constants

$$C_1 = \frac{\pi - 2}{8\pi}, \qquad C_2 = \frac{1}{8}. \tag{6.2.13}$$

Therefore, the $\mathcal{O}(\delta^2)$ solution is given by

$$g_2(\eta) = \frac{1}{8\pi}\left(\pi\left(1 - \operatorname{erf}\left(\frac{\eta}{\sqrt{2}}\right)^2\right) + \sqrt{2\pi}\exp\left(-\frac{\eta^2}{2}\right)\eta\operatorname{erfc}\left(\frac{\eta}{\sqrt{2}}\right) - 2\exp\left(-\eta^2\right)\right). \tag{6.2.14}$$

We remark that if we considered a uniform flow, that is, $\lambda = 1$, (6.2.3) has the exact solution $g = 1$, or $u = u_2$, as expected.

In Figure 6.2, we compare numerical solutions of (6.2.3) to the asymptotic approximation to (a) first order and (b) second order for different values of λ. We observe that the streamwise velocity profile is such that it satisfies the far-field boundary conditions with a smooth transition in the middle corresponding to the shear layer. Note that in order to conduct the numerical simulations, we have used the open-source software system Chebfun [21].

We plot the maximum absolute error between the numerics and asymptotics with respect to δ in Figure 6.3 with solid lines. It is clear that as δ increases, that is, as λ decreases and the difference in velocity between the two streams is larger, the error increases and the asymptotic approximation loses validity. However, we find a very good agreement even for values of δ close to 1. For instance, from Figure 6.3, we observe that for $\delta = 0.8$, the absolute error in both approximations is below 0.1, and approximately 0.05 for the second order asymptotics. Moreover, whereas the asymptotic approximation to second order performs considerably better than the first order one for small values of δ, both errors become very similar as δ approaches 1. This is due to the absolute errors being $\mathcal{O}(\delta^2)$ and $\mathcal{O}(\delta^3)$ for the first and second order asymptotics, respectively (see dashed lines in Figure 6.3).

6.2.2 Chemical-temperature subsystem

Since the remaining system of equations, (6.1.22), depends explicitly on the streamwise velocity u, we will use the results obtained in the previous section when solving for the chemicals, temperature and particle size distribution. As a consequence, the error found in the approximation for u will also show in the approximate solution for the rest of the variables.

To make progress on the system (6.1.22) outside of numerical simulations, we make

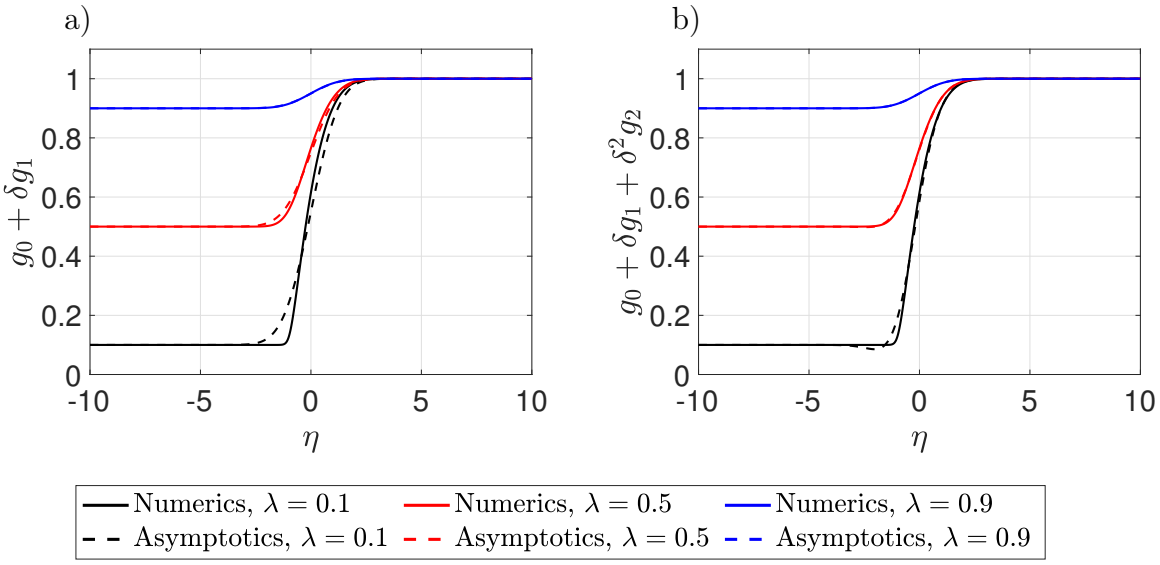

Figure 6.2: (a) Asymptotic approximation (6.2.4) to first order and (b) to second order (dashed lines) for different values of λ compared to numerical simulations (solid lines).

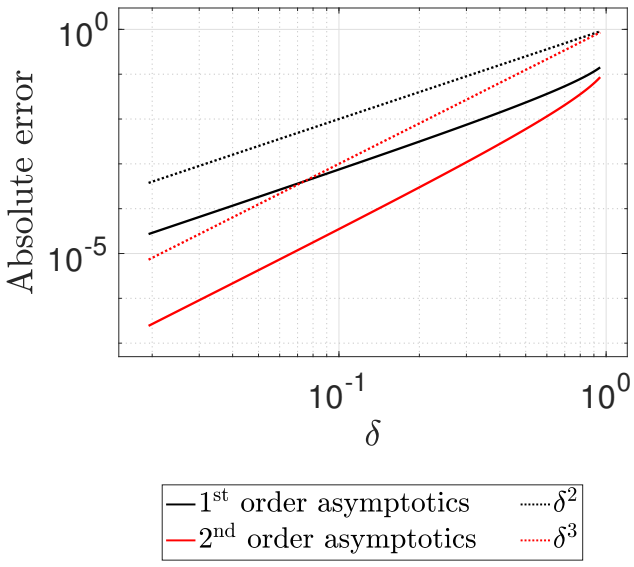

Figure 6.3: Maximum absolute error between the numerical simulations and asymptotic solution (6.2.4) to first order (black solid line) and second order (red solid line), from solving problem (6.2.3) for different values of δ. Recall that $\delta = 1 - \lambda$. The dashed lines correspond to the order of the error in the respective asymptotic approximation.

some simplifying assumptions. Similarly to Chapter 5, we neglect the slower reaction and the coupling to the particles by setting $\varepsilon = 0$ and $\zeta_1 = \zeta_2 = 0$. Furthermore, since d_{SiO} and Le are of order one, we set $d_{\mathrm{SiO}} = \mathrm{Le} = 1$, which will make our analysis easier. We remark that these assumptions are valid for early times in the process or in cases where more SiO_2 is produced than is consumed by particles. We will solve the full system numerically without taking any parameter sublimits in Section 6.3.

Under these assumptions, the chemical-temperature subsystem for the dominant reaction and without the effect of the particles becomes

$$\frac{\partial C_{\mathrm{O}_2}}{\partial x} - \frac{\partial}{\partial \psi}\left(u \frac{\partial C_{\mathrm{O}_2}}{\partial \psi}\right) = -\frac{a}{2u} f_1(T) C_{\mathrm{O}_2} C_{\mathrm{SiO}}, \tag{6.2.15a}$$

$$\frac{\partial C_{\mathrm{SiO}}}{\partial x} - \frac{\partial}{\partial \psi}\left(u \frac{\partial C_{\mathrm{SiO}}}{\partial \psi}\right) = -\frac{1}{u} f_1(T) C_{\mathrm{O}_2} C_{\mathrm{SiO}}, \tag{6.2.15b}$$

$$\frac{\partial T}{\partial x} - \frac{\partial}{\partial \psi}\left(u \frac{\partial T}{\partial \psi}\right) = \frac{1}{u} f_1(T) C_{\mathrm{O}_2} C_{\mathrm{SiO}}, \tag{6.2.15c}$$

with boundary conditions

$$C_{\mathrm{O}_2} = \mathcal{H}(\psi), \quad C_{\mathrm{SiO}} = \mathcal{H}(-\psi), \quad T = \mathcal{H}(-\psi) \quad \text{at} \quad x = 0. \tag{6.2.15d}$$

We note that system (6.2.15) is very similar to (5.3.1) and we will therefore analyse it in an analogous way, while making use of the approximation found for u, which appears as the diffusion coefficient and also in the reaction terms of all three equations.

Defining the quantities

$$w_1 = C_{\mathrm{O}_2} - \frac{a}{2} C_{\mathrm{SiO}}, \quad w_2 = T + h_1 C_{\mathrm{SiO}}, \tag{6.2.16}$$

we find from problem (6.2.15) that they satisfy the following two equations,

$$\frac{\partial w_1}{\partial x} = \frac{\partial}{\partial \psi}\left(u \frac{\partial w_1}{\partial \psi}\right), \tag{6.2.17a}$$

$$\frac{\partial w_2}{\partial x} = \frac{\partial}{\partial \psi}\left(u \frac{\partial w_2}{\partial \psi}\right), \tag{6.2.17b}$$

with far-field conditions

$$w_1 \to 1, \quad w_2 \to 0 \quad \text{as} \quad \psi \to \infty, \tag{6.2.17c}$$

$$w_1 \to -\frac{a}{2}, \quad w_2 \to 1 + h_1 \quad \text{as} \quad \psi \to -\infty. \tag{6.2.17d}$$

We notice that $u\left(x, \sqrt{\mathrm{Sc}}\psi\right)$ is a solution for both (6.2.17a) and (6.2.17b), since it satisfies (6.2.1a), and therefore, using the boundary conditions (6.2.17c)-(6.2.17d), we find solutions for w_1 and w_2 in terms of u, namely

$$w_1 = \frac{1}{u_2 - u_1}\left(\left(1 + \frac{a}{2}\right) u\left(x, \sqrt{\mathrm{Sc}}\psi\right) - u_1 - \frac{a}{2}u_2\right), \tag{6.2.18a}$$

$$w_2 = \frac{1 + h_1}{u_2 - u_1}\left(u_2 - u\left(x, \sqrt{\mathrm{Sc}}\psi\right)\right), \tag{6.2.18b}$$

for $u_2 \neq u_1$. For the uniform flow case, $u = u_2 = u_1$, we can solve (6.2.17) directly with appropriate Heaviside functions consistent with the boundary conditions to give

$$w_1 = \frac{1}{4}\left((2 + a)\,\mathrm{erf}\left(\frac{\psi}{2\sqrt{u_2 x}}\right) + 2 - a\right), \tag{6.2.19a}$$

$$w_2 = \frac{1 + h_1}{2}\left(1 - \mathrm{erf}\left(\frac{\psi}{2\sqrt{u_2 x}}\right)\right), \tag{6.2.19b}$$

which is equivalent to (5.3.4) in Chapter 5. Note that in the uniform flow case the stream function is given in terms of y by $\psi = u_2 y$.

From the definitions of w_1 and w_2, (6.2.16), we write

$$C_{\mathrm{O}_2} = w_1 + \frac{a}{2}C_{\mathrm{SiO}}, \tag{6.2.20a}$$

$$T = w_2 - h_1 C_{\mathrm{SiO}}, \tag{6.2.20b}$$

and using these expressions in (6.2.15b), the equation for the SiO concentration decouples from the others and becomes

$$\frac{\partial C_{\mathrm{SiO}}}{\partial x} - \frac{\partial}{\partial \psi}\left(u\frac{\partial C_{\mathrm{SiO}}}{\partial \psi}\right) = -\frac{1}{u}f_1\left(w_2 - h_1 C_{\mathrm{SiO}}\right)\left(w_1 + \frac{a}{2}C_{\mathrm{SiO}}\right)C_{\mathrm{SiO}}, \tag{6.2.21a}$$

which is subject to the inlet condition

$$C_{\mathrm{SiO}} = \mathcal{H}(-\psi) \quad \text{at} \quad x = 0. \tag{6.2.21b}$$

Hence, we have reduced the system of three PDEs (6.2.15) to a single PDE (6.2.21a). Applying the change of variables $x = H^2\tilde{x}$ and $\psi = H\tilde{\psi}$ into (6.2.21), in the next sections we will look for a solution of the SiO equation for two different regimes: $H \ll 1$ and $H \gg 1$. Note that the latter rescalings for x and ψ have been chosen such that the variable η defined in (6.2.2) is invariant under the transformation. That is, the small H limit corresponds to $\eta = \mathcal{O}(1)$ and $x, \psi \to 0$, whereas for the large H

limit we have $\eta = \mathcal{O}(1)$ and $x, \psi \to \infty$.

We remark that in this chapter, H represents an arbitrary parameter that has been introduced and is not related to the initial separation distance, H_s, mentioned in Chapter 5. Furthermore, as we already discussed in Chapter 5, to avoid introducing new parameters into our problem, we could instead write equations (6.2.21) in terms of x and η variables and then take the small and large x limits directly.

6.2.2.1 The small x regime: $H \ll 1$

Applying the latter change of variables, equation (6.2.21a) becomes

$$\frac{\partial C_{\mathrm{SiO}}}{\partial \tilde{x}} - \frac{\partial}{\partial \tilde{\psi}}\left(u \frac{\partial C_{\mathrm{SiO}}}{\partial \tilde{\psi}}\right) = -\frac{H^2}{u} f_1 \left(w_2 - h_1 C_{\mathrm{SiO}}\right)\left(w_1 + \frac{a}{2} C_{\mathrm{SiO}}\right) C_{\mathrm{SiO}}. \tag{6.2.22}$$

Taking the regular perturbation expansion

$$C_{\mathrm{SiO}} = C_{\mathrm{SiO}}^{(0)} + H^2 C_{\mathrm{SiO}}^{(2)} + \mathcal{O}(H^4), \tag{6.2.23}$$

the leading order problem is diffusion dominated and is given by

$$\frac{\partial C_{\mathrm{SiO}}^{(0)}}{\partial \tilde{x}} = \frac{\partial}{\partial \tilde{\psi}}\left(u \frac{\partial C_{\mathrm{SiO}}^{(0)}}{\partial \tilde{\psi}}\right), \tag{6.2.24a}$$

$$C_{\mathrm{SiO}}^{(0)} = \mathcal{H}(-\tilde{\psi}) \quad \text{at} \quad \tilde{x} = 0. \tag{6.2.24b}$$

As in the previous section, the solution to (6.2.24) can be written in terms of u, namely

$$C_{\mathrm{SiO}}^{(0)} = \frac{1}{u_2 - u_1}\left(u_2 - u\left(\tilde{x}, \sqrt{\mathrm{Sc}}\tilde{\psi}\right)\right) \tag{6.2.25}$$

for $u_1 \neq u_2$, and

$$C_{\mathrm{SiO}}^{(0)} = \frac{1}{2}\left(1 - \mathrm{erf}\left(\frac{\tilde{\psi}}{2\sqrt{u_2 \tilde{x}}}\right)\right) \tag{6.2.26}$$

for the uniform case, $u_1 = u_2$. We do not solve for higher order terms in the expansion (6.2.23) since the leading order approximation already shows a good agreement with the numerics. Note that the leading order approximations (6.2.25)-(6.2.26) found for C_{SiO} in the small x regime remain the same when we change back to our original coordinates x and ψ due to the similarity behaviour of the solution. Therefore, writing (6.2.25)-(6.2.26) in terms of our original coordinates and using (6.2.20), we have found the following approximate solutions to the system (6.2.15) for small x,

$$C_{\mathrm{SiO}}(x,\psi) = \begin{cases} \frac{1}{u_2-u_1}\left(u_2 - u\left(x,\sqrt{\mathrm{Sc}}\psi\right)\right) + \mathcal{O}(H^2), & u_1 \neq u_2, \\ \frac{1}{2}\left(1-\operatorname{erf}\left(\frac{\psi}{2\sqrt{u_2 x}}\right)\right) + \mathcal{O}(H^2), & u_1 = u_2, \end{cases} \tag{6.2.27a}$$

$$C_{\mathrm{O}_2}(x,\psi) = \begin{cases} \frac{1}{u_2-u_1}\left(u\left(x,\sqrt{\mathrm{Sc}}\psi\right) - u_1\right) + \mathcal{O}(H^2), & u_1 \neq u_2, \\ \frac{1}{2}\left(1+\operatorname{erf}\left(\frac{\psi}{2\sqrt{u_2 x}}\right)\right) + \mathcal{O}(H^2), & u_1 = u_2, \end{cases} \tag{6.2.27b}$$

$$T(x,\psi) = \begin{cases} \frac{1}{u_2-u_1}\left(u_2 - u\left(x,\sqrt{\mathrm{Sc}}\psi\right)\right) + \mathcal{O}(H^2), & u_1 \neq u_2, \\ \frac{1}{2}\left(1-\operatorname{erf}\left(\frac{\psi}{2\sqrt{u_2 x}}\right)\right) + \mathcal{O}(H^2), & u_1 = u_2. \end{cases} \tag{6.2.27c}$$

Alternatively, since $u_1 = \lambda u_2$, the latter approximations, as well as the rest of results in this chapter, can be written in terms of λ and u_2; for the asymptotic approximations, u_2 would only appear in the definition of the similarity variable η as in (6.2.2). Therefore, in all the plots that we will show in this chapter we have chosen to fix $u_2 = 10$ and only change the value of u_1, which we do by varying λ. Note that picking a different value for u_2 would only affect the plotting region for x (or x scale).

In Figure 6.4, we plot the approximations (6.2.27) (circles) for the O_2 (blue) and SiO (black) concentrations, and for the temperature (red) for small x, and compare them to numerical solutions (solid lines) of the system (6.2.15). We remark that we have used the approximation obtained for u in the previous section up to second order into (6.2.27), and we also plot it in Figure 6.4 with green circles. We solve the subsystem (6.2.15) numerically using the same numerical scheme that was employed in Section 5.3 for an equivalent system, that is, by the method of lines where we discretise the variables in ψ and treat x time like. This time we also need to include into the scheme the numerical solution for u that was obtained separately in Section 6.2.1.

We compare the results for different values of λ: $\lambda = 1$ (uniform flow), $\lambda = 0.7$ and $\lambda = 0.3$ from top to bottom in Figure 6.4, and at three different positions x along the mixing layer from left to right. Since the solution for the small x regime is purely diffusive, as x increases we observe all species diffusing into each other for all values of λ. Furthermore, as λ decreases, the reaction zone, which is roughly the area where both SiO and O_2 coexist, is narrower. As we expect, the small x approximation for the concentrations and temperature loses validity as x increases and the reactions

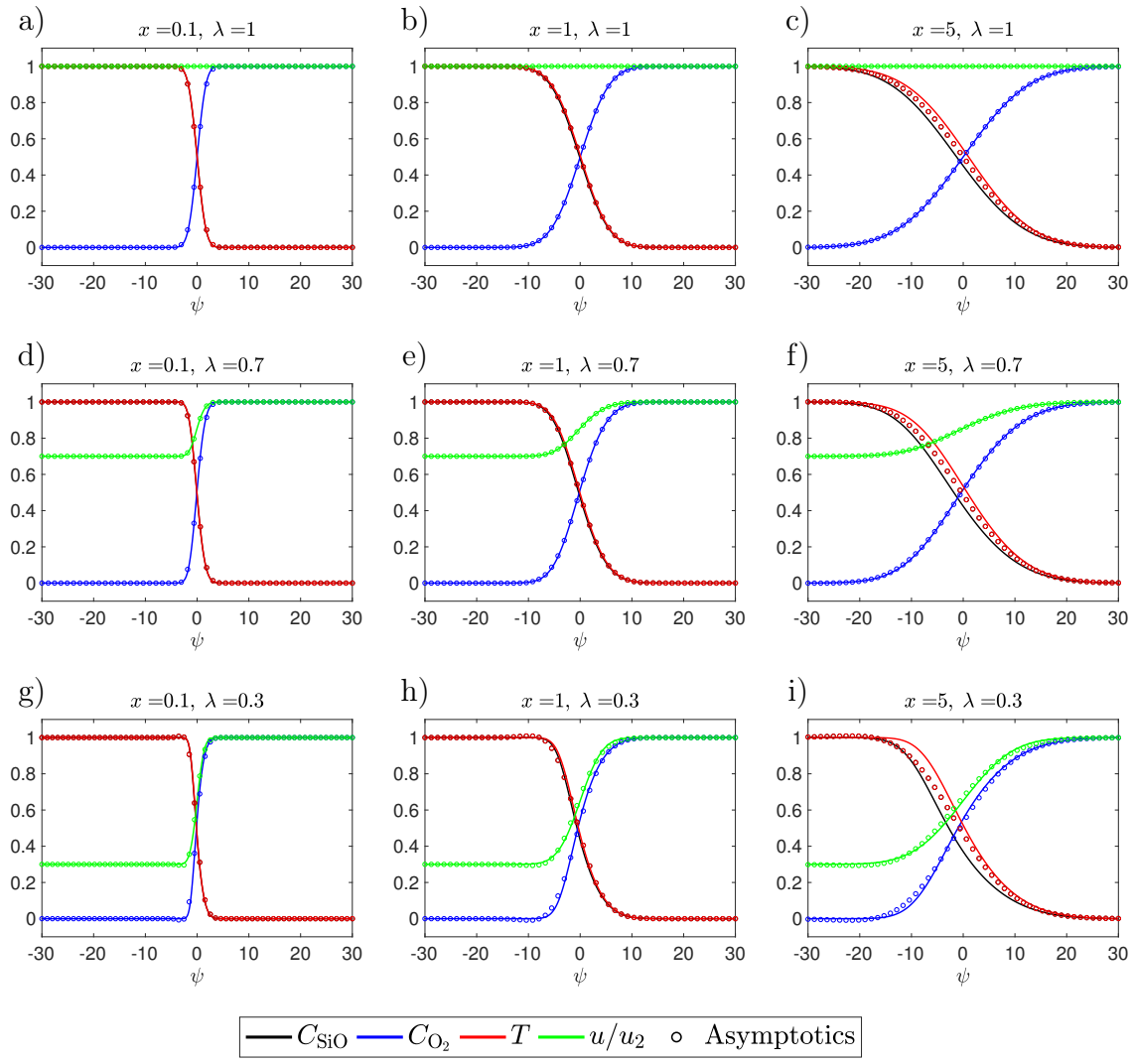

Figure 6.4: Asymptotic approximations for small x (6.2.27) (circles) compared to numerical simulations (solid lines) for $\lambda = 1, 0.7, 0.3$ from top to bottom and increasing values of x from left to right. Note that in some of the panels, especially (a), (d), and (g), the SiO concentration profile (black) is almost identical to the temperature profile (red) and therefore is hidden underneath the red line.

kick off, moving the SiO front towards the left of the domain. This approximation also becomes worse as λ decreases, and δ increases, since it depends directly on the approximation obtained for u.

6.2.2.2 The large x regime: $H \gg 1$

Whereas in the previous section, the solutions are mainly diffusive, in the large x regime reactions become more relevant. Setting $\epsilon = 1/H \ll 1$, equation (6.2.22) transforms to

$$\epsilon^2 \left(\frac{\partial C_{\mathrm{SiO}}}{\partial \tilde{x}} - \frac{\partial}{\partial \tilde{\psi}} \left(u \frac{\partial C_{\mathrm{SiO}}}{\partial \tilde{\psi}} \right) \right) = -\frac{1}{u} f_1 \left(w_2 - h_1 C_{\mathrm{SiO}} \right) \left(w_1 + \frac{a}{2} C_{\mathrm{SiO}} \right) C_{\mathrm{SiO}}. \quad (6.2.28)$$

As in Chapter 5, in order to solve (6.2.28) we use the WKB ansatz

$$C_{\mathrm{SiO}} = \exp\left(-\frac{V(\tilde{x}, \tilde{\psi})}{\epsilon} \right), \quad (6.2.29)$$

which puts (6.2.28) into the following form

$$\epsilon \left(\frac{\partial V}{\partial \tilde{x}} - \frac{\partial}{\partial \tilde{\psi}} \left(u \frac{\partial V}{\partial \tilde{\psi}} \right) \right) = \frac{1}{u} f_1(w_2) w_1 - u \left(\frac{\partial V}{\partial \tilde{\psi}} \right)^2 + \mathcal{R}. \quad (6.2.30)$$

We have neglected the small parameter a and define the error term

$$\mathcal{R} = \frac{w_1}{u} \left(f_1 \left(w_2 - h_1 C_2 \right) - f_1 \left(w_2 \right) \right), \quad (6.2.31)$$

which can be shown to be exponentially small in the regimes under study, similarly to Chapter 5. Expanding V as

$$V = V_0(\tilde{x}, \tilde{\psi}) + \epsilon V_1(\tilde{x}, \tilde{\psi}) + \mathcal{O}(\epsilon^2) \quad \text{as} \quad \epsilon \to 0, \quad (6.2.32)$$

at leading order, (6.2.30) becomes

$$u \left(\frac{\partial V_0}{\partial \tilde{\psi}} \right)^2 = \frac{1}{u} f_1(w_2) w_1. \quad (6.2.33)$$

Solving for V_0 and taking the positive root so that the expansion in the WKB ansatz gives decay rather than blow-up for large x, we find

$$V_0(\tilde{x},\tilde{\psi}) = \sqrt{2\mathrm{Sc}u_2\tilde{x}}\int_{-\infty}^{\frac{\tilde{\psi}}{\sqrt{2\mathrm{Sc}u_2\tilde{x}}}-\eta_0}\frac{1}{u(\sigma)}\sqrt{f_1(w_2(\sigma))w_1(\sigma)}\mathrm{d}\sigma, \tag{6.2.34}$$

where we have chosen the integration limits so that the solution for C_{SiO} satisfies the far-field conditions given by (6.2.15d), and where we have applied an appropriate change of variables so that the form of the solution is consistent with our previous analysis. Hence, changing back to our original coordinates, the final solution for the SiO concentration is approximated by

$$C_{\mathrm{SiO}} \sim \exp\left(-\sqrt{2\mathrm{Sc}u_2x}\int_{-\infty}^{\frac{\psi}{\sqrt{2\mathrm{Sc}u_2x}}-\eta_0}\frac{1}{u(\sigma)}\sqrt{f_1(w_2(\sigma))w_1(\sigma)}\mathrm{d}\sigma\right), \tag{6.2.35}$$

with $x \gg 1$. Since information about the initial configuration is lost in this large x limit, we have shifted the upper limit of the integral in (6.2.34) by η_0. This parameter will be used to calibrate the approximation to numerical simulations. In order to obtain the approximate solutions for the O_2 concentration and the temperature, we substitute (6.2.35) into (6.2.20).

In Figure 6.5, we show the large x approximations (circles) for the chemicals and temperature as given by (6.2.35) and using (6.2.20), for $\lambda = 1$ (uniform flow), $\lambda = 0.7$ and $\lambda = 0.5$ from top to bottom, and for increasing values of x from left to right. Unlike with the small x case, in (6.2.35) we use the approximate solution obtained for u to first order since we encounter integration issues when using the second order term, especially for small values of λ. We compare the approximations to numerical solutions (solid lines) of the system (6.2.15). Moreover, we have taken the free parameter η_0 found in (6.2.35) such that the numerics and asymptotics match at the unique value where $C_{\mathrm{SiO}} = 0.5$, for $x = 1000$. Note that this parameter will change depending on the value of λ. We observe that the large x asymptotic solutions agree well with the numerics, especially for large values of x as expected, and for large values of λ where the error from the approximation of u is smaller.

Looking at the dynamics of all variables in Figure 6.5, we notice that as x increases, the SiO front moves towards the left as it is being used up in the reaction, while O_2 diffuses towards the region mostly occupied by SiO. As the reaction takes place, the temperature increases within the reaction zone. The main differences between the numerics for $\lambda = 1$, which corresponds to both streams having the same velocity, and

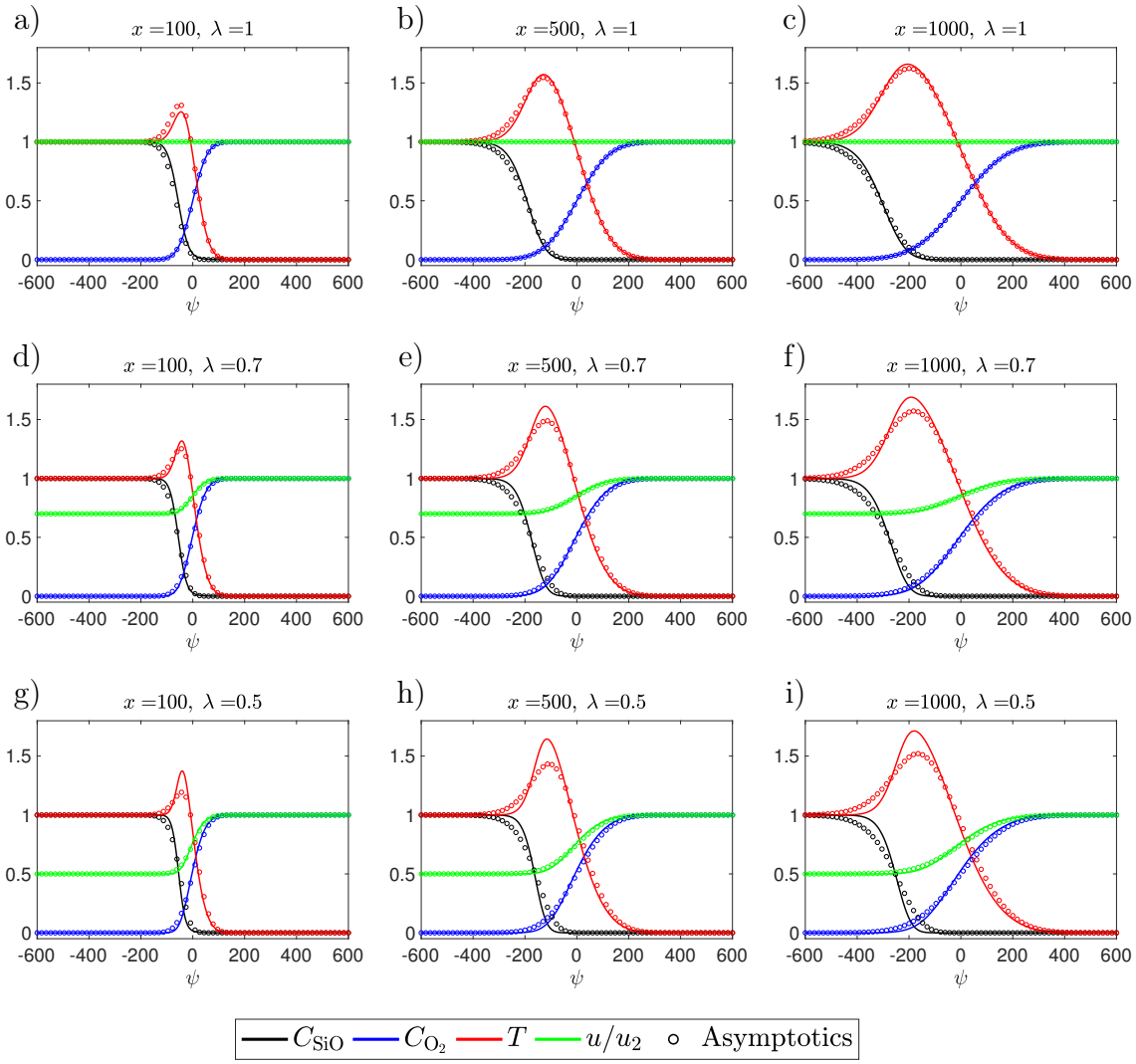

Figure 6.5: Asymptotic approximations (circles) for large x compared to numerical simulations (solid lines) for $\lambda = 1, 0.7, 0.5$ from top to bottom and increasing values of x from left to right. We show the solution for the SiO (black) and O_2 (blue) concentrations, temperature (red), and streamwise velocity (green).

for $\lambda = 0.5$, for instance, where the velocity of one stream doubles the other, are the extent of the reaction zone and the temperatures reached in it. With similar velocities in both streams, the spatial extent of the reaction zone is larger and the temperature increase is smaller. The opposite effect is found when the difference in velocities is large. Note that we may draw different conclusions after transforming back the results to our original coordinates, (x, y), and after re-incorporating the effect of the particles in the chemical-thermal system, which we will do when we solve the fully-coupled system numerically in Section 6.3.

In Figure 6.6 we show heatmaps for the large x asymptotic approximations that we have obtained, with respect to the original independent variables (x, y). For this, we have used the von Mises inversion formula (6.1.24). These plots will prove useful later on for comparison with the numerical solution of the fully-coupled problem shown in Figure 6.8. As before, we show the solution for the SiO and O_2 concentration, and for the temperature, for $\lambda = 1, 0.7, 0.5$ from top to bottom. Note that in all cases we take $x \in [100, 1000]$ since the approximations are only valid for large x. From these panels, it is even clearer that the SiO is being pushed down by the oxygen, which is more plentiful and is mainly present at the top of the domain. Furthermore, as λ becomes closer to 1 and the flow is almost uniform, the chemicals spread less across the domain. On the other hand, our asymptotic approximations predict a lower temperature when λ is small, but this will not be the case when we re-incorporate the heat source due to particle formation in the fully-coupled case in Section 6.3.

6.2.3 Sensitivity analysis

In all the plots that we have shown so far in this section (Figures 6.4-6.5), we have taken $\mathrm{Sc} = 0.9$, computed from values in Table 2.2, and $\mathrm{Le} = d_{\mathrm{SiO}} = 1$ and $a = 0$ to be consistent with the assumptions taken in the asymptotic approximations. We will now explore how the numerical solution for the subsystem (6.2.15) changes as we vary the value of these parameters. As a reminder, the latter dimensionless parameters are defined as follows

$$\mathrm{Sc} = \frac{\nu}{D_{\mathrm{O_2}}}, \quad \mathrm{Le} = \frac{\kappa}{D_{\mathrm{O_2}}}, \quad d_{\mathrm{SiO}} = \frac{D_{\mathrm{SiO}}}{D_{\mathrm{O_2}}}, \quad a = \frac{C_{\mathrm{SiO},0}}{C_{\mathrm{O_2},0}}. \tag{6.2.36}$$

The Schmidt (Sc) and Lewis (Le) numbers are used to comparing the thickness of the viscous and thermal boundary layers to the diffusional boundary layer thickness, respectively. The parameter d_{SiO} indicates how fast SiO diffuses relative to the oxygen, and a represents the ratio between the input concentrations of SiO and O_2. We remark

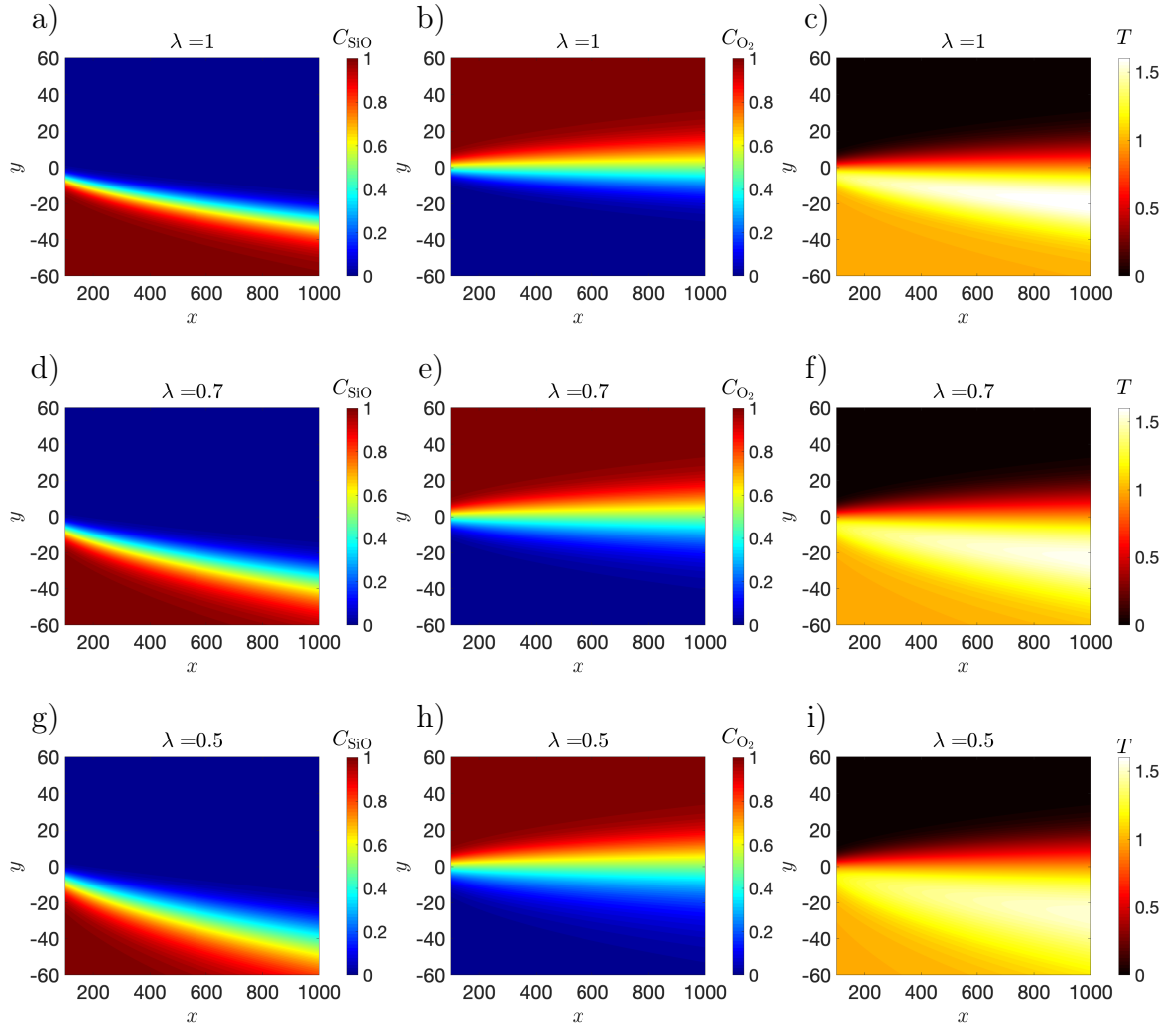

Figure 6.6: Asymptotic approximation for large x for the SiO concentration, O_2 concentration and temperature from left to right, and for $\lambda = 1, 0.7, 0.5$ from top to bottom. Note that we are showing heatmaps of the solution with respect to the original coordinates (x, y).

that in order to solve the system (6.2.15) numerically, we first use the open-source software system Chebfun [21] to obtain a numerical approximation for the streamwise velocity u. We then proceed in a similar manner to how we solved the subsystem (5.3.1) in Chapter 5, and use the method of lines by discretising the PDEs (6.2.15) in ψ and integrating the resulting ODEs in x.

In Figure 6.7, we show the numerical results for the subsystem (6.2.15) at a fixed position along the mixing layer, $x = 500$, and for $\lambda = 0.9, 0.5$, while increasing the values of the parameters described in (6.2.36) as indicated by the direction of the black arrow. First, in Figures 6.7 (a)-(b) we compare the numerical results for three different values of the Schmidt number: $\mathrm{Sc} = 0.1$ with diffusion occurring in a layer of thickness larger than the viscous boundary layer, $\mathrm{Sc} = 1$ where the viscous and diffusion boundary layer thickness are the same, and $\mathrm{Sc} = 10$ with the diffusion boundary layer being much smaller than the viscous one. From the plots we deduce that changes in the parameter Sc will only affect the width of the viscous boundary layer (see green lines), whereas the chemical concentrations and temperature remain almost the same, especially for large values of λ.

We observe a similar effect when varying the Lewis number in Figures 6.7 (c)-(d), since only the thickness of the thermal boundary layer and the magnitude of the temperature within it are affected, with the other variables remaining the same. On the other hand, when we increase the dimensionless diffusivity of SiO, d_{SiO}, in Figures 6.7 (e) and (f), more SiO diffuses into the region where oxygen is present, making the reaction more powerful since there is more material available for the reaction, and therefore the SiO is consumed more quickly and its front moves towards the left. This has an effect on the temperature within the reaction zone which experiences a further increase since more material reacts.

Finally, we have only selected values for a that are smaller than 1, and in the range defined in Table 4.1, since throughout this thesis we have considered that the input concentration of O_2 is always much larger than the one corresponding to the other chemicals. From Figures 6.7 (g) and (h) we deduce that the larger a is, the smaller the reaction zone will be, since there is not as much oxygen pushing the SiO front towards the left. This also means that less heat is generated from the reactions and thus the temperature within the reaction zone is smaller. However, we conclude that changes in the parameter a do not strongly affect the results.

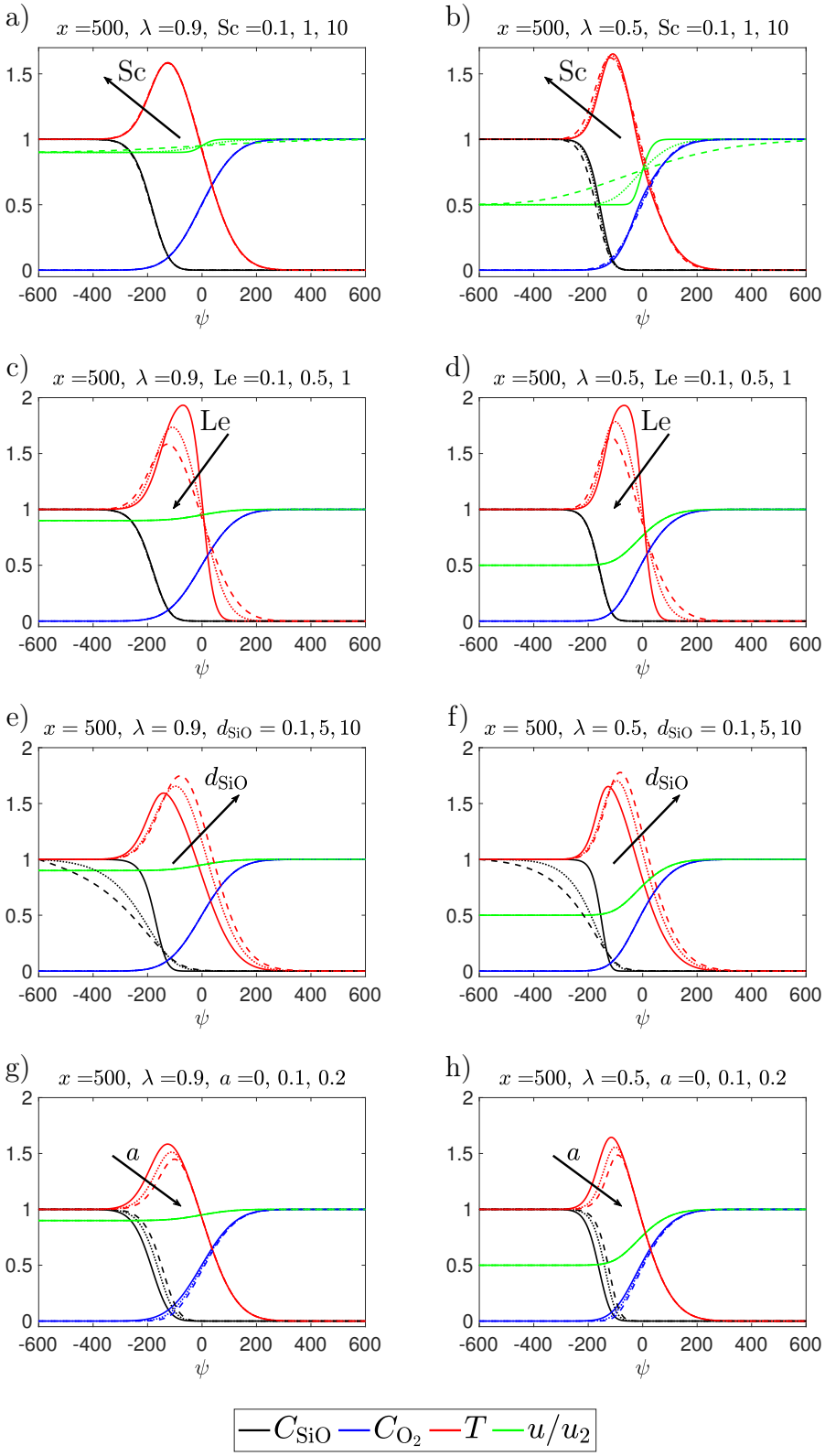

Figure 6.7: Numerical solution of the system (6.2.15) for $\lambda = 0.9, 0.5$ from left to right and $x = 500$. In (a)-(b) we vary the parameter Sc, in (c)-(d) we vary Le, in (e)-(f) we vary d_{SiO}, and in (g)-(h) we vary a. In all figures, the value of the varying parameter increases with the direction of the arrow.

6.3 Numerical solution to the stationary fully-coupled mixing layer problem

In the previous sections, we obtained solutions for a chemical-thermal subsystem, and one of the major assumptions that we took was neglecting the effect of particle formation and growth. However, in reality we know that at later stages in the process when particle formation dominates, the loss of SiO_2 and heat source due to material condensing into particles become relevant aspects that need to be included in the modelling. In this section, we numerically solve the fully-coupled problem (6.1.21)-(6.1.22) in terms of the transformed variables (x, ψ). In the second part of this section, we will use these results to compute the particle size distribution in a similar manner to Chapters 4 and 5. In all cases, we will present the solutions after transforming the independent variable ψ back to our original coordinate y by making use of the von Mises inversion formula (6.1.24). Furthermore, we are interested in comparing how the solution is affected by different velocity ratios, λ, and will therefore show all results in this section for $\lambda = 0.9$ (almost uniform flow) and $\lambda = 0.3$.

6.3.1 Chemical-thermal problem coupled to the moments of the particle size distribution

Since the momentum equation (6.1.21) decouples from the rest, we use for u the numerical solution obtained in Section 6.2.1. Then we solve for the concentrations, temperature, and moments using the same numerical scheme as in Section 5.4 of Chapter 5, that is, with the method of lines by discretising all variables in ψ and treating x as time like.

In Figure 6.8 we show heatmaps for the (a)-(b) SiO and (c)-(d) SiO_2 concentrations, and for the (e)-(f) temperature, with the flow streamlines represented by dashed lines, the latter obtained by solving the system (6.1.21)-(6.1.22) numerically. The colours of the heatmaps represent the magnitudes of the variables and the spatial domain where it is plotted corresponds to the same configuration presented in the schematic in Figure 6.1. That is, with x on the horizontal axis being the streamwise coordinate, and y the transverse coordinate to the mixing layer. We observe that the SiO in (a)-(b) is consumed as the reactions occur and it is pushed by the more plentiful oxygen towards the bottom of the domain. At the same time, SiO_2 is produced, as in (c)-(d), which is then consumed in the streamwise direction due to the formation and growth of the particles. With respect to the temperature, it is lowest on the top of the domain which

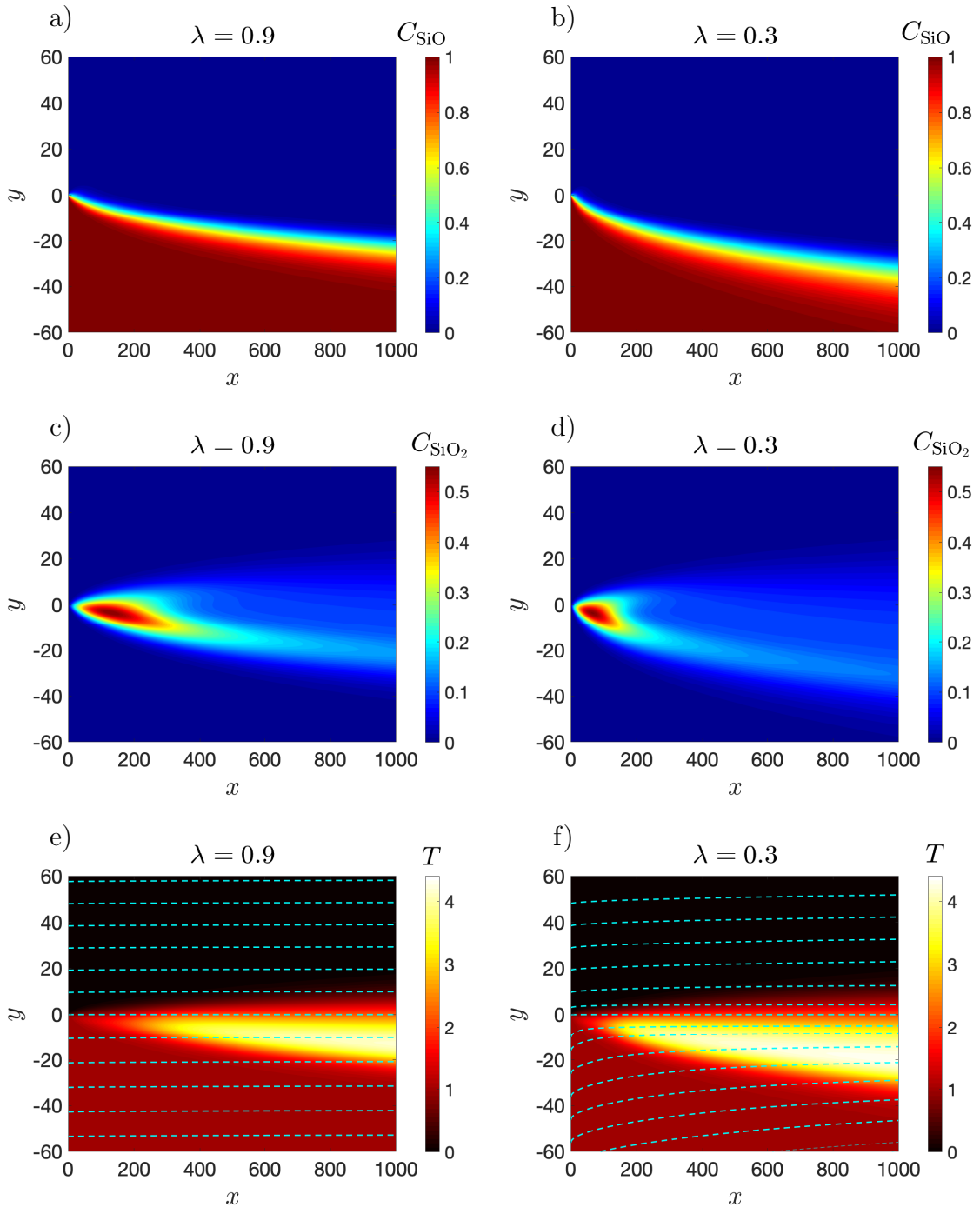

Figure 6.8: Numerical solution of the fully coupled system (6.1.21)-(6.1.22) for (a)-(b) SiO concentration, (c)-(d) SiO_2 concentration, and (e)-(f) temperature with dashed lines indicating the flow streamlines. We compare the cases: $\lambda = 0.9$ (almost uniform flow) and $\lambda = 0.3$.

is mostly occupied by oxygen, and it takes an intermediate value in the bottom region where the SiO is located. As both streams mix and react, the temperature increases within the reaction zone, before experiencing at larger x a further increase within the region where particles form and grow. Comparing the results for the two different values of λ, we conclude that when λ is small, there is more mixing of the chemicals initially, making the reactions more powerful. Therefore, for the $\lambda = 0.3$ case, the rate of SiO consumption is larger and therefore the majority of SiO_2 is produced at earlier stages of the process. As a consequence, the temperature reaches a larger value within the reaction zone when $\lambda = 0.3$. The latter statements are consistent with the conclusions that we drew from the COMSOL simulations of the furnace hood in Chapter 3 when comparing two velocity ratios.

The results for the particle size distribution are shown in Figure 6.9 where we plot (a)-(b) the number of particles density, M_0, (c)-(d) mean particle size, $\mu = M_1/M_0$, and (e)-(f) variance, $\sigma^2 = M_2/M_0 - \mu^2$, over space. As expected, the majority of the particles are located toward the middle of the reaction zone, and their number is larger further along the streamwise direction, similar to the behaviour seen from the COMSOL simulations in Chapter 3. However, the largest particles are found initially around the area where the SiO_2 reaches its maximum value, with smaller particles forming further along due to less SiO_2 being available for condensation. The variance is the largest towards the middle of the mixing layer where the particle size is the largest. There is a clear difference in the moments of the distribution between the two cases, $\lambda = 0.9$ and $\lambda = 0.3$. First, we notice that the number of particles density is larger when there is more mixing involved and $\lambda = 0.3$, similarly to what we found in the COMSOL simulations in Chapter 3. This is likely because when $\lambda = 0.3$, many more small particles are found especially towards the bottom part of the reaction layer, as seen in (d).

The latter conclusions about the number density and size of the particles are quantified further in Figure 6.10 where we integrate the results in space for four different values of λ. The three panels on the top of Figure 6.10 correspond to integrating along y, the total number of particles density, the mean particle size, and also the amount of material consumed by the particles, from left to right. The latter quantity comes from the sink of material included in the equation for the SiO_2 concentration, (6.1.15c), which is proportional to the growth rate times the second moment of the distribution, and inversely proportional to the streamwise velocity, that is, $\zeta_1 G M_2/u$. In the panels in the middle we show the same variables as before but the results are integrated along x. This allows us to understand the variations in the

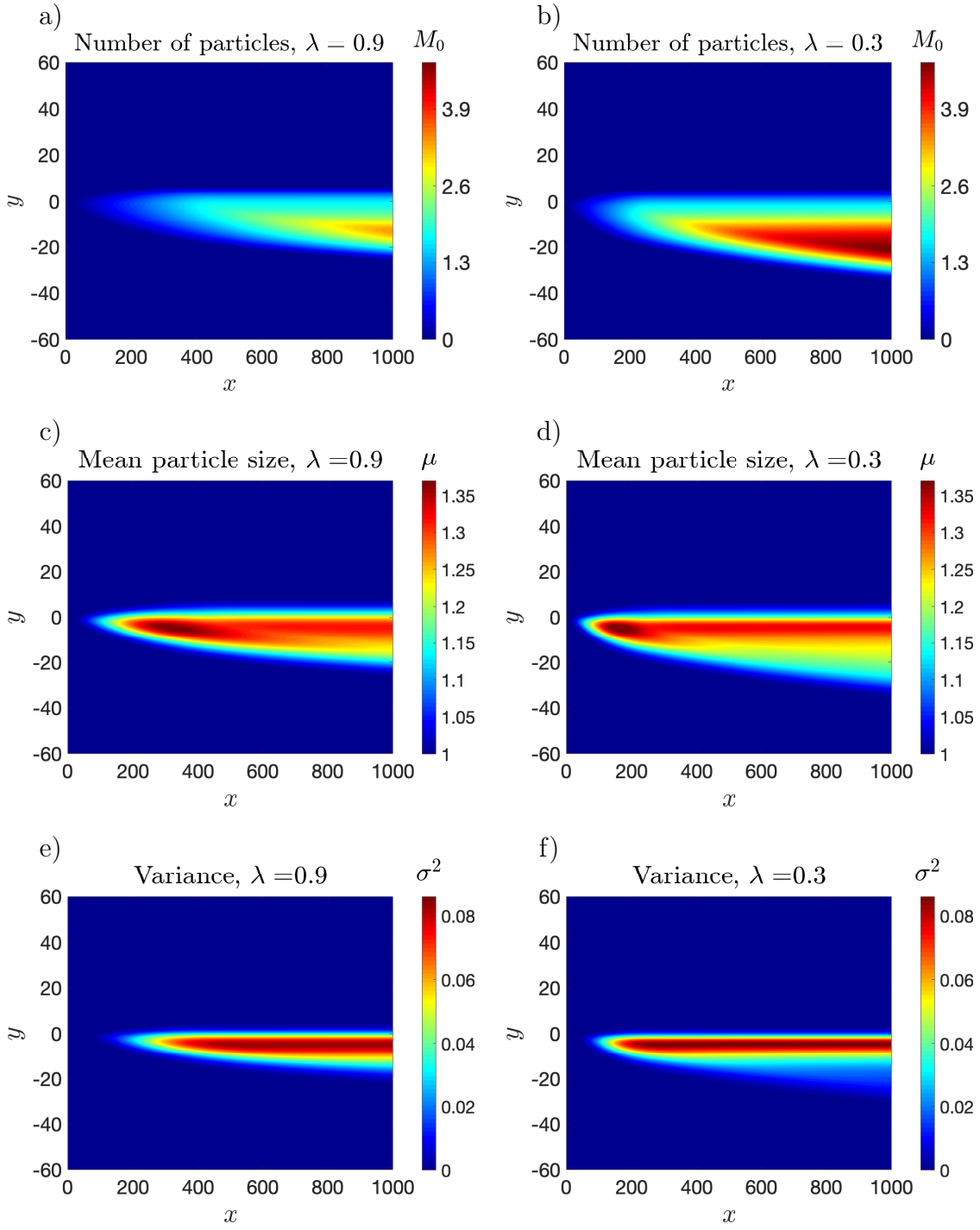

Figure 6.9: Number of particles density, M_0, mean particle size, $\mu = M_1/M_0$, and variance, $\sigma^2 = M_2/M_0 - \mu^2$, of the particle size distribution, from top to bottom. The panels on the left correspond to $\lambda = 0.9$ and the panels on the right to $\lambda = 0.3$. These results are from solving the system (6.1.21)-(6.1.22) numerically.

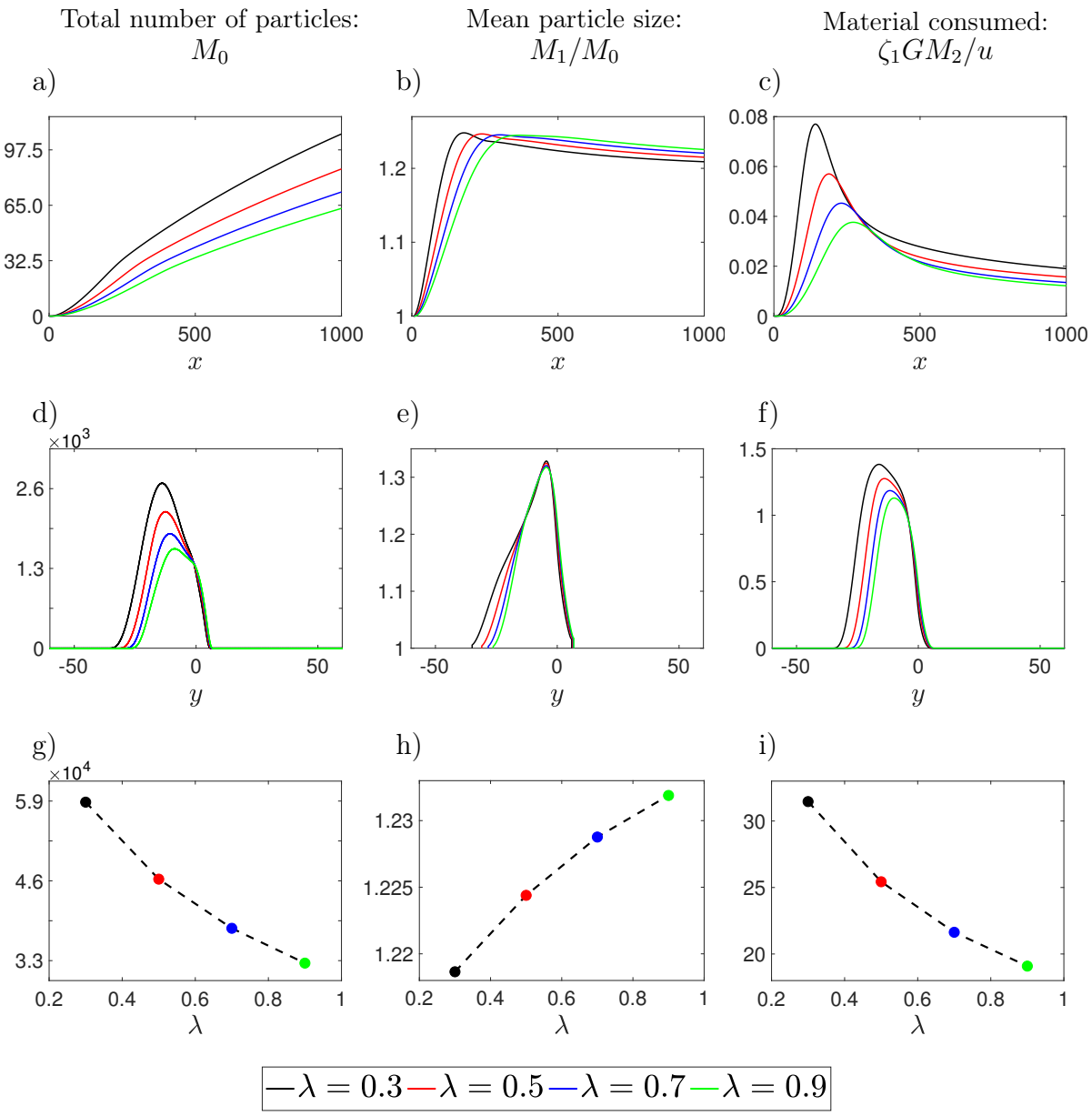

Figure 6.10: (a), (d) and (g) Total number of particles, (b), (e) and (h) mean particle size, and (c), (f) and (i) material consumed from particle formation and growth, for $\lambda = 0.3, 0.5, 0.7, 0.9$. The panels on the top correspond to the results from solving (6.1.21)-(6.1.22) integrated along y, the panels in the middle from integrating the results along x, and the panels on the bottom correspond to the results integrated along the whole spatial domain.

distribution of particles perpendicular to the main direction of the flow, and therefore to compare the current solution to the results from Chapter 5 where we looked at a cross-section of the reaction zone.

The three panels on the bottom of Figure 6.10 correspond to the solution integrated across the whole spatial domain, since ultimately we are interested in the final output of microsilica particles. We conclude that when the velocities of the two streams are very different, and hence λ is small, more particles form, and they are smaller overall. From (b) we notice that the mean particle size increases very rapidly initially in the mixing layer, especially for small λ, reaching a maximum value, and then decreasing very slightly due to smaller particles forming, which decreases the mean. Additionally, more material is consumed by the particles when λ is small and there is more mixing between the two streams, which is consistent with the larger heat release due to the particles apparent in Figure 6.8 (f) compared to (e).

6.3.2 Particle size distribution

The reduced population balance equation in terms of (x, ψ, s), (6.1.23), resembles the population balance equation that we solved for in the spatially separated case in Chapter 5. However, the incorporation of fluid flow will affect the size of the particles and, as it can be seen from the form of (6.1.23), the growth rate is inversely proportional to the streamwise velocity, u.

We solve for (6.1.23) subject to the boundary conditions (6.1.17) by the method of characteristics, as we have done so in the previous two chapters, and we obtain a very similar implicit solution to (5.2.1), namely

$$n = \frac{J(x_1, \psi)}{G(x_1, \psi)}, \quad s = 1 + G^* \int_{x_1}^{x} \frac{G(\tilde{x}, \psi)}{u(\tilde{x}, \psi)} \mathrm{d}\tilde{x}, \quad x_1 > x_{\min}(\psi). \tag{6.3.1}$$

Note that the critical value $x = x_{\min}$ such that $C_{\mathrm{SiO_2}} = C_{\mathrm{sat}}$ now depends on ψ. In other words, we first need to find the spatial domain of definition of the solution (6.3.1), (x_0, ψ_0), such that, $C_{\mathrm{SiO_2}}(x_0, \psi_0) \geq C_{\mathrm{sat}}$. Outside of this region, $n = 0$, since the growth rate is zero by definition.

In Figure 6.11 (a)-(d), we plot heatmaps for the number density function, n, with the vertical axis indicating particle size, s, and the horizontal axis representing the position across the mixing layer, y. We compare the results for two different positions along the streamwise direction, $x = 250$ and $x = 1000$ from top to bottom, and for two different velocity ratios, $\lambda = 0.9$ and $\lambda = 0.3$ from left to right. Heatmaps allow

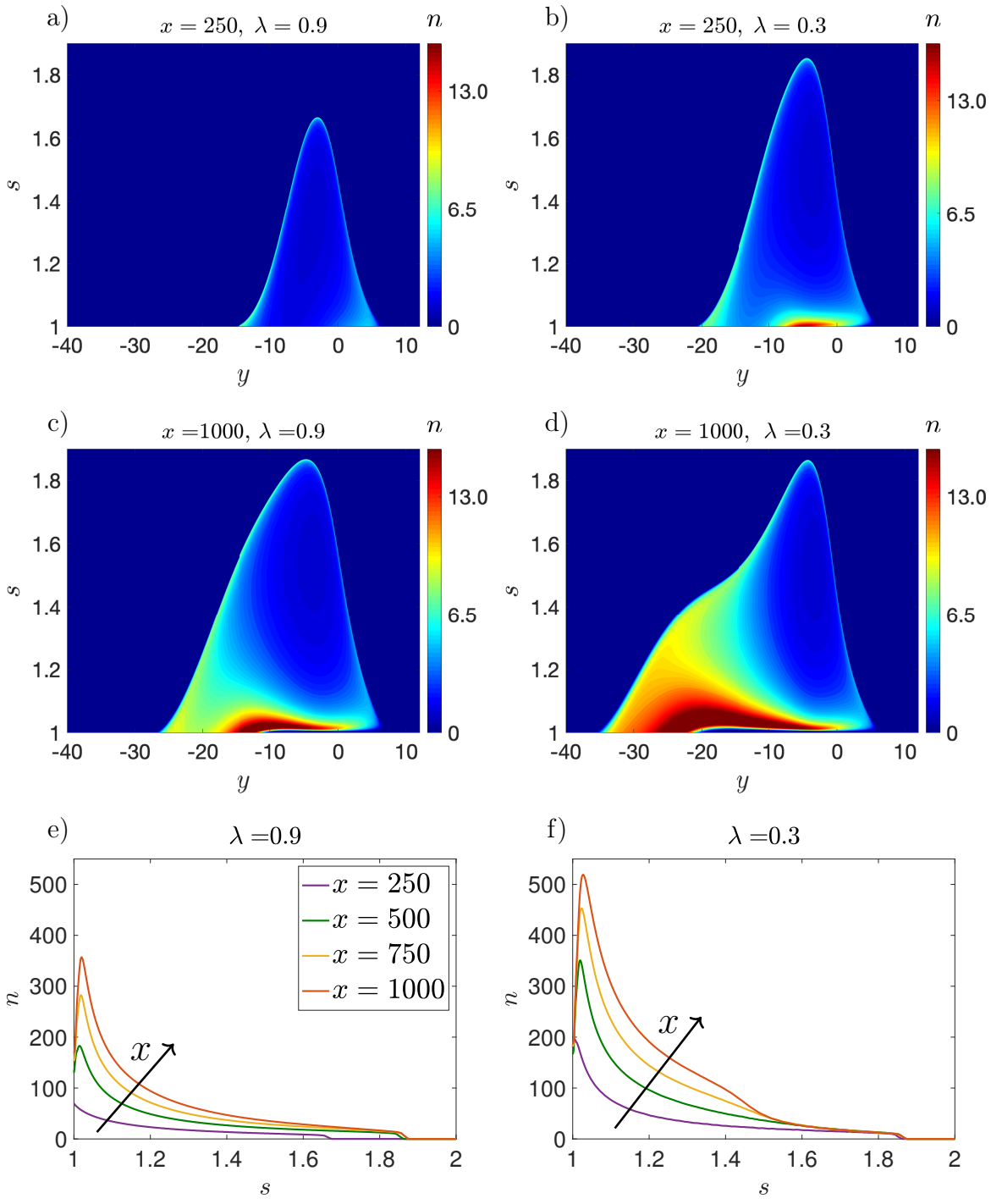

Figure 6.11: (a)-(d) Heatmaps for the number density function as given by (6.3.1) and using the numerical solution for C_{SiO_2} and T obtained from solving (6.1.22), at two different positions along the mixing layer, $x = 250$ and $x = 1000$, from top to bottom. (e)-(f) Particle size distribution after integrating the results for n along y, for increasing values of x as indicated by the direction of the arrow. In all cases, the solutions are for $\lambda = 0.9$ and $\lambda = 0.3$ from left to right.

us to see how the different-size particles are distributed in space. As expected, as x increases, the number and size of the particles increases, with smaller particles found around the edges of the mixing layer, and larger ones located in the middle. As x increases we also observe a high production of very small particles across the whole reaction zone (red regions in the bottom of (c)-(d)), due to the lack of enough material for particle growth. In order to better understand how the number density function of particles evolves as x increases, we have integrated the solution for n along y and show the results in Figure 6.11 (e)-(f) for increasing values of x, as indicated by the direction of the arrow, and for (e) $\lambda = 0.9$ and (f) $\lambda = 0.3$.

From Figure 6.11, we see a clear difference between different flow configurations. When there is more mixing of the streams initially, and $\lambda = 0.3$, there is more material available originally and therefore particles grow faster, and as a consequence they reach their maximum possible size earlier in the mixing layer compared to the $\lambda = 0.9$ case. This is expected from the form of equation (6.1.23), which implies that growth rates are larger when the flow is slower. As a consequence, less material is available downstream for $\lambda = 0.3$, and therefore, more particles will form but they will be smaller, and we obtain the asymmetric shape found in (d) and (f). Whereas for $\lambda = 0.9$, the flow is more uniform and therefore the distributions remain more symmetric, as in (c) and (e). Note that in both cases, the reaction zone moves towards the left (or bottom of the mixing layer) due to the oxygen being more plentiful, and therefore we will find more particles forming around this area. Since the width of the reaction zone, as in Figure 6.8, is wider when $\lambda = 0.3$, so is the spatial extent of the region where particles are present, as in Figure 6.11 (d). In conclusion, when the velocities of both streams are similar, fewer particles form but they are larger, and this is due to longer retention times in high SiO_2 concentration areas.

In order to further quantify these conclusions, we compute the total particle size distribution obtained in the whole mixing layer. This is useful for practical purposes, since ultimately Elkem ASA is interested in the specifics of the total microsilica output from a furnace. We integrate the results obtained in Figure 6.11 along x and y and show the normalised version of the total particle size distribution in Figure 6.12 (a) for different values of λ. We have normalised n by the corresponding total number of particles for each λ so that we can make better comparisons between each of the cases. We conclude that the total particle size distribution of microsilica is not greatly affected by the ratio of velocities although the number of particles in a particular region of space is. However, if we plot the particle mass distribution, as in Figure 6.12 (b), we observe that as λ increases, more of the particle mass in the final product

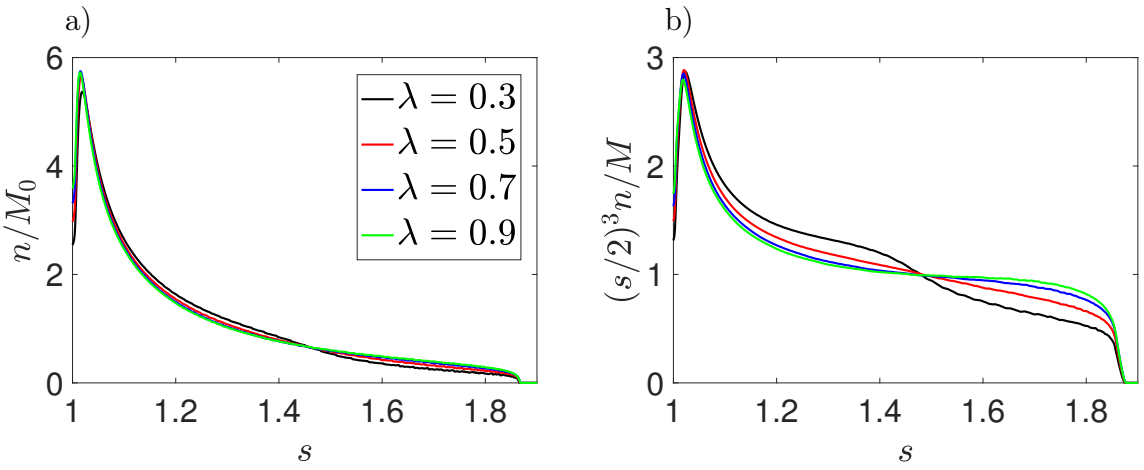

Figure 6.12: Total particle (a) size and (b) mass distributions for different values of the ratio of velocities, λ. These results are obtained from integrating the solution for n along x and y. We have normalised the results in (a) by the total number of particles, M_0, and the plots in (b) by the total particle mass, $M = \int_{s_{\min}}^{\infty} (s/2)^3 n \mathrm{d}s$, for each value of λ.

corresponds to larger particles. On the other hand, when λ is small, more of the mass is allocated towards smaller sizes. We have also normalised these plots by dividing by the total particle mass, $M = \int_{s_{\min}}^{\infty} (s/2)^3 n \mathrm{d}s$, for each λ value. One interesting aspect of the results shown in Figure 6.12 is that the maximum particle size found, approximately $s = 1.875$, is independent of the value of λ.

6.3.3 Experimental data

The asymptotic approximations obtained for the different models considered so far in this thesis have been validated with numerical simulations. However, it would also be beneficial to compare the results with experimental data. Due to the high temperatures within the reaction zones and the high speed of the combustion reactions, experiments are challenging to perform. Furthermore, only particle size distributions of the final microsilica output after filtering and bagging are usually measured. These samples contain agglomerate structures which form after particles leave the furnace hood, and therefore comparisons with our current results are more difficult. In addition, particle size distributions of samples are generally obtained using a laser diffraction particle size analyser. This technique consists on exposing the particles to a laser beam, causing the laser to scatter and diffract, and a sensor measures the intensity of the light that is received. This data is then processed and fitted to a prescribed distribution [22].

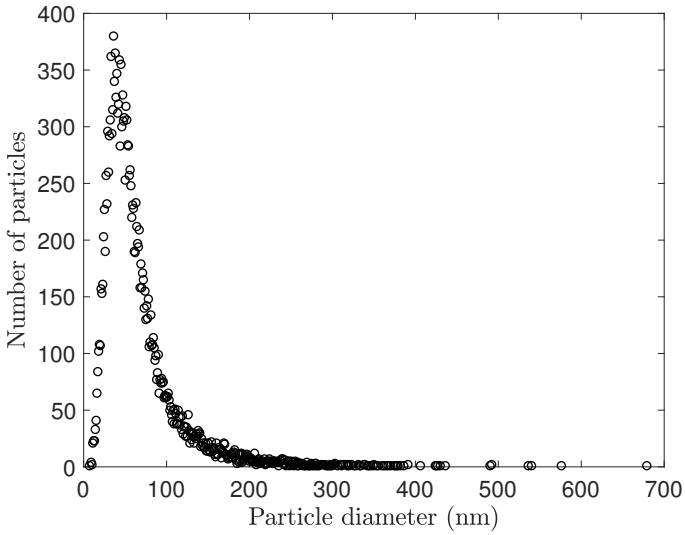

Figure 6.13: Experimental data obtained from SEM pictures of microsilica samples taken from the furnace exhaust pipe. We acknowledge Elkem ASA for collecting the samples and providing the data.

As part of some experiments performed by Elkem ASA aiming to collect primary microsilica particles, samples were collected from the furnace exhaust pipe. In order to overcome the fact that a distribution is fitted to the data when using laser diffraction, the particle size distribution was obtained by extracting data from SEM pictures of the new samples. In Figure 6.13, we show the results for a total of approximately 2×10^4 particles. The distribution has the same qualitative behaviour to the one obtained both in Chapter 5 and in the current chapter after integrating n in space. This corresponds to Figures 5.7 (b) and 5.12 (e) for large times, and Figure 6.12, respectively. The particle size distribution in Figure 6.13 also contains a peak towards the smallest particle sizes with a tail towards larger particles, which means that we have replicated the trend in the way in which particles form and grow. However, particles seem to be larger in the experiments, which may be due to the presence of aggregation which has not been studied in our work. A more robust comparison with the work presented in this thesis could be made by first, increasing the sample size of particles in the experiments, and second, by analysing data obtained from furnaces operating under different strategies.

6.4 Conclusions

Motivated by the results from the COMSOL simulations in Chapter 3, we have extended the work from Chapters 4 and 5 to two dimensions, by focusing on a reaction zone while considering more realistic fluid mechanics. Since the reaction zone where the combustion reactions occur is narrow and long, diffusion in the streamwise direction can be neglected, and the boundary layer equations for all variables were derived. Under the mixing layer configuration, the focus of the chapter was to explore the effects of mixing between the two streams that interact, on the reactions, and ultimately on the particle growth.

Before attempting a solution to the system, we transformed all equations by applying the von Mises transformation. Under this change of variables, the reaction-diffusion-convection equations for the chemicals, temperature and moments of the distribution become reaction-diffusion PDEs with a non-constant diffusion coefficient equal to the streamwise velocity. Moreover, the equations for the flow transform to a diffusion equation for the streamwise velocity, u, and we lose the dependence on the transverse velocity, v. The resulting steady-state equation for u decouples from the rest of equations and was solved numerically and asymptotically by perturbing the boundary data and assuming that the ratio of velocities of both streams, $0 < \lambda < 1$, is close to one. The asymptotic approximations agreed well with the numerics, even for small values of the velocity ratio λ.

The reduced steady-state system corresponding to the chemicals, temperature and moments of the distribution was then solved in a similar manner to the previous two chapters. First, we focused our attention on the dominant reaction, corresponding to the SiO combustion responsible for the formation of microsilica, and neglected the effect of the particles on the chemical-thermal subsystem. Under these limits, we obtained asymptotic approximations for the silicon monoxide, oxygen and temperature, for two different regimes: small and large x. In the small x regime we obtained a regular perturbation solution, whereas for the large x regime we used the WKB method. In both cases, the results depend directly on the approximation obtained for u, and therefore their error increases as the parameter λ becomes smaller.

We then investigated the effect of the particles on the chemical-thermal system by solving the fully-coupled problem numerically, that is, by re-incorporating the sink of material and heat released due to the condensation of SiO_2 into particles. After transforming the results to the original coordinates by inverting the von Mises transformation, we showed heatmaps in space for all the variables. We concluded that

when the velocity ratio is small and there is more mixing involved at early stages, the reactions are more powerful initially and there is a large production of SiO_2 earlier on in the mixing layer and over a smaller region. As a consequence, more and smaller particles form in this case, whereas for almost uniform flows the mean particle size is larger and fewer particles form. Additionally, since more material is consumed by the particles for small λ values, the temperature within the reaction zone is much larger.

Finally, an implicit formula for the number density function, n, was derived depending on the previous results for the streamwise velocity, SiO_2 concentration and temperature. The distribution of particles in space is such that more and larger particles are found as we move further along the streamwise direction, x, and in all cases smaller particles are located towards the top and bottom boundaries of the mixing layer with larger particles in the middle. However, as x increases and less material is available for condensation, many smaller particles form that do not grow as much. This is particularly noticeable for smaller values of λ, with wider reaction zones and therefore shorter retention times for particles in high SiO_2 concentration areas. Integrating the results for n in space, we conclude that the final particle size distribution is not strongly influenced by the ratio of velocities, however, the particle mass allocation is. We found that when the ratio of velocities is small, more of the total particle mass corresponds to smaller particles. In contrast, when the flow is nearly uniform, particle mass allocation is almost uniform away from the peak found at the smallest particle size. These conclusions are consistent with what is seen in reality, with smaller particles forming when the furnace door is opened and the velocity of the air is much larger than the fuel velocity, causing the SiO to be depleted faster.

Chapter 7

Discussion

7.1 Summary and discussion of the thesis

In this thesis, we have studied the mechanisms for microsilica particle formation and growth inside silicon furnaces by focusing on the dynamics of the relevant chemical species and temperature within the furnace hood.

We began in Chapter 1 by introducing the silicon production process and chemical reactions taking place within a silicon furnace. We then focused on the processes occurring inside the silicon furnace hood and defined the mechanisms responsible for the formation and growth of the microsilica particles. We finished by giving an overview of previous works on topics relevant to this thesis. These included modelling of reactive gas mixtures, aerosol nucleation and growth modelling, the coupling between the latter two topics, and mathematical modelling of different processes happening within a silicon furnace.

In Chapter 2 we used ideas from the latter works to develop a mathematical model for a general furnace hood geometry. In the first part of the chapter, we derived a detailed model from first principles that captured the interactions between fluid flow, heat transfer, and chemical species and reactions. In the second part, we introduced the concept of a population balance equation as a mean to model the formation and growth of particles. This equation included terms for the nucleation and growth by condensation of particles, and the form of these terms was derived. In order to study the effects of the local conditions in a furnace hood on the final particle size distribution, both models were coupled through rate terms for nucleation and growth, and also through material sink and heat source terms.

We started the mathematical analysis of our problem in Chapter 3, where we non-dimensionalised the previous fully-coupled model and performed two-dimensional

numerical simulations using the software COMSOL. We looked at different configurations and concluded that the size of the fuel inlet did not strongly affect the results, with the reactions occurring more towards the middle of the furnace and slightly fewer particles forming for smaller inlets. However, the velocity at which the air and the fuel enter the furnace hood did influence the strength of the reactions and the final particle size distribution. Our results suggested that fewer and larger particles form when the velocities of the two streams were similar, with the opposite effect happening when the velocities are very different. The latter configurations were explored further in the chapters that followed. However, the most notable feature of these simulations was the fact that most of the dynamics occurred within a narrow reaction zone. Moreover, the order of magnitude of certain terms, such as the reaction, material consumption, and heat production rates, had to be reduced in order for the simulations to converge. This difficulty led us to focus for the remaining chapters of the thesis on smaller lengthscales and timescales through asymptotic analysis in order to capture the behaviour of the different variables within the reaction layer where particles form.

The simplest configuration, in which the chemicals are initially well-mixed, was considered in Chapter 4. Under this limit, where diffusion is instantaneous, our problem becomes a time-dependent ODEs system. Since the chemical-thermal system only depends on the second moment and not on the full particle size distribution, the population balance equation for the particles was solved separately from the ODEs system. We applied the method of characteristics and obtained an implicit solution for the particle size distribution in terms of the nucleation and growth rates. In order to solve the chemical-thermal system of equations we looked at two different regimes: zero coupling of the particles, where the mass and energy equations inform the particle growth equation but not the other way around, and the fully-coupled problem. These two cases were also explored in the following two chapters. In the decoupled case, asymptotic approximations were obtained under the assumption of an oxygen-rich environment. Our analysis suggested that the silicon monoxide reaction is much faster than the carbon monoxide one, and that if enough oxygen is available, the reactants will be depleted and hence the maximum possible number of moles of the respective product will be produced. The latter is favourable for microsilica particle formation in contrast to partial combustion of silicon monoxide. Since for the decoupled case the sink of material from particle formation was neglected, particles continued growing without bound, causing the particle size distribution to be unimodal with a peak towards the largest particle size. This limit is useful for understanding early-time dynamics or for situations where the rate of depletion of silicon monoxide

is small. On the other hand, when we incorporated the effects of the particles on the chemical-thermal subsystem, in which case only numerical simulations were possible, particle formation and growth stop once the silicon dioxide has been depleted. As a consequence, the particle size distribution becomes bimodal at later times, with a second peak appearing towards the smallest particle size due to the lack of material for the growth of new large particles.

Since the particle size distribution is highly dependent on the local conditions of the furnace hood, we would obtain different results depending on the exact spatial location. Therefore, spatial variations need to be considered when predicting the final microsilica particle size distribution. In Chapter 5, we considered a one-dimensional geometry given by a cross-section of the reaction zone. The initial spatial configuration is such that the chemicals are separated, with the fuel plentiful on one side and the oxygen plentiful on the other side of the domain. Moreover, we neglected the effects of fluid flow. The resulting system of reaction-diffusion PDEs was solved following a similar procedure to the earlier chapter. First, we looked at the decoupled case and focused on a reduced chemical-thermal system that only takes into account the dominant reaction, that is, the silicon monoxide reaction which is responsible for the formation of the particles. This subsystem was solved in two regimes, small and large time. For small times, we performed a regular perturbation analysis and obtained asymptotic approximations with diffusion as the dominant mechanism. For large times, when the reaction terms become more relevant, we used the WKB method to obtain an approximate solution. We then solved the fully-coupled system numerically, and the only differences we found were on the silicon dioxide and temperature variations. When including the effects of the particles, the silicon dioxide is depleted due to particle formation and growth, and the temperature experiences a further increase within the reaction zone due to the heat released from condensation. We used the previous results for the chemicals and temperature, for both decoupled and fully-coupled cases, into an implicit solution for the number density of particles, equivalent to the one derived in Chapter 4. We obtained similar conclusions to the well-mixed case within the core of the reaction zone, with a large number of particles of the largest possible size in both cases, and a resurgence of small particles at later times in the fully-coupled problem. In addition, the spatial distribution across the reaction zone is such that the longest-lived and thus largest particles are located toward the middle of the reaction zone, with smaller particles around the boundaries. Since the particle size distribution varies within the cross-section of the reaction zone, we integrated the results in space to gain further insight into the final microsilica output. We concluded that if we take

into account all particles in the domain, the smallest particle size peak dominates and hence is the only one apparent in the final particle size distribution. This is due to a high proportion of small particles present throughout the domain, with large ones only appearing in a narrow region at the centre of the reaction zone. The shape of the final microsilica particle size distribution is consistent with what is seen in experiments. Finally, we repeated the previous analysis considering an initial separation distance between the reactants. Our results suggested that increasing the distance that the fuel and oxidizer need to travel before interacting with each other has an effect on the final particle size distribution. Smaller and fewer particles were obtained for larger initial separation distances since the chemicals have more time to diffuse throughout the domain before encountering each other.

In Chapter 6, we explored the effects of fluid flow on the particles and included an additional spatial dimension streamwise to the reaction layer. The flow configuration taken was that of a mixing layer, with two parallel flows entering the domain at different speeds and temperatures; one composed of oxygen and the other one of silicon monoxide and carbon monoxide. We considered the steady-state problem and used the von Mises transformation to convert the reaction-diffusion-convection equations for the chemicals, temperature, and moments of the distribution into reaction-diffusion PDEs similar to those in Chapter 5. Moreover, only solving for the streamwise velocity of the flow was required. Since the velocity equation decoupled from the rest of the system, we solved it separately and obtained asymptotic approximations of the solution assuming the velocities of both streams to be similar. Thereafter, we followed a similar structure to the previous two chapters. We obtained asymptotic approximations for two different spatial regimes in the decoupled subsystem, and numerical simulations for the fully coupled problem which were then used in the particle size distribution formula. In all cases, we compared the results obtained for all variables for different values of the ratio between the initial velocities of the streams. Our results suggested that when the velocities of both streams are very different and there is a lot of mixing involved initially, more material is consumed and therefore more heat is released; additionally, a larger number of particles are produced but they are smaller. Slightly different conclusions were drawn when the results for the particle size distribution were integrated in the whole spatial domain. The results suggested that the final number density function is not hugely affected by the velocity ratio. However, the particle mass allocation does depend on the flow configuration, and we found that when the velocities ratio is small, more of the total mass corresponds to small particles.

In conclusion, in each chapter we have built on ideas from the previous ones and

extended the analysis by including additional physical effects into the model under study. Even though the well-mixed case is very simple, it still gives an effective representation of the dynamics within the flame. However, it is clear that spatial variations and the fluid flow configuration play a fundamental role in the final microsilica particle size distribution. Moreover, in Chapters 4-6 we obtained asymptotic solutions for the decoupled problem, where the particles do not influence the chemicals and the temperature, which are most useful at initial times or in situations where there is such a large quantity of silicon monoxide that is not depleted rapidly by condensation into particles.

7.2 Industrial findings and knowledge transfer

This thesis was motivated by an industrial problem proposed by Elkem ASA, who are interested in understanding how the local conditions of a silicon furnace affect the formation and growth of microsilica particles. Therefore, our aim is that the models and analyses presented here are not only of academic interest but are also useful in practical terms for our industrial partner. In this section, we will give some guidelines and advice on how to use the models and results that we have derived.

The full model derived in Chapter 2 from physical principles can be used as a starting point to study a variety of processes occurring within a silicon furnace hood or similar combustion chambers. Since it was formulated for a general furnace hood geometry, it can easily be extended to more complicated geometries and furnace configurations. Moreover, additional chemicals and reactions present in the furnace hood could be added into the model by including equivalent mass equations for the new chemical species, and by incorporating source and sink terms into the mass and heat equations corresponding to the new reactions. The particle formation and growth model could in general be used to predict particle size distributions of aerosols formed under similar conditions to condensation. It is valid for particles of a wide range of sizes, since the growth rate was derived for both the kinetic and continuum regimes. Moreover, the growth rate is given in terms of the molar concentration of the condensing material, and therefore the particles could have a different chemical composition to microsilica. Additional particle growth mechanisms, such as aggregation, could also be incorporated into the population balance equation derived in this chapter, and these will be discussed further in the next section.

The COMSOL simulations of the previous fully-coupled model, performed in Chapter 3, are most useful for understanding the general behaviour of all variables

in the system for a lengthscale and geometry representative of a real furnace. These simulations could in practice be modified in order to study different scenarios.

The well-mixed problem studied in Chapter 4 is a simple yet accurate representation of the dynamics of the chemicals, temperature and particles, and is valid on a small lengthscale within the reaction zone. For the case where particle formation does not largely affect the chemicals and temperature, we obtained asymptotic solutions for a chemical-thermal subsystem. These approximations show the dominant phenomena under the assumption of an oxygen rich environment, which is the case in most furnace operations. They are also useful for understanding the impact of model parameters, such as the ratio between the CO and SiO reaction rates, the heat generated by the reactions, and initial temperatures of the fuel and the oxidizer, on the furnace dynamics. The implicit solution obtained for the number density function of particles, n, which is similar in all chapters, is valid for any form of the nucleation rate, and of the growth rate as long as it does not depend directly on the particle size. Otherwise, an equivalent derivation of the solution may be possible for simple cases, such as for linear dependencies on s. This solution allows us to understand the effect of certain system parameters and terms on the particle size distribution. For instance, it shows that the form of the nucleation and growth rates strongly influences the shape of the distribution, with the appearance of peaks due to short times where nucleation dominates over the growth of particles. Furthermore, the approximations for n near the peak of the distribution give further insight into how the shape of the distribution is influenced by dimensionless parameters. We found that the value of the saturation concentration affects the position and height of the peak, with smaller and fewer particles forming for larger values. However, this parameter may be more challenging to control in practice. The numerical results obtained from solving the fully-coupled problem highlight the importance of including the effects of the particles on the chemical-thermal system for later stages in the process, with the appearance of a peak towards the smallest particle size, in addition to the one at the largest size. A bimodal size distribution for microsilica particles has also been found experimentally in the literature for localised areas in the furnace hood [20], with a submicron range of particle sizes containing most of the particle mass, and a micron range with fewer but much larger particles.

In Chapter 5, we extended the latter model by including a spatial dimension given by the cross-section of a reaction zone and by allowing the chemicals to diffuse prior to reacting. Our results suggest that the temperature is the highest in the middle of the reaction zone and so is the silicon dioxide concentration. The solutions to this model

also give us intuition into how particles are spatially distributed near and within the reaction zone, with smaller particles located towards its boundaries. The importance of including spatial variations is further evidenced by the change in the shape of the particle size distribution when integrating the results along the cross-section of the reaction zone, that is, when we include all particles present in the whole domain. The final particle size distribution found in this case is closer to what is observed in the microsilica output of the furnace, with a large peak located around the smallest particle size. In the final part of the chapter, we explored the effect of changing the initial separation distance between the fuel and oxidizer. Our results suggest that both chemical inputs should be placed further away from each other if slower and less powerful reactions, and therefore smaller particles are sought.

Finally, in Chapter 6 we explored the effects of fluid flow on the system by considering a two-dimensional mixing layer configuration. The asymptotic and numerical solutions derived in this chapter are useful to examine how the temperature, chemicals and particles are influenced by changes to certain flow parameters, such as the initial velocity ratio of the interacting streams, which is investigated in depth in this chapter. These results can be exploited in practice to suggest modifications to the furnace operation and design, depending on the particular furnace production objectives. Making the velocities of the two streams very different from each other, by either increasing the input velocity of the oxygen (for instance, by opening the furnace doors rather than letting the air in through the gap between the furnace and its hood) or decreasing the silicon monoxide velocity, is advised in order to increase the mixing between both streams. From our analysis, increased mixing results in wider and hotter reaction layers, and also in more and smaller particles due to shorter residence times in high SiO_2 concentration areas. The latter particle characteristics are generally preferred for many applications of microsilica [22]. Additionally, we varied other parameter values, such as the ratio between the initial concentration of oxygen to other chemicals. We concluded that oxygen availability, in addition to a sufficiently high temperature, is essential for the combustion reactions to occur, strongly influencing both the width of the reaction zone and the particle size distribution. A decrease in the availability of O_2 results in a more narrow reaction zone and hence limits SiO_2 production over a given time interval. Regarding industrial scale processes, this finding suggests that operators should provide an adequate inflow of oxygen, particularly if smaller microsilica particles are sought.

7.3 Future work

Understanding the exact mechanisms of microsilica particle formation and growth within silicon furnaces is a complex task, and therefore there are a variety of ways in which the work developed in this thesis could be extended. In this section, we discuss possible ways to build on our research and some aspects of the problem to consider in the future.

7.3.1 Introduction of further chemistry

In our model we have only considered the SiO and CO combustion reactions as the main mechanisms for microsilica particle formation. However, secondary reactions such as the Boudouard reaction or the condensation of SiO into Si+SiO_2, also take place inside the silicon furnace hood. Moreover, the presence of other elements, such as volatiles and water, can affect microsilica properties in many ways. For instance, the presence of water which evaporates would decrease the temperature of the system, so the reactions and particle growth would be slower. These can be modelled by adding conservation equations for the new chemical species, including the additional reaction rates. Furthermore, volatiles are responsible for the impurities that are sometimes present in microsilica particles. We can model these impurities by considering diffusion of the extra species to the surface of the particles, as well as diffusion of silicon dioxide which is the dominant component. The conservation equations for these extra chemicals would also have to include a sink term due to their consumption by the particles, as with the SiO_2 equation.

7.3.2 Aggregation of particles

Aggregation of particles is of particular interest to Elkem ASA since it is undesirable for good quality microsilica. By aggregation we mean coalescence between at least two particles, that is, two particles with a specific size merge completely to form a larger particle. In general, aggregation also covers intermediate situations where particles may be in physical contact with each other but without completely merging.

We can incorporate this mechanism into the population balance equation by setting h in (2.3.5) to be the respective death and birth processes of particles undergoing aggregation. Since under this mechanism, smaller particles disappear, and larger particles form, h needs to include both a sink and a source term, and the form of each of these terms is given as an integral. In this case, the population balance equation

reads

$$\begin{aligned}\frac{\partial n}{\partial t} + \boldsymbol{\nabla}\cdot(n\mathbf{v} - D_p\boldsymbol{\nabla}n) + \frac{\partial}{\partial s}\left(n\hat{G} - D_s\frac{\partial n}{\partial s}\right) \\ = \int_{s_{\min}}^{\infty}\beta(s-\hat{s},\hat{s})n(s-\hat{s})n(\hat{s})d\hat{s} - \int_{s_{\min}}^{\infty}\beta(s,\hat{s})n(s)n(\hat{s})d\hat{s},\end{aligned} \tag{7.3.1}$$

as in, *e.g* , [65, 80]. The function $\beta(s_0, s_1)$ found in the integrand of both integrals in (7.3.1) represents the aggregation frequency or probability that two parent particles of sizes s_0 and s_1 meet and merge. Furthermore, this term is multiplied by the density function of the particle-pair aggregating, which is approximated as the product of the number density of each, implying that there is no statistical correlation between the colliding parent particles [80].

The latter integro-differential equation is more challenging to solve than the one studied in this thesis, that is, (2.3.5) with $h = 0$, and in most cases the full particle size distribution cannot be retrieved. The usual approach is to use moment methods by integrating the population balance equation with respect to the particle size, which also overcomes the high dimensionality of the equation, similarly to what was done in Chapter 2. This method solves for lower-order moments of the number density function, which are usually sufficient for characterising the fine particles [64, 66].

7.3.3 Incorporation of more realistic domains and flow configurations

Whereas in this thesis we have considered the oxygen and fuel streams to be parallel to each other as they enter the domain, in reality the oxygen enters the furnace hood from the sides and the other reactants from the bottom through the charge surface. We could therefore explore the effects of this new spatial configuration on the particles formation and consider the problem of a boundary layer with fuel injection. In this case, the domain would be given by $(x, y) \in [0, \infty) \times [0, \infty)$, with oxygen being advected in through $x = 0, y > 0$, and the fuel, SiO and CO, being injected at $y = 0, x > 0$. We would use the same boundary layer equations as derived in Chapter 6 but with slightly different boundary conditions. Similar problems have been considered in the literature, for instance, in [36], where a combustible is injected through a permeable flat plate. This could be useful in our case since SiO and CO enter the furnace through voids in the charge surface.

Furthermore, one could extend our current study of the flow problem by performing a stability analysis of the laminar mixing layer, as in, *e.g.*, [74]. The predictions

obtained in Chapter 6 are only valid as long as the steady solutions remain stable, which may not be the case at higher Reynolds number due to the Kelvin-Helmholtz instability [33]. If the flow is unstable to perturbations, the discontinuous jump in velocity may induce vorticity at the interface [27]; as a result, vortices may form that could trap particles, increasing their residence time in high saturation areas and hence influencing their growth. Analysing where and under what circumstances instabilities occur in the flow would allow us to further understand our problem. However, it may be that SiO_2 depletion from particle condensation takes place before larger vortical structures form, and thus it may be more relevant when studying other particle growth mechanisms such as aggregation and agglomeration.

7.3.4 Study of compressibility effects

In Chapter 2 we derived a full model taking into account compressibility effects. However, only COMSOL simulations of this model were performed, and we assumed our flow to be incompressible thereafter in the thesis, in Chapters 4-6.

This is one of our main modelling assumptions and we will now discuss two ways in which it could be relaxed. Firstly, we notice that in our problem the Mach number, which represents the ratio of a typical flow velocity and the speed of sound, is very small, $Ma = u/\bar{c} \sim 10^{-2}$. This means that our flow is weakly compressible and this leads to important simplifications of the governing equations (2.4.1). For instance, in the small Mach number approximation, the kinetic energy is small compared to the thermal energy and so it can be neglected, and likewise the viscous term in the energy equation is negligible [10]. This is usually the case for many flames, where velocities are small and temperatures are large, leading to a small Mach number. Note however that for fast flames or detonation problems the Mach number is nonvanishing.

Secondly and more specifically, when looking at plane laminar mixing layers, the most common approach, as in, *e.g.*, [44, 51], is employing the Dorodnizyn-Howarth transformation [35, 70] into the steady-state compressible boundary layer equations, which introduces a new vertical scale

$$\bar{y} = \int_0^y \rho \mathrm{d}y. \tag{7.3.2}$$

Using (7.3.2), and the compressible stream function, Ψ, derived from the respective

continuity equation, namely

$$\frac{\partial \Psi}{\partial x} = -\rho v, \qquad \frac{\partial \Psi}{\partial y} = \rho u, \tag{7.3.3}$$

we obtain the new velocity components

$$\bar{u} = u, \qquad \bar{v} = \rho v + u \int_0^y \frac{\partial \rho}{\partial x} \mathrm{d}y. \tag{7.3.4}$$

Under the latter transformations, it can be shown that the boundary layer equations become almost identical to the corresponding ones for an incompressible flow, and therefore are equivalent to the steady-state versions of (6.1.14)-(6.1.15). However, the latter only holds under very restrictive conditions that may not be physically realistic for our particular problem. See, *e.g.*, [16, 51, 70], for a derivation of the equations and assumptions taken.

Bibliography

[1] D. V. Alexandrov (2014). *Nucleation and crystal growth in binary systems*. Journal of Physics A: Mathematical and Theoretical 47 (12):125102.

[2] A. Alshaarawi and F. Bisetti (2015). *The effect of mixing rates on the formation and growth of condensation aerosols in a model stagnation flow*. Journal of Aerosol Science 81:34–46.

[3] C. Artelt, H. Schmid, and W. Peukert (2006). *Modelling titania formation at typical industrial process conditions: effect of surface shielding and surface energy on relevant growth mechanisms*. Chemical Engineering Science 61 (1):18–32.

[4] F. Babick (2016). *Suspensions of Colloidal Particles and Aggregates*. Springer International Publishing.

[5] R. Becker and W. Döring (1935). *Kinetische behandlung der keimbildung in übersättigten dämpfen*. Annalen der Physik 416 (8):719–752.

[6] A. Bermúdez, J. L. Ferrín, and S. A. Halvorsen (2013). *Process models for the production of Microalumina*. Technical report. 97 European Study Group with Industry.

[7] E. Bouin, V. Calvez, N. Meunier, S. Mirrahimi, B. Perthame, G. Raoul, and R. Voituriez (2012). *Invasion fronts with variable motility: phenotype selection, spatial sorting and wave acceleration*. Comptes Rendus Mathematique 350 (15-16):761–766.

[8] C. E. Brennen (2005). *Fundamentals of multiphase flows*. Cambridge University Press.

[9] R. Brun (2009). *Introduction to reactive gas dynamics*. OUP Oxford.

[10] J. Buckmaster (1985). *The Mathematics of Combustion*. Society for Industrial and Applied Mathematics.

[11] S. P. Burke and T. Schumann (1928). *EW.: Diffusion Flames. 1st Symposium on Combustion*.

[12] A. Burshtein (2008). *Introduction to Thermodynamics and Kinetic Theory of Matter*. Wiley.

[13] A. Casaccio (1964). *Similar solutions for the laminar mixing of reactive gases*. AIAA Journal 2 (8):1403–1409.

[14] *CFD Module User's Guide* (2017). COMSOL Multiphysics® v. 5.3. COMSOL AB, Stockholm, Sweden, pages 120–126.

[15] P. L. Chambre and A. Acrivos (1956). *On chemical surface reactions in laminar boundary layer flows*. Journal of Applied Physics 27 (11):1322–1328.

[16] D. R. Chapman (1950). *Laminar mixing of a compressible fluid*. N.A.C.A. T.R. No. 958.

[17] D. S. Cohen, F. C. Hoppensteadt, and R. M. Miura (1977). *Slowly modulated oscillations in nonlinear diffusion processes*. SIAM Journal on Applied Mathematics 33 (2):217–229.

[18] C. Cuesta and J. King (2010). *Front propagation in a heterogeneous Fisher equation: the homogeneous case is non-generic*. The Quarterly Journal of Mechanics & Applied Mathematics 63 (4):521–571.

[19] P. F. DeCarlo, J. G. Slowik, D. R. Worsnop, P. Davidovits, and J. L. Jimenez (2004). *Particle morphology and density characterization by combined mobility and aerodynamic diameter measurements. Part 1: Theory.* Aerosol Science and Technology 38 (12):1185–1205.

[20] E. Dingsøyr, M. Dåstøl, and W. Wedberg (1992). *Particle size and particle size distribution of Elkem Microsilica and its relevance to technical application. Proceedings of the 5. European Symposium Particle Characterization, Nurnberg, Germany*, p. 24–26.

[21] T. A. Driscoll, N. Hale, and L. N. Trefethen (2014). *Chebfun Guide.* Oxford. Pafnuty Publications.

[22] Elkem (2018). Personal communication.

[23] P. Fidjestol and M. Dastol (2008). *The history of silica fume in concrete–From novelty to key ingredient in high performance concrete. Proceedings of the Congresso Brasileiro do Concreto. 4th-9th Sept.*

[24] R. Flagan and J. Seinfeld (2012). *Fundamentals of Air Pollution Engineering.* Dover.

[25] R. C. Flagan and M. M. Lunden (1995). *Particle structure control in nanoparticle synthesis from the vapor phase.* Materials Science and Engineering: A 204 (1):Proceedings of the Symposium on Engineering of Nanostructured Materials, 113–124.

[26] S. Friedlander (2000). *Smoke, Dust, and Haze: Fundamentals of Aerosol Dynamics.* Oxford University Press.

[27] S. Friedlander and A. Lipton-Lifschitz (2003). *Chapter 8 - Localized Instabilities in Fluids.* Volume 2. Handbook of Mathematical Fluid Dynamics. North-Holland, p. 289–354.

[28] D. R. Gaskell and D. E. Laughlin (2017). *Introduction to the Thermodynamics of Materials.* CRC Press.

[29] R. González-Fariña, A. Münch, J. M. Oliver, and R. A. Van Gorder (2020). *Modeling Microsilica particle formation and growth due to the combustion reaction of silicon monoxide with oxygen.* SIAM Journal on Applied Mathematics 80 (2):1003–1033.

[30] C. Grosch and T. Jackson (1991). *Ignition and structure of a laminar diffusion flame in a compressible mixing layer with finite rate chemistry.* Physics of Fluids A: Fluid Dynamics 3 (12):3087–3097.

[31] S. A. Halvorsen, A. Shei, and J. H. Downing (1992). *A unidimensional model for the (ferro)silicon process. Electric Furnace Conference Proceedings.* Volume 50.

[32] T. Hannesson (2016). *The Si Process Drawings.* Elkem Iceland.

[33] H. von Helmholtz (1868). *über discontinuirliche Flüssigkeits-Bewegungen.* Akademie der Wissenschaften zu Berlin.

[34] L. N. Howard and N. Kopell (1977). *Slowly varying waves and shock structures in reaction-diffusion equations.* Studies in Applied Mathematics 56 (2):95–145.

[35] L. Howarth (1948). *Concerning the effect of compressibility on laminar boundary layers and their separation.* Proceedings of the Royal Society of London. Series A. Mathematical and Physical Sciences 194 (1036):16–42.

[36] A. Ishak, R. Nazar, and I. Pop (2007). *Boundary layer on a moving wall with suction and injection.* Chinese Physics Letters 24 (8):2274.

[37] M. Kadkhodabeigi (2011). *Modeling of Tapping Processes in Submerged Arc Furnaces.* PhD thesis. Norwegian University of Science and Technology.

[38] M. Kadkhodabeigi, H. Tveit, and K. H. Berget (2010). *Silicon process - New hood design for tapping gas collection*. INFACON XII – June 6-9, 2010, Helsinki, Finland.

[39] N. E. Kamfjord (2012). *Mass and Energy Balances of the Silicon Process - Improved Emission Standards*. PhD thesis. Norwegian University of Science and Technology.

[40] T. V. Karman (1921). *Über laminare und turbulente Reibung*. ZAMM-Journal of Applied Mathematics and Mechanics/Zeitschrift für Angewandte Mathematik und Mechanik 1 (4):233–252.

[41] I. Kennedy (1985). *Flow field effects on nucleation in a reacting mixing layer*. The Physics of fluids 28 (12):3515–3524.

[42] G. Lee, I. Dobbs-Dixon, C. Helling, K. Bognar, and P. Woitke (2016). *Dynamic mineral clouds on HD 189733b*. Astronomy & Astrophysics 594:A48.

[43] P. A. Libby (1962). *Theoretical analysis of turbulent mixing of reactive gases with application to supersonic combustion of hydrogen*. ARS Journal 32 (3):388–396.

[44] P. A. Libby and J. A. Schetz (1963). *Approximate analysis of the slot injection of a gas in laminar flow*. AIAA Journal 1 (5):1056–1061.

[45] M. J. Lighthill (1950). *Contributions to the theory of heat transfer through a laminar boundary layer*. Proceedings of the Royal Society of London. Series A. Mathematical and Physical Sciences 202 (1070):359–377.

[46] H. B. Lim, T. H. Kim, S. H. Eom, Y.-i. Sung, M. H. Moon, and D. W. Lee (2002). *Vaporization process of SiO2 particles for slurry injection in inductively coupled plasma atomic emission spectrometry*. Journal of Analytical Atomic Spectrometry 17:109–114.

[47] J. Lothe and G. M. Pound (1962). *Reconsiderations of nucleation theory*. The Journal of Chemical Physics 36 (8):2080–2085.

[48] B. F. Lund, B. A. Foss, and K. R. Løvåsen (2006). *Analysis and characterization of complex reactor behaviour: A case study*. Journal of Process Control 16 (7):711–718.

[49] B. Lund, B. Foss, K. Løvåsen, and B. Ydstie (2004). *Sensitivity analysis of a dynamic model for submerged arc silicon furnaces. Proceedings: Tenth International Ferroalloys Congress*. Volume 1, p. 4.

[50] E. V. Makoveeva and D. V. Alexandrov (2018). *A complete analytical solution of the Fokker–Planck and balance equations for nucleation and growth of crystals*. Philosophical Transactions of the Royal Society of London A: Mathematical, Physical and Engineering Sciences 376 (2113).

[51] F. E. Marble and T. C. Adamson Jr (1954). *Ignition and combustion in a laminar mixing zone*. Journal of Jet Propulsion 24 (2):85–94.

[52] D. L. Marchisio and R. O. Fox (2005). *Solution of population balance equations using the direct quadrature method of moments*. Journal of Aerosol Science 36 (1):43–73.

[53] W. J. Massman (1998). *A review of the molecular diffusivities of H2O, CO2, CH4, CO, O3, SO2, NH3, N2O, NO, and NO2 in air, O2, and N2 near STP*. Atmospheric Environment 32 (6):1111–1127.

[54] R. McGraw (1997). *Description of aerosol dynamics by the quadrature method of moments*. Aerosol Science and Technology 27 (2):255–265.

[55] D. Mueller, R. Dillenbeck III, et al. (1991). *The versatility of silica fume as an oilwell cement admixture. SPE Production Operations Symposium*. Society of Petroleum Engineers.

[56] W. Nachbar, F. Williams, and S. Penner (1959). *The conservation equations for independent coexistent continua and for multicomponent reacting gas mixtures*. Quarterly of Applied Mathematics 17 (1):43–54.

[57] M. K. Næss (2013). *Mechanisms and Kinetics of Liquid Silicon Oxidation*. PhD thesis. Norwegian University of Science and Technology.

[58] M. K. Næss, G. Tranell, J. E. Olsen, N. E. Kamfjord, and K. Tang (2012). *Mechanisms and Kinetics of Liquid Silicon Oxidation During Industrial Refining*. Oxidation of Metals 78 (3):239–251.

[59] K. Okuyama, Y. Kousaka, D. R. Warren, R. C. Flagan, and J. H. Seinfeld (1987). *Homogeneous nucleation by continuous mixing of high temperature vapor with room temperature gas*. Aerosol Science and Technology 6 (1):15–27.

[60] N. Peters (2000). *Turbulent Combustion*. Cambridge University Press.

[61] S. Pope (2000). *Turbulent Flows*. Cambridge University Press.

[62] S. E. Pratsinis (1988). *Simultaneous nucleation, condensation, and coagulation in aerosol reactors*. Journal of Colloid And Interface Science 124 (2):416–427.

[63] R. Prud'homme (2010). *Flows of Reactive Fluids*. Birkhäuser Boston.

[64] V. Raman and R. O. Fox (2016). *Modeling of Fine-Particle Formation in Turbulent Flames*. Annual Review of Fluid Mechanics 48 (1):159–190.

[65] D. Ramkrishna (2000). *Population Balances: Theory and Applications to Particulate Systems in Engineering*. Elsevier Science.

[66] S. Rigopoulos (2010). *Population balance modelling of polydispersed particles in reactive flows*. Progress in Energy and Combustion Science 36 (4):412–443.

[67] S. Rigopoulos (2007). *PDF method for population balance in turbulent reactive flow*. Chemical Engineering Science 62 (23):6865–6878.

[68] A. Roine (2018). *HSC Chemistry®*. Software available at `www.outotec.com/HSC`. Outotec, Pori.

[69] A. Schei, J. K. Tuset, and H. Tveit (1998). *Production of High Silicon Alloys*. Tapir, Trondheim, Norway.

[70] H. Schlichting and K. Gersten (2016). *Boundary-layer theory*. Springer.

[71] J. Seinfeld and S. Pandis (2016). *Atmospheric Chemistry and Physics: From Air Pollution to Climate Change*. Wiley.

[72] N. Settumba and S. C. Garrick (2003). *Direct numerical simulation of nanoparticle coagulation in a temporal mixing layer via a moment method*. Journal of aerosol science 34 (2):149–167.

[73] F. Sewerin and S. Rigopoulos (2017). *An LES-PBE-PDF approach for modeling particle formation in turbulent reacting flows*. Physics of Fluids.

[74] D. Shin and J. H. Ferziger (1991). *Linear stability of the reacting mixing layer*. AIAA journal 29 (10):1634–1642.

[75] R. Siddique (2011). *Utilization of silica fume in concrete: Review of hardened properties*. Resources, Conservation and Recycling 55:923–932.

[76] B. M. Sloman, C. P. Please, R. A. Van Gorder, A. M. Valderhaug, R. G. Birkeland, and H. Wegge (2017). *A Heat and Mass Transfer Model of a Silicon Pilot Furnace*. Metallurgical and Materials Transactions B 48 (5):2664–2676.

[77] B. M. Sloman, C. P. Please, and R. A. Van Gorder (2018). *Asymptotic analysis of a silicon furnace model*. SIAM Journal on Applied Mathematics 78 (2):1174–1205.

[78] B. M. Smirnov (2012). *Nanoclusters and microparticles in gases and vapors*. Walter de Gruyter.

[79] M. V. Smoluchowski (1918). *Versuch einer mathematischen Theorie der Koagulationskinetik kolloider Lösungen*. Zeitschrift für physikalische Chemie 92 (1):129–168.

[80] J. Solsvik and H. A. Jakobsen (2015). *The foundation of the population balance equation: a review*. Journal of Dispersion Science and Technology 36 (4):510–520.

[81] S. Stankic, M. Cottura, D. Demaille, C. Noguera, and J. Jupille (2011). *Nucleation and growth concepts applied to the formation of a stoichiometric compound in a gas phase: The case of MgO smoke*. Journal of Crystal Growth 329 (1):52–56.

[82] W. Tsang and R. F. Hampson (1986). *Chemical kinetic data base for combustion chemistry. Part I. Methane and related compounds*. Journal of Physical and Chemical Reference Data 15 (3):1087–1279.

[83] S. R. Turns (2000). *An Introduction to Combustion: Concepts and Applications*. 2nd. McGraw-Hill Science Engineering.

[84] G. D. Ulrich (1971). *Theory of Particle Formation and Growth in Oxide Synthesis Flames*. Combustion Science and Technology 4 (1):47–57.

[85] J. Vasiliu (1962). *Turbulent mixing of a rocket exhaust jet with a supersonic stream including chemical reactions*. Journal of the Aerospace Sciences 29 (1):19–28.

[86] G. Wang and S. C. Garrick (2006). *Modeling and simulation of titania formation and growth in temporal mixing layers*. Journal of Aerosol Science 37 (4):431–451.

[87] P. K. Wang (2013). *Physics and Dynamics of Clouds and Precipitation*. Cambridge University Press.

[88] D. R. Warren and J. H. Seinfeld (1985). *Prediction of aerosol concentrations resulting from a burst of nucleation*. Journal of Colloid and Interface Science 105 (1):136–142.

[89] E.-M. Wartha, M. Bösenhofer, and M. Harasek (2020). *Characteristic Chemical Time Scales for Reactive Flow Modeling*. Combustion Science and Technology:1–26.

[90] S. Whitaker (2009). *Derivation and application of the Stefan-Maxwell equations*. Revista Mexicana de Ingenieria Quimica 68:213–243.

[91] F. A. Williams (2018). *Combustion Theory*. CRC Press.

[92] F. Williams (1971). *Theory of combustion in laminar flows*. Annual Review of Fluid Mechanics 3 (1):171–188.

[93] Y. Xiong and S. E. Pratsinis (1991). *Gas phase production of particles in reactive turbulent flows*. Journal of Aerosol Science 22 (5):637–655.

[94] K. Zhou, A. Attili, A. Alshaarawi, and F. Bisetti (2014). *Simulation of aerosol nucleation and growth in a turbulent mixing layer*. Physics of Fluids 26 (6):065106.

[95] A. Zucca, D. L. Marchisio, A. A. Barresi, and R. O. Fox (2006). *Implementation of the population balance equation in CFD codes for modelling soot formation in turbulent flames*. Chemical Engineering Science 61 (1):87–95.